Monolithic III–V quantum-dot light sources on silicon for silicon photonics

Mengya Liao

A thesis submitted to University College London for the degree of
Doctor of Philosophy (PhD)

Department of Electrical and Electronic Engineering
University College London

September 2019

Statement of originality

I, Mengya Liao, confirm that the work presented in this thesis is my own. Where information has been derived from other sources, I confirm that this has been indicated in the thesis.

Signed: Mengya Liao

Date: 12/12/2019

Abstract

Epitaxial growth of III–V materials on silicon (Si) substrates is one of the most promising techniques for generating coherent light on Si and offers a low-cost and high-yield solution for Si photonics. The main challenge of this technique is the large material dissimilarity between group IV and III–V compounds. These differences between group IV and III–V tend to produce various types of defects which all generate non-radiative recombination centres and dramatically undermine the promise of III–V materials. Multiple strategies for novel epitaxial growth technologies have been employed in order to reduce the defect density, resulting in high-quality III–V materials on Si.

Very recently, III–V quantum-dot (QD) structures have drawn increasing attention for the implementation of compound semiconductor lasers on Si, due to their low threshold current density and reduced temperature sensitivity. In addition, QD structures have also been proven to be less sensitive to defects than conventional bulk materials and quantum well structures, mainly due to the stronger carrier localisation and hence reduced interaction with the defects. As a result, high-performance Si-based QD laser devices have been developed intensively. In order to fully utilize the advantages of Si photonics, the next challenge is to monolithically integrate the high-performance III-V QD lasers with other components, such as modulators and waveguides on a Si platform for information processing and transmission systems.

In this thesis, an investigation of Si-based QD laser performance in a practical data communication system has been carried out in Chapter 3. An ultra-low relative intensity noise of <–150 dB/Hz and 25.6 Gb/s data transmission over a 13.5 km single-mode fibre by an externally modulated QD laser on Si have been demonstrated. Post-fabrication of Si-based QD lasers by focused ion beam and selective area intermixing of III–V QD on Si is discussed in Chapters 4 and 5, respectively. All of the studies aim to prove the feasibility of enabling the direct integration of Si-based QD lasers with other Si photonics components to provide a comprehensive Si photonic integration technology.

Impact statement

The ever-growing increase in global internet traffic imposes significant challenges on data centre operators. Traditional copper cabling with a slow data transfer capacity and expensive III-V optical transceivers are stifling data centre evolution. Silicon photonics, on the other side, offers the promise of low-cost solutions for optical communications and high-speed interconnects as a result of the maturity of CMOS processing technology. Over the last 30 years, many CMOS-compatible silicon photonics components have been realised, including optical modulators, high-speed photodetectors and various waveguide structures. However, the lack of a reliable and efficient integrated light source has become the bottleneck of the whole silicon photonics industry due to the indirect bandgap of silicon. In contrast, direct bandgap III–V compounds have robust photonic properties that can be tailored for III–V emitters operating at various wavelengths with high efficiency, large direct modulation bandwidth and sufficient optical power output for many photonic applications. Monolithically integrating III–V photonic components with silicon microelectronics would thus provide the ideal solution for silicon photonics with low-cost and high-volume manufacturability. Moreover, use of the novel material of self-assembled III–V quantum dots as the active region of the lasers brings superior benefits of temperature stability and high-temperature operation. However, the application of monolithically grown III–V quantum dot lasers on silicon in photonic integration circuits is still in the research stage, and there are still challenges remaining before commercialisation can be achieved.

This PhD research project firstly focuses on the demonstration of high-performance III–V quantum dot lasers directly grown on silicon substrates that can be fully utilised as reliable light sources in 25 Gb/s data transmission. This work shows that the 4 × 25 Gb/s optical transmitters, which are compatible with the IEEE 100 Gb/s Ethernet standard, can be developed by our monolithically grown lasers for future intra-data centre communication. Our work has been selected as the cover story in the high-profile journal *Photonics research.*

Moreover, the feasibility and implementation methods of the integration of grown lasers with electro-absorption modulators on the same silicon platform have been studied in this thesis. These works will make significant contributions towards the realisation of comprehensive low-cost optical transmitters for silicon photonics. The final goal of our work is to develop low-cost silicon photonics chips containing dozens or even hundreds of compact monolithic III–V lasers, which will expedite the progress toward terabyte-scale data transfer. We believe it will have a decisive impact on the data communication industry.

Acknowledgements

Undertaking this PhD has been a truly life-changing experience for me, and it would not have been possible to do without the support and guidance that I received from many people.

Firstly, I would like to express my sincere gratitude to my primary supervisor, Dr Siming Chen, for his support, encouragement and guidance throughout this work. Without his help and invaluable insights, it would not have been as comprehensive or complete. I also would like to express thanks to my secondary supervisor, Prof. Huiyun Liu, for his kind guidance and full support of MBE growth. Moreover, I would like to thanks Dr Chin-Pang Liu for his help and fruitful discussion in my study period.

I would like to acknowledge my colleagues from the MBE group of UCL: Dr Jiang Wu, Dr Mingchu Tang, Dr Dongyoung Kim, Dr Jae-Seong Park, Dr Yunyan Zhang, Dr Pamela Jurczak, Mr Kevin Lee, Dr Arthur Onno, Dr Xuezhe Yu, Dr Hao Xu, Mr Shun Chan, Mr Zizhuo Liu, Miss Shujie Pan, Miss Ying Lu, Miss Victoria Cao, Mr Keshuang Li and Mr Huiwen Deng, for their wonderful collaboration. Research is not always easy, but thanks to all of you, it has been a pleasure. Also, I would like to give special thanks to Mr Daqian Guo, who has always been by my side. I really appreciate him making my life easier and happier.

During my exchange visit in China, I would like to thank Prof. Zhaoyu Zhang and other colleagues from The Chinese University of Hong Kong, Shenzhen and Southern University of Science and Technology, for hosting me and invaluable assistance in laser device fabrication.

Finally, I would like to thank my family, my parents and sister, for their continued support and believing in me and giving me the confidence. You are always there for me. I hope I make you proud and appreciated.

Table of Contents

List of Abbreviations

ADC: Analogue-to-digital converter

AFM: Atomic force microscope

APB: Antiphase boundaries

APD: Antiphase domains

ASE: Amplified spontaneous emission

BCB: Benzocyclobutene

BER: Bit-error rate

BSE: Back-scattered electrons

CMOS: Complementary metal-oxide semiconductor

CPW: Coplanar waveguide

CVD: Chemical vapour deposition

CW: Continuous-wave

DFB: Distributed feedback

DFL: Dislocation filter layer

DML: Directly modulated laser

DOS: Density of state

DWELL: Dot-in-well

EA: Electro-absorber

EBL: Electron beam lithography

EL: Electroluminescence

EML: EA-modulated laser

EQE: External quantum efficiency

FEC: Forward error correction

FIB: Focused ion beam

FP: Fabry-Perot

FWHM: Full width at half maximum

GoVS: GaAs-on-v-groove Si

GS: Ground state

HAADF: High angle annular dark field

HF: Hydrofluoric acid

HSQ: Hydrogen silsesquioxane

ICP: Inductively coupled plasma

InP: Indium phosphide

IPA: Isopropyl alcohol

ISI: Inter-symbol interference

ISO: Optical isolator

I-V: Current-voltage

LEF: Linewidth enhancement factor

L-I: Light-current

L-I-V: Light-current-voltage

MBE: Molecular beam epitaxy

ML: Monolayer

MOCVD: Metal-organic chemical vapour deposition

MOVPE: Metal-organic vapour phase epitaxy

MZM: Mach-Zehnder modulator

NL: Nucleation layer

PD: Photodetector

PECVD: Plasma-enhanced chemical vapour deposition

PL: Photoluminescence

PPG: Pseudorandom pattern generator

PVD: Physical vapour deposition

QCSE: Quantum confined Stark effect

QD: Quantum dot

QW: Quantum well

RIE: Reactive ion etcher

RIN: Relative intensity noise

RMS: Root-mean-square

RT: Room temperature

RTA: Rapid thermal annealing

RTP: Rapid thermal process

SE: Secondary electrons

SEM: Scanning electron microscopy

Si: Silicon

S-K: Stranski–Krastanov

SLD: Superluminescent light-emitting diode

SLS: Strained layer superlattice

SMF: Single-mode fibre

SNR: Signal-to-noise ratio

SOA: Semiconductor optical amplifier

SOI: Silicon-on-insulator

SRL: Strain reduced layer

STEM: Scanning transmission electron microscopy

TEM: Transmission electron microscope

TW: Traveling wave

VPE: Vapour phase epitaxy

WDM: Wavelength division multiplexing

WPE: Wall-plug efficiency

List of Figures

List of Tables

List of Publications

Journal Publications

[1] **Liao, M.**, Li, W., Tang, M., Li, A., Chen, S., Seeds, A., and Liu, H. “Selective area intermixing of III-V quantum-dot lasers grown on silicon with two wavelength lasing emissions,” *Semicond. Sci. Technol.*, vol.33, no.8, 2019.

[2] **Liao, M.**, Chen, S., Park,J. S., Seeds, A., and Liu, H. “III–V quantum-dot lasers monolithically grown on silicon,” *Semicond. Sci. Technol.*, vol. 33, no. 12, p. 123002, Dec. 2018.

[3] **Liao, M.**, Chen, S., Liu, Z., Wang, Y., Ponnampalam, L., Zhou, Z., Wu, J., Tang, M., Shutts, S., Liu, Z., Smowton, P., Yu, S., Seeds, A. and Liu, H. “Low-noise 1.3 μm InAs/GaAs quantum dot laser monolithically grown on silicon,” *Photonics Research*, vol. 6, no. 11, pp. 1062-1066, 2018.

[4] **Liao, M**., Chen, S., Hou, S., Chen, S., Wu, J., Tang, M., Kennedy, K., Li, W., Kumar, S., Martin, M., Baron, T., Jin, C., Ross, I., Seeds, A. and Liu, H. “Monolithically Integrated Electrically Pumped Continuous-Wave III-V Quantum Dot Light Sources on Silicon,” *IEEE Journal of Selected Topics in Quantum Electronics*, p. 1900910, 2017.

[5] Chen, S., **Liao, M**., Tang, M., Wu, J., Martin, M., Baron, T., … Liu, H., “Electrically pumped continuous-wave 1.3 μm InAs/GaAs quantum dot lasers monolithically grown on on-axis Si (001) substrates,” *Opt. Express*, vol. 25, no. 5, p. 4632, 2017.

[6] Li, K., Liu, Z., Tang, M., **Liao, M.**, Kim, D., Deng, H., Sanchez, A., Beanland, R., Martin, M., Baron, T., Chen, S., Wu, J., Seeds, A. and Liu, H. “O-band InAs/GaAs quantum dot laser monolithically integrated on exact (001) Si substrate,”, *Journal of Crystal Growth*, vol.511, pp. 56-60, 2019.

[7] Liu, Z., Hantschmann, C., Tang, M., Lu, Y., Park,J. S., **Liao, M**., Pan, J., Sanchez, A., Beanland, R., Martin, M., Baron,. T, Chen, S., Seeds, A., White, I., Penty, R. and Liu, H. “Origin of defect tolerance in InAs/GaAs quantum dot lasers grown on silicon,” *J. Light. Technol.*, pp. 240–248, 2019.

[8] Hantschmann, C., Vasil’ev, P. P., Wonfor, A., Chen, S., **Liao, M.**, Seeds, A., Liu, H., Penty, R. and White, I., “Understanding the Bandwidth Limitations in Monolithic 1.3 µm InAs/GaAs Quantum Dot Lasers on Silicon,” *J. Light. Technol.*, pp. 949-955, 2018.

[9] Hantschmann, C., Vasil’ev, P. P., Chen, S., **Liao, M.**, Seeds, A., Liu, H., Penty, R. and White, I.,, “Gain Switching of Monolithic 1.3 µm InAs/GaAs Quantum Dot Lasers on Silicon,” *J. Light. Technol.*, pp. 3837-3842, 2018.

[10] Wang, Y., Chen, S., Yu, Y., Zhou, L., Liu, L., Chuan, Y. C., **Liao, M.**, Tang, M., Liu, Z., Wu, J., Li, W., Ross, I., Seeds, A., Liu, H. and Yu, S. “Monolithic Quantum-Dot Distributed Feedback Laser Array on Si,” *Optica*, 5(5), pp. 528-533, 2018.

[11] Kryzhanovskaya, N., Moiseev, E., Polubavkina, Y., Maximov, M., Kulagina, M., Troshkov, S., Zadiranov, Y., Guseva, Y., Lipovskii, A., Tang, M., **Liao, M.**, Wu, J., Chen, S., Liu, H. and Zhukov, A. “Heat-sink free CW operation of injection microdisk lasers grown on Si substrate with emission wavelength beyond 1.3 µm,” *Optics Letters*, vol. 42, no.17, p. 3319, 2017.

[12] Kryzhanovskaya, N., Moiseev, E., Polubavkina, Y., Maximov, M., Mokhov, D., Morozov, I., Kulagina, M., Zadiranov, Y., Lipovskii, A.,Tang, M., **Liao, M.**, Wu, J., Chen, S., Liu, H., and ZhukovElevated, A. “Temperature lasing from injection microdisk lasers on silicon,” *Laser Physics Letters*, vol.15, no.1, p. 15802, 2017.

[13] Tang M., Chen S., Wu J., Jiang Q., Kennedy K., Jurczak P., **Liao M.**, Beanland R., Seeds A., and Liu H., “Optimizations of Defect Filter Layers for 1.3-µm InAs/GaAs Quantum-Dot Lasers Monolithically Grown on Si Substrates,” *IEEE Journal of Selected Topics in Quantum Electronics,* vol. 22, no. 6, pp. 50-56, 2016.

Selected Conference Proceedings

[1] **Liao, M.**, et al. “Monolithic Integration of 1.3 μm III-V Quantum-Dot Lasers on Si for Si Photonics,” *Conference on Lasers and Electro-Optics (CLEO),* San Jose, CA, pp. 1-2, 2018.

[2] **Liao, M.**, et al. “High-performance InAs/GaAs quantum-dot laser diodes monolithically grown on silicon for silicon photonics,” *The European Conference on Lasers and Electro-Optics*, Optical Society of America, CB_4_3 2017.

[3] **Liao, M.**, et al. “Integrating III-V quantum dot lasers on silicon substrates for silicon photonics,” *Proc. SPIE 10108, Silicon Photonics XII,* 101081A. 2017.

[4] **Liao, M.**, et al. “InAs/GaAs quantum-dot light emitters monolithically grown on Si substrate,” *Proc. SPIE 9758, Quantum Dots and Nanostructures: Growth, Characterization, and Modeling XIII,* 975803, 2016.

Conference Presentations

[1] “Electrically pumped continuous-wave 1.3 μm InAs quantum dot lasers directly grown on on-axis Si (001)” CLEO-PR, OECC and PGC, Photonics 2017 @SG in Singapore (31st July- 4th August 2017)

[2] “Continuous-wave III-V Quantum Dot broadband light source on silicon” UK semiconductor conference 2017 in Sheffield (12th and 13th July 2017)

[3] “Continuous-wave III-V Quantum Dot broadband light source on silicon” Semiconductor and Integrated Optoelectronics (SOIE) in Cardiff (18th-20th April 2017)

[4] “Practical III-V Quantum Dot laser on Silicon” UK semiconductor conference 2016 in Sheffield (6th and 7th July 2016)

Chapter 1

Introduction

1.1 On-chip light emitters for silicon photonics

The explosive growth of global internet protocol traffic is predicted to reach 3.3 ZB (ZB=1000 EB) in 2021 according to a Cisco forecast [1], which brings a huge challenge for the data communication industry, and especially for data centres. As the need for data channel rates inside data centres scales to 100 Gb/s and beyond [2], traditional copper cabling is stifling this data centre evolution because of its slow data transfer capacity [3]. New interconnection schemes with optical interconnect for data transmission have been launched to provide higher throughput and reduced power consumption [4]. Figure 1.1 summarizes the evolution of Google intra-data centre optical interconnect technology [5]. In the first design of the data centre in 2004, only the copper cables were utilized. In 2007, Google was likely the first to adopt optical interconnection, i.e. 10 Gb/s vertical-cavity surface-emitting laser (VCSEL) in multi-mode fibre (MMF) in the data centre. By increasing the number of lanes and doubling the data rate, the second generation of 40 Gb/s and third generation of 100 Gb/s were achieved [5]. However, MMF transmission using VCSEL (850 nm) is typically limited to a link distance of below 300 m [6]. It can be only used for transmission between servers and top of rack switch. Wavelength-division multiplexing (WDM) with directly modulated laser (DML) array and single-mode fibre (SMF) technology was used for more extended reach (leaf to spine and above) [7]. The fourth generation of 400Gb/s optical transceivers are also being deployed in the data centres by using more bandwidth-efficient external modulation (PAM4: four-level pulse amplitude modulation) and further increasing the lane number [6].

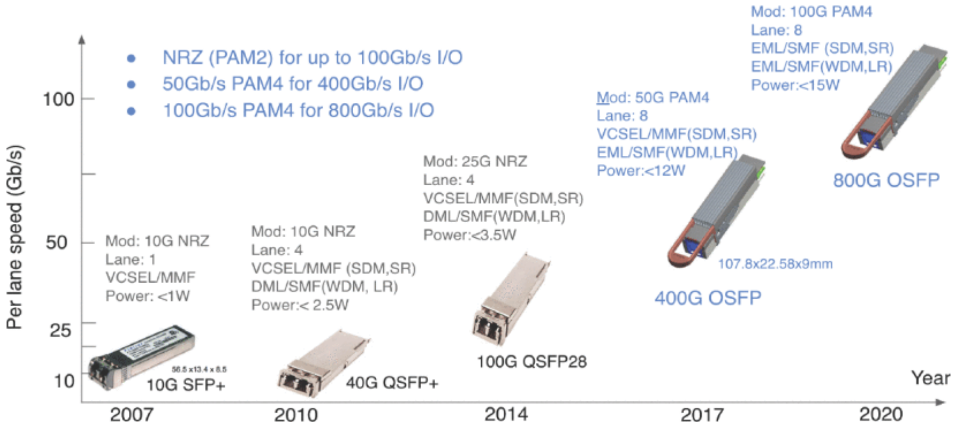

Figure 1.1 Evolution of Google intra-data centre interconnects technology [8].

In today’s data centre, for example, in Google Jupiter data centre, a mix of copper, short-reach multimode optics, and long-reach single-mode optics are employed to achieve the maximum cost effectiveness [5]. The total number of optical transceivers used is more than 100,000 per fabric [5]. Therefore, to reduce the price of the transceivers is significant for data centre development. Indium phosphide (InP) and silicon (Si) are the commonly used platforms for large-scale integration of the optical components for the medium and long optical links [9]. Although InP-based photonic integration circuits offer a state-of-the-art performance of optoelectronic devices and dominate the transceiver market for metro and long-haul telecom transmission [10], the high substrate cost ($4.55/cm^2) and small wafer size of InP (maximum 150 mm) [11] limit the substantial applications for the shorter-reach (from hundreds metres up to 10 km) intra-data centre networking [12]. In contrast, the Si complementary metal-oxide-semiconductor (CMOS) platform allows higher volume manufacture of Si optical component technology at much larger wafer sizes (maximum 450 mm) [13]. Benefiting from the low-cost Si substrate ($0.20/cm^2) and the advanced CMOS techniques, Si photonics offers the tantalising promise of cost-effectively fulfilling the ever-growing requirements for hyper-scale data centres [14]–[17].

Si photonics research can be dated back to the 1980s. Over the last few decades, the Si photonics community has made tremendous progress towards developing individual Si-based photonic building blocks, including Si-on-insulator (SOI) waveguides [18][19], Si modulators [20]–[23], multiplexers/demultiplexers [24][25] and Ge photodetectors [26]–[28]. However, full utilisation of silicon photonics has been severely limited due to the indirect bandgap of Si and Ge, a significant challenge posed by nature [29]. Thus, it is challenging to use group IV materials as efficient light emitters. All recent lasers developed on group IV materials, such as Si Raman lasers [30] and Ge lasers by band engineering [31][32], have resulted in high threshold current and low quantum efficiency. To circumvent the inefficient light emission from Si, current approaches for realising on-chip light sources typically utilise heterogeneous integration of well-established III–V semiconductor lasers with Si substrates via three methods: die bonding, wafer bonding or direct epitaxial growth [29], [33]–[38].

Firstly, die bonding is used to integrate pre-fabricated photonic components on Si with III–V lasers grown on their native substrates [39]. This method allows the pre-testing of laser devices before integration and potentially retains the high reliability of the photonic chips. The conventional die bonding method has a high assembly cost, and large-scale integration is disabled by the accuracy alignment requirements [37][39]. Novel approaches [40]–[42] have been taken to increase the alignment tolerance and improve the fabrication volume for the new generation of die bonding. On the other hand, the wafer bonding allows the wafer-scale process after bonding III–V thin film on Si/SOI substrates, which enables potential lower cost, better alignment and higher density of integration [38]. Both of die [41] and wafer bonding [43] can realise the efficient waveguide coupling from the III–V laser to the patterned SOI wafer via “evanescent coupling” by the refractive index contrast. Recently, Intel has successfully launched the 100 Gb/s Si-based optical transceivers via the hybrid Si laser (wafer bonding) technique [39] and is shipping them in volume.

Although the integration of III–V lasers on Si via die/wafer bonding has already been commercialised, the manufacturing volume is still limited by the wafer size of III–V substrates. The third approach, direct epitaxial growth of III–V materials on Si substrates, allows III–V compound materials to be grown directly on large-size Si wafers using molecular beam epitaxy (MBE), chemical vapour deposition (CVD) or vapour phase epitaxy (VPE) [44] technologies. Thus, it seems more promising for low-cost and high-volume manufacturability in the long-term [37]. For applications such as ultra-high-bandwidth optical interconnections, the required number of light sources may exceed 1000 for over 10 Tb/s bandwidth by assuming 10 Gb/s per channel [45]. Achieving a large number of lasers required is only viable economically using the monolithic integration approach. The comparison between different heterogeneous integration strategies on Si is summarised in Table 1.1.

Table 1.1 Comparison of different heterogeneous integration methods on Si substrates.

Integration method	Integration density	CMOS compatibility	Cost	Overall maturity
Die bonding	Low	Back-end compatible	High	Mature
Wafer bonding	Medium	Back-end compatible	Medium	Mature
Monolithic growth	High	Potentially front-end compatible	Potentially very low	R&D

1.2 Challenges and strategies for monolithic integration of III–V on Si

The idea of monolithic integration of III–V materials on a Si platform is, of course, not a new topic. The first attempts to grow GaAs thin films on Si substrates were made in the 1980s [46][47] and continued in the 1990s with InP-based materials on Si, especially at NTT in Japan [48][49]. This approach, despite being investigated for decades, made little progress. This is because, unfortunately, monolithic III–V-on-Si integration faces significant challenges stemming from the large material dissimilarity between group III–V and group IV materials, including polar III–Vs versus non-polar Si surfaces, different thermal expansion coefficients and large lattice mismatch [50]–[52]. In this section, the defects caused by each material dissimilarity and the corresponding strategies to suppress different types of defects during the III–V growth are discussed in detail, respectively.

1.2.1 Antiphase boundaries

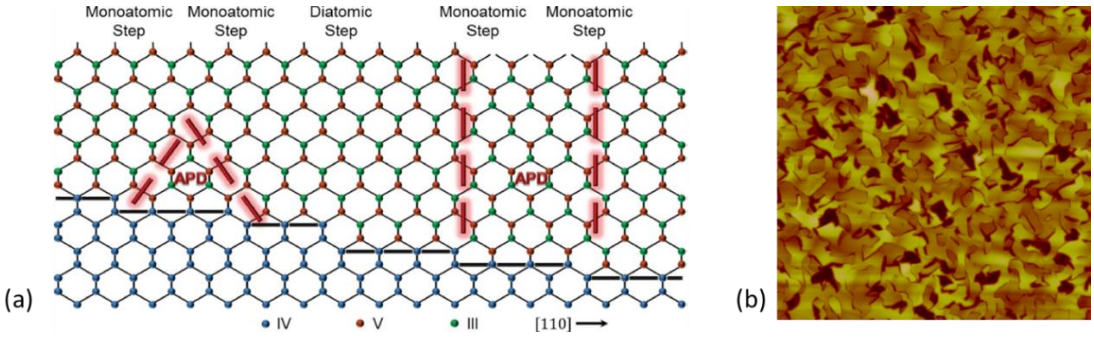

Figure 1.2 (a) Schematic diagram of polar and non-polar surfaces between III–V and Si, where the monoatomic steps result in APBs [53]. *(b) AFM image of the APDs raised to wafer surface.*

The first issue, as seen in Figure 1.2 (a), is the formation of antiphase domains (APDs) when growing polar III–Vs on non-polar Si substrates. In practice, monoatomic steps (or an odd number of atomic steps) exist on the clean Si (001) surface [53], which induces the formation of two domains as the III–V epitaxial growth proceeds with opposite sub-lattice allocation [54]. The APDs are separated by homo-atomic bonds, either III–III or V–V bonds, which are known as antiphase boundaries (APBs). The APBs can be self-annihilated or rise to the surface (Figure 1.2 (b)). APBs are electrically charged planar defects and act as non-radiative recombination centres and leakage paths for optoelectronics devices and electronic devices, respectively. The negative influence of APBs on the optical properties of III–V materials is evidenced by photoluminescence (PL) quenching and spectral linewidth broadening [54]–[56], while their impact on electronic devices is characterised by significantly reduced electron mobility [56][57]. It has been shown that APB-free GaAs/Si can be achieved by the self-annihilation of the APBs or by the perfect doubling of the height of all silicon surface steps, as demonstrated in Figure 1.3 (a) and (b), respectively. An effective approach for the double atom step formation of the Si surface is a 4–6° miscut angle oriented towards the [011] Si plane, and this has been widely used in the monolithic growth of GaAs on Si substrates [58]–[60].

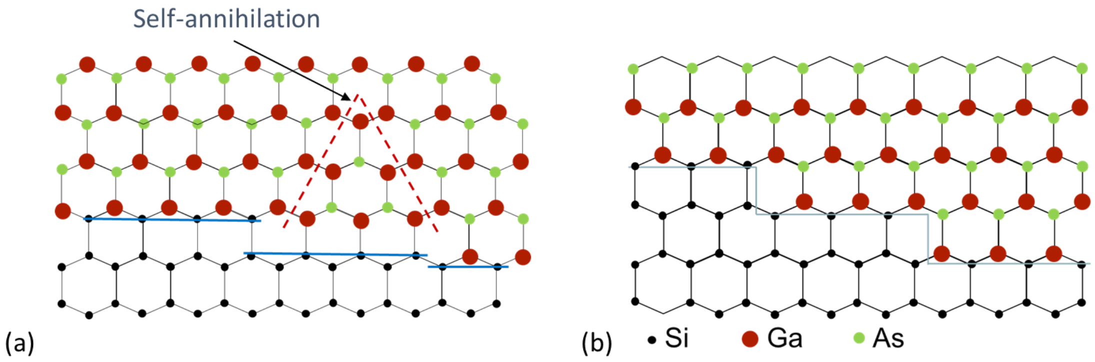

Figure 1.3 Schematic diagram of polar and non-polar surfaces between III–V and Si. (a) Self-annihilation of APBs occurring in monoatomic steps. (b) APB-free state achieved by double steps.

However, Si (100) substrates with an offcut of 4–6° to the [100] plane have the disadvantage of not being readily compatible with standard CMOS fabrication, where wafers with nominally (001) silicon substrates are used. In general, nominal silicon substrates, i.e. so-called “exact” (001) silicon substrates with a miscut angle less than 0.5° [50][61], have been used in standard microelectronics fabrication. There are four main methods which have demonstrated successfully grown APB-free GaAs on “exact” (001) Si substrates.

The first approach used a GaP/Si template grown by VPE and metal-organic vapour phase epitaxy (MOVPE) [62], as shown in Figure 1.4 (a). After the deoxidisation of a Si substrate with a slight off-orientation of 0.12° towards [110], by chemical treatment and high-temperature baking, a 500 nm homoepitaxial Si buffer was grown at high growth temperature (850 ℃) and pressure (200 mbar) by VPE. The Si surface then underwent thermal annealing under a very high hydrogen pressure of 950 mbar in the VPE chamber. A clear tendency of step doubling along both <110> directions was observed after this annealing (Figure 1.4 (b)). A thin GaP nucleation layer (NL) was then grown at a low growth temperature by MOVPE in order to achieve a charge-neutral interface [63] and two-dimensional (2-D) growth. A high-temperature overgrowth GaP layer was grown afterwards to promote self-annihilation of the remaining APDs. Based on this APB-free GaP/Si template, electrically pumped III–V lasers directly grown on (001) Si have been reported recently [64][65].

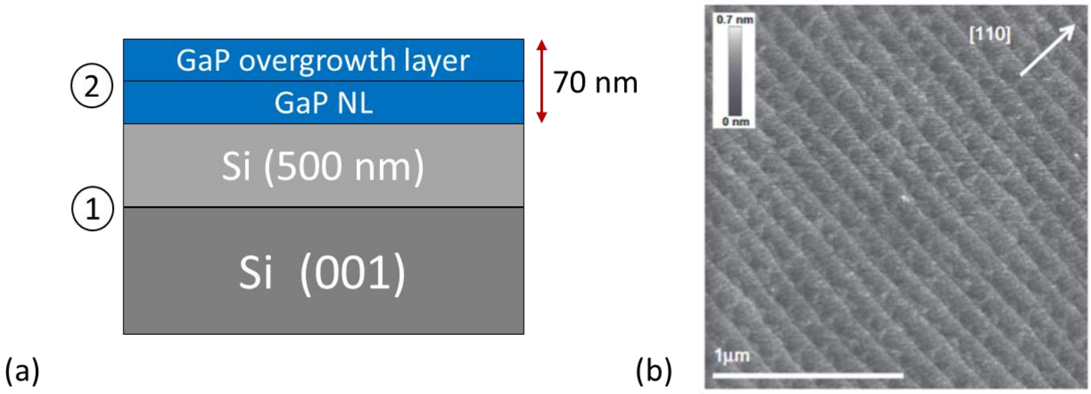

Figure 1.4 (a) Schematic diagram of the epitaxial layer of a GaP/Si template. (b) AFM image of exact (001) orientated Si sample with a miscut of 0.12° towards [110] plane [62].

Another direct growth approach uses a GaAs-on-v-groove Si (GoVS) template [66] instead of a GaP intermediate buffer layer to prevent the formation of APBs and to reduce the threading dislocations of the epitaxial GaAs layer. Figure 1.5 (a) shows the growth method. In this approach, the N-doped on-axis Si substrates were firstly patterned with SiO_2 stripes using standard dry etching techniques, followed by an RCA-1 clean ($NH_4OH:H_2O_2:H_2O = 1:1:5$) and a rapid HF (1%) dip to remove the native oxide before immediately wet etching the v-grooves using KOH solutions [67]. The epitaxial growth of GaAs on the patterned v-groove substrate was performed by metal-organic chemical vapour deposition (MOCVD) in the following sequence: thermal cleaning of patterned Si substrates, selective area heteroepitaxy of GaAs nanowires [68], SiO_2 stripe removal, the coalescence of GaAs to form GaAs planar film, growth of superlattices, and finally the growth of a GaAs buffer layer to complete the growth of the GoVS template. The great promise of this growth method comes not only from the ability to form a unique defect trapping effect (see Figure 1.5 (c)) [54][69] but also from the removal of the difficulties in achieving coalescence over dielectric patterns [54]. AFM measurement has been employed to assess the quality of the GoVS template and has revealed a root-mean-square (RMS) roughness of 0.9 nm [54], as shown in Figure 1.5 (b), indicating a good template quality without APBs.

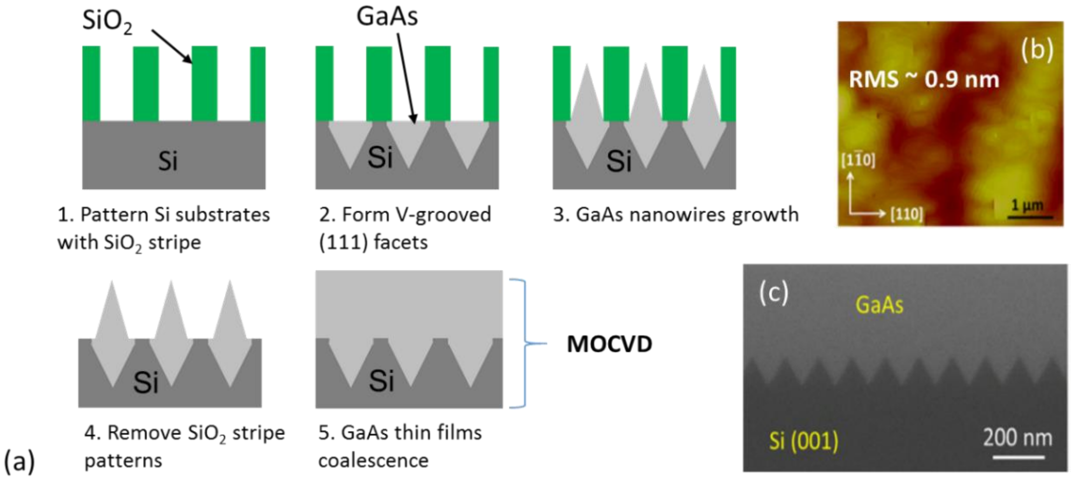

Figure 1.5 (a) Flow chart of GoVS template by MOCVD. (b) AFM image and (c) TEM image of ~300 nm coalesced GaAs thin film grown on a nanowire array [68].

The third growth method for APB-free GaAs is direct growth on on-axis Si (001) substrate without the use of any intermediate buffer layers or patterned Si substrates by MOCVD [56]. In the initial growth step, on-axis Si (001) wafers were deoxidised by the SiConi [70] process using NF_3/NH_3 remote plasma, and then transferred into an MOCVD reactor to perform H_2 annealing at 900 °C, forming a bi-atomic step surface structure (see Figure 1.6 (b)). The height of each step is around two atoms. Subsequently, the chamber was quickly cooled down to 700 °C within 30 s to freeze the Si surface structure. Afterwards, the 400 nm GaAs buffer layer was grown by a two-step process: a 40 nm NL was deposited at a low temperature (400–500 °C); the other 360 nm was then deposited at high temperature (600–700 °C). Thus, APD-free GaAs thin films on normal Si substrates were achieved with a surface roughness of 0.8 nm, as shown in Figure 1.6 (c) [56]. By applying this GaAs/Si virtual substrate, an electrically pumped III–V laser on on-exact Si has been reported [71].

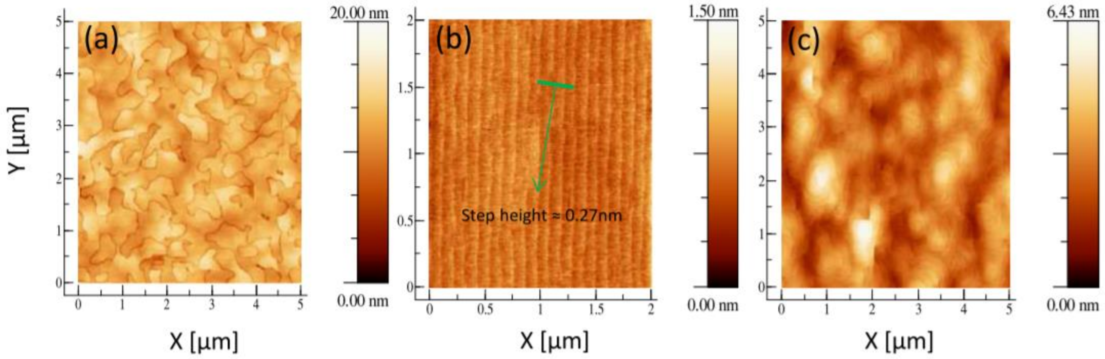

Figure 1.6 (a) 5 × 5 μm^2 AFM image of 400 nm thick GaAs grown on unoptimised Si (001): high density of APBs with RMS roughness of 1.6 nm. (b) 2 × 2 μm^2 AFM image of double-stepped 0.15 ° Si (001) substrate after optimised preparation (annealing under H^2). (c) 5 × 5 μm^2 AFM image of APB-free 150 nm thick GaAs grown on optimised 0.15 ° Si (001) with RMS roughness of 0.8 nm [56].

More recently, an APB-free GaAs buffer grown on on-axis Si (100) was demonstrated by using only the MBE process [72]. In this work, a 40 nm $Al_{0.3}Ga_{0.7}As$ seed layer was grown on Si (001) substrate at a relatively high temperature (500 °C) and high growth rate of 1.1 µm h^{-1}. The APBs could be annihilated within the following GaAs buffer layer of less than 400 nm, as shown in Figure 1.7.

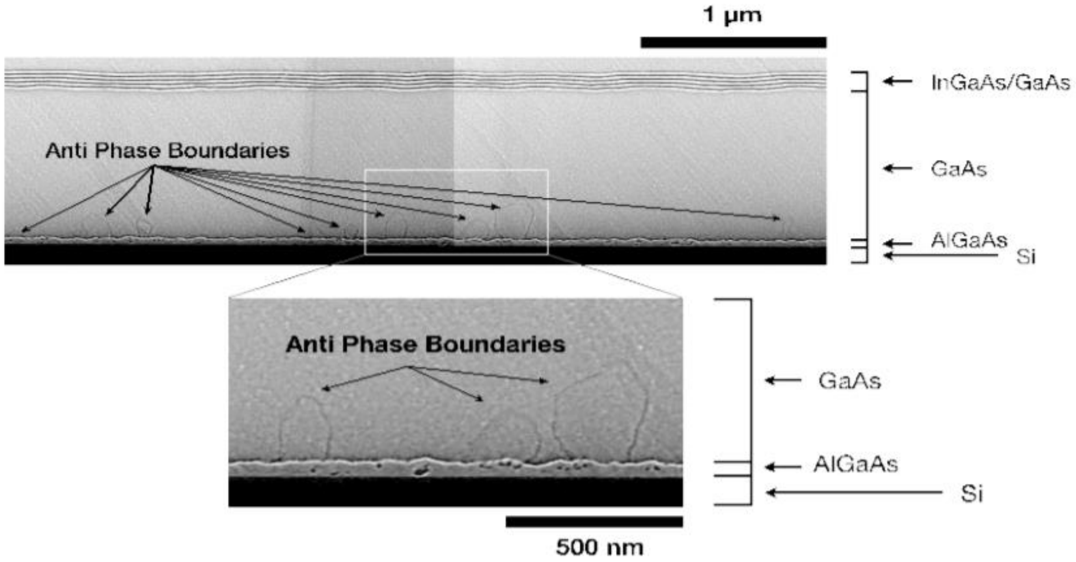

Figure 1.7 TEM image of GaAs buffer grown on Si (001) substrates by MBE. The arrows indicate the APBs which were self-annihilated within the GaAs buffer less than 400 nm [72].

1.2.2 Thermal cracks

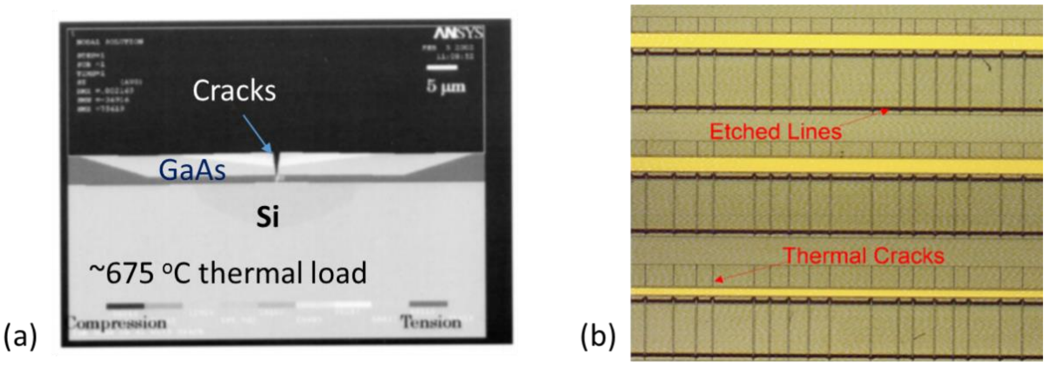

Figure 1.8 (a) SEM image of a thermal crack of GaAs buffer grown on Si [73]. *(b) Top view of thermal cracks on the wafer surface.*

The second issue is related to the creation of thermal cracks, as seen in Figure 1.8, due to the difference in the thermal expansion coefficients between group III–V and group IV materials. This difference promotes the accumulated thermal stress, which is then relieved by emerging thermal micro-cracks in the epi-layer during cooling from the growth temperature to room temperature (RT). The thermal expansion difference limits the maximum thickness of III–Vs that can be grown on Si, and the typical critical thickness for the onset of crack formation in GaAs epi-layers on Si is ~7 µm for a growth temperature of ~575 °C [73]. The equation of the critical thickness (t_c) is given by

$$t_c = \frac{\Gamma \overline{E_f}}{Z\sigma^2} \qquad \text{Equation 1.1}$$

where Γ is the fracture resistance, $\overline{E_f}$ is the biaxial modulus of the epitaxial layer, Z is a dimensionless driving force number, and σ is the stress value, which is equal to

$$\sigma = \overline{E_f}(\alpha_f - \alpha_s)\Delta T \qquad \text{Equation 1.2}$$

where α_f and α_s are the thermal expansion coefficients of the grown film and substrate and ΔT is the change in temperature. Figure 1.9 shows the critical thickness of the thermal crack as a function of the change in temperature when the GaAs buffers were grown on Si and SiGe substrates.

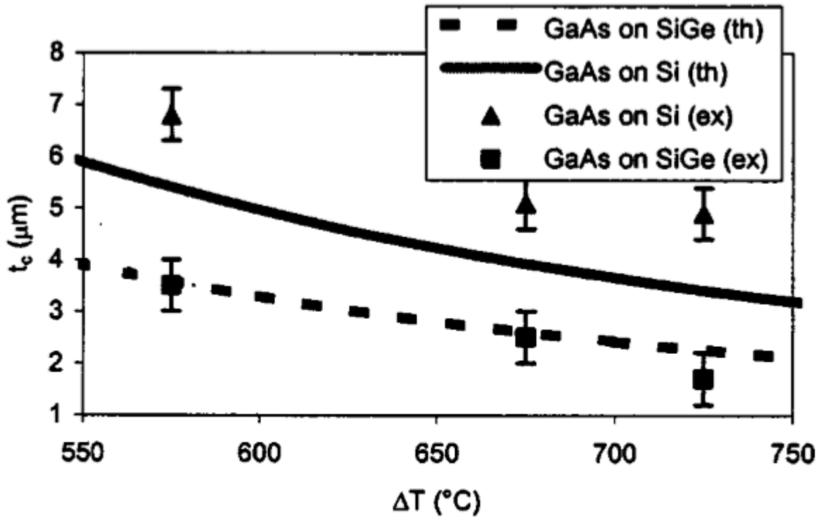

Figure 1.9 Experimental data (labelled ex) and theoretical data (labelled th) of the critical thickness of crack formation of GaAs on SiGe and Si substrates against the change in temperature [73].

From equations 1.1 and 1.2, it can be seen that the probability of forming cracks depends on many parameters including III–V material properties, total layer thickness and composition, and also on the growth conditions [74]. The thermal cracks can be reduced by strain compensation [75]. Another approach is to release the large thermal stress by employing selective area growth and growth on pre-patterned Si substrates due to strain relaxation near the pattern edge [76][77].

1.2.3 Threading dislocations

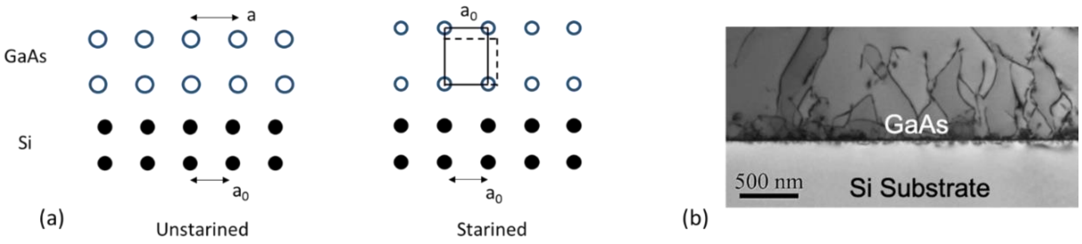

Figure 1.10 (a) Stained lattice of GaAs grown on Si by the mismatched lattice constant. (b) TDs at the interface of GaAs and Si substrate.

The last issue, as seen from Figure 1.10 is related to the formation of threading dislocations (TDs) in the III–V layers grown on Si. The lattice mismatch between GaAs (InP) and Si is about 4% (7.5%). This mismatch results in a strain on the lattice of the epi-layer, and the strain energy is proportional to the deposition thickness. If the thickness of the epi-layer is over the pseudomorphic critical point, the accumulated strain is energetically relaxed during epitaxial growth through the nucleation of dislocations at the interface [54], creating two types of dislocations: misfit dislocations and TDs on the order of 10^9–10^{10} cm^{-2}. The former, concentrated at the III–V/Si interface, enable the release of the strain energy, while the latter propagate into the III–V materials acting as non-radiative recombination centres and eventually promote defect diffusion along the dislocation line [78], and hence reduce the quality of III–V materials as well as the operating performance and lifetime of devices fabricated from them [52].

Multiple strategies have been developed by different research groups to suppress TD generation and propagation. For example, the GoVS template described above also brings benefits in reducing the TD density due to its unique "aspect ratio trapping" effect [54]. For unpatterned Si substrates, a typical III–V NL grown at relatively low growth temperature could help to reduce the TD density and smooth the surface roughness as mentioned above [71], [79], [80] An optimisation study of the growth temperature of NL on off-cut Si has been reported, and it was shown that when the initial layer of thin GaAs was grown at the optimised temperature of 400 ℃ with a low growth rate of 0.1 monolayer (ML)/s, a lower density of defects was propagated into the GaAs buffer layer (Figure 1.11). Moreover, a higher quality of GaAs buffer was achieved by replacing the GaAs NL with an AlAs NL [81]. As shown in Figure 1.12, compared with GaAs NL, AlAs NL could confine more defects effectively and provided a better interface for succeeding III–V layer growth. After the NL, an improved morphology of the GaAs buffer layer can be obtained by a multi-step growth method [57][79]. The AlAs NL and multi-step growth temperature confine most of the defects in the first 200 nm of the GaAs buffer layer [60]. However, the TD density is still relatively high at this stage and needs to be further suppressed.

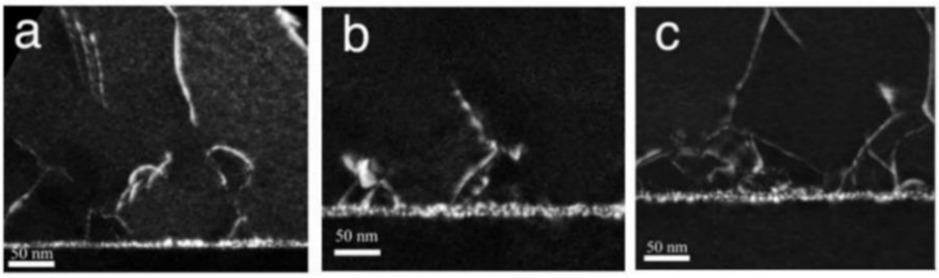

Figure 1.11 TEM images of GaAs/Si for GaAs NL grown at (a) 380 ℃, (b) 400 ℃ and (c) 420 ℃ [79].

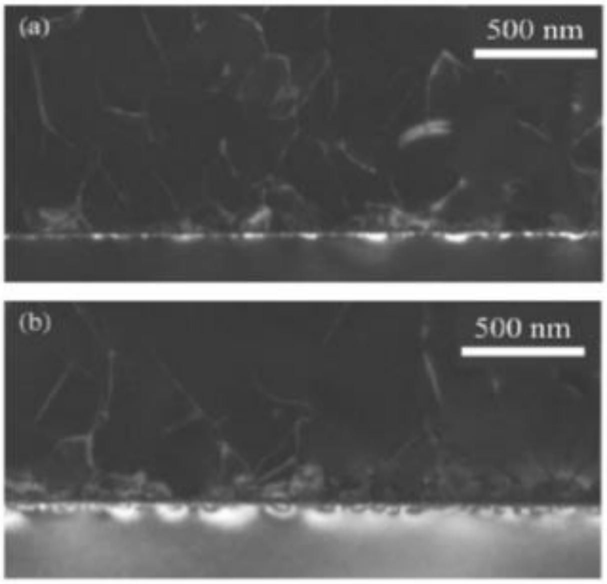

Figure 1.12 Dark field cross-section of TEM image of GaAs/Si interface with (a) GaAs NL and (b) AlAs NL [81].

It is also known that the TD density decreases with increasing layer thickness [82], but unfortunately, the thickness required to reach a relatively low TD density is much larger than the critical thickness for cracking. It is not applicable to this situation [83]. Apart from simply growing thick epitaxial layers, it is possible to reduce TD densities by intentionally designed thin layers, which are known as dislocation filter layers (DFLs) assembled by strained-layer superlattices (SLSs). Each SLS is made of a few periods of InGaAs/GaAs or InAlAs/GaAs, which are repeated several times, separated by GaAs spacing layers. The role of SLSs is to inhibit dislocation propagation by bending them into the growth plane and allowing two TDs to meet and annihilate [84]. The optimisation of InGaAs/GaAs DFLs was investigated by adjusting the growth conditions and structure of InGaAs/GaAs SLSs, in order to improve the filter efficiency [85]. By using five layers of InAlAs/GaAs SLSs as DFLs, the density of TDs after these DFLs could be effectively reduced to the order of ~10^6 cm^{-2} [86]. In addition, the *in situ* thermal annealing technique, whereby annealing is carried out at a high temperature for a certain time in the MBE reactor while the epitaxial growth is paused (Figure 1.13), has been seen to be an effective approach to improve the DFLs' effect further. This can be explained by the increased kinetic energy of the dislocations, which in turn increases the in-plane movement of the TDs, therefore further enhancing the annihilation efficiency [84].

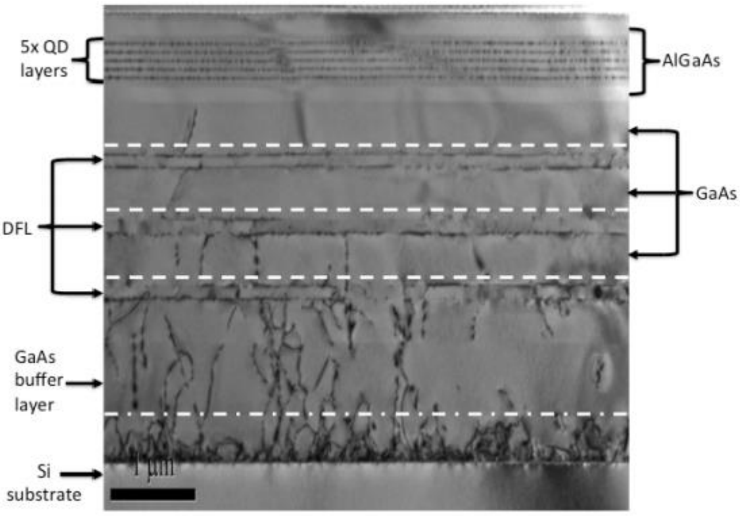

Figure 1.13 TEM image of GaAs buffer grown on Si with three DFLs. The dashed lines indicate the positions where in situ annealing was performed [84].

Multiple growth strategies were applied to achieve high-quality epitaxy layers. At first, the AlAs NL and multi-step GaAs buffer growth were utilised, as shown in Figure 1.14 (a). The optimised four-layer $In_{0.18}Ga_{0.82}As$/GaAs SLSs were then grown as DFLs to block the propagation of TDs, and *in situ* thermal annealing was also performed before and during the DFL growth to further improve the material qualities. Figure 1.14 (c) presents the density of TDs at the different positions indicated in Figure 1.14 (b). After these four layers of DFLs, the TD density is reduced from 10^9 cm^{-2} to 10^5 cm^{-2} [60].

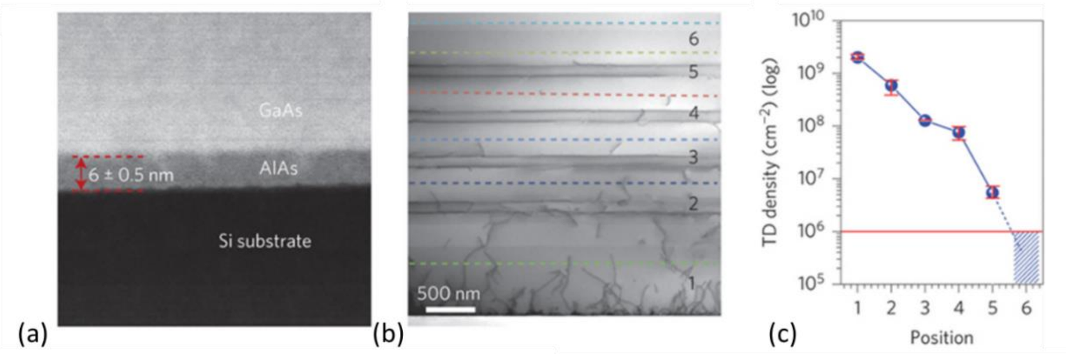

Figure 1.14 (a) Dark field TEM image of GaAs/Si interface with 6 nm AlAs NL. (b) Bright field cross-section TEM image of four-layer DFLs. (c) Dislocation density measured in different positions, as indicated in (b) [60].

However, compared with the III–V laser structure grown on a native substrate with a defect density of <10^4 cm^{-2}, the relatively high dislocation density of III–V grown on Si leads to device failure and shorter lifetime of lasing [74]. Specifically, the GaAs quantum well lasers grown on Si with relatively high defect density (> 10^6 cm^{-2}) have only shown a few seconds [87] and up to 200 hours lifetime [88]. These results have not reached the demand of long-time reliable operation (over 10^6 hours lifetime) in commercial telecommunication applications [89]. Fortunately, the use of a novel material based on quantum dots (QDs) as the active region for the semiconductor laser has shown a tremendous behaviour of high dislocation tolerance. Besides, the QD laser also shows benefits in threshold current, differential gain, thermal stability and other dynamic properties. Thus, in the next section, the details of the QD theory and its advantages will be discussed, respectively.

1.3 III–V QD laser

1.3.1 QD theory

The idea of using a heterostructure as the active region was first theoretically predicted by Kroemer in 1963 [90]. However, it was not until the demonstration of the first double-heterostructure semiconductor lasers in 1970 [91] that the importance of carrier confinement to the active region was discovered. Since then, the semiconductor laser community has made tremendous progress in implementing quantum-confined semiconductor lasers.

In a bulk semiconductor material, carriers within the structure are only restricted by the band offset, which means the carriers could easily move to other states with additional thermal energy ($k_B T$). Because of this excess thermal energy, the need for energy for photon emission will be more than the expected bandgap energy ($E_g + k_B T$). On the other hand, increasing temperature will aggravate the thermal spreading of injection carriers from ground states (GSs), resulting in a rise of threshold current, leading a strong temperature-dependent behaviour.

In a quantum-confined structure, the spatial dimension is ultra-small and comparable to the electron wavelength (de Broglie wavelengthλ_{deB}). Thus the movement of the electron is confined. The momentum (p) and average kinetic energy (E) of an electron in three degrees of freedom can be written as [92]:

$$p = \frac{h}{\lambda_{deB}} = \hbar \frac{2\pi}{\lambda_{deB}} \quad \text{Equation 1.3}$$

$$E = \frac{p^2}{2m} \approx \frac{3}{2} k_B T \qquad \text{Equation 1.4}$$

where $\hbar$ is the reduced Planck's constant, and m is the mass of the electron. Therefore, the de Broglie wavelength associated with kinetic energy equals

$$\lambda_{deB} = \sqrt{\frac{4\pi^2\hbar^2}{3mk_BT}} \qquad \text{Equation 1.5}$$

According to the above equation, the size scale for effective quantum confinement can be estimated. It has been shown that the small structure causes the band of energies to turn into discrete energy levels. We call this phenomenon the energy sub-band, and it can be examined by Schrodinger's wave equation. According to the time-independent wave equation [93]:

$$[-\frac{\hbar^2}{2m}\frac{\partial^2}{\partial x^2} + V(x)]\varphi(x) = \varepsilon\varphi(x) \qquad \text{Equation 1.6}$$

where $V(x)$ is potential energy, $\varphi(x)$ is the electron wave function and ε is the total energy of the electron. The term in square brackets is defined as the Hamiltonian operator,

$$\widehat{H} = -\frac{\hbar^2}{2m}\frac{\partial^2}{\partial x^2} + V(x) \qquad \text{Equation 1.7}$$

which is associated with the kinetic energy (first term on the right-hand side) and potential energy (second term on the right-hand side) [94]. Moreover, equation 1.6 can be rewritten as a second-order differential equation,

$$\frac{d^2\varphi(x)}{dx^2} + k^2\varphi(x) = 0 \qquad \text{Equation 1.8}$$

where

$$k^2 = \frac{2m}{\hbar^2}[E - V(x)] \qquad \text{Equation 1.9}$$

The general solution for equation 1.8 is

$$\varphi(x) = Ae^{\pm ikx} = Asin(kx) + Bcos\,(kx) \qquad \text{Equation 1.10}$$

Assuming an electron is confined in a 1-D well in the x axis with well width $\Delta\, x$ and infinite barrier height, as shown in Figure 1.15, the potential energy in the box model will be [93]:

$$V(x) = \begin{cases} 0,\ if\ 0 \leq\ x \leq \Delta x \\ \infty,\ otherwise \end{cases} \qquad \text{Equation 1.11}$$

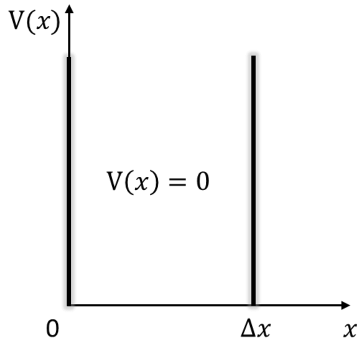

Figure 1.15 Schematic diagram of the infinite potential well.

The infinite potential barriers mean the probability for the electron at the wall and outside of the box is zero. Thus, the boundary conditions for this situation can be written as [93]:

$$\varphi(0) = \varphi(\Delta x) = 0 \qquad \text{Equation 1.12}$$

Thus, we find that *B* is equal to 0 in equation 1.10, and the wave function is then equal to

$$\varphi(\Delta x) = Asin(k\Delta x) = 0 \qquad \text{Equation 1.13}$$

$$k\Delta x = n\pi, \;\; n = 1, 2, 3 \ldots \qquad \text{Equation 1.14}$$

$$k_n^2 = \frac{n^2\pi^2}{\Delta x^2}, \;\; n = 1, 2, 3 \ldots \qquad \text{Equation 1.15}$$

where *n* is an integer and represents the energy state levels, for example, *n*=1 means GS, *n*=2 means the first excited state and so on. Combined with equation 1.9, the discrete confined energy in the *x*-direction for the box model is

$$E_{conf}(n) = \frac{\hbar^2}{2m}k_n^2 = \frac{\hbar^2 n^2\pi^2}{2m(\Delta x)^2} \qquad \text{Equation 1.16}$$

If a particle is confined in one direction and free in the other two dimensions, we call this material a 2-D quantum well (QW) structure. It is also possible to confine electrons in more directions. Two-directional confinement produces a 1-D quantum wire (nanowire) structure, and confinement in all three directions would produce a 0-D QD structure. The total energy of the electron in three directions for QW, nanowire and QD can be written as [95]:

$$E_{QW} = E_{conf}(n_x) + E_{y,z} = \frac{\hbar^2 n_x^2\pi^2}{2m(\Delta x)^2} + \frac{\hbar^2(k_y^2 + k_z^2)}{2m} \qquad \text{Equation 1.17}$$

$$E_{nanowire} = E_{conf}(n_x, n_y) + E_z = \frac{\hbar^2\pi^2}{2m}\left(\frac{n_x^2}{(\Delta x)^2} + \frac{n_y^2}{(\Delta y)^2}\right) + \frac{\hbar^2 k_z^2}{2m} \qquad \text{Equation 1.18}$$

$$E_{QD} = E_{conf}(n_x, n_y, n_z) = \frac{\hbar^2\pi^2}{2m}\left(\frac{n_x^2}{(\Delta x)^2} + \frac{n_y^2}{(\Delta y)^2} + \frac{n_z^2}{(\Delta z)^2}\right) \qquad \text{Equation 1.19}$$

From equation 1.19 for a QD structure, we can see that only discrete energies depending on n are allowed in the QD structure due to the three-directional confinements. Figure 1.16 demonstrates the functions of the density of states (DOS) for electrons in the conduction band with the energy in bulk, 2-D QW, 1-D nanowire and 0-D QD structures. The unique delta-like DOS of the QD demonstrates that the carriers are localised in the discrete energy levels.

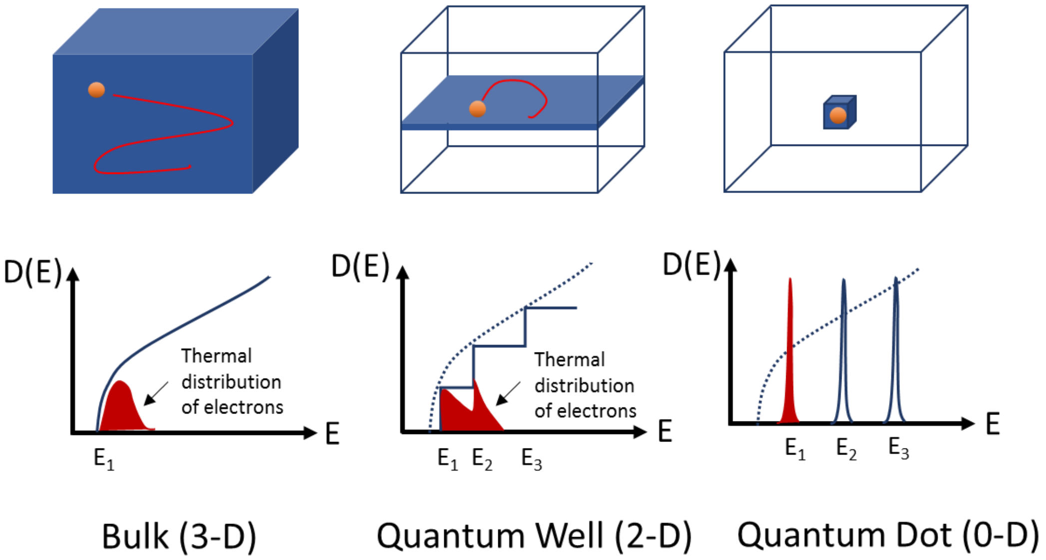

Figure 1.16 Schematic diagram of DOS and thermal distribution of electrons in bulk, QW and QD structures [96].

Although the three-directional confinements of the QD concept were first theoretically proposed by Arakawa and Sakaki in 1982 [97], the practical application was limited by the production technique of QDs in the early stage. The turning point was when the Stranski–Krastanov (S-K) growth method to form self-assembled QDs came into use in the early 1990s [98]. The S-K growth method, alternatively known as the layer-island growth method, was proposed by Ivan Stranski and Lyubomir Krastanov in 1938 [99]. In 1994, researchers from Fujitsu Laboratories coincidentally realised InAs QDs on GaAs by MBE, which emitted a telecommunication wavelength of 1.3 μm [100]. Figure 1.17 shows sketch diagrams of the growth of InAs QDs on GaAs by the S-K growth method. A 2-D thin layer of GaAs was grown on the substrate first, and several monolayers of InAs were then grown as follows. Due to the 7% mismatch in lattice constant between GaAs and InAs compounds, when the thickness of the InAs layer exceeds a critical value, the deposition layer will be nucleated and assembled as an "island" in order to release the strain energy between the GaAs and InAs interface; the QDs thus are self-organised [100]. The size, uniformity and density of QDs grown depend on the growth conditions, such as the growth temperature and growth rate, and these need to be studied intensively to obtain the maximum advantages of QDs.

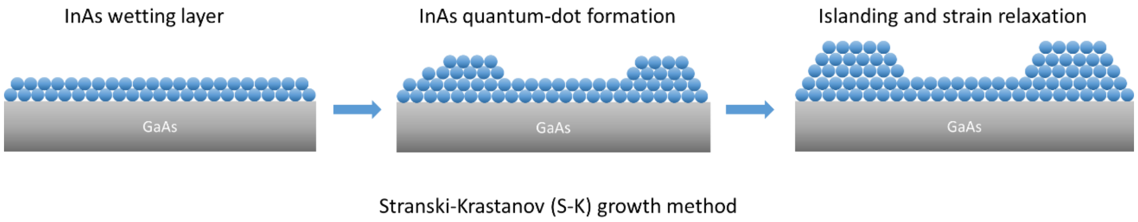

Figure 1.17 S-K growth method of InAs/GaAs QD structure.

The main driving force behind the utilisation of QD technology for the active layers of semiconductor lasers is the superior device performance obtained by taking advantage of the delta-function-like DOSs of the QD structure. Compared with conventional QW lasers, the main advantages of QD lasers are discussed in the following.

1.3.2 Ultra-low threshold current

The first benefit of the QD structure for the laser device is the ultra-low threshold current. The 3-D confinements in QDs focus the injection carriers into a narrower energy range than the QW structure. Thus, the population inversion can be satisfied with fewer injection carriers by the rapid filling of charge carriers into working energy states [52][101]. Although QD lasers soon exhibited the predicted outstandingly low thresholds, the early devices suffered from inhomogeneous broadening arising from the QD size fluctuation [102]. Therefore, reducing the inhomogeneous broadening of the QDs is one of the key factors in realising a high-performance QD laser with a low threshold current [103][104]. To this day, academic research groups all over the world have been competing against each other to demonstrate QD lasers with dramatically reduce threshold current densities by improving the QD epitaxy layer quality [105]–[110]. As shown in Figure 1.18 , in a period of less than ten years the performance of QD lasers (regarding threshold current density) has surpassed that of state-of-the-art QW lasers, which have been under development over the last few decades [52].

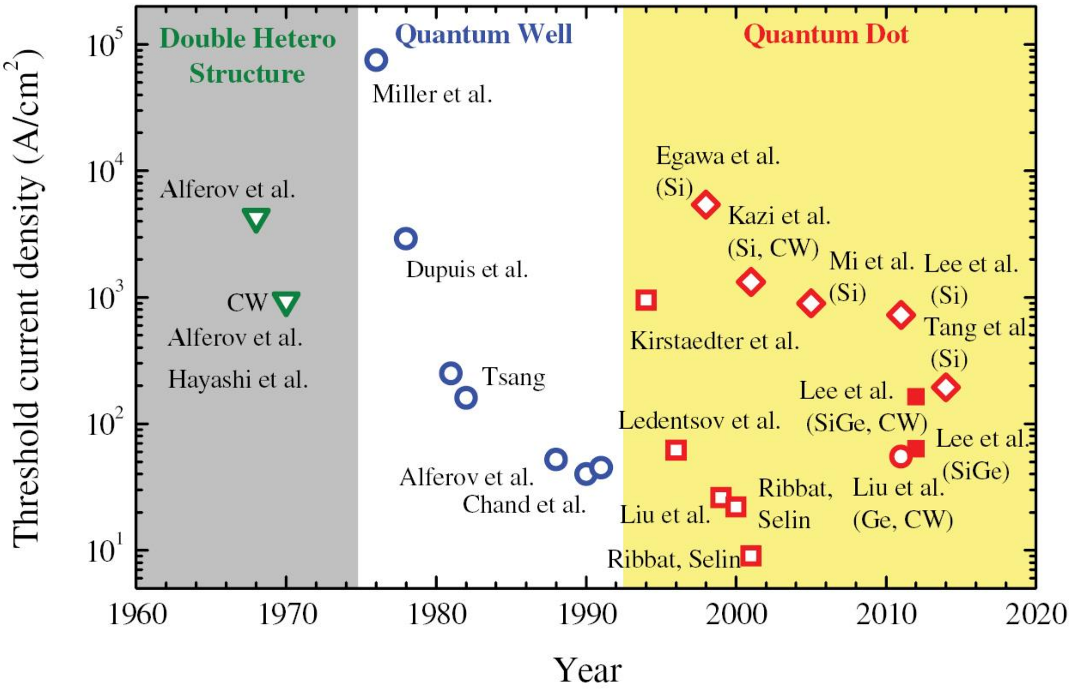

Figure 1.18 Historical development of heterostructure lasers with record threshold current density at the time of publication (☐ QD laser on GaAs; ▰ QD laser on Ge; ○ QD laser on SiGe; ♦ QD laser on Si). CW indicates that the threshold current values were obtained from QD lasers under continuous operation. The rest were obtained from QD lasers tested in pulse mode [52].

1.3.3 Improved temperature insensitivity

In addition to the low threshold current, the improved temperature characteristics of the QD laser bring intense research attention and will open new markets [102]. In real applications, the ambient temperature for the laser operation is always in a wide range and even at very high surrounding temperatures (~200 ℃) [102]. The thermoelectric cooler, which requires a bulky power supply and increases the power consumption, is prerequisite to keep the active components within their operating temperature range. Thus, lasers that enable high-temperature operation and temperature-insensitive threshold current are highly desirable for telecommunications to avoid the cost and power consumption of thermoelectric coolers. The improved temperature insensitivity of QDs comes from the significantly enhanced energy separations between the discrete adjacent energy states, which can prevent thermal population by the charge carriers. However, the early QD devices did not show the predicted good temperature stability, mainly due to the thermally broadened hole distributions through the closely spaced hole levels [111].

A typical electron energy separation in the conduction band is around 64 meV, while only ~11 meV energy difference appears in the hole region. A breakthrough that helped QD lasers to get off the ground, regarding the temperature stability, was the utilisation of p-type modulation doping during the QD growth. The key, at this point, was to counter the closely spaced energy levels by filling the excess holes [111][112].

QD Laser Inc. is currently one of the world-leading suppliers of QD lasers and has delivered commercial products with nearly temperature-insensitive operation up to 100 ℃, as we can see from Figure 1.19 [113]. In contrast, such temperature-insensitive operation had been impracticable with QW active regions. Moreover, the maximum operating temperature that could be achieved from their QD laser was as high as 220 ℃ [102].

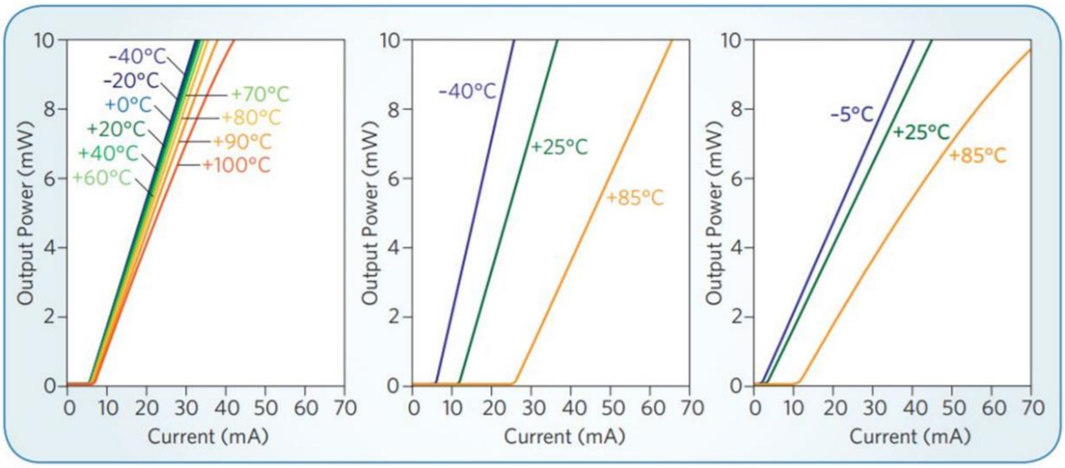

Figure 1.19 L-I curves of QD (left) and QW (other two-plane) Fabry-Perot lasers at different working temperatures [113].

1.3.4 Modulation bandwidth

In the short-reach photonic networks markets, directly modulated lasers are attractive owing to their advantages of low cost and power consumption [114]. QD lasers have also demonstrated a compatible modulation bandwidth by optimising the laser cavity designs [115] and improving the maximum modal gain via the *K* factor [116]. The equation of -3 dB modulation bandwidth is:

$$f_{-3dB,max} = \frac{2^{1.5}\pi}{K} \qquad \text{Equation 1.20}$$

The *K* factor defines the highest modulation rate of a laser diode [117]:

$$K \approx \frac{2\pi\Gamma}{{f_r}^2} \qquad \text{Equation 1.21}$$

where Γ is the confinement factor and f_r is the relaxation oscillation frequency, which equals

$$f_r = \frac{1}{2\pi}\sqrt{\frac{\partial G}{\partial n}\frac{S_0(1-\varepsilon S_0)}{\tau_{ph}}} \qquad \text{Equation 1.22}$$

where $\frac{\partial G}{\partial n}$ is the differential gain, ε is the gain saturation coefficient, S_0 is the photon density and τ_{ph} is the photon lifetime. According to the above three equations, the maximum modulation bandwidth is related to the photon lifetime. A short photon lifetime has shown a more significant relaxation frequency, thus resulting in an increased response frequency via a low value of K factor. The reduced photon lifetime can be achieved by a shorter laser cavity length [115], according to the equation:

$$\frac{1}{\tau_{ph}} = \frac{c}{n_r}\left(\alpha_i + \frac{1}{2L} ln \frac{1}{R_1R_2}\right) \qquad \text{Equation 1.23}$$

Here, c is the light speed, n_r is the equivalent refractive index, α_i is the internal loss, L is the laser cavity length and $R_{1,2}$ is the reflectivity index of mirrors of the laser cavity.

However, the total optical loss is varied by changing the laser cavity. A shorter laser cavity tends to increase the mirror loss by equation ln $(1/\mathrm{R_1R_2})/2L$, thereby raising the threshold gain of lasing. Once the threshold gain is larger than the maximum GS modal gain of QD material, the first excited state lasing takes place rather than the GS lasing [117]. In general, the excited states are working on higher threshold current densities, which causes the issues of lower injection efficiency and higher power consumption compared with GS lasing. On the other hand, the maximum GS mode gain is associated with the QD density and inhomogeneous broadening [118]. Therefore, the high quality of QDs with high dot density and large uniformity is also key for QD lasers in high-speed applications. The details of improving modal gain of QDs are discussed in Chapter 6. Figure 1.20 (a) displays the frequency response measurement of a 1.3 µm QD laser with various injection currents; a 3 dB bandwidth f_{-3dB} of 12 GHz is achieved at 50 mA bias current by employing the high modal gain [119]. Although the modulation bandwidth of the QD laser is lower than that of the QW laser, the superior thermal stability of QDs in the dynamic characteristics still makes it competitive in practical applications. Many reports describe the temperature-stable modulation bandwidth of QD lasers [120][121].

Figure 1.20 (b) demonstrates the temperature dependence of the extinction ratio of the QD laser at 10 Gb/s modulation using the technology of modulated doping with an acceptor impurity [120]. The almost unchanged extinction ratio between 20 ℃ and 70 ℃ proves the superior temperature characteristics of QDs.

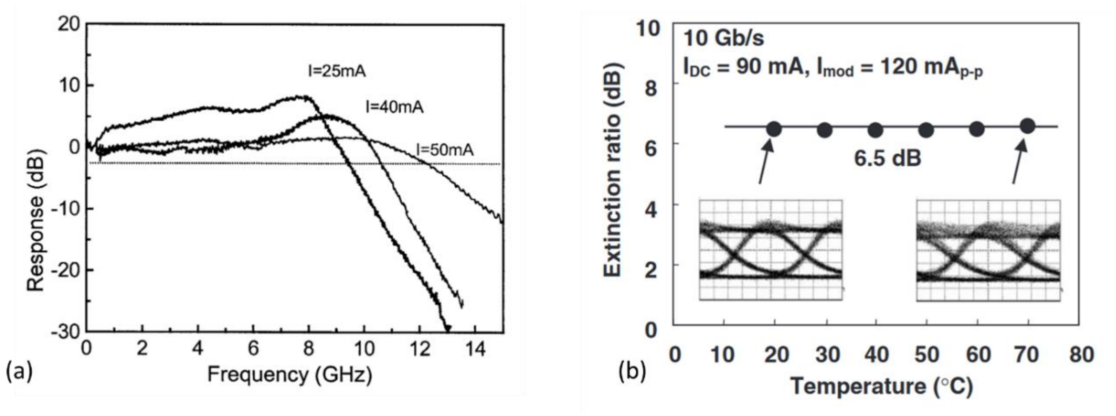

Figure 1.20 (a) RT small-signal modulation response of 1.3 μm QD laser with various injection currents (CW) [119]. *(b) Temperature dependence of extinction ratio under modulation. Inset: eye diagrams at 20 ℃ and 70 ℃* [120].

1.3.5 Narrow spectrum linewidth

Because of the existence of spontaneous emission in the laser cavity, the optical spectrum of lasing has a finite linewidth for a single-frequency laser. Unfortunately, it has been shown that the semiconductor laser has even higher linewidth compared with the solid-state laser, due to the dependence of the refractive index (n) on the carrier density (N) in the semiconductor [122]. The broad lasing linewidth is undesired for data transmission since it will cause a significantly increased phase noise, thus introduce errors during the data transmission [123][124]. As the injected current changes, the varied n leads to a coupling between the amplitude and phase, thus, the factor of spectral line broadening is referred to as the coefficient of amplitude-phase coupling (α factor), or the linewidth enhancement factor (LEF) [125]:

$$\alpha = -\frac{4\pi}{\lambda}\frac{dn/dN}{dg/dN} \qquad \text{Equation 1.24}$$

where λ is the wavelength and g is the gain per unit length. It has been shown that the coupling of phase and intensity fluctuation increases the laser linewidth by $1+\alpha^2$ [122]. Ideally, owing to the symmetric gain spectrum of the QD structure relative to its maximum, the α factor value and the variance of the refractive index are close to zero

[117][126] according to Kramers–Kronig relations [127], in comparison with the commonly observed α factor value in QW laser of 1.5 – 3 [128].

However, the ideal QD properties are challenging to realise as the presence of the inhomogeneous broadening and the excited states alter the gain spectrum [118]. The α factor was found to be increased with the injection current and raised quickly from 0 to more than 8 when the GS gain was near-saturated [129]. Still, the QD laser shows a relatively narrow linewidth [130][131], and the LEF value was reported to be 0.15 [132]. Moreover, the temperature independence of the QD laser is also applicable to the LEF value. It has been shown [133] that the values of α remained constant at ~3 from 20 °C to 80 °C by p-type doping in the active region.

1.3.6 High optical feedback tolerance

In the practical applications, for example, the coupling of a laser into a fibre, a fraction of laser radiation emitted can again enter the laser cavity by external reflections. This disruption of coherence in laser radiation increases the relative intensity noise (RIN), and causes an enhanced probability of bit error in data transmission [134]. Optical isolators are typically employed to prevent this optical feedback and improve the stability of laser diodes; however, the utilisation of the isolators aggravates the cost and process complexity. The ability to operate laser devices without isolators is strongly desirable for cost-effective optical systems. In general, a theoretical expression for predicting the critical feedback level (f_{crit}) for the disruption of coherence in the laser cavity is derived by [135][136]:

$$f_{crit} = \frac{\tau_L^2 (K f_r^2 + \gamma_0)^2}{16|C_e|^2} \left(\frac{1+\alpha^2}{\alpha^4}\right) \qquad \text{Equation 1.25}$$

where τ_L is the roundtrip delay within the laser cavity, γ_0 is the damping factor offset and $|C_e| = \frac{1-R}{2\sqrt{R}}$. From the equation, a higher K factor and smaller α factor value will lead to an increased feedback tolerance. Thus, QD lasers have shown superior performance in optical feedback tolerance in theory and also in experiments [136]–[138]. For example, it was reported that the InAs/GaAs QD lasers exhibited a fairly high coherence collapse threshold of –8 dB, ascribed to the low value of α factor and large gain compression (higher K factor) by the QD gain media. This value is higher than the f_{crit} of approximately –30 dB of the QW laser reported [139]. Figure 1.21 shows a direct comparison of the calculated coherence collapse threshold of the QD laser and QW laser with different K factors as a function of the LEF. It reveals a 10 dB increase of f_{crit} for the QD laser by the larger K factors with the LEF kept the same [136].

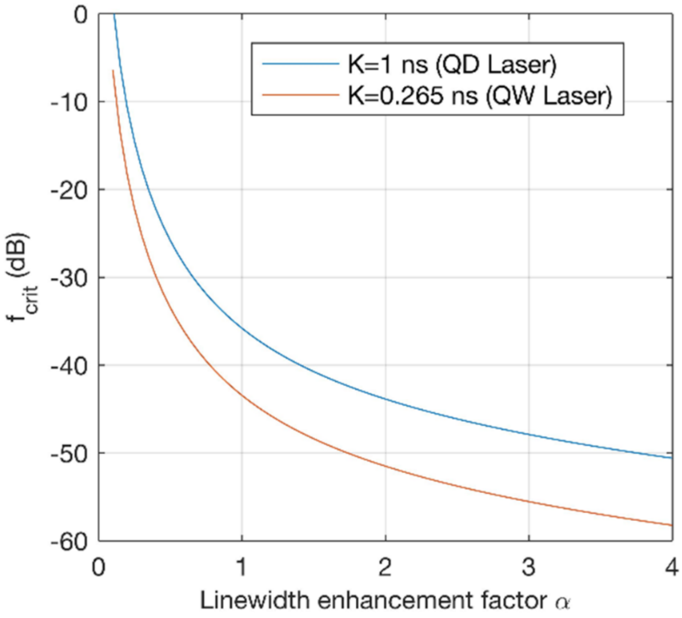

Figure 1.21 Coherence collapse threshold against the LEF of the QD laser and QW laser with different K factors [136].

1.3.7 High defect tolerance

As described in section 1.2.3, one of the great benefits of QDs is that they have been proven to be less sensitive to defects than conventional bulk materials and QW structures, due to carrier localisation and hence reduced interaction with the defects [140]. As shown in Figure 1.22 (a), for conventional QW lasers, any TDs propagating through the QWs will become a non-radiative recombination centre. It leads to an increased threshold current or even “kills” the device. In contrast, for QDs structures, one TD can only kill one or a very limited number of dots, while still leaving the rest of dots intact and capable of providing sufficient optical gain to achieve lasing. Moreover, it is well-known that the QD structures are able to bend the TDs and hence reduce the density of TDs [140]–[142]. As shown in Figure 1.22 (b), the dislocation bending can occur beneath the QDs when strain energy is released through the generation of the misfit dislocation under the assumption that the shape of self-assembled QDs is a pyramid and a TD propagates towards the bottom of a QD. Consequently, the bending of dislocations generated a segment of misfit dislocations gliding below the island [140]. This concept was observed by transmission electron microscopy (TEM) measurements, as shown in Figure 1.22 (c).

The TD was slightly bent around the QD array due to the strong strain field of the QDs (left side of Figure 1.22 (c)), and even one of these QDs is able to help the TD bending toward the sample edge, rather than propagating perpendicularly to the surface (right side of Figure 1.22 (c)) [143]. Therefore, even in the presence of high-density dislocations, QD lasers are able to provide superior reliability compared to QW or bulk devices [144][54].

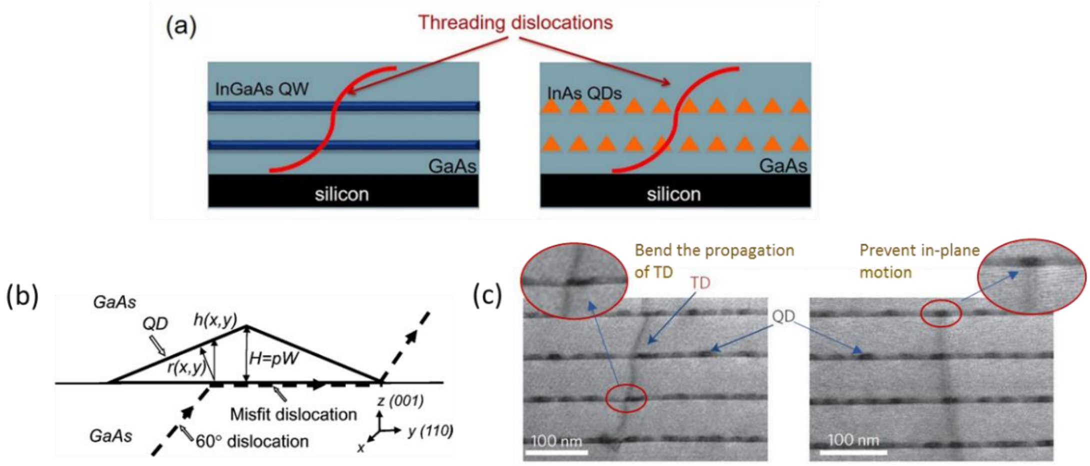

Figure 1.22 (a) Schematic illustration of the interaction of a TD with a QW and QD laser [143]. *(b) Cross-section schematic diagram of the mechanism of dislocation bending by a QD* [140]. *(c) TEM images of the TD in the QD region* [143].

To further confirm this hypothesis, Liu *et al.* from UCSB [145] made a direct comparison of QD lasers with QW lasers, all grown on Si substrates with similar dislocation densities. To make a solid comparison and separate this effect away from other factors that may influence the laser performance, the growth, processing and measurement techniques employed in their study were kept identical. Figure 1.23 (a) and (b) compare the PL spectra of identical QD (QW) structures grown on Si and native GaAs substrates, respectively, at RT. While the integrated PL intensity of InAs QDs grown on Si only dropped roughly by 20%, the integrated PL intensity of $In_{0.2}Ga_{0.8}As$ QW was degraded by more than a factor of 10 when moving the substrates from native GaAs to Si [145]. Two nominally identical laser structures (except for the active region) were grown as shown in the inset of Figure 1.23 (a) and (b) and then fabricated into ridge-waveguide lasers using the same processing procedure. Despite the similar current-voltage (I-V) characteristics obtained from those two different kinds of lasers [145], the behaviour of RT continuous-wave (CW) light-current (L-I) characteristics between Si-based QD and QW lasers was totally different. This is consistent with PL observations, with reasonable

CW lasing achieved only from Si-based QD lasers, while none of the QW samples was able to achieve RT CW lasing.

Moreover, a theoretical explanation of the enormous performance disparity between Si-based QW and QD structures by the impact of the dislocations has been reported in Liu *et al.* from UCL [146]. Using a rate equation travelling-wave model, the calculated L-I curves of QD lasers and QW lasers grown on Si with different dislocation densities are presented in Figure 1.24. The theoretical calculation has a good qualitative agreement with the experimental results and indicates a much higher defect tolerance of QD lasers compared with QW lasers.

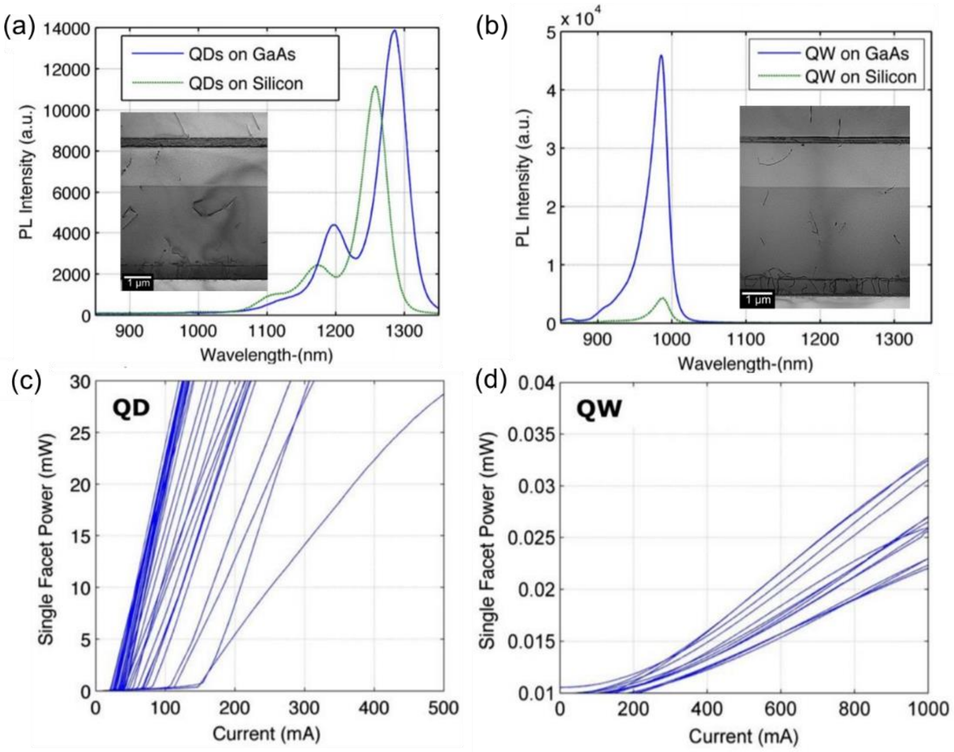

Figure 1.23 Comparison of PL measurement from (a) single InAs QD layer and (b) single InGaAs QW grown on GaAs and Si substrates. The insets of (a) and (b) are the TEM images of QD laser and QW laser grown on Si. Single-facet L-I curves for (c) QD laser and (d) QW laser grown on Si [145].

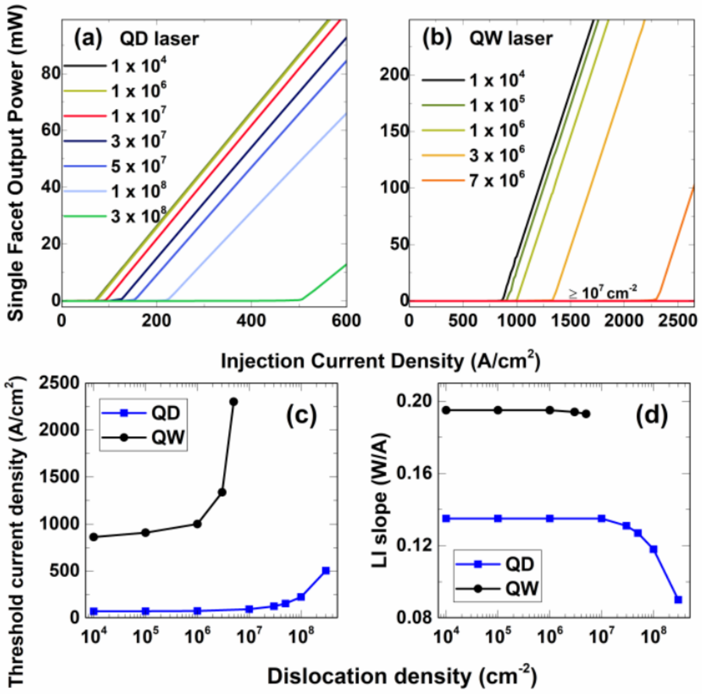

Figure 1.24 Calculated L-I curves for (a) QD laser and (b) QW laser as a function of dislocation density. (c) and (d) show the threshold current density and L-I slope against dislocation density for QD and QW laser [146].

Thanks to the high-quality III–V buffer grown on Si by the various strategies and the QD structure as the active region, significant pioneering works on the monolithic integration of III–V QD lasers on Si have been reported by different research groups. The recent achievements are summarised in Table 1.2.

Table 1.2 Representative milestone of III–V/IV QD edge-emitting lasers by monolithic integration.

Year	λ (nm)	Substrates	Equipment	Operation condition	J_{th} (A/cm^{-2})	T_{max} (°C)	Ref.
2005	1100	Si (001) misoriented 4° towards [111]	MBE	RT (Pulsed)	~ 1500	95	[58]
2011	1302	Si (001) misoriented 4° towards [110]	MBE	RT (Pulsed)	725	42	[59]
2012	1280	Ge/Si (001) misoriented 6° towards [111]	MBE	RT (Pulsed / CW)	64.3 / 163	84 / 30	[147]
2014	~1250	Ge/Si (001) misoriented 6° towards [111]	MBE	RT (CW)	~426	119	[148]
2016	1315	Si (001) misoriented 4° towards [110]	MBE	RT (Pulsed / CW)	~ 50 / 62.5	120 / 75	[60]
2017	1280	GaP/Si (001)	VPE+MOVPE+MBE	RT (CW)	860	90	[64]
2017	1250	V-groove Si (001)	MOCVD+MBE	RT (CW)	333	80	[66]
2017	1292	Si (001)	MOCVD+MBE	RT (Pulsed / CW)	240 / 425	102 / 36	[71]
2018	1299	GaP/Si (001)	VPE+MOVPE+MBE	RT (CW)	229.8	80	[65]
2018	1250	Si (001)	MBE	RT (Pulsed)	320	70	[72]
2019	1225	Si (001)	MBE	RT (CW)	370	101	[149]
2019	1284	V-groove Si (001)	MOCVD+MBE	RT (CW)	286	80	[150]

RT, CW, J_{th} and T_{max} represent room temperature, continuous-wave, threshold current density and maximum lasing temperature, respectively.

1.4 Perspective: integrated III-V QD photonic transmitter on Si platform

Over the past decade, the Si photonics community has made tremendous progress on individual building blocks of Si photonics, and many Si photonics components have been realized, including modulators [20]–[23], high-speed photodetectors [26]–[28], and various waveguide structures [18][19], as described earlier. However, the lack of a reliable and efficient Si-based laser has become the bottleneck of the whole Si photonics industry [29]. In a breakthrough development, our group at UCL has shown that it is possible to grow high-performance III-V QD semiconductor lasers directly on Si substrates [60], opening up the possibility to create a new Si technology that monolithically integrates individual photonic devices. Given that, following this achievement on monolithic III-V QD lasers on Si, our next goal is to develop a fully integrated Si photonic III-V QD transmitter chip. As shown in Figure 1.25, the proposed Si-based optical transmitter consists of a QD distributed feedback (DFB) laser operating at O-band, an QD electro-absorption (EA) modulator and SOI waveguide.

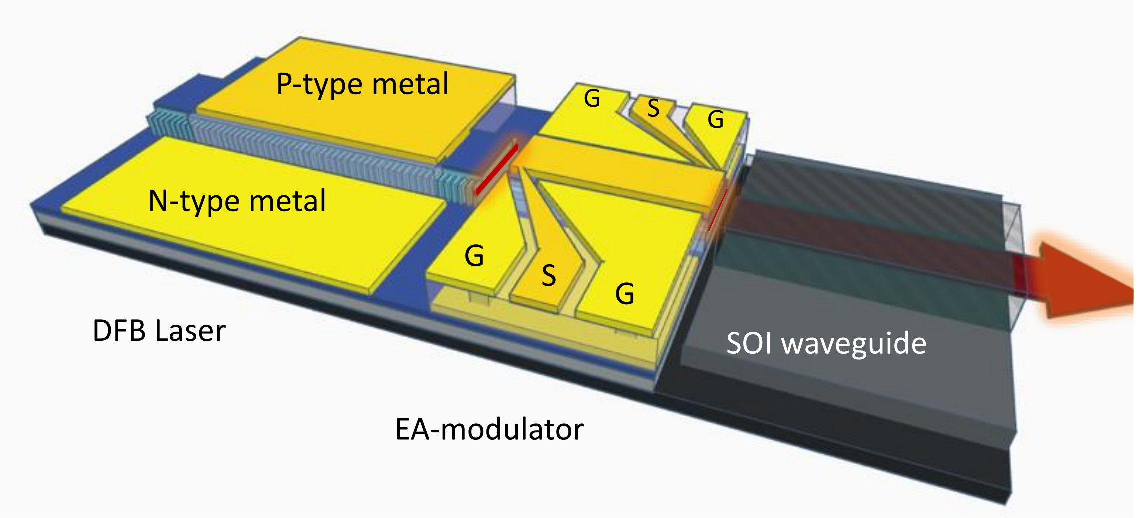

Figure 1.25 Schematic diagram of monolithic integration of a DFB laser, EA modulator and SOI waveguide on Si platform.

- QD DFB laser: To achieve the single optical channel interconnects for the WDM, the single-mode DFB laser with careful cavity/grating design is one of the keys for the transmitter. For the conventional DFB laser development, two epitaxial growth sequences are normally involved in realising the feedback grating paralleled to growth plane, either below or above the active region [151]. This approach undoubtedly aggravates the fabrication complexity and cost. Alternatively, a simplified technique named lateral surface gratings has been developed for the DFB laser, which avoids the complicated regrowth step [152][153]. As shown in Figure 1.25, the DFB grating can be realised by etching along the side of the laser stripe in a single post-growth processing step. Recently, based on this lateral surface gratings technique, the first QD DFB laser array directly grown on Si has been demonstrated with single-mode side mode suppression ratios as high as 50 dB and a wavelength covering a range of 100 nm at O-band [154]. Unfortunately, the DFB laser has shown second order transverse mode lasing, which is impractical for data transmission and still needs more effort.

- QD EA modulator: The single-frequency lasing emitted from the DFB laser is then modulated by the EA modulator. In this design, the laser diode and EA modulator section have the same epitaxy layers by MBE growth. Thus the light can be easily coupled by butt-jointed coupling at the same height without requiring a regrowth scheme. The laser facet quality, dimension of the groove between laser and modulator, are important factors that influence the optical mode profile and coupling efficiency and should be carefully investigated and optimized. Another critical point is to shift the bandgap of EA modulator regions away from that of the laser region to reduce the optical loss. However, the bandgap needs to be in a specific region enabling a strong absorption via the quantum-confined Stark effect (QCSE) [134] when an appropriate transverse bias is applied. The details of the bandgap shift will be discussed in Chapter 5.

- SOI waveguide: In general, the planar Si waveguides have shown lower transmission loss than the III-V waveguides for wavelength in the 1.3-1.6 μm range, detailed comparison can be found in ref [155]. The recorded ultra-low loss of < 0.03 dB/cm has been achieved by SOI waveguide recently [156]. The demand of low propagation loss and large volume manufacturing via the CMOS foundry, drive the use of SOI waveguides in dense integrated optics and optical interconnection. However, due to the thick buffer layer underneath the active region, the evanescent coupling method from the hybrid integration becomes impractical for the heteroepitaxy growth. In this design, the modulated signal is coupled into the SOI strip waveguide via the butt-jointed coupling. Selectively dry etching will be implemented first to delineate the regions where the waveguide will be subsequently deposited. The low-defect SiO_x/Si waveguide will be deposited by plasma-enhanced chemical vapour deposition (PECVD) and can be etched to a tapered shape for better coupling efficiency [157]. The core Si waveguide then can be covered by SiO_x or polymer. This SOI waveguide development is a broad topic, and it will not be discussed in this thesis.

To our best knowledge, no practical III-V laser monolithically integrated with EA-modulator on SOI or Si has yet been reported. To realise this rather complicated device on the Si platform, multi-solutions and intensive efforts are required. Thus, the aim of this thesis is to make contributions of the active components, towards the realisation of this comprehensive low-cost optical transmitters for Si photonics.

1.5 Objective and of outline thesis

In a nutshell, the objectives of the thesis are, firstly, the investigation of the noise floor and performance of our Si-based lasers acting as on-chip light emitters; secondly, the etched laser facet and the groove for a multi-cavity device; thirdly, the bandgap shift for the potential laser and EA modulator integration. Based on these topics, the research works performed in the present study will be presented in six chapters in this thesis.

In Chapter 1, a brief introduction to the integrated III–V lasers on Si as on-chip light sources for Si photonics is first presented. The challenges and strategies for monolithic integration III–V on Si by different research groups have been reviewed. After that, the novel material structure of the QD, its basic theory and its advantages as the active region of the laser device are introduced.

An introduction to the facilities and equipment used to establish the material characteristics, for device fabrication and for laser device measurements is given in Chapter 2. The optimisations of the laser fabrication process are discussed in detail, in order to improve the laser performance and meet the requirements of reliable light sources.

Chapter 3 presents the experimental results of the measurement of RIN and 25.6 Gb/s data transmission of our Si-based QD narrow-ridge laser with a fundamental mode lasing. The noise floor is as low as −150 dB/Hz in the 4–16 GHz range. The high performance and low noise feature of the QD laser on Si prove that our laser could be used as a light emitter source for Si photonics.

Chapter 4 describes the post-fabrication of QD lasers for different applications by the focused ion beam (FIB) technique. The FIB-made laser facet was firstly compared with the as-cleaved facet; it showed only slight degradation which did not prevent the etched laser facet from being employed in photonic integration. Further angled facet etching by FIB is investigated to inhibit the optical feedback into the cavity, resulting in a device with amplified spontaneous emission (ASE). This kind of device has the potential to be utilised as a broadband light source or semiconductor optical amplifier (SOA) for Si photonics. Groove etching by FIB for potential applications of integration of laser and EA on Si substrate is also presented.

Chapter 5 demonstrates the selective area intermixing study of the QD laser on Si. By using different dielectric materials as the capping layers, after the rapid thermal annealing (RTA) process, the bandgap energy of the wafer can be engineered intentionally up to 28 meV. This result meets the requirement of the bandgap difference between the laser and EA modulator.

Finally, in Chapter 6, the conclusion and future work towards to the Si-based transmitter are presented. The subsequent works, including improving QD modal gain for active components, and travelling wave electrode design for high-speed EA modulator are discussed respectively.

1.6 References

[1] Cisco, “Cisco Annual Internet Report (2018–2023) White Paper,” 2020. [Online]. Available: https://www.cisco.com/c/en/us/solutions/collateral/executive-perspectives/annual-internet-report/white-paper-c11-741490.html. [Accessed: 13-Feb-2020].

[2] O. Graydon, “The data centre challenge,” *Nat. Photonics*, vol. 9, no. 10, pp. 637–638, Oct. 2015.

[3] J. A. Davis *et al.*, “Interconnect limits on gigascale integration (GSI) in the 21st century,” *Proc. IEEE*, vol. 89, no. 3, pp. 305–322, Mar. 2001.

[4] W. Bogaerts, “14 Optical Interconnects,” in *Advanced Interconnects for ULSI Technology*, L. Pavesi and G. Guillot, Eds. Chichester, UK: John Wiley & Sons, Ltd, 2012, pp. 503–542.

[5] X. Zhou, R. Urata, and H. Liu, “Beyond 1 Tb/s Intra-Data Center Interconnect Technology: IM-DD OR Coherent?,” *J. Light. Technol.*, vol. 38, no. 2, pp. 475–484, Jan. 2020.

[6] Y. Li, Y. Zhang, L. Zhang, and A. W. Poon, “Silicon and hybrid silicon photonic devices for intra-datacenter applications: state of the art and perspectives [Invited],” *Photonics Res.*, vol. 3, no. 5, p. B10, Oct. 2015.

[7] R. Blum, “Silicon photonics the key to data centre connectivity,” *Intel*, 2017. [Online]. Available: https://www.intel.com/content/dam/www/public/us/en/documents/product-briefs/silicon-photonics-the-key-to-data-centre-connectivity-robert-blum.pdf. [Accessed: 01-Feb-2020].

[8] X. Zhou, R. Urata, and H. Liu, “Beyond 1Tb/s Datacenter Interconnect Technology: Challenges and Solutions (Invited),” in *Optical Fiber Communication Conference (OFC)*, 2019, p. Tu2F.5.

[9] D. Liang and J. E. Bowers, “Photonic integration: Si or InP substrates?,” *Electron. Lett.*, vol. 45, no. 12, p. 578, 2009.

[10] F. A. Kish *et al.*, “Current status of large-scale InP photonic integrated circuits,” *IEEE J. Sel. Top. Quantum Electron.*, vol. 17, no. 6, pp. 1470–1489, Nov. 2011.

[11] T. Morishita, K. Kounoike, S. Fujiwara, Y. Hagi, and Y. Yabuhara, “Crystal growth and wafer processing of 6" Indium Phosphide substrate,” *Proc. 2016 Int. Conf. Compd. Semicond. Manuf. Technol.*, p. 5b.1, 2016.

[12] “Understanding data center interconnect: intra-data center.” [Online]. Available: https://www.neophotonics.com/understanding-intra-data-center-interconnect/. [Accessed: 15-Aug-2019].

[13] N. Izhaky *et al.*, “Development of CMOS-compatible integrated silicon photonics devices,” *IEEE J. Sel. Top. Quantum Electron.*, vol. 12, no. 6, pp. 1688–1697, Nov. 2006.

[14] M. Asghari and A. V. Krishnamoorthy, “Silicon photonics: Energy-efficient communication,” *Nat. Photonics*, vol. 5, no. 5, pp. 268–270, May 2011.

[15] D. Miller, “Device requirements for optical interconnects to CMOS silicon chips,” in *Integrated Photonics Research, Silicon and Nanophotonics and Photonics in Switching*, 2010, p. PMB3.

[16] A. Rickman, “The commercialization of silicon photonics,” *Nat. Photonics*, vol. 8, no. 8, pp. 579–582, Aug. 2014.

[17] C. Zhang and J. E. Bowers, “Silicon photonic terabit/s network-on-chip for datacenter interconnection,” *Opt. Fiber Technol.*, vol. 44, pp. 2–12, Aug. 2018.

[18] J. F. Bauters *et al.*, “Silicon on ultra-low-loss waveguide photonic integration platform,” *Opt. Express*, vol. 21, no. 1, p. 544, Jan. 2013.

[19] D. Dai, J. Bauters, and J. E. Bowers, “Passive technologies for future large-scale photonic integrated circuits on silicon: polarization handling, light non-reciprocity and loss reduction,” *Light Sci. Appl.*, vol. 1, no. 3, p. e1, Mar. 2012.

[20] D. J. Thomson *et al.*, “50-Gb/s silicon optical modulator,” *IEEE Photonics Technol. Lett.*, vol. 24, no. 4, pp. 234–236, Feb. 2012.

[21] X. Xiao *et al.*, “High-speed, low-loss silicon Mach–Zehnder modulators with doping optimization,” *Opt. Express*, vol. 21, no. 4, p. 4116, Feb. 2013.

[22] M. Streshinsky *et al.*, “Low power 50 Gb/s silicon traveling wave Mach-Zehnder modulator near 1300 nm,” *Opt. Express*, vol. 21, no. 25, p. 30350, Dec. 2013.

[23] G. T. Reed, G. Mashanovich, F. Y. Gardes, and D. J. Thomson, "Silicon optical modulators," *Nat. Photonics*, vol. 4, no. 8, pp. 518–526, Aug. 2010.

[24] X. Zheng *et al.*, "A tunable 1x4 silicon CMOS photonic wavelength multiplexer/demultiplexer for dense optical interconnects," *Opt. Express*, vol. 19, no. 3, p. 5151, Mar. 2010.

[25] D. T. H. Tan *et al.*, "Wide bandwidth, low loss 1 by 4 wavelength division multiplexer on silicon for optical interconnects," *Opt. Express*, vol. 19, no. 3, pp. 2401-2409, 2011.

[26] O. I. Dosunmu, D. D. Cannon, M. K. Emsley, L. C. Kimerling, and M. S. Ünlü, "High-speed resonant cavity enhanced Ge photodetectors on reflecting Si substrates for 1550-nm operation," *IEEE Photonics Technol. Lett.*, vol. 17, no. 1, pp. 175–177, Jan. 2005.

[27] T. Yin *et al.*, "31 GHz Ge n-i-p waveguide photodetectors on Silicon-on-Insulator substrate," *Opt. Express*, vol. 15, no. 21, p. 13965, Oct. 2007.

[28] L. Vivien *et al.*, "Zero-bias 40Gbit/s germanium waveguide photodetector on silicon," *Opt. Express*, vol. 20, no. 2, p. 1096, Jan. 2012.

[29] D. Liang and J. E. Bowers, "Recent progress in lasers on silicon," *Nat. Photonics*, vol. 4, no. 8, pp. 511–517, Aug. 2010.

[30] H. Rong *et al.*, "A continuous-wave Raman silicon laser," *Nature*, vol. 433, no. 7027, pp. 725–728, Feb. 2005.

[31] J. Liu *et al.*, "Tensile-strained, n-type Ge as a gain medium for monolithic laser integration on Si," *Opt. Express*, vol. 15, no. 18, p. 11272, Sep. 2007.

[32] A. Camacho *et al.*, "An electrically pumped germanium laser," *Opt. Express*, vol. 20, no. 10, p. 11316, May 2012.

[33] B. Jiang *et al.*, "A hybrid silicon evanescent quantum dot laser," *Appl. Phy. Express*, vol. 9, no. 9, p. 092102, Aug. 2016.

[34] H.-H. Chang *et al.*, "1310 nm silicon evanescent laser," *Opt. Express*, vol. 15, no. 18, p. 11466, Sep. 2007.

[35] M. Liao *et al.*, "Monolithically integrated electrically pumped continuous-wave

III-V quantum dot light sources on silicon," *IEEE J. Sel. Top. Quantum Electron.*, vol. 23, no. 6, p. 1900910, Nov. 2017.

[36] S. Tanaka, S.-H. Jeong, S. Sekiguchi, T. Kurahashi, Y. Tanaka, and K. Morito, "High-output-power, single-wavelength silicon hybrid laser using precise flip-chip bonding technology," *Opt. Express*, vol. 20, no. 27, p. 28057, Dec. 2012.

[37] Z. Zhou, B. Yin, and J. Michel, "On-chip light sources for silicon photonics," *Light Sci. Appl.*, vol. 4, no. 11, p. e358, Nov. 2015.

[38] K. Tanabe, K. Watanabe, and Y. Arakawa, "III-V/Si hybrid photonic devices by direct fusion bonding," *Sci. Rep.*, vol. 2, no. 1, p. 349, Dec. 2012.

[39] M. Paniccia *et al.*, "A hybrid silicon laser: silicon photonics technology for future tera-scale computing," *Intel white paper*, 2006. [Online]. Available: https://www.intel.com/content/dam/www/public/us/en/documents/technology-briefs/intel-labs-hybrid-silicon-laser-uses-paper.pdf. [Accessed: 13-Sep-2019].

[40] A. Moscoso-Mártir *et al.*, "Hybrid silicon photonics flip-chip laser integration with vertical self-alignment," in *2017 Conference on Lasers and Electro-Optics Pacific Rim (CLEO-PR), Singapore, 2017, p. s2069.*

[41] A. De Groote *et al.*, "Transfer-printing-based integration of single-mode waveguide-coupled III-V-on-silicon broadband light emitters," *Opt. Express*, vol. 24, no. 13, p. 13754, Jun. 2016.

[42] N. Hatori *et al.*, "Quantum dot laser for a light source of an athermal silicon optical interposer," *Photonics*, vol. 2, no. 2, pp. 355–364, Apr. 2015.

[43] A. W. Fang, H. Park, O. Cohen, R. Jones, M. J. Paniccia, and J. E. Bowers, "Electrically pumped hybrid AlGaInAs-silicon evanescent laser," *Opt. Express*, vol. 14, no. 20, p. 9203, Oct. 2006.

[44] M. Tang *et al.*, "Integration of III-V lasers on Si for Si photonics," *Prog. Quantum Electron.*, vol. 66, pp. 1–18, Aug. 2019.

[45] T. Shimizu *et al.*, "Optical characteristics of a multichannel hybrid integrated light source for ultra-high-bandwidth optical interconnections," *Photonics*, vol. 2, no. 4, pp. 1131–1138, Nov. 2015.

[46] R. Fischer *et al.*, “Growth and properties of GaAs/AlGaAs on nonpolar substrates using molecular-beam epitaxy,” *J. Appl. Phys.*, vol. 58, no. 1, pp. 374–381, 1985.

[47] W. I. Wang, “Molecular beam epitaxial growth and material properties of GaAs and AlGaAs on Si (100),” *Appl. Phys. Lett.*, vol. 44, no. 12, pp. 1149–1151, Jun. 1984.

[48] M. Sugo, H. Mori, Y. Itoh, Y. Sakai, and M. Tachikawa, “1.5 μm-long-wavelength multiple quantum well laser on a Si substrate,” *Jpn. J. Appl. Phys.*, vol. 30, no. 12, pp. 3876–3878, Dec. 1991.

[49] T. Yamada, M. Tachikawa, T. Sasaki, H. Mori, and Y. Kadota, “7000 h continuous wave operation of multiple quantum well laser on Si at 50 °C,” *Appl. Phys. Lett.*, vol. 70, no. 12, pp. 1614–1615, Mar. 1997.

[50] E. Tournié, L. Cerutti, J.-B. Rodriguez, H. Liu, J. Wu, and S. Chen, “Metamorphic III–V semiconductor lasers grown on silicon,” *MRS Bull.*, vol. 41, no. 03, pp. 218–223, Mar. 2016.

[51] H. K. Zimmermann, *Integrated Silicon Optoelectronics*, vol. 148. Berlin, Heidelberg: Springer, 2010.

[52] J. Wu, S. Chen, A. Seeds, and H. Liu, “Quantum dot optoelectronic devices: lasers, photodetectors and solar cells,” *J. Phys. D. Appl. Phys.*, vol. 48, no. 36, p. 363001, Sep. 2015.

[53] R. J. Hamers, R. M. Tromp, and J. E. Demuth, “Scanning tunneling microscopy of Si(001),” *Phys. Rev. B*, vol. 34, no. 8, pp. 5343–5357, Oct. 1986.

[54] Q. Li and K. M. Lau, “Epitaxial growth of highly mismatched III-V materials on (001) silicon for electronics and optoelectronics,” *Prog. Cryst. Growth Charact. Mater.*, vol. 63, no. 4, pp. 105–120, Dec. 2017.

[55] G. Brammertz *et al.*, “Low-temperature photoluminescence study of thin epitaxial GaAs films on Ge substrates,” *J. Appl. Phys.*, vol. 99, no. 9, p. 093514, May 2006.

[56] R. Alcotte *et al.*, “Epitaxial growth of antiphase boundary free GaAs layer on 300 mm Si(001) substrate by metalorganic chemical vapour deposition with high mobility,” *APL Mater.*, vol. 4, no. 4, p. 046101, Apr. 2016.

[57] M. Akiyama, Y. Kawarada, and K. Kaminishi, "Growth of single domain gaas layer on (100)-oriented Si substrate by MOCVD," *Jpn. J. Appl. Phys.*, vol. 23, no. 11, pp. 843–845, Nov. 1984.

[58] Z. Mi, P. Bhattacharya, J. Yang, and K. P. Pipe, "Room-temperature self-organised $In_{0.5}Ga_{0.5}As$ quantum dot laser on silicon," *Electron. Lett.*, vol. 41, no. 13, p. 742, 2005.

[59] T. Wang, H. Liu, A. Lee, F. Pozzi, and A. Seeds, "1.3-µm InAs/GaAs quantum-dot lasers monolithically grown on Si substrates," *Opt. Express*, vol. 19, no. 12, p. 11381, Jun. 2011.

[60] S. Chen *et al.*, "Electrically pumped continuous-wave III–V quantum dot lasers on silicon," *Nat. Photonics*, vol. 10, no. 5, pp. 307–311, May 2016.

[61] K. Volz *et al.*, "GaP-nucleation on exact Si (001) substrates for III/V device integration," *J. Cryst. Growth*, vol. 315, no. 1, pp. 37–47, 2011.

[62] B. Kunert, I. Németh, S. Reinhard, K. Volz, and W. Stolz, "Si (001) surface preparation for the antiphase domain free heteroepitaxial growth of GaP on Si substrate," *Thin Solid Films*, vol. 517, no. 1, pp. 140–143, Nov. 2008.

[63] W. A. Harrison, E. A. Kraut, J. R. Waldrop, and R. W. Grant, "Polar heterojunction interfaces," *Phys. Rev. B*, vol. 18, no. 8, pp. 4402–4410, Oct. 1978.

[64] A. Liu *et al.*, "Electrically pumped continuous-wave 1.3 µm quantum-dot lasers epitaxially grown on on-axis (001) GaP/Si," *Opt. Lett.*, vol. 42, no. 2, p. 338, Jan. 2017.

[65] D. Jung *et al.*, "Highly reliable low-threshold InAs quantum dot lasers on on-axis (001) Si with 87% injection efficiency," *ACS Photonics*, vol. 5, no. 3, pp. 1094–1100, Mar. 2018.

[66] J. Norman *et al.*, "Electrically pumped continuous wave quantum dot lasers epitaxially grown on patterned, on-axis (001) Si," *Opt. Express*, vol. 25, no. 4, p. 3927, 2017.

[67] Q. Li *et al.*, "1.3-µm InAs quantum-dot micro-disk lasers on V-groove patterned and unpatterned (001) silicon," *Opt. Express*, vol. 24, no. 18, p. 21038, Sep. 2016.

[68] Q. Li, K. W. Ng, and K. M. Lau, “Growing antiphase-domain-free GaAs thin films out of highly ordered planar nanowire arrays on exact (001) silicon,” *Appl. Phys. Lett.*, vol. 106, no. 7, p. 072105, Feb. 2015.

[69] J. Z. Li, J. Bai, C. Major, M. Carroll, A. Lochtefeld, and Z. Shellenbarger, “Defect reduction of GaAs/Si epitaxy by aspect ratio trapping,” *J. Appl. Phys.*, vol. 103, no. 10, p. 106102, May 2008.

[70] T. Jing, N. Ingle, and D. Yang, “Smooth SiConi etch for silicon-containing films.,” U.S. Patent No. 8501629, 2013.

[71] S. Chen *et al.*, “Electrically pumped continuous-wave 1.3 µm InAs/GaAs quantum dot lasers monolithically grown on on-axis Si (001) substrates,” *Opt. Express*, vol. 25, no. 5, pp. 4632–4639, Mar. 2017.

[72] J. Kwoen, B. Jang, J. Lee, T. Kageyama, K. Watanabe, and Y. Arakawa, “All MBE grown InAs/GaAs quantum dot lasers on on-axis Si (001),” *Opt. Express*, vol. 26, no. 9, p. 11568, Apr. 2018.

[73] V. K. Yang, M. Groenert, C. W. Leitz, A. J. Pitera, M. T. Currie, and E. A. Fitzgerald, “Crack formation in GaAs heteroepitaxial films on Si and SiGe virtual substrates,” *J. Appl. Phys.*, vol. 93, no. 7, pp. 3859–3865, Apr. 2003.

[74] B. Kunert, Y. Mols, M. Baryshniskova, N. Waldron, A. Schulze, and R. Langer, “How to control defect formation in monolithic III/V hetero-epitaxy on (100) Si? A critical review on current approaches,” *Semicond. Sci. Technol.*, vol. 33, no. 9, p. 093002, Sep. 2018.

[75] B. Wang *et al.*, “Control wafer bow of InGaP on 200 mm Si by strain engineering,” *Semicond. Sci. Technol.*, vol. 32, no. 12, p. 125013, Dec. 2017.

[76] H. Huang *et al.*, “Crack-free GaAs epitaxy on Si by using midpatterned growth: Application to Si-based wavelength-selective photodetector,” *J. Appl. Phys.*, vol. 104, no. 11, p. 113114, Dec. 2008.

[77] A. Scaccabarozzi *et al.*, “Integration of InGaP/GaAs/Ge triple-junction solar cells on deeply patterned silicon substrates,” *Prog. Photovoltaics Res. Appl.*, vol. 24, no. 10, pp. 1368–1377, Oct. 2016.

[78] S. F. Fang *et al.*, “Gallium arsenide and other compound semiconductors on

silicon," *J. Appl. Phys.*, vol. 68, no. 7, pp. R31–R58, Oct. 1990.

[79] T. Wang, H. Liu, A. Lee, F. Pozzi, and A. Seeds, "1.3-μm InAs/GaAs quantum-dot lasers monolithically grown on Si substrates," *Opt. Express*, vol. 19, no. 12, p. 11381, Jun. 2011.

[80] D. Jung, P. G. Callahan, B. Shin, K. Mukherjee, A. C. Gossard, and J. E. Bowers, "Low threading dislocation density GaAs growth on on-axis GaP/Si (001)," *J. Appl. Phys.*, vol. 122, no. 22, p. 225703, Dec. 2017.

[81] A. D. Lee, Q. Jiang, M. Tang, Y. Zhang, A. J. Seeds, and H. Liu, "InAs/GaAs quantum-dot lasers monolithically grown on Si, Ge, and Ge-on-Si substrates," *IEEE J. Sel. Top. Quantum Electron.*, vol. 19, no. 4, p. 1901107, Jul. 2013.

[82] D. A. Grenning and A. H. Herzog, "Dislocations and their relation to irregularities in zinc-diffused GaAsP p-n junctions," *J. Appl. Phys.*, vol. 39, no. 6, pp. 2783–2790, 1968.

[83] I. George, F. Becagli, H. Y. Liu, J. Wu, M. Tang, and R. Beanland, "Dislocation filters in GaAs on Si," *Semicond. Sci. Technol.*, vol. 30, no. 11, p. 114004, Nov. 2015.

[84] J. R. Orchard *et al.*, "In situ annealing enhancement of the optical properties and laser device performance of InAs quantum dots grown on Si substrates," *Opt. Express*, vol. 24, no. 6, p. 6196, Mar. 2016.

[85] M. Tang *et al.*, "Optimizations of defect filter layers for 1.3-μm InAs/GaAs quantum-dot lasers monolithically grown on Si substrates," *IEEE J. Sel. Top. Quantum Electron.*, vol. 22, no. 6, pp. 50–56, Nov. 2016.

[86] M. Tang *et al.*, "Optimisation of the dislocation filter layers in 1.3-μm InAs/GaAs quantum-dot lasers monolithically grown on Si substrates," *IET Optoelectron.*, vol. 9, no. 2, pp. 61–64, May 2015.

[87] J. P. van der Ziel, R. D. Dupuis, R. A. Logan, and C. J. Pinzone, "Degradation of GaAs lasers grown by metalorganic chemical vapor deposition on Si substrates," *Appl. Phys. Lett.*, vol. 51, no. 2, pp. 89–91, Jul. 1987.

[88] Z. I. Kazi, P. Thilakan, T. Egawa, M. Umeno, and T. Jimbo, "Realization of GaAs/AlGaAs Lasers on Si Substrates Using Epitaxial Lateral Overgrowth by

Metalorganic Chemical Vapor Deposition," *Jpn. J. Appl. Phys.*, vol. 40, no. 8, pp. 4903–4906, Aug. 2001.

[89] J. Jiménez, "Laser diode reliability: crystal defects and degradation modes," *Comptes Rendus Phys.*, vol. 4, no. 6, pp. 663–673, Jul. 2003.

[90] H. Kroemer, "A proposed class of hetero-junction injection lasers," *Proc. IEEE*, vol. 51, no. 12, pp. 1782–1783, Dec. 1963.

[91] Z. Alferov, "AlAs-GaAs heterojunction injection lasers with a low room-temperature threshold," *Sov. Phys. Semicond.*, vol. 3, pp. 1107–1110, 1970.

[92] M. J. Moran and H. N. Shapiro, *Fundamentals of Engineering Thermodynamics, Second Edition*, vol. 18, no. 2. John Wiley & Sons, Inc., 1993.

[93] D. J. Griffiths and D. F. Schroeter, *Introduction to Quantum Mechanics*. Cambridge University Press, 2018.

[94] J. W. Haus, *Fundamentals and Applications of Nanophotonics*. Elsevier, 2016.

[95] M. Fox, "Quantum-confined structures," in *Optical properties of solids*, Oxford University Press, 2010, pp. 141–144.

[96] M. Liao, S. Chen, J.-S. Park, A. Seeds, and H. Liu, "III–V quantum-dot lasers monolithically grown on silicon," *Semicond. Sci. Technol.*, vol. 33, no. 12, p. 123002, Dec. 2018.

[97] Y. Arakawa and H. Sakaki, "Multidimensional quantum well laser and temperature dependence of its threshold current," *Appl. Phys. Lett.*, vol. 40, no. 11, pp. 939–941, Jun. 1982.

[98] N. Kirstaedter *et al.*, "Low threshold, large To injection laser emission from (InGa)As quantum dots," *Electron. Lett.*, vol. 30, no. 17, pp. 1416–1417, Aug. 1994.

[99] J. Venables, *Introduction to surface and thin film processes*. Cambridge: Cambridge University Press, 2000.

[100] QDLaser, "White paper: New era of quantum dot lasers with evolution history of semiconductor lasers," 2008. [Online]. Available: http://www.qdlaser.com/pdf/White-Paper-technology-trend-of-quantum-dot-lasers-1.pdf. [Accessed: 24-May-

2017].

[101] M. Asada, Y. Miyamoto, and Y. Suematsu, “Gain and the threshold of three-dimensional quantum-box lasers,” *IEEE J. Quantum Electron.*, vol. 22, no. 9, pp. 1915–1921, Sep. 1986.

[102] K. Nishi, K. Takemasa, M. Sugawara, and Y. Arakawa, “Development of quantum dot lasers for data-com and silicon photonics applications,” *IEEE J. Sel. Top. Quantum Electron.*, vol. 23, no. 6, pp. 1–7, Nov. 2017.

[103] L. V Asryan and R. A. Suris, “Inhomogeneous line broadening and the threshold current density of a semiconductor quantum dot laser,” *Semicond. Sci. Technol.*, vol. 11, no. 4, pp. 554–567, Apr. 1996.

[104] K. Nishi, H. Saito, S. Sugou, and J. S. Lee, “A narrow photoluminescence linewidth of 21 meV at 1.35 μm from strain-reduced InAs quantum dots covered by $In_{0.2}Ga_{0.8}As$ grown on GaAs substrates,” *Appl. Phys. Lett.*, vol. 74, no. 8, pp. 1111–1113, Feb. 1999.

[105] G. Park, O. B. Shchekin, S. Csutak, D. L. Huffaker, and D. G. Deppe, “Room-temperature continuous-wave operation of a single-layered 1.3 μm quantum dot laser,” *Appl. Phys. Lett.*, vol. 75, no. 21, p. 3267, Nov. 1999.

[106] X. Huang, A. Stintz, C. P. Hains, G. T. Liu, J. Cheng, and K. J. Malloy, “Very low threshold current density room temperature continuous-wave lasing from a single-layer InAs quantum-dot laser,” *IEEE Photonics Technol. Lett.*, vol. 12, no. 3, pp. 227–229, Mar. 2000.

[107] G. Park, O. B. Shchekin, D. L. Huffaker, and D. G. Deppe, “Low-threshold oxide-confined 1.3-μm quantum-dot laser,” *IEEE Photonics Technol. Lett.*, vol. 12, no. 3, pp. 230–232, Mar. 2000.

[108] H. Liu *et al.*, “Improved performance of 1.3 μm multilayer InAs quantum-dot lasers using a high-growth-temperature GaAs spacer layer,” *Appl. Phys. Lett.*, vol. 85, no. 5, pp. 704–706, Aug. 2004.

[109] S. Freisem, G. Ozgur, K. Shavritranuruk, H. Chen, and D. G. Deppe, “Very-low-threshold current density continuous-wave quantum-dot laser diode,” *Electron. Lett.*, vol. 44, no. 11, p. 679, 2008.

[110] K. Nishi *et al.*, “Molecular beam epitaxial growths of high-optical-gain InAs quantum dots on GaAs for long-wavelength emission,” *J. Cryst. Growth*, vol. 378, pp. 459–462, Sep. 2013.

[111] O. B. Shchekin and D. G. Deppe, “1.3 μm InAs quantum dot laser with To=161 K from 0 to 80 °C,” *Appl. Phys. Lett.*, vol. 80, no. 18, pp. 3277–3279, May 2002.

[112] I. C. Sandall *et al.*, “The effect of p doping in InAs quantum dot lasers,” *Appl. Phys. Lett.*, vol. 88, no. 11, p. 111113, Mar. 2006.

[113] M. Sugawara and M. Usami, “Handling the heat,” *Nat. Photonics*, vol. 3, no. 1, pp. 30–31, Jan. 2009.

[114] N. H. Zhu *et al.*, “Directly modulated semiconductor lasers,” *IEEE J. Sel. Top. Quantum Electron.*, vol. 24, no. 1, pp. 1–19, Jan. 2018.

[115] M. Ishida *et al.*, “Low-driving-current temperature-stable 10Gbit/s operation of p-doped 1.3 μm quantum dot lasers between 20 and 90°C,” *Electron. Lett.*, vol. 43, no. 4, pp. 219–221, 2007.

[116] M. Ishida *et al.*, “Photon lifetime dependence of modulation efficiency and K factor in 1.3μm self-assembled InAs⁄GaAs quantum-dot lasers: Impact of capture time and maximum modal gain on modulation bandwidth,” *Appl. Phys. Lett.*, vol. 85, no. 18, pp. 4145–4147, Nov. 2004.

[117] A. E. Zhukov, M. V. Maksimov, and A. R. Kovsh, “Device characteristics of long-wavelength lasers based on self-organized quantum dots,” *Semiconductors*, vol. 46, no. 10, pp. 1225–1250, Oct. 2012.

[118] A. A. Ukhanov, A. Stintz, P. G. Eliseev, and K. J. Malloy, “Comparison of the carrier induced refractive index, gain, and linewidth enhancement factor in quantum dot and quantum well lasers,” *Appl. Phys. Lett.*, vol. 84, no. 7, pp. 1058–1060, Feb. 2004.

[119] S. M. Kim, Y. Wang, M. Keever, and J. S. Harris, “High-frequency modulation characteristics of 1.3-μm InGaAs quantum dot lasers,” *IEEE Photonics Technol. Lett.*, vol. 16, no. 2, pp. 377–379, Feb. 2004.

[120] K. Otsubo *et al.*, “Temperature-insensitive eye-opening under 10-Gb/s modulation of 1.3-μm p-doped quantum-dot lasers without current adjustments,” *Jpn. J. Appl.*

Phys., vol. 43, no. No. 8B, pp. L1124–L1126, Jul. 2004.

[121] K. Takada *et al.*, “Wide-temperature-range 10.3 Gbit/s operations of 1.3 µm high-density quantum-dot DFB lasers,” *Electron. Lett.*, vol. 47, no. 3, p. 206, 2011.

[122] C. H. Henry, “Theory of the linewidth of semiconductor lasers,” *IEEE J. Quantum Electron.*, vol. 18, no. 2, pp. 259–264, Feb. 1982.

[123] C. Henry, “Phase noise in semiconductor lasers,” *J. Light. Technol.*, vol. 4, no. 3, pp. 298–311, 1986.

[124] R. Tkach and A. Chraplyvy, “Phase noise and linewidth in an InGaAsP DFB laser,” *J. Light. Technol.*, vol. 4, no. 11, pp. 1711–1716, 1986.

[125] S. Melnik, G. Huyet, and A. Uskov, “The linewidth enhancement factor α of quantum dot semiconductor lasers,” *Opt. Express*, vol. 14, no. 7, p. 2950, Apr. 2006.

[126] Y. Miyake and M. Asada, “Spectral characteristics of linewidth enhancement factor α of multidimensional quantum wells,” *Jpn. J. Appl. Phys.*, vol. 28, no. 7 R, pp. L1959–L1962, Jul. 1989.

[127] R. Paiella, “Quantum Cascade Lasers,” in Comprehensive Semiconductor Science and Technology, P. Bhattacharya, R. Fornari, and H. Kamimura, Eds. Elsevier, 2011, pp. 683–723.

[128] F. Kano et al., “Reduction of linewidth enhancement factor in InGaAsP-InP modulation-doped strained multiple-quantum-well lasers,” IEEE J. Quantum Electron., vol. 29, no. 6, pp. 1553–1559, Jun. 1993.

[129] A. Markus, J. X. Chen, O. Gauthier-Lafaye, J. Provost, C. Paranthoen, and A. Fiore, “Impact of intraband relaxation on the performance of a quantum-dot laser,” *IEEE J. Sel. Top. Quantum Electron.*, vol. 9, no. 5, pp. 1308–1314, Sep. 2003.

[130] A. Martinez *et al.*, “Static and dynamic measurements of the α-factor of five-quantum-dot-layer single-mode lasers emitting at 1.3 µm on GaAs,” *Appl. Phys. Lett.*, vol. 86, no. 21, p. 211115, May 2005.

[131] D. Y. Cong *et al.*, “Optimisation of α-factor for quantum dot InAs/GaAs Fabry-Pérot lasers emitting at 1.3 µm,” *Electron. Lett.*, vol. 43, no. 4, pp. 222–224, 2007.

[132] P. K. Kondratko, S. L. Chuang, G. Walter, T. Chung, and N. Holonyak, “Observations of near-zero linewidth enhancement factor in a quantum-well coupled quantum-dot laser,” *Appl. Phys. Lett.*, vol. 83, no. 23, pp. 4818–4820, Dec. 2003.

[133] D. Y. Cong *et al.*, “Temperature insensitive linewidth enhancement factor of p -type doped InAsGaAs quantum-dot lasers emitting at 1.3 μm,” *Appl. Phys. Lett.*, vol. 92, no. 19, p. 191109, May 2008.

[134] G. P. Agrawal, *Fiber-optic communication systems*. John Wiley & Sons, 2010.

[135] J. Helms and K. Petermann, “A simple analytic expression for the stable operation range of laser diodes with optical feedback,” *IEEE J. Quantum Electron.*, vol. 26, no. 5, pp. 833–836, May 1990.

[136] A. Y. Liu, T. Komljenovic, M. L. Davenport, A. C. Gossard, and J. E. Bowers, “Reflection sensitivity of 1.3 μm quantum dot lasers epitaxially grown on silicon,” *Opt. Express*, vol. 25, no. 9, p. 9535, May 2017.

[137] G. Huyet *et al.*, “Quantum dot semiconductor lasers with optical feedback,” *Phys. Status Solidi Appl. Res.*, vol. 201, no. 2, pp. 345–352, Jan. 2004.

[138] D. O’Brien, S. P. Hegarty, G. Huyet, and A. V. Uskov, “Sensitivity of quantum-dot semiconductor lasers to optical feedback,” *Opt. Lett.*, vol. 29, no. 10, p. 1072, May 2004.

[139] D. O’Brien *et al.*, “Feedback sensitivity of 1.3 μm InAs⁄GaAs quantum dot lasers,” *Electron. Lett.*, vol. 39, no. 25, p. 1819, 2003.

[140] Z. Mi, J. Yang, P. Bhattacharya, G. Qin, and Z. Ma, “High-performance quantum dot lasers and integrated optoelectronics on Si,” *Proc. IEEE*, vol. 97, no. 7, pp. 1239–1249, Jul. 2009.

[141] I. Ovid’ko, “Relaxation mechanisms in strained nanoislands,” *Phys. Rev. Lett.*, vol. 88, no. 4, p. 046103, Jan. 2002.

[142] J. Yang, P. Bhattacharya, and Z. Mi, “High-performance $In_{0.5}Ga_{0.5}As$/GaAs quantum-dot lasers on silicon with multiple-layer quantum-dot dislocation filters,” *IEEE Trans. Electron Devices*, vol. 54, no. 11, pp. 2849–2855, Nov. 2007.

[143] B. Shi, Q. Li, and K. M. Lau, “Self-organized InAs/InAlGaAs quantum dots as dislocation filters for InP films on (001) Si,” *J. Cryst. Growth*, vol. 464, pp. 28–32, Apr. 2017.

[144] R. Beanland *et al.*, “Structural analysis of life tested 1.3 µm quantum dot lasers,” *J. Appl. Phys.*, vol. 103, no. 1, p. 014913, Jan. 2008.

[145] Y. Arakawa, “Quantum dot lasers for silicon photonics,” *21st Optoelectron. Commun. Conf. OECC*, vol. 3, no. 5, p. B1, Oct. 2016.

[146] Z. Liu *et al.*, “Origin of Defect Tolerance in InAs/GaAs Quantum Dot Lasers Grown on Silicon,” *J. Light. Technol.*, vol. 38, no. 2, pp. 240–248, Jan. 2020.

[147] A. Lee, Q. Jiang, M. Tang, A. Seeds, and H. Liu, “Continuous-wave InAs/GaAs quantum-dot laser diodes monolithically grown on Si substrate with low threshold current densities,” *Opt. Express*, vol. 20, no. 20, pp. 22181–22187, 2012.

[148] A. Y. Liu *et al.*, “High performance continuous wave 1.3 µm quantum dot lasers on silicon,” *Appl. Phys. Lett.*, vol. 104, no. 4, p. 041104, Jan. 2014.

[149] J. Kwoen, B. Jang, K. Watanabe, and Y. Arakawa, “High-temperature continuous-wave operation of directly grown InAs/GaAs quantum dot lasers on on-axis Si (001),” *Opt. Express*, vol. 27, no. 3, p. 2681, Feb. 2019.

[150] C. Shang *et al.*, “Low-Threshold Epitaxially Grown 1.3-µm InAs Quantum Dot Lasers on Patterned (001) Si,” *IEEE J. Sel. Top. Quantum Electron.*, vol. 25, no. 6, pp. 1–7, Nov. 2019.

[151] S. Chuang, *Physics of Photonic Devices*. Wiley, 2009.

[152] K. Mathwig *et al.*, “DFB lasers with deeply etched vertical grating based on InAs–InP quantum-dash structures,” *IEEE Photonics Technol. Lett.*, vol. 19, no. 5, pp. 264–266, 2007.

[153] A. I. Laakso, J. Karinen, and M. Dumitrescu, “Modeling and design particularities for distributed feedback lasers with laterally coupled ridge-waveguide surface gratings,” *Proc. SPIE 7933, Physics and Simulation of Optoelectronic Devices XIX*, p. 79332K, 2011.

[154] Y. Wang *et al.*, “Monolithic quantum-dot distributed feedback laser array on

silicon," *Optica*, vol. 5, no. 5, p. 528, May 2018.

[155] M. J. R. Heck, J. F. Bauters, M. L. Davenport, D. T. Spencer, and J. E. Bowers, "Ultra-low loss waveguide platform and its integration with silicon photonics," Laser Photon. Rev., vol. 8, no. 5, pp. 667–686, Sep. 2014.

[156] G. Li *et al.*, "Ultralow-loss, high-density SOI optical waveguide routing for macrochip interconnects," *Opt. Express*, vol. 20, no. 11, pp. 12035–12039, May 2012.

[157] G. Roelkens, D. Van Thourhout, R. Baets, R. Nötzel, and M. Smit, "Laser emission and photodetection in an InP/InGaAsP layer integrated on and coupled to a Silicon-on-Insulator waveguide circuit," *Opt. Express*, vol. 14, no. 18, p. 8154, 2006.

Chapter 2

Experimental methods

In this chapter, the detailed experimental methods are introduced in order to provide a coherent overview of all techniques utilised in this thesis. Firstly, three techniques for material characteristics will be introduced, namely photoluminescence (PL) spectroscopy, atomic force microscopy (AFM) and scanning electron microscopy (SEM). In section two, the general fabrication procedures for two different laser structures, the broad-area laser and narrow-ridge laser will be demonstrated. The optimisations and comparative studies for each fabrication step will be discussed afterwards. In section three, the testing and characteristics of laser diodes in terms of principal static properties and RIN are introduced in detail.

2.1 Material characteristics

2.1.1 Photoluminescence spectroscopy

PL is the process of light re-emission after absorbing a photon with higher energy, and can be used to determine the character and quality of III–V QD materials. Figure 2.1 shows a schematic diagram of the PL process for bulk material. The III–V material has absorbed a photon for an excitation source, where the incident photon energy hv_{exc} is bigger than the bandgap energy of this material. An electron is, thus, excited from the valence band to the conduction band with a high energy state, and a hole is left in the valence band. However, the electron and hole are not able to remain in their original states for a long time, and instead, they lose their energy rapidly by emitting phonons. As shown in Figure 2.1, these cascaded transitions of electrons and holes lead to a fast "relaxation" to the GSs. Each step corresponds to a phonon emitting with a specific momentum to observe the energy conservation law. This phonon scattering takes place in a very short time (~10^{-13} s), which is much faster than the radiative lifetime of nanosecond time (~10^{-9} s). Therefore, the relaxation of the electron and hole to the GSs only happens after the occurrence of the electron–hole or other non-radiative recombination. The radiative recombination emits a photon whose emitting energy is equal to the material bandgap [1].

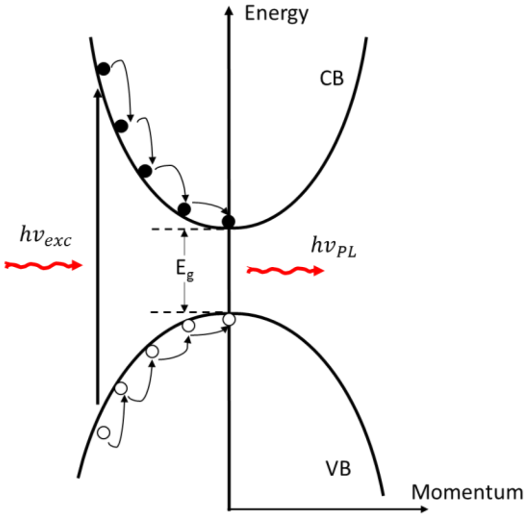

Figure 2.1 Interband transitions of the PL process [1].

According to the principle of PL, PL spectroscopy is classed as a powerful and non-destructive technique to learn the properties of materials. A simplified experimental arrangement of PL spectroscopy is illustrated in Figure 2.2. The sample is mounted on a temperature-controllable stage within a cryostat. Liquid helium is used to maintain a low temperature of the cryostat, in a range from 10 K to 320 K. A commercial diode-pumped solid-state laser of 532 nm wavelength takes the role of excitation source to provide continuous and constant lasing light. The incident light from the laser passes through a chopper, which "chops" the light with a specific frequency, such as 210 Hz, which is aimed to be a reference for a lock-in amplifier. After the chopper, the chopped light is focused on the sample and leads to PL. A portion of the PL signals will be collected by a lens and dispersed into a selected range of wavelengths by the monochromator. Then, a narrow range of wavelength of light is measured by a sensitive InGaAs detector, which is used for a near-infrared range of 1.1–1.35 µm. Finally, the received signal from the detector is transmitted back to the lock-in amplifier. The lock-in amplifier is a technique which can single out the signal at the specific reference frequency. The noise signals at other frequencies are filtered out. Therefore, the noise bandwidth can be significantly reduced. In this case, the reference signal is multiplied with the received signal with the surrounding noise. A DC output signal proportional to the signal amplitude is then obtained after passing a low-pass filter. Hereby, the profile of the light intensity against the light wavelength is recorded and plotted by the computer.

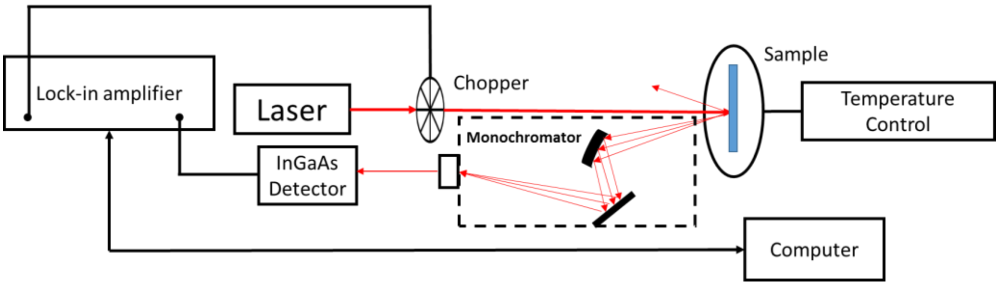

Figure 2.2 Simplified schematic diagram of PL experimental setup.

This plotted PL spectrum can be used to investigate the optical properties of the materials. From the PL spectrum, the bandgap energies for each transition state of the QDs can be determined. Figure 2.3 displays a typical PL spectrum of the InAs/GaAs QDs, which shows the excitonic peak of GS at 1310 nm (946.4 meV) and the first excited state at 1230 nm (1008 meV). In addition to the emission wavelength, the peak intensity of PL involves the impurities or defects contained in the semiconductor materials. As we know, the impurities or defects act as non-radiative recombination centres, which degenerate the quality of the materials and decrease PL intensity [2]. Moreover, in the detection of QD structures, the full width at half maximum (FWHM) of the PL spectrum can also be used for examining the homogeneity of the QD structure. A narrower FWHM means the size of the QDs is more identical.

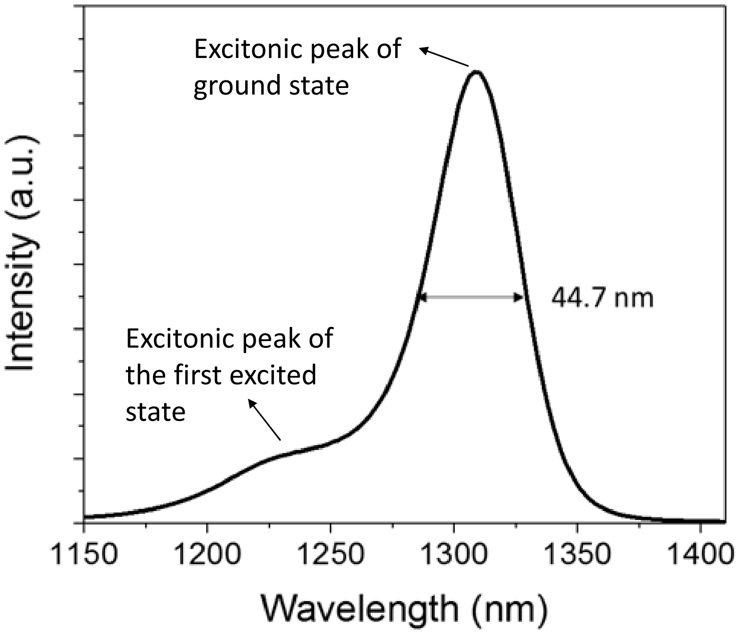

Figure 2.3 PL spectrum of III–V QD on Si.

2.1.2 Atomic force microscopy

In addition to PL spectroscopy, AFM is an efficient and straightforward technique of understanding QD topography. AFM uses a kind of scanning probe microscope with high resolution. Figure 2.4 (a) shows a schematic diagram of an AFM, which contains a free cantilever with a nanoscale-size (20 nm radius is used) and sharp pyramid tip, as shown in Figure 2.4 (b). When the tip is in proximity to the sample surface, the force between the tip and sample leads a deflection of the cantilever [3]. The AFM scanning images are acquired by measuring the vertical and lateral deflection of the cantilever; this measurement is performed by reflecting a laser beam from the optical level to a sensitive detector (Figure 2.4 (a)).

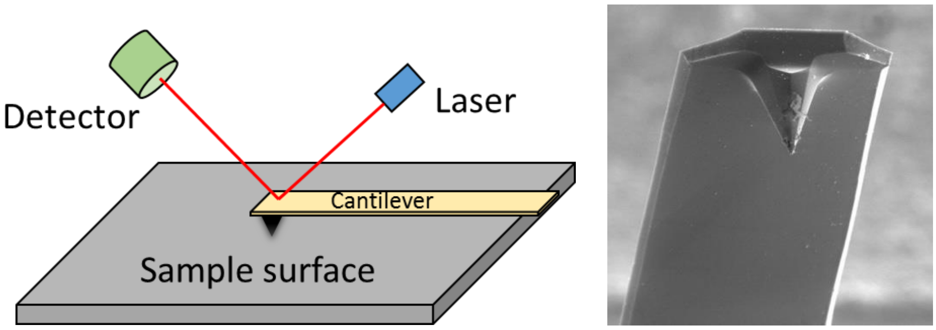

Figure 2.4 (a) Schematic diagram of the AFM system. (b) A tip of AFM.

There are two modes of imaging mode: contact mode and non-contact mode, also known as static mode and dynamic mode. For the contact mode, the tip is “dragged” over the surface and traces the shape of the sample by touching the sample. Because the attractive force of the contact mode is quite strong and may easily damage either the tip or surface of the sample, it is commonly used on a firm and solid surface. In our experiments, AFM is normally applied for detecting the topography of QDs which are quite fragile, so the non-contact mode is employed. In the non-contact mode, the cantilever oscillates up and down with a constant frequency, where the oscillation amplitude is only nanometres or picometres [4]. By adjusting the distance between the tip and surface, the frequency and amplitude of oscillation can remain constant and combine with the feedback loop system, so that topographic images of the sample surface can be constructed. Figure 2.5 shows a 2-D (a) and 3-D (b) AFM image of an uncapped QD structure. From graph (a), we can easily measure the dot size of the QDs as well as the QD density, and graph (b) presents the height of the QDs.

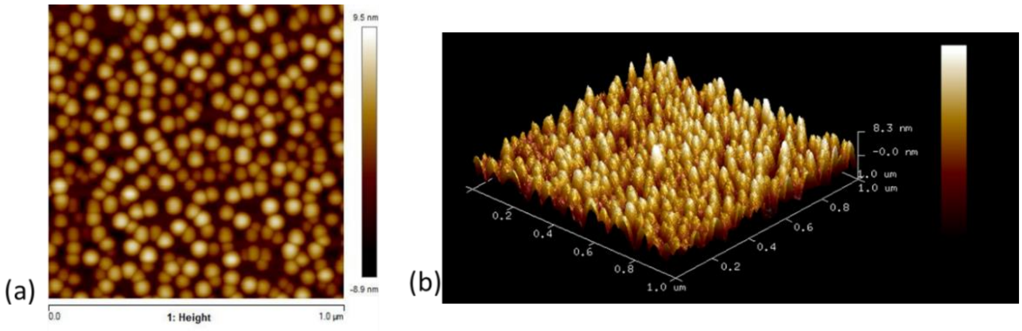

Figure 2.5 (a) 2-D and (b) 3-D AFM image of InAs/GaAs QDs on Si substrate.

2.1.3 Scanning electron microscopy

In SEM, the microscope uses a focused electron beam to scan the surface of the sample to produce images. Although AFM may provide more detailed information on the surface, it is only suitable for film surfaces, and it is difficult to observe whole device structures. SEM is able to achieve the depth of field for stereo images as shown in Figure 2.6, which illustrates a part of a laser structure device (p-content) with a mirror-like as-cleaved facet, where we can readily measure the dimensions of the laser stripe. Apart from that, SEM can also be used for distinguishing and measuring the thickness of each epitaxial layer with different compositions, as shown in Figure 2.7. It is a crucial step before device fabrication to minimise manufacturing errors, especially in the etching process.

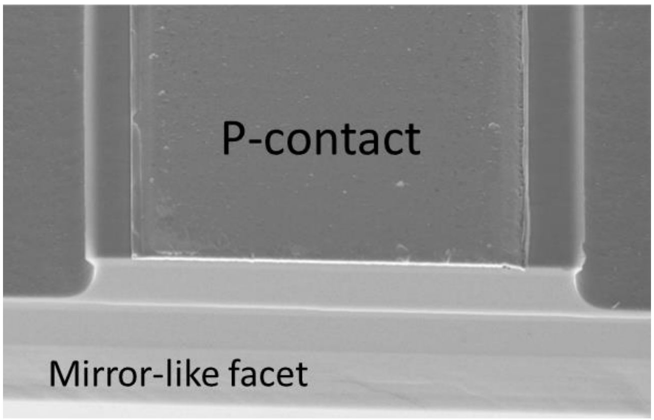

Figure 2.6 SEM image of the p-contact of a laser device with the as-cleaved facet.

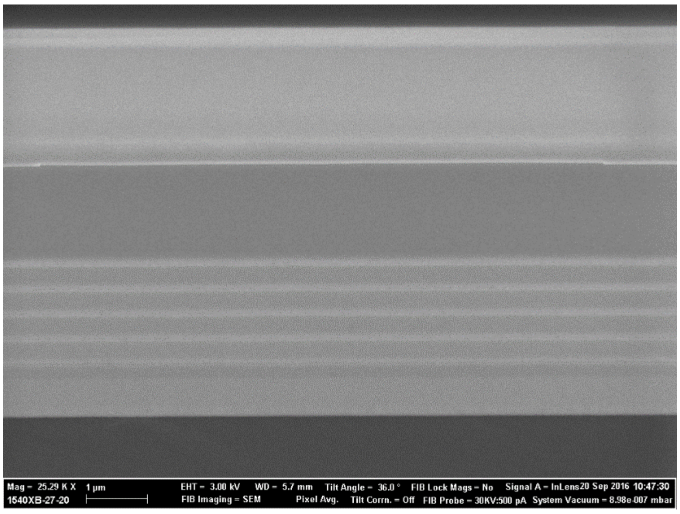

Figure 2.7 SEM image of epitaxially grown layers of a laser structure sample before fabrication.

A schematic diagram of the SEM is shown in Figure 2.8, where the primary electrons were created from the electron source and accelerated down by passing a combination of condenser lens and apertures to the scanner in a raster pattern of the sample surface. The sample is mounted on a rotating stage, which allows observation of the specimens from different angles. There are various signals, including secondary electrons (SEs), back-scattered electrons (BSEs) and X-rays, generated and emitted out from samples. The emitted signals from the sample have different energy levels and thus have selective energy detectors. The SEs are generated from the inelastic collisions between the primary electrons and sample, and have lower energy than the BSEs or X-rays. Since the SEs can only be emitted near the surface, the mean escape depth (~ 1 nm from metal) is much shorter than other signals. Normally it is assumed that the escape probability for SEs produced decreases with the increased mean escape depth [5]. Therefore, the higher SEs yield leads to a better resolution with more detailed surface information [6][7]. In general, the SE yield depends on the work function of the materials, which defines the energy level that the electron can overcome from the Fermi level to the vacuum level to escape from the sample surface. The work function is determined by the material composition and the atomic packing at the surface. Therefore, the elemental compositions of the sample can be obtained from the SEM image.

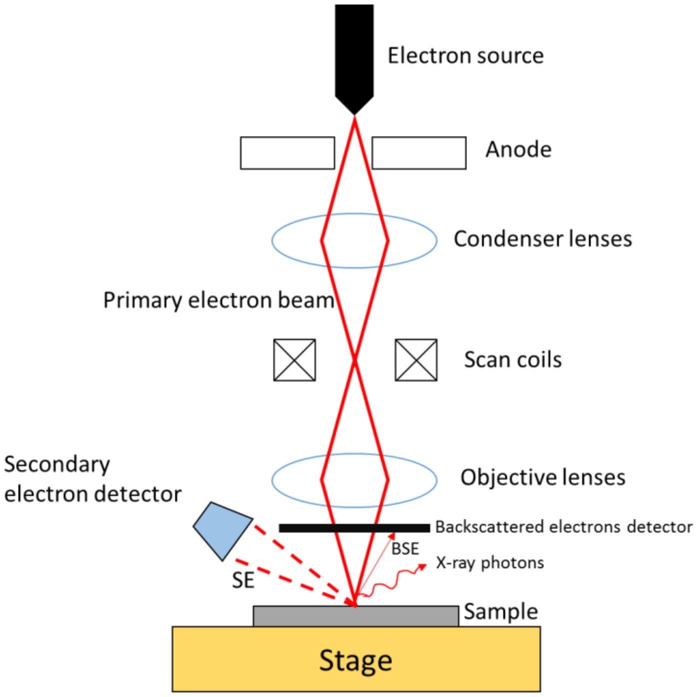

Figure 2.8 Schematic diagram of the working principle of the SEM system.

Besides SEM, another microscope, known as the transmission electron microscope (TEM), also uses electron beams to form an image with much higher resolution on an atomic scale. The main difference between TEM and SEM is that TEM is based on the transmitted electrons rather than the scattering electrons as in SEM. TEM can provide more details from inside the materials, such as crystallisation, lattice stress and dislocations. Although we use TEM to learn the QD morphology, dislocations and surface boundaries of epitaxial wafers, these works are usually done by our cooperating organisations or universities due to the complicated sample preparation and TEM machine operation.

2.2 Device fabrication

2.2.1 General laser fabrication process

After obtaining the material characteristics, the grown wafers are ready for device fabrication. Figure 2.9 displays the full laser fabrication flow chart. The wafer cleaning process is the first step, and is critical for the semiconductor fabrication work since contaminants on the wafer surface can lead to device failure and low yield. In our works, the sample cleaning is done by dipping the wafer into acetone and isopropyl alcohol (IPA) and performing ultrasonic vibration cleaning for 5 minutes, respectively. The use of acetone combined with the ultrasonic cleaning can effectively remove the organic and ionic particles on the sample surface. The purpose of the IPA washing after the use of acetone is to remove any acetone traces from the sample surface. Finally, the wafer is blown dry by a nitrogen gun. The sample surface is then inspected under a microscope to ensure there are less than four particles per field of view at 50 x magnification; if not, the sample cleaning step is repeated until there are no obvious stains.

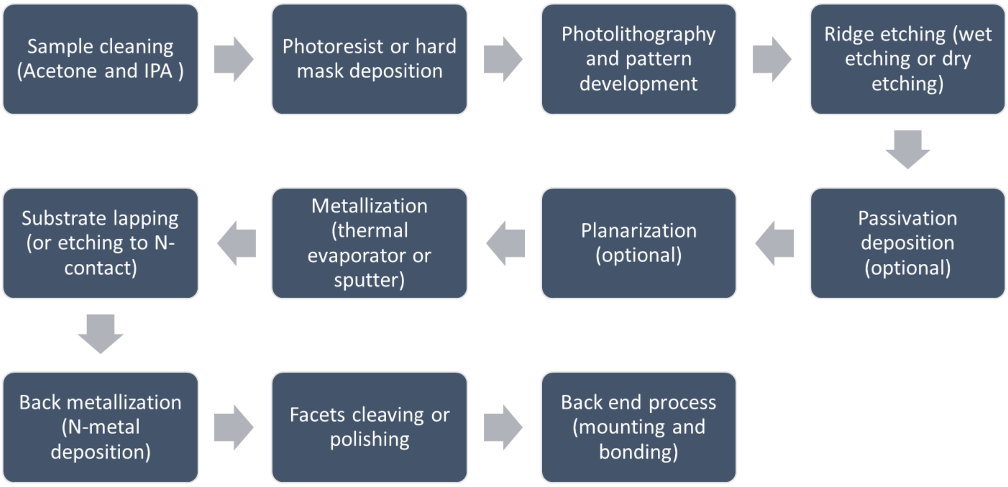

Figure 2.9 Flow chart of the laser fabrication process.

After the wafer preparation, the sample is placed on a hotplate with a temperature of 120–140 °C for several minutes for dehydration. Then, the photoresist can be deposited on the clean and dry sample surface. There are several different methods for the photoresist coating; the spin-coating method is one of the simplest and fastest, and this method is widely used in research labs. The photoresist thickness can be varied in a range by the spinning speed. After soft-baking the deposited photoresist, the sample is ready for photolithography by the patterning process. The sample is then etched by wet/dry etching techniques to define a mesa as a laser cavity ridge. The passivation and planarisation steps are optional, depending on the device structure. After that, p-type and n-type electrodes are deposited by thermal evaporator or sputter. The substrate of the laser device is lapped to 120 μm for better heat dissipation and precise cleaving. Hence, the sample is cleaved into several laser bars with desired cavity lengths. In order to achieve better temperature characteristics, the laser bars are mounted on heatsinks (copper plates) by indium solder paste, and the p-contact and n-contact are bonded with bond pads by gold wire to enhance the heat dissipation of the laser diodes. The fabrication progress of the laser device is thus complete.

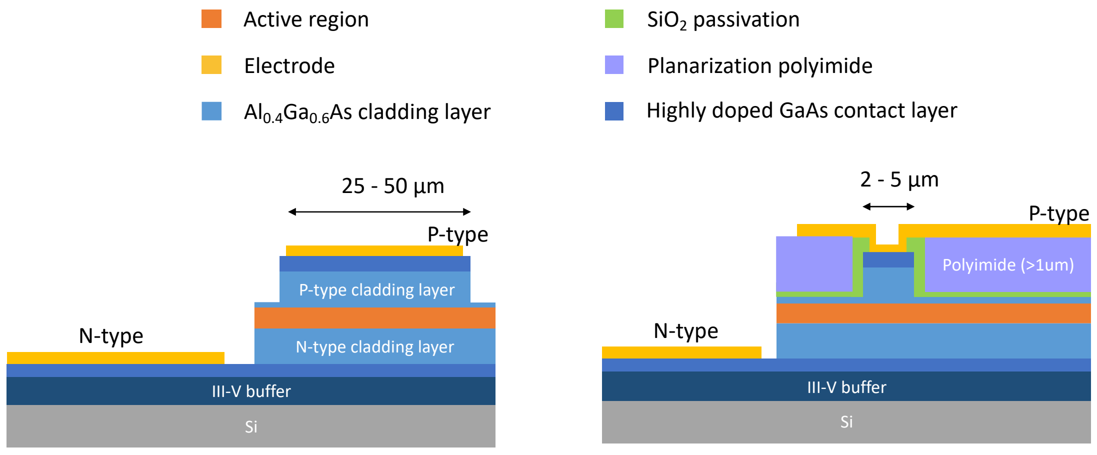

Broad-area laser

Narrow-ridge laser

Figure 2.10 Cross-section diagrams of two bottom-up III–V FP laser structures: broad-area laser and gain-guided narrow-ridge laser.

Figure 2.10 shows two different Si-based III–V Fabry-Perot (FP) lasers with bottom-up structure: a broad-area laser and a narrow-ridge waveguide laser. Both lasers have the same epitaxy layers, grown by MBE. After the well-developed III-V buffer grown on Si substrate (discussed in section 1.2), a highly doped n-GaAs contact layer with 1×10^{18} cm^{-3} is deposited. The QD active region is sandwiched by n-type $Al_{0.4}Ga_{0.6}As$ and p-type $Al_{0.4}Ga_{0.6}As$ cladding layer with $\sim 10^{17}$ cm^{-3}. Finally, the highly doped p-type GaAs with 1×10^{19} cm^{-3} doping level finish the laser epi-layers. The broad-area laser has a broader laser ridge which is normally greater than 25 μm and the top electrode is deposited on the ridge directly without passivation and planarisation. The fabrication process of the broad-area laser is relatively simpler than the narrow laser structures, and it requires four steps of photolithography. The four-step process flow is including:

1. P-type etching: The broad laser ridge is defined by wet etching. The etching depth is 200 nm above the active region for the effective carrier confinement as well as leaving active region undisturbed.
2. P-type metallisation: The patterns for metallisation have been transferred on the photoresist. The p-type electrode is deposited on the p-type GaAs contact layer by sputter and followed by a lift-off process.
3. N-type etching: The device is then etched to the n-type contact layer by wet etching.
4. N-type metallisation: The n-type electrode is deposited by thermal/e-beam evaporator and annealed by a rapid thermal process for better ohmic contact.

The details and recipes of each fabrication flow are discussed in the following sections. Due to the wider laser cavity width ($\gg \lambda$), the broad-area FP laser contains a lot of longitudinal and transverse lasing modes, which is unpractical for light emitter sources in data communication systems. Thus, the narrow-ridge laser with single transverse mode lasing has also been investigated in this thesis.

The cross-section of the gain-guided ridge laser structures is shown in Figure 2.10. The narrow-ridge mesa is defined by the shallow etch, and the remaining active region is undisturbed so that the etching profile only partly penetrates into the top cladding layer. In this thesis, the mesa ridge is 2–5 μm in width and has been etched 200 nm above the active region. The p-type mesa is isolated by the dielectric material of SiO_2 as the passivation layer. The planarisation polyimide is then deposited around the ridge after the open-windowed passivation layer. The thickness of the polyimide should be larger than 1 μm to minimise the parasitic capacitance. After that, the p-type metal is deposited by the sputtering or e-beam evaporation. For the n-type region, the same fabrication process as used for the broad-area laser device is implemented.

2.2.2 Photolithography and electron beam lithography

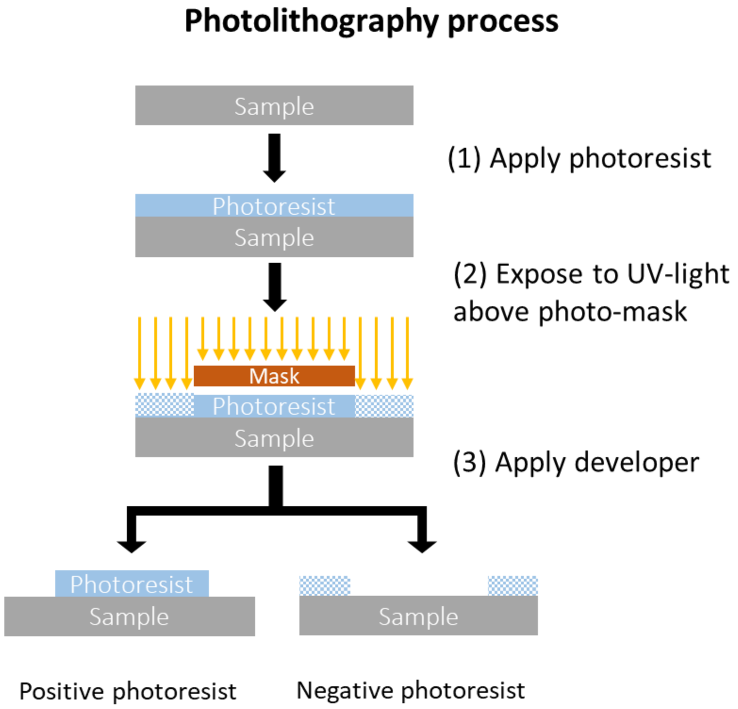

Figure 2.11 A standard photolithography process of positive and negative photoresist by photo-mask.

Photolithography is the first and most essential step in the device fabrication since the quality of the photolithograph has a strong impact on the final performance of the laser devices. The wafer sample with the deposited photoresist is selectively exposed to UV light via a photo-mask, leaving the lateral image that can be selectively dissolved to transfer the pattern onto the underlying surface. In general, there are two kinds of photoresists: positive and negative photoresists, which display totally different chemical properties when exposed to UV light. As shown in Figure 2.11, the area exposed to UV light becomes more soluble in the developer for a positive photoresist. In contrast, the negative photoresist becomes cross-linked/polymerised when it is exposed to the light. The unexposed area of the negative photoresist will be removed in the developer. Both positive and negative photoresists work well in the semiconductor fabrication process, and the choice depends on the relevant applications. In general, the positive resist has the advantages of a larger depth of focus [8] and higher resolution [9] than the negative resist. Because of the larger depth of focus, the thickness of positive resist can be thicker than the negative resist, thus, resulting in a higher aspect ratio and fewer pinholes of positive resist. Nevertheless, the negative photoresist shows the strengths of stronger adhesion, excellent etching resistance and less cost compared with positive resist [10]. More importantly, the choice of photoresist is also depended on the geometries of printed patterns [11]. The comparison between the positive and negative photoresist is summarised in Table 2.1. In this thesis, most of the process steps use positive photoresists, with the exception of the negative resist hydrogen silsesquioxane (HSQ) used in electron beam lithography (EBL), which will be discussed later.

Table 2.1 Comparison of positive and negative photoresist

Parameters	Positive photoresist	Negative photoresist
Resolution	Higher	
Depth of focus	Larger	
Thickness	Thicker	
Pinholes	Less	
Contrast	Better	
Adhesion		Better
Etching resistance		Better
Exposure speed		Faster
Cost		Lower

Photoresist exposure parameters are often described in terms of specific emission lines from a mercury lamp. The most common lines are referenced to the G-line at 436 nm, H-line at 405 nm and I-line at 365 nm. Because the absorption coefficient of the photoresist is significantly varied at different exposure wavelengths, different exposure doses may be required depending on the wavelength being employed [12]. The smallest linewidth resolution is decided by both the resolving capability of the photoresist and the UV exposed line. Although pattern features with sub-micrometre linewidth can be theoretically obtained by the standard research mask aligner (Suss MA3/MB6), the achievable resolution is also dependent on the wafer size, wafer flatness, cleanroom conditions, etc.; therefore, it varies significantly for different processes [13]. Among the varied impact factors of the photolithography quality, the edge-bead effect is one of the reasons causing the inferior pattern feature and is frequently ignored. As illustrated in Figure 2.12 (a), the photoresist may build up at the wafer edges during the spin-coating and soft-baking process, which is an aggravating issue for small wafer samples or photoresists with high viscosity. This edge bead will lead to a gap of several micrometres between the photo-mask and sample surface and make proper exposure during contact lithography difficult. One can pre-expose the beaded-up area and remove it before proceeding with the patterning lithography, as shown in Figure 2.12 (b).

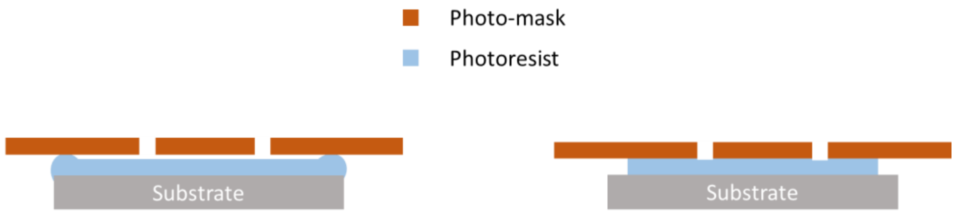

(a) With edge bead (b) Edge bead removed

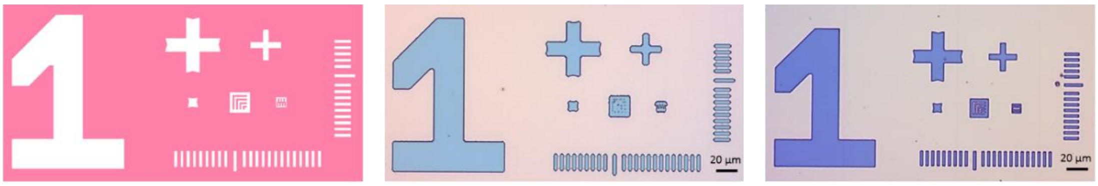

(c) Designed pattern **(d)** With edge bead **(e)** Edge bead remove

Figure 2.12 Cross-section of wafer sample (a) with edge bead and (b) without edge bead in contact mode photolithography. (c) Photolithography features of the designed pattern. Microscope images of the print pattern (d) with edge bead and (e) without edge bead after developing.

Figure 2.12 (c–e) compare the designed photo-mask pattern and photolithography results with and without edge bead under the same exposure dose and developing time. It can be seen that the minimum linewidth under the edge bead condition is ~3 µm, while ~1 µm linewidth is achievable after removing the edge bead. Although the 1 µm linewidth pattern can be achieved by the photolithography technique, corrugated features can still be found on the sidewall of the photoresist, as shown in Figure 2.13. It can be explained by the uneven sample surface by the small wafers. For narrow-ridge laser etching, these unsmooth features are transferred from the hard mask to the III–V ridge mesa, which is undesirable and will cause severe light scattering/loss in such a narrow laser cavity (≤ 5µm). Thus, it is recommended to employ EBL if the sample size is small and severe edge bead problem has happened in the research lab.

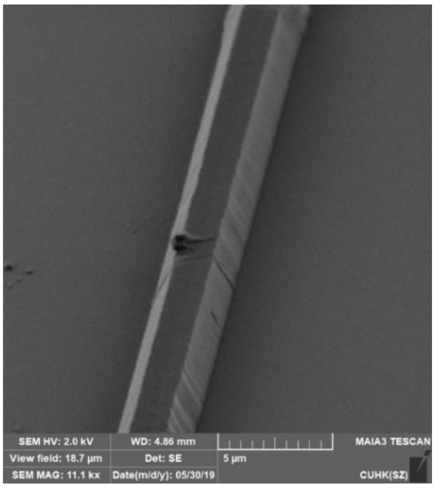

Figure 2.13 SEM image of the sidewall of a positive photoresist (S1813).

Compared with standard photolithography, the reason for the nanoscale features achievable by EBL is the utilisation of a focused electron beam with much shorter wavelength instead of the light. A typical EBL system is similar to an SEM system, whereas EBL only scans onto the sample region according to the designed pattern. Thus, the selective sample surface that is coated by the electron-sensitive resist can be dissolved or cross-linked in the developer. There are many processing parameters and conditions of the EBL that will affect the lithography quality, which requires long-term optimisation and working experience. Thus, in the current works, the EBL operation is carried out by an experienced engineer, and only the effect of the different exposure doses on HSQ is discussed. The exposure dose is defined as the total amount of electrons that have been deposited per unit area, µC/cm^2.

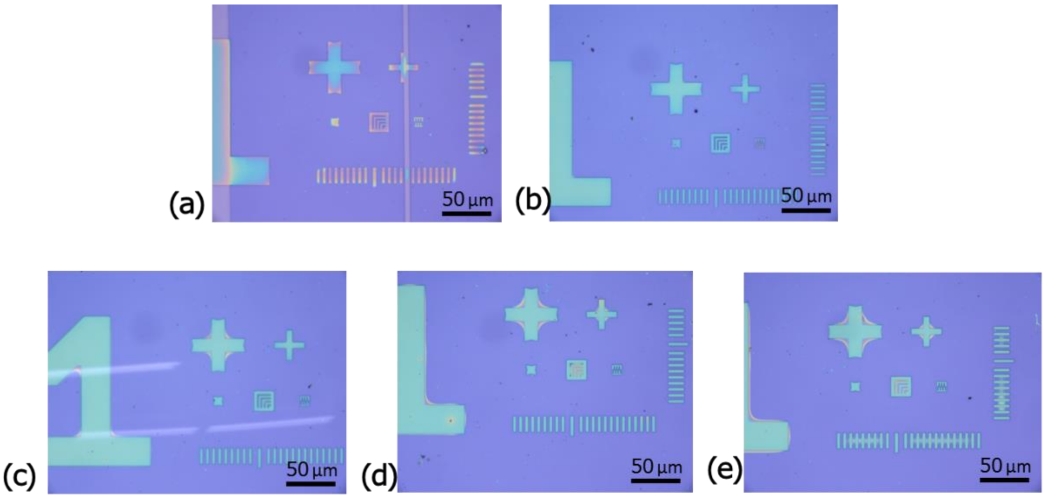

Figure 2.14 Microscope images of developed HSQ resist with exposure base dose of (a) 300, (b) 400, (c) 500, (d) 600 and (e) 700 µC/cm^2.

A negative electron resist HQS with 6% concentration is used in the EBL study. The maximum thickness is ~190 nm under 1000 rpm spin speed. After 4 mins soft-baking on a hotplate at 80 ℃, the sample should be exposed to EBL as quickly as possible. Many works have found that the time delay between soft-baking and exposure will affect the quality of the HSQ pattern features [14][15]. The EBL equipment used is Raith 150-TWO [16] with a beam energy of 30 kV and beam current of 1 nA. Figure 2.14 demonstrates the HSQ patterns after development for 2 mins in MF319 with all other processing conditions the same except for the exposure dose. It can be seen that the exposure dose not only depends on the thickness of the resist but also on the size of the pattern. When the exposure dose is 300 µC/cm^2, the insufficient energy leads to very thin and damaged patterns. As the exposure dose increases to 400 µC/cm^2, clean and distinguished features can be observed for the larger patterns (>50 µm), but it is still under-exposed for small patterns, especially for the 3 µm ridge waveguide. A good pattern result is achieved when the base dose is 600 µC/cm^2; however, the large patterns are over-exposed due to the proximity effects by the scattered electrons. Due to this situation, different exposure doses should be applied for different pattern features by separating them into different pattern layers in the EBL system. Figure 2.15 shows the SEM images of the 3 µm laser ridge patterned by HSQ with a 600 µC/cm^2 base dose. A smoother and more uniform sidewall has been achieved compared with the resist pattern produced by the photolithograph in Figure 2.13.

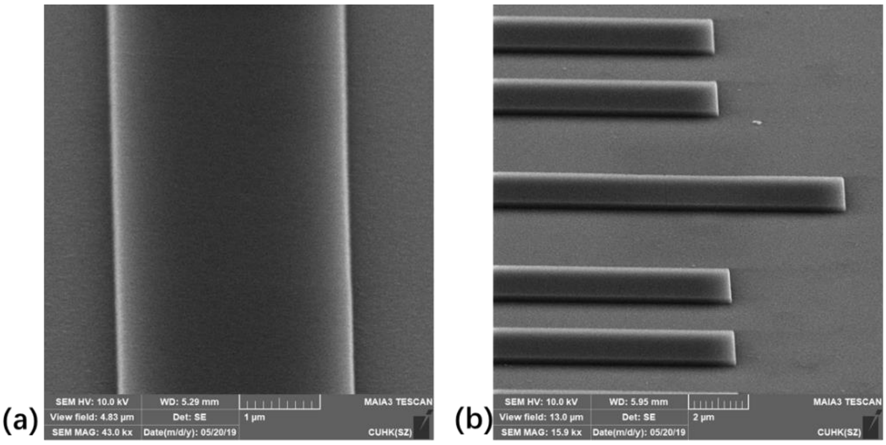

Figure 2.15 SEM images of the small features of HSQ resist by EBL with 600 µC/cm^2 base dose.

After the photoresist development for both conventional photolithography and EBL, a final clean-up of residual organics from the developed sample surface is necessary to avoid the unwanted particles acting as micro-mask for the following fabrication processes. It can be done by a very-low-energy oxygen plasma etching.

2.2.3 Wet and dry etching

After photolithography, the laser mesa is defined by the wet or dry etching process. In this section, the mechanisms and investigation of wet and dry etching techniques of III–V materials are discussed. Both of the etching processes have advantages and disadvantages; the key issues to be considered in selecting a particular etching process for any application are the etching rate, selectivity, feature profile, uniformity, surface damage and reproducibility. Compared with dry etching which requires expensive facilities, wet etching is much simpler to implement. Moreover, the most favourable characteristics of wet etching are the extremely high selectivity of photo-mask and III–V material, and its ability to cause virtually no surface electronic damage [12].

Wet etching (using liquid-based etchants) removes materials by immersing the wafer into a chemical solution that reacts with the selective wafer area and forms soluble by-products. Most wet etchants consist of an oxidising agent, an agent for dissolving the oxides and a dilute solvent, such as water. The underlying chemical mechanism of general GaAs wet etching is the oxidation of the surface to form Ga and As oxides by the oxidising agent (e.g. H_2O_2 and HNO_3); the oxides are then dissolved in acids or bases (e.g. H_2SO_4, HCl, HF and H_3PO_4) [17]. The wet etching process for GaAs and related compounds has been developed over a long period and is already a mature and stable technique. A lot of standard wet etching recipes have been developed for different etching rate requirements. In our lab, the etchant mixture of H_2SO_4: H_2O_2: H_2O (1: 10: 80) is utilised with an etching rate of ~900 nm/min. Based on this wet etching recipe, a flat step and smooth etched surface can be obtained. For the broad-area laser fabrication in this thesis, the wet etching process is employed for both p-type and n-type etching. Also, because of the very high selectivity between the III–V materials and photoresist mask in the wet etching process, the hard mask process can be omitted to simplify the fabrication flow.

However, an isotropic etching profile has occurred when the GaAs is etched by the wet etching, as illustrated in Figure 2.16 (a). The etching profile of GaAs depends on crystallographic orientation, the H_2SO_4: H_2O_2: H_2O etchant is influenced by Ga {111} slow-etch planes, which reduce the etching rate in the direction normal to these planes and cause undercut [18][19]. Figure 2.16 (c) and (d) show the InAs/GaAs QD device profiles in broad-area and narrow-ridge laser fabrication by wet etching, in which the whole narrow ridge is lifted off by the severe undercut in (d). Fortunately, the anisotropic etching profiles of GaAs can be achieved by dry etching, where the etching rate in the vertical direction is much faster than that in the lateral direction, as shown in Figure 2.16 (b) and (e).

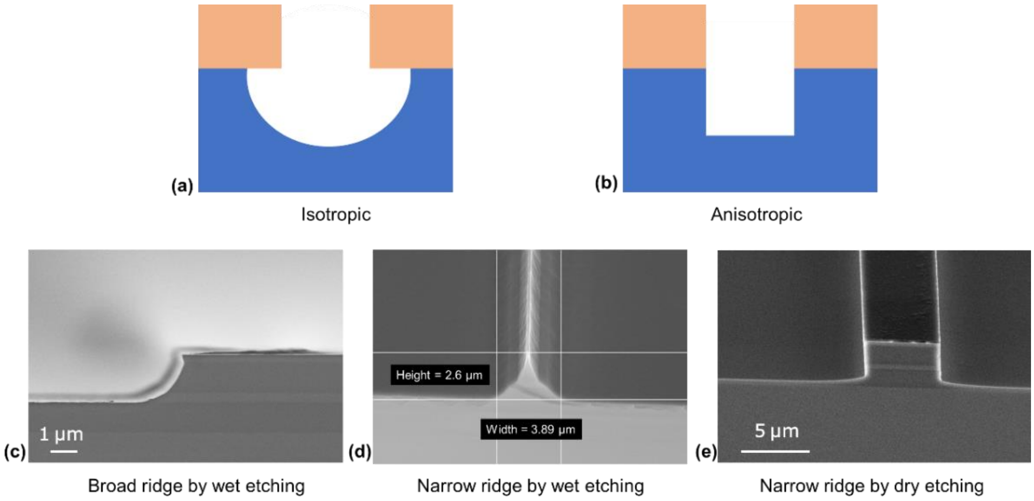

Figure 2.16 (a) Isotropic and (b) anisotropic profiles. SEM images of etch profiles: (c) broad ridge by wet etching, (d) narrow ridge by wet etching and (e) narrow ridge by dry etching.

Dry etching utilises an accelerated plasma instead of liquid etchants to remove the materials. Thus, it is more precise, controllable and highly anisotropic compared to wet etching. The mechanism of wet and dry etching is shown in Figure 2.17. Unlike the wet etching with the chemical reaction only, chemical and physical reactions have occurred simultaneously in the dry etching process. Due to the applied electric field, the inducted ions are travelling highly directionally, which enable the fine patterns with anisotropic profiles.

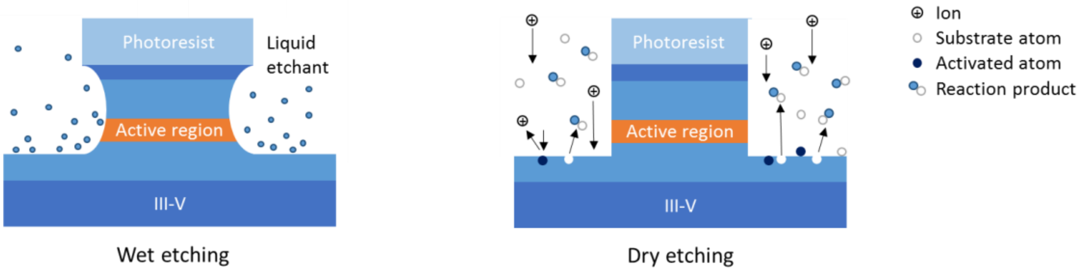

Figure 2.17 Working mechanism of wet and dry etching.

There are two kinds of high-vacuum equipment used in the dry etching process: the reactive ion etcher (RIE) and inductively coupled plasma (ICP), as demonstrated in Figure 2.18. For RIE, the ionised gas (plasma), consisting of electrons, positive ions and radicals, is generated and accelerated by two plane-parallel electrodes with an applied RF power of 13.56 MHz frequency. Since the electrons are more mobile compared to positive ions due to their small mass, they are able to follow the varied electrical field and collide more frequently with the chamber and electrodes. Because a blocking capacitor is connected with the lower electrode, it is gradually biased to a negative potential. This self-biased DC electric field is referred to as V_{dc}, which depends on the RF power. In the RIE chamber, there is a region called the “ion sheath”, that is filled with ions and a very low density of electrons near the lower electrode, as shown in Figure 2.18 (a). Thus, the positive ions in the ion sheath can be accelerated by the negative DC bias and strike the target material in a straight direction, producing an anisotropic profile. In our works, RIE is generally used to etch hard mask and dielectric material, such as SiO_2 and SiN_x. The etching gases are normally fluorine-based gases, such as CHF_3, SF_6 and CF_4. They are ionised into electrons and F^+ ions and reacted as

$$12F + Si_3N_4 \rightarrow 3SiF_3 + 2N_2$$

$$4F + SiO_2 \rightarrow SiF_4 + O_2$$

In addition, the inert gases, N_2 and Ar, assist with the reactive gases to increase the physical bombardment, resulting in a smoother surface due to the increased sputtering contribution.

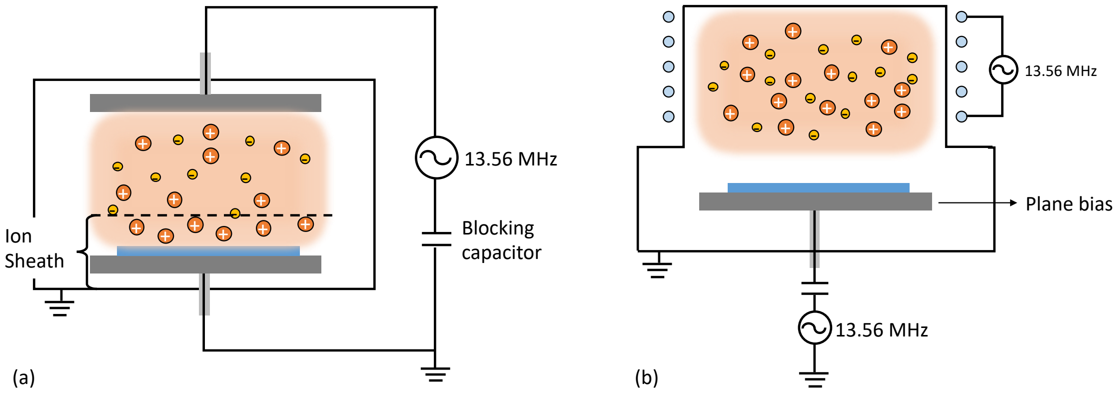

Figure 2.18 Simplified schematic diagram of the working principle of (a) RIE and (b) ICP.

For ICP, the high density of plasma is generated by the electromagnetic induction coil at 13.56 MHz RF power and accelerated by a plane bias (Figure 2.18 (b)). In other words, the plasma density and bombardment energy of ICP are controlled independently, which provide a greater tunability compared with RIE. There is also an important concept called the mean free path (λ) of the ions in examining the strengths and weaknesses of ICP and RIE. The mean free path describes the average distance that an ion can travel without a collision. A higher chamber pressure will cause a shorter mean free path because more collisions will happen when more molecules exist. Moreover, the thickness of the ion sheath is an important factor for evaluating the scattering of ions. Due to the fact that a higher density of plasma can be generated by ICP, the ion sheath thickness of ICP is smaller than RIE [17]. As illustrated in Figure 2.19, when the mean free path is larger than the ion sheath thickness, ions go through almost no scattering upon their arrival at the sample surface. These highly directional ions mean that ICP is more suitable for anisotropic etching [12][17]. The reactive gases for GaAs and relative compound etching are normally chlorine-based gases, such as Cl_2, $SiCl_4$ and BCl_3, which can react with GaAs rapidly and produce $GaCl_x$ and $AsCl_x$ by-products. The inert gases N_2 and Ar can assist in increasing the sputtering.

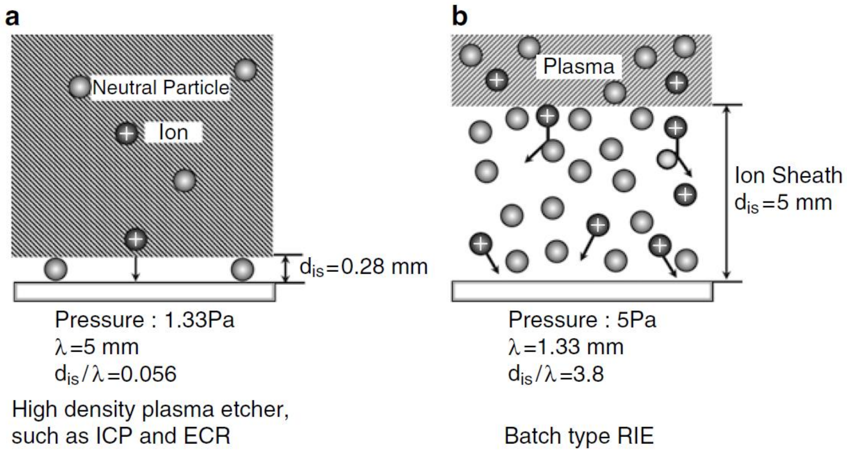

Figure 2.19 Ion scattering in ICP and RIE with different ion sheath [17].

Although the GaAs dry etching technique by ICP has been widely studied for a long period [12][17], different ICP equipment and different pattern features have often led to totally disparate etching results, even with an identical etching recipe. Therefore, the choice of process parameters for the particular etch process requires many additional experiments to figure out an optimal recipe. There are several basic process parameters of ICP that will affect the etching performance:

- ICP power: this denotes the RF power of the electromagnetic induction coil; the larger the ICP power, the higher the plasma density generated. The increased ion density means the etch rates are considerably higher due to the stronger chemical reaction, and it also helps to achieve a higher selectivity for deep etching. Although the higher plasma density can decrease the ion sheath thickness, as mentioned above, redundant ions will also cause ion scattering, thus resulting in a poor anisotropic profile.
- RF plane bias power: this denotes the plane bias of the up and down electrodes for the ion accelerations in the vertical direction. By increasing the bias power, the accelerated ions obtain larger bombardment energy to increase the anisotropic etching effects. However, a too large bias power will damage the sample surface and consume the hard mask excessively (mask selectivity is reduced).
- Chamber temperature: a higher chamber temperature means more collisions between ions, thus leading to isotropic etching. Nevertheless, a proper temperature could help the volatilisation of the by-products to reduce re-deposition.
- Chamber pressure: this is the indicator of the particle density of the reaction chamber. As described above, a high chamber pressure will reduce the mean free path of ions, giving rise to isotropic etching, but also increase the etching rate.

Although the etching depth is only required to be ~1.7 μm (above the InAs/GaAs QD region) for this thesis, an optimised recipe is developed for both gain-guided and index-guided (deep etching to n-type region) lasers for our future work. Therefore, the etching effects of the recipes for the active region will also be considered. In the following works, the etching recipe is optimised in considering of cleanness of sample surface, damage and smoothness of etched surface and effect of etching time.

• Cleanness of sample surface

In this work, the etch gas chosen is a mixture of Cl_2, BCl_3 and N_2. In this gas mixture, Cl_2 is the primary etching gas, and BCl_3 is normally used to remove the native oxide and reduce residue formation [20]. The purpose of N_2 is to balance the chemical and physical reactions [21], and also reduce the roughness of the etched surface by increasing the physical bombardments, thus, sputtering contribution [22].

Table 2.2 InAs/GaAs QD etching recipes with different gas flow rates.

No.	Chamber temperature (℃)	Pressure (mT)	Cl_2 (sccm)	BCl_3 (sccm)	N_2 (sccm)	Bias power (W)	ICP power (W)	Selectivity ($GaAs/SiO_2$)	Rate (μm/min)	Comment
1.1	50	3	16	8	10	90	350	19.2	1.55	Very strong re-deposition
1.2	50	3	6	12	10	90	350	14.8	1.51	Strong re-deposition
1.3	50	3	10	20	5	90	350	14	1.73	Medium re-deposition
1.4	50	3	12	28	3	90	350	8	1.6	Clean surface

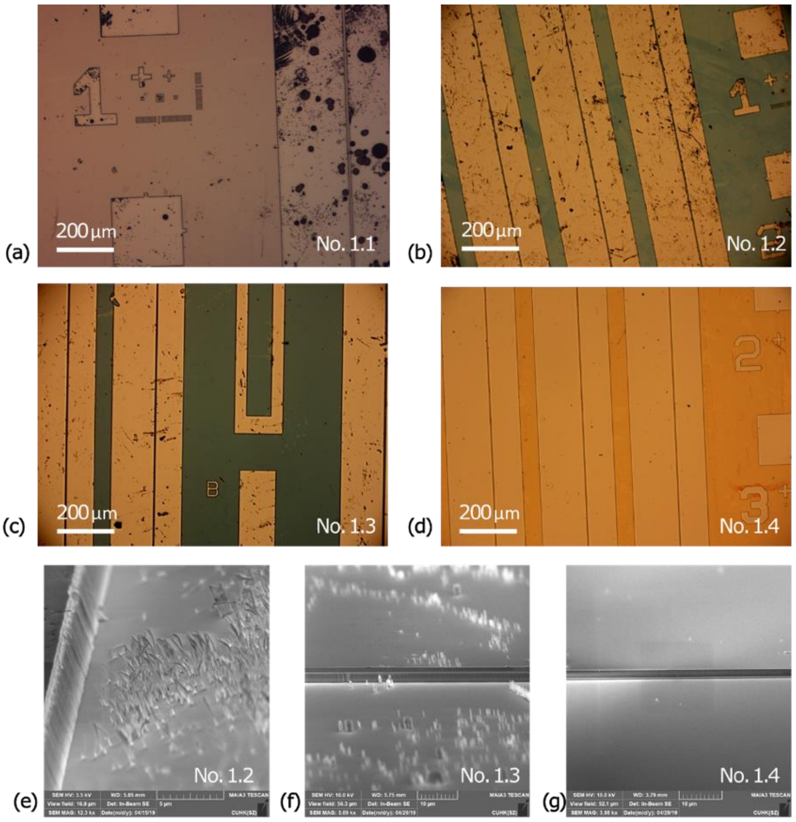

Figure 2.20 Microscope images of the etched sample with different flow gas ratios for sample (a) No. 1.1, (b) No. 1.2, (c) No. 1.3 and (d) No. 1.4. SEM images of the etched samples of (e) No. 1.2, (f) No. 1.3 and (g) No. 1.4.

Table 2.2 demonstrates the GaAs etching recipes with different flow rate ratios of the etch gases, and the microscope and SEM images of etched samples by each recipe are shown in Figure 2.20. When the ratio of Cl_2/BCl_3 is 2, and the ratio of Cl_2+BCl_3/N_2 is 12/5, a very dirty surface was obtained due to the very strong re-deposition, as shown in Figure 2.20 (a). Because the highest chamber temperature of the utilised ICP equipment can only be set to 50 °C, the re-deposition issue can only be solved by changing other parameters. As the Cl_2/BCl_3 ratio decreases to 0.5, the cleanness of the etched sample is slightly improved, but the contamination is still severe on the surface (Figure 2.20 (b) and (e)). Figure 2.20 (c) and (f) show the etched surface of sample 1.3; the Cl_2/BCl_3 ratio is kept at 0.5, but the ratio of Cl_2+BCl_3/N_2 is increased to 6/1, and the re-deposition phenomenon is controlled effectively. For sample 1.4, the clean surface is shown in Figure 2.20 (d) and (g) was achieved by the 3/7 Cl_2/BCl_3 ratio and the reduction of N_2 gas flow to 3 sccm. This demonstrates that a higher ratio of chemical reaction, which produces more volatilisable by-products, will improve the sample cleanness significantly.

- **Damage and smoothness of the etched surface**

However, due to the larger gas flow in sample 1.4, the mask selectivity becomes smaller compared with other recipes. Moreover, the sidewall of the etched surface is not desirable due to the reduced assistance of the N_2 gas. Table 2.3 shows the etching recipes based on the gas flow rate of sample 1.4 with different ICP and bias powers. The SEM images of the etched surfaces for each recipe are demonstrated in Figure 2.21. Samples 2.1, 2.2 and 2.3 compare the effect of the bias power on the sidewall of the etched samples. As we can see from Figure 2.21 (a), the high bias power of 150 W causes a severely damaged surface and corrugated features on the sidewall. This recipe has a very fast etch rate, and the SiO_2 hard mask is depleted after 3 minutes of etching. When the bias power is reduced to 90 W in sample 2.2, the smoothness of the etched surface is improved, but a poor surface morphology remains on the top region of the ridge, as shown in Figure 2.21 (b). An interesting phenomenon occurred when the bias power was decreased to 60 W, the rough surface in the InAs/GaAs QD region has appeared, as shown in Figure 2.21 (c). This phenomenon can be explained by the weaker control of ions in the vertical direction, and the strong chemical reactions occurring in the In-rich region. We tried different gas flow rates, but the rough morphology was always found in the active region with 60 W bias power. In sample 2.4, the bias power is set back to 90 W while the ICP power is reduced to 300 W; a smooth morphology in the QD region is obtained (Figure 2.21 (d)), but a damaged surface still appeared in the top region. Comparing samples 2.2 and 2.4, the lower ICP power causes a reduced plasma density, resulting in a better sidewall and a reduced degree of damage. Figure 2.21 (e) displays the etched sample 2.5, where there is almost no damage in the top region, but the rough morphology in the active region is observed again when the bias power is 75 W. The corrosion in the QD region becomes weaker as the ICP power decreases from 350 W to 300 W. From this study, we see there is a trade-off between bias and ICP power in order to achieve a smooth and undamaged etched surface.

Table 2.3 InAs/GaAs QD etching recipe for bias and ICP power optimisation.

No.	Chamber temperature (℃)	Pressure (mT)	Cl_2 (sccm)	BCl_3 (sccm)	N_2 (sccm)	Bias power (W)	ICP power (W)	Selectivity ($GaAs/SiO_2$)	Rate (μm/min)
2.1	50	3	12	28	5	150	350	N/A	>1.8
2.2	50	3	12	28	3	90	350	8	1.6
2.3	50	3	12	28	3	60	350	17	1.5
2.4	50	3	12	28	3	90	300	16.3	1.484
2.5	50	3	12	28	3	75	300	13.1	1.35

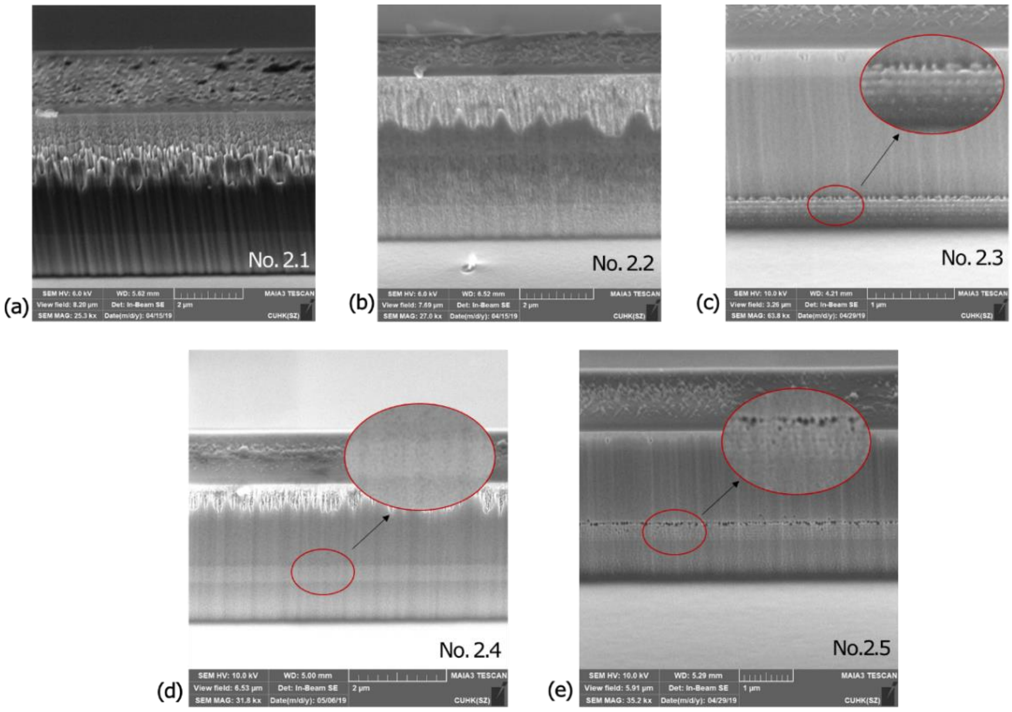

Figure 2.21 SEM images of the etched sidewall with different bias and ICP powers according to Table 2.2.

- **Effect of etching time**

Besides the ICP power and bias power, it has been found that the dry etching time is also an important parameter which will cause the sidewall damage on the top region of the mesa ridge. When the hard mask experiences a long-time etch, the top corner is easily exhausted by the physical bombardment, as displayed in Figure 2.22 (a). Therefore, the round mask corner cannot protect the underlying GaAs layer very well, resulting in sidewall damage of the mesa ridge. Figure 2.22 (b) and (c) compare the etch results by using an identical recipe but with different etching times, and the SiO_2 hard mask is 300 nm in thickness. A smooth etched surface without obvious surface damage is achieved with 1 min 18 s etching time, which gives an etching depth of ~1.6 µm. As the etch time increases to 3 mins for 3 µm deep etching, although the ~100 nm hard mask is left on top, the sidewall of the ridge is damaged by the round top corner. This issue can be solved by increasing the thickness of the SiO_2 hard mask or using SiN_x material with higher hardness.

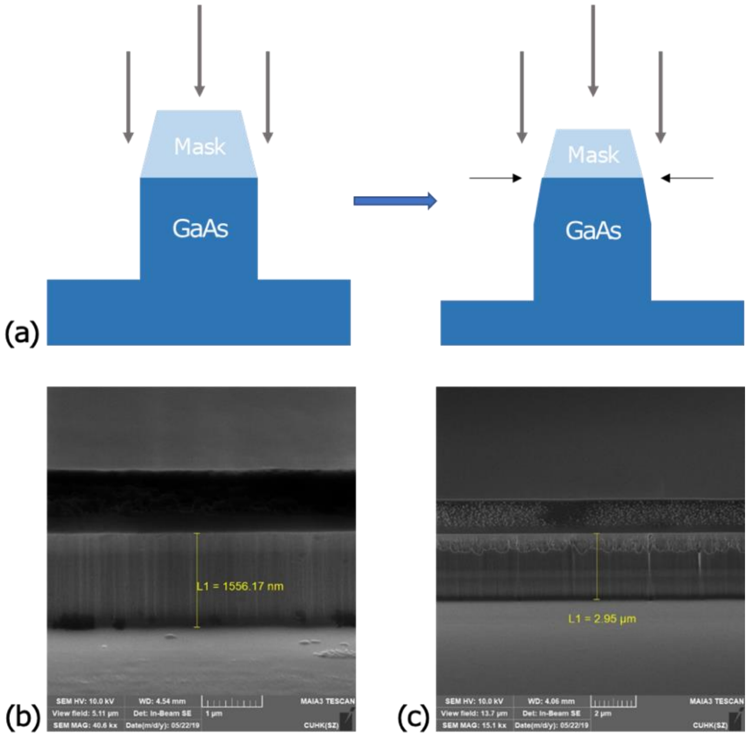

Figure 2.22 (a) Schematic diagrams of the cornered mask edge when the mask thickness becomes small [23]. *SEM images of the etched sidewall with (b) shallow etch of 1.6 µm depth and (c) deep etch with 3 µm depth.*

After the dry etching process, chemical cleaning should be implemented to smooth the etched surface further, even for clean etch surfaces. The common chemical solvent used is a mixture of citric acid: H_2O_2 at 20:1. Figure 2.23 shows the SEM images of an etched sample with strong contamination before and after the chemical cleaning. As we can see, the re-deposition by-products can be removed partially, but more importantly, the sidewall of the etched mesa becomes smoother after this chemical treatment.

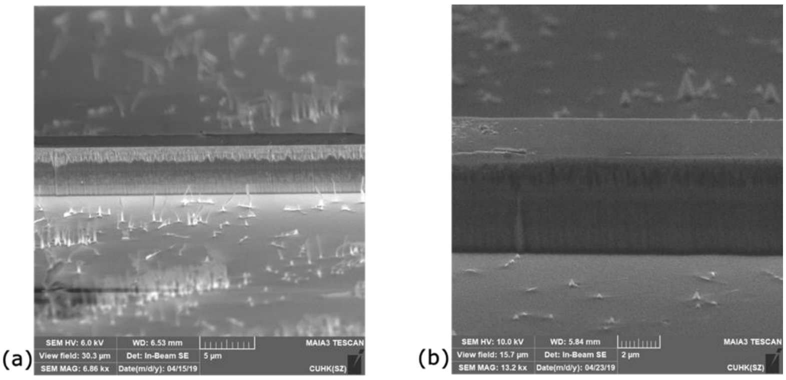

Figure 2.23 SEM images of etched sample (a) before and (b) after chemical cleaning by citric.

As a result, the optimal etching recipe is shown in Table 2.4, which achieved a good anisotropic profile (Figure 2.24 (a)), a smooth and undamaged sidewall (Figure 2.24 (b)) and a very clean etched surface after the chemical treatment (Figure 2.24 (c)).

Table 2.4 Optimal recipe for InAs/GaAs QD etching.

Chamber temperature (°C)	Pressure (mT)	Cl_2 (sccm)	BCl_3 (sccm)	N_2 (sccm)	Bias power (W)	ICP power (W)	Selectivity ($GaAs/SiO_2$)	Rate (μm/min)
50	3	12	28	3	90	280	17.2	1.4

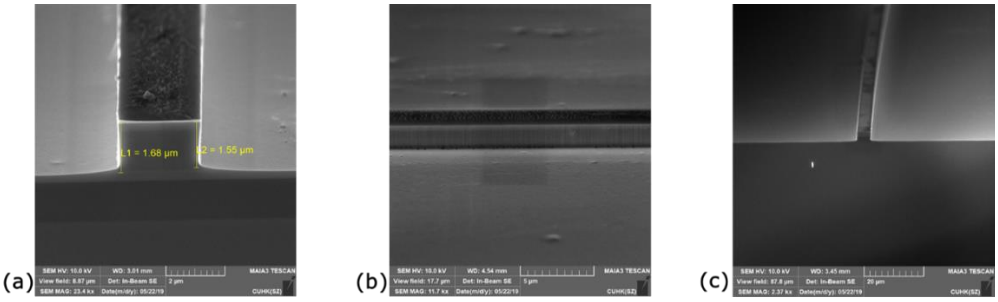

Figure 2.24 SEM images of a narrow-ridge etching by ICP dry etching with an optimal recipe at different magnifications.

2.2.4 Passivation and planarisation

After the mesa etch process, the passivation layer and polyimide for the planarisation are necessary for the narrow-ridge laser to maximise the contact area of the electrodes. Dielectric materials, such as SiO_2 and SiN_x, are normally chosen to prevent the oxidation of $Al_xGa_{1-x}As$ and electrical insulation of electrodes. As shown in Figure 2.25, 200 nm SiO_2 is deposited on the etched mesa as the passivation layer by PECVD, and the selective area is etched away to expose the contact layer of III–V for metal interconnection. Figure 2.25 (c) shows an SEM image of the top view of the laser ridge after this "open window" process.

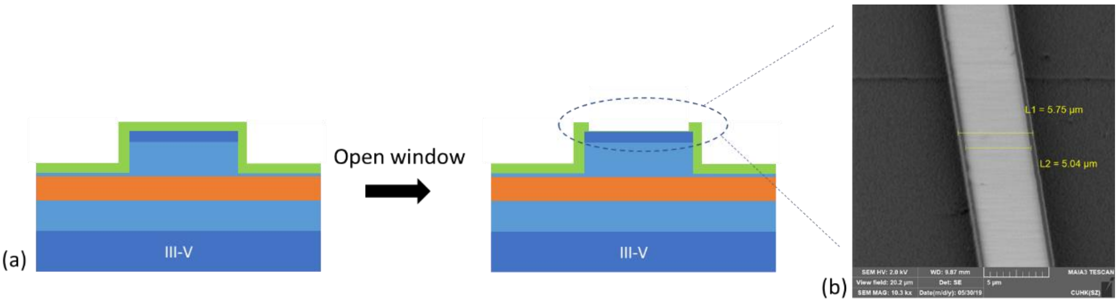

Figure 2.25 (a) Schematic diagrams of passivation planarisation process. (b) SEM image of a top view of the laser ridge after open window process.

Planarisation is a crucial step for the following metallisation; it increases the flatness of the sample surface to avoid the occurrence of discrete metal. Figure 2.26 demonstrates the etched mesa deposition by the p-type metal without any planarisation material, where the failure of the electrode metallisation was caused by the large step height of the ridge. A good planarisation should meet the requirement that the sidewalls of the ridges are always sealed, and the top surface is levelled by the surrounding planarisation materials. Currently, the planarisation process for III–V devices is generally accomplished by the use of polymer-based material, such as HSQ and benzocyclobutene (BCB), which can be spun on the wafer. The thickness of the spun-on polymer can be controlled by the spinning speed and should be thicker than the step height of the ridge mesa.

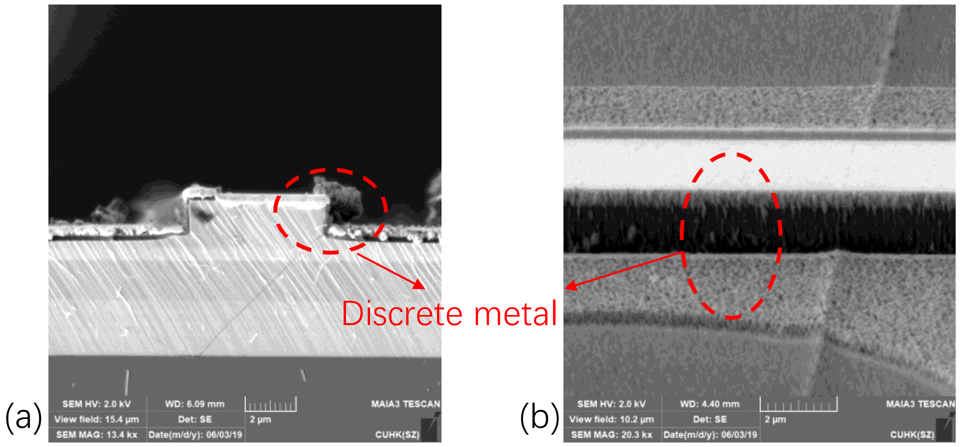

Figure 2.26 SEM images of the discontinued metal on etched mesa without planarisation in (a) cross-section front view and (b) side view of the ridge.

After the spin-coating process, the polymer is firstly baked on a hotplate to remove solvent and stabilise the polymer film. Then, thermal curing is performed to achieve the final properties on the wafers. Different polymer materials have different curing temperatures. Figure 2.27 (a)–(c) show the BCB film after thermal curing by a furnace with inert nitrogen gas at 250 ℃ for 2 hours. As shown in Figure 2.27 (d), the planarisation is finished by etch-back of polymer to the device top to expose the top surface. For BCB, the mixture of oxygen and a fluorine-containing gas (CF_4 and SF_6) has been found to produce a controllable etch rate by RIE [24]. In this work, the plasma etch gases of SF_6:O_2 (1:5) with ~500 nm/min etch rate are utilised. It should be noted that because of the high viscosity of the polymer for planarisation and relatively small wafer sample, the height of all-polymer films on the sample features may vary on the same wafer, which makes it impossible to land the mesa top surfaces at the same time during the etch-back process. A sufficient etch time is required to ensure a clear polymer on the top of all the mesas. Thus, the passivation layer of SiO_2 is necessary to prevent the leakage current where the polymer is over-etched.

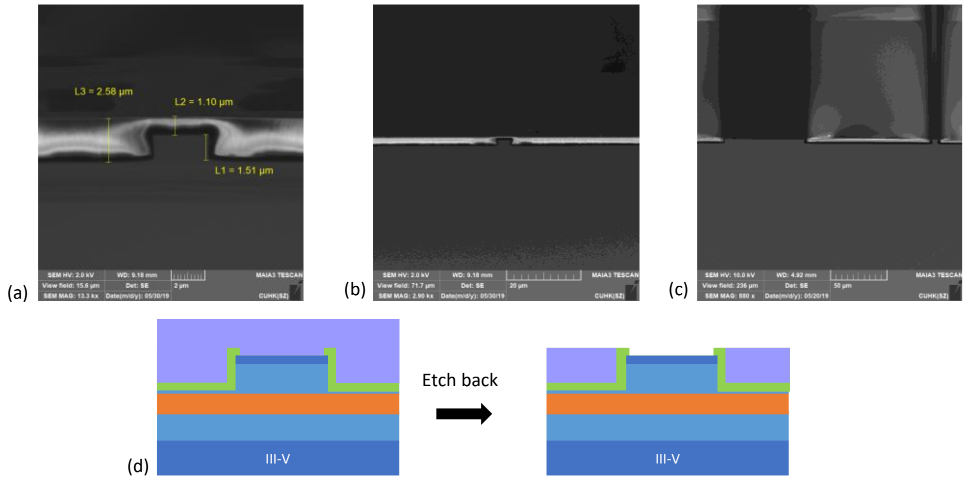

Figure 2.27 (a)-(b) SEM images of the cross-section of the p-type laser ridge covered by BCB with different magnifications. (d) Schematic diagrams of planarisation process.

2.2.5 Metallisation

For high-performance semiconductor laser devices, forming good anode and cathode electrodes by the metal/semiconductor ohmic contact with an ultra-low resistance is one of the key elements. In principle, most metal/semiconductor interfaces have barriers which affect the carrier mobility. Thus the ohmic contact should be designed so that these barriers are low enough that the carriers can cross the interface by thermionic emission, or narrow enough that the carriers can tunnel across the interface by field emission [12]. For thermionic emission, the work function of metal should be low for an n-type semiconductor and high for a p-type semiconductor to obtain a low barrier height. However, this requirement of the metal work function limits the metal options. In practical works, a thin layer of very heavily doped semiconductor causing a very narrow depletion region with the metal contact is most often used to increase the carrier tunnelling probability by field emission. In our works, n-type and p-type GaAs contact layers with a high doping level of 10^{18} cm^{-3} are grown by MBE in order to achieve low contact resistances.

For the p-type electrode, a Ti/Pt/Au (20 nm/50 nm/400 nm) layer was deposited by the sputtering system without a rapid thermal process (RTP) as a non-alloyed ohmic contact. The Ti/Pt/Au layer on p-GaAs has a low barrier height; thus, carriers can move across the junction easily. One concern with this layer is the potential for a greater reaction between Au and Ga with an excess tendency to spike during the process. A Ti layer has been recommended as the first deposition layer to prevent the diffusion of Au [12]; more importantly, it can increase the adhesive ability between GaAs and succeeding metals significantly. The existence of a Pt layer underneath the gold top layer also acts as a barrier layer to avoid Au diffusion into the GaAs layer during the subsequent thermal processing in n-type metallisation. It has been shown that the Ti/Pt/Au has much better long-term thermal stability compared with a Ti/Au ohmic contact [25] owing to the less reactive property of Pt. A 400 nm thick Au layer is deposited finally to provide an ultra-low resistance with no oxide formation, resulting in good bonding and high reliability [26]. The measured contact resistance for the p-type electrode is around 5.8×10^{-5} Ωcm^2.

An alloyed (diffusion) ohmic contact of Ni/GeAu/Ni/Au (10 nm/100 nm/30 nm/200 nm) is utilised with a 380 °C thermal annealing for the n-GaAs electrode. The first layer of Ni can react with GaAs at low temperature to form binary or ternary compounds (Ni_xGaAs), which results in a good adhesive ability [27]. The alloy of 88–12 Au–Ge (wt%) with a 361 °C eutectic point is then deposited, where the Ge acts as a dopant into the GaAs region near the metal interface when the annealing temperature is higher than the eutectic point of GeAu [28]. This Ge-doped GaAs region forms a small heterostructure barrier, which leads to very good electrical properties [27]. The third layer of Ni plays the role of a barrier layer to avoid GaAu formation, which will cause an undesired "balling-up" morphology during the RTP. A final layer of thick Au is deposited for better probe contact and wire bonding. This metal system for an n-type electrode achieved a contact resistance of 4×10^{-6} Ωcm^2.

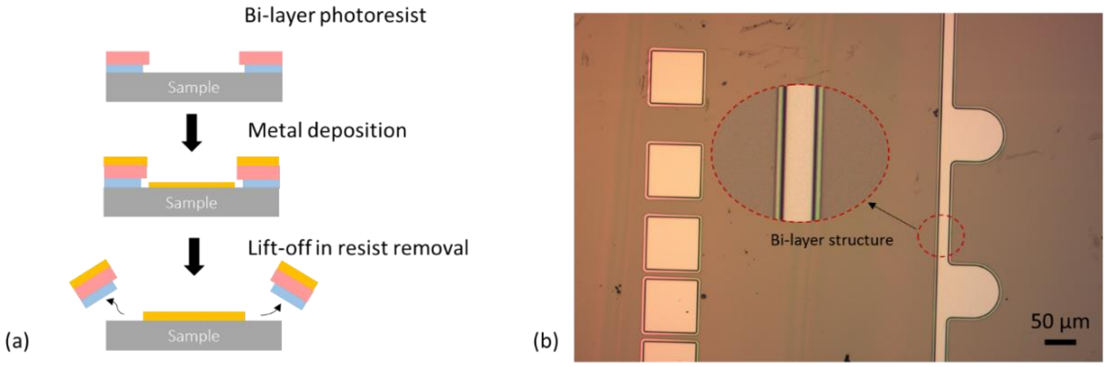

Figure 2.28 (a) Schematic diagrams of how the bi-layer photoresist works for the metal lift-off. (b) Microscope image of bi-layer re-entrant sidewall profile of LOR 10B and S1818 after development. (c) Microscope image of a laser device after p-type metallisation.

In this work, the metallisation process firstly involves patterning the sample and then forming a contact pattern by a lift-off process. A conventional bi-layer (re-entrant) photoresist profile is employed to discontinue metal films during the lift-off process, as shown in Figure 2.28 (a). Two different kinds of resists, a normal positive photoresist (such as S1818) and a non-photosensitive but more soluble resist (such as LOR 10B), are chosen for the bi-layer structure after the developer, as illustrated in Figure 2.28 (b). Before the metal deposition, the pre-cleaning step is critical for enhancing the adhesive ability between semiconductor and metals. The native oxide of GaAs should be removed by dilute acids or bases, for example, NH_4OH:H_2O at a 1:19 ratio. After the metal deposition, the sample is immersed in a photoresist stripper for the lift-off. Thanks to the bi-layer profile, the photoresist and unwanted metal are removed completely [29]. Figure 2.29 shows the SEM images of the p-type narrow-ridge laser after planarisation and metallisation. A uniform and smooth metal contact are achieved with a very good adhesive ability between the metal and GaAs and underlying polymer.

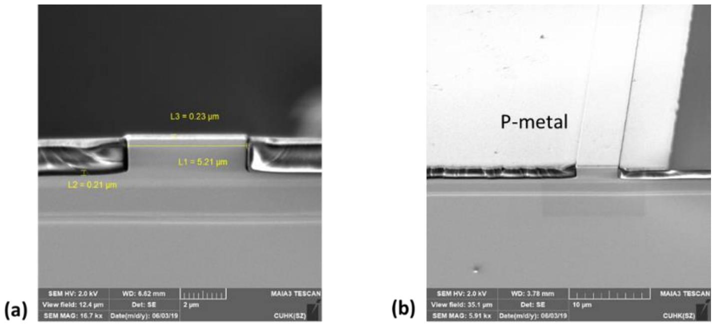

Figure 2.29 Ti/Pt/Au on the p-type narrow ridge planarised by BCB in (a) cross-section view and (b) top view.

2.2.6 Focused ion beam

For the production of the device in the industry, photolithography is the dominant patterning technique as it allows the patterning of an entire 300 mm (and larger) wafer in a short time with high yield. However, it is wasteful and time-consuming to make photo-masks for the unoptimized device structures during the prototyping development. It is, therefore, attractive to use prototyping technologies that enable rapid and flexible fabrication of nanophotonic components, ranging from micro- to nanometre scales [30]. Among these approaches, FIB is an valuable alternative as it allows photoresist-free and direct writing, which enables the post-fabrication of devices with more complex topography such as ridge waveguides and laser facets. Chapter 4 gives a detailed discussion of how FIB enables facet creation for Si-based light sources. In this section, a brief introduction to the instrument and the working principle of FIB is presented.

The FIB instrument is almost identical to the SEM, the difference being that SEM uses a focused electron beam, while FIB uses a focused ion beam. In general, FIB columns are always incorporated into other analytical instruments, such as SEM or TEM. It consists of a vacuum system and chamber, a liquid metal ion source, an ion column, a sample holder and a detector [31]. A schematic of the FIB setup within the SEM instrument is shown in Figure 2.30. There is a 55° angle difference between the SEM column and FIB column, which ensures the specimens can be imaged during FIB milling. A vacuum chamber is required to avoid contamination from the environment or the milled materials of specimens and to prevent electrical discharges in the high-voltage ion column [31]. FIB normally uses a liquid metal ion source (LMIS) for small probe sputtering, which has the ability to provide an ion source of ~5 nm diameter [31]. The most common of these is gallium (Ga^+) due to its low melting point ($T_{mp} = 29.8$ °C) and excellent mechanical, electrical and vacuum properties [31]. The Ga^+ ions are extracted from the LMIS and accelerated through an ion column to hit the sample surface; the typical range of acceleration voltage is from 3–30 keV and the probe (beam) current is from 1 pA to 50 nA. Besides Ga^+, helium (He) and neon (Ne) ion sources with much smaller probe currents (down to 0.1 pA) can also be employed for more precise milling or polishing for small features (nanometer scalar) [32][33]. Similar to the SEM system, the ion column includes two lenses: a condenser lens and objective lens for probe forming and sample surface focus. A set of apertures is used to define the different probe sizes and ion currents for different applications. The rotated sample holder ensures the focused ion beam is normal to the specimen surface (Figure 2.30 (b)).

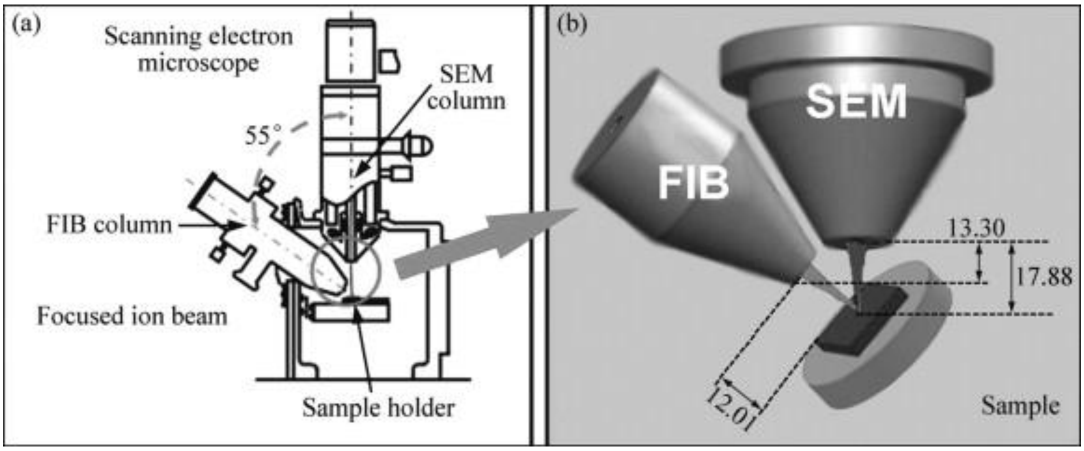

Figure 2.30 Schematic diagram of SEM-FIB combined system [34].

The working principle of FIB is based on the nature of the ion beam – solid interaction [35]. When the incident ions are sputtered to the target atoms, the momentum is transferred from the ion beam to the target solid, resulting in a series of elastic collisions, as shown in Figure 2.31. A surface atom may be ejected as a sputtering particle if it receives enough kinetic energy to overcome the surface binding energy of the target materials [35]. A portion of the ejected atoms may be ionised and collected by the FIB detector to form images. Inelastic collisions also occur during the ion bombardment, which leads to the production of phonons, plasmons (in metals) and SEs. SEs are also collected by the detector to form an image. The complementary information can be obtained from both images by SIs and SEs.

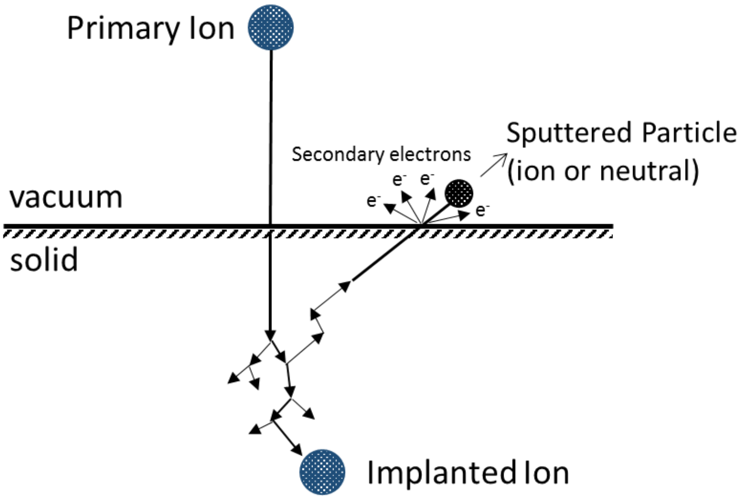

Figure 2.31 Schematic diagram of the sputtering process and ion–solid interactions [36].

In addition to the described characteristics of the ion beam, such as acceleration voltage and beam current, there is another important parameter – the dose – which decides the milling pattern by the FIB. Dose, in general, denotes the quantity of energy or particles absorbed by the medium. In the case of the ion beam, it has units of ions/cm^2 and refers to the number of ions that impacted and were absorbed into the target in a defined area [35]. In other words, an increase in dose means an increase in the milling time per unit area by FIB. Thus, the depth of the FIB milled box cut could be determined by understanding dose values. A further description of the FIB operation has been included in Chapter 4.

2.3 Laser measurement and characteristics

2.3.1 Static characteristics

After the device fabrication, it is essential to measure the characteristics and device performance of lasers by performing a series of experiments, in order to determine whether the lasers meet the desired specifications of lasing. One of the most important parameters is the function of light output power, and device voltage against the injection current called the light-current-voltage (L-I-V) curve. From the L-I curve, the laser threshold current density, slope of L-curve and external differential quantum efficiency can be calculated. The turn-on voltage and serial resistance can be determined from the I-V curve. Another significant parameter of lasers is the temperature dependence (T_0), which describes the sensitivity of laser devices to the temperature changes. Besides that, the optical power spectrum, which displays how the optical power varied with different wavelengths, is also captured to determine the lasing peak wavelength and lasing linewidth. In this section, a detailed description of static laser characteristics will be introduced.

- **L-I curve, threshold current density and slope efficiency**

The L-I curve is one of the most crucial parameters of the semiconductor laser. Shown in Figure 2.32 are the typical L-I characteristics (in black colour) of a function of injection current versus output power per mirror facet. Before the threshold current (I_{th}) point, the laser is operated by spontaneous emission, where the output power rises gently with the increasing injection current. When the injection current is bigger than the threshold current, stimulated emission dominates in the laser cavity, and the laser is operational while the optical amplification is larger than the output and internal loss.

The threshold current is the critical value for the laser. However, this value is dependent on the size of the laser cavity. It is hard to compare the performance of laser devices of different sizes. Therefore, it is more sensible to use the threshold current density denoted by J_{th}; the equation for J_{th} is [37]:

$$J_{th} = {}^{I_{th}}/_{A} \qquad \text{Equation 2.1}$$

where A is the area of the laser ridge ($ridge\ width \times cavity\ length$).

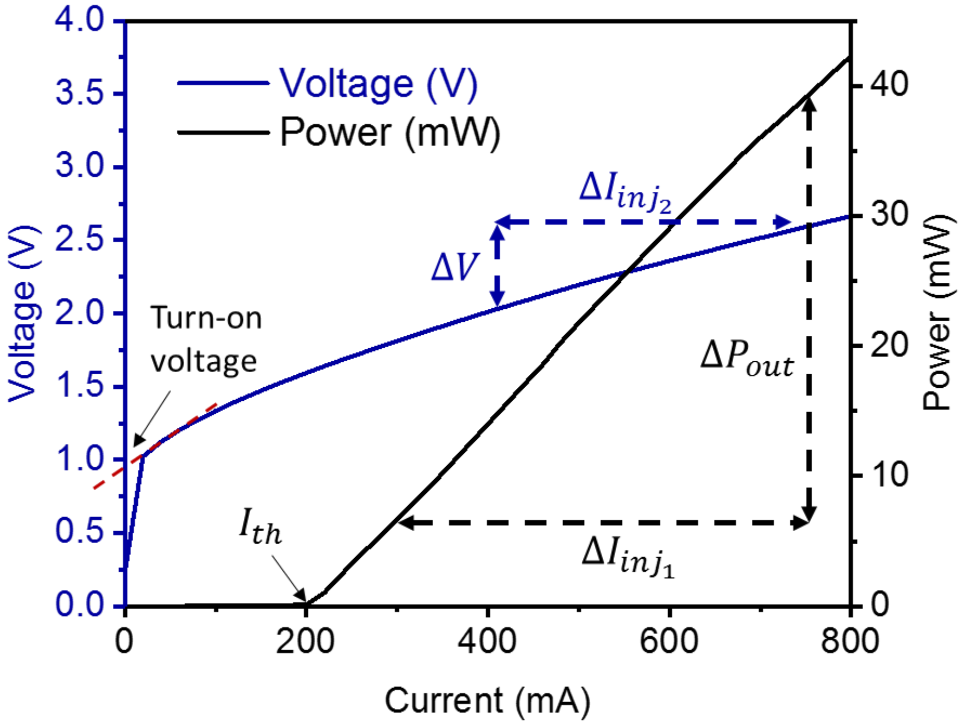

Figure 2.32 Output power and voltage against the current (L-I-V curve).

The slope of the L-I curve is another important parameter to indicate the performance of laser devices; it is always desirable to get more output light from laser facets with less injection current. As shown in Figure 2.32 the slope efficiency is calculated by $\Delta P_{out}/\Delta I_{inj_1}$ after the threshold current point in units of watts per amperes (W/A). It represents how many watts of output power is produced by the lasers for every ampere of current injected into them.

- **External quantum efficiency**

When we discuss the efficiency of lasers, there is another important indicator, referred to as the external quantum efficiency (EQE), η_d, and expressed as a percentage. This parameter presents the efficiency of the laser in converting the injected electrical charges (electron-hole pairs) to output light (photons emitted) from lasers. Under ideal conditions, the EQE of a perfect laser should be 100%, which means all of the injected electron-hole pairs were converted to photons emitted from laser facets, and no waste of electrical charges was caused. To be more specific, one photon is generated by the recombination of an electron-hole pair and then travels through the laser cavity structure to contribute to the output light of the laser. However, in the real situation, not all of the recombination of electron and hole pairs prefer to generate photons; some of them produce another form of undesirable energy, such as heat or phonons. Even worse, some of the generated photons are reabsorbed by the laser device rather than contributing to the output light. Therefore, the EQE of a real laser is lower and depends on the quality of device materials and fabrication technology. For example, by adjusting the strain of QW barriers and reducing the carrier leakage, the ultra-high η_d of up to 86% has been realized by a 970 nm pump laser [38]. Moreover, a strained-layer QW laser emitting at 1500 nm has been reported with 82 % EQE [39]. Compared with QW laser, the commercial QD laser shows a relative low EQE (~35%) [40]. The possible reason for the degraded EQE may be relevant to the reduced carrier density by the discrete energy states and phonon bottleneck effect of the QDs [41].

In order to measure and calculate the EQE of real lasers, we need to calculate the slope of the L-I curve of real lasers after threshold current and compare it to that of perfect lasers (100% efficiency) [37]. The detailed derivation process of this ratio equation can be explained as follows.

The slope of the L-I curve of real lasers can be easily achieved by measurement of the L-I curve, and that for theoretical lasers can be calculated from basic theory equations. The energy of a photon with wavelength λ is

$$E_{photon} = \frac{hc}{\lambda} \qquad \text{Equation 2.2}$$

The unit of energy is the joule and one joule per second is one watt of power (P), thus

$$P = \frac{E}{t} \qquad \text{Equation 2.3}$$

where t is time. Moreover, one electron has 1.6×10^{-19} Coulombs, where one Coulomb is an electric charge (q) equal to one amp transferred current in one second, thus $I = \frac{q}{t}$.

If we combine these three equations together, the expression of the slope of the L-I curve of a theoretical laser can be written as:

$$\frac{P}{I} = \frac{hc}{q\lambda} \qquad \text{Equation 2.4}$$

Therefore, the equation of EQE is written as:

$$\eta_d = {}^{\frac{\Delta P}{\Delta I}}\!\Big/\!{}_{\frac{hc}{q\lambda}} \qquad \text{Equation 2.5}$$

- **Turn-on voltage, series resistance and wall-plug efficiency**

From the I-V curve in Figure 2.32 (navy colour), the turn-on voltage, which is also called the forward-biased voltage, can be obtained. After this turn-on voltage, significant electron-hole pairs start to generate at the active region of the laser diode.

Moreover, the series resistance (R_s) can also be obtained from the I-V curve. The series resistance defines the laser diode resistance when the injection current is larger than the threshold current. The voltage is increased linearly with the injection current; thus, R_s can be simply calculated by $\Delta V/\Delta I_{inj_2}$ [42], as shown in Figure 2.32. A high value of series resistance for a laser could be the result of the low quality of metal ohmic contacts. Thus, measurement of series resistance is a simple way to assess the quality of the metallic contact deposition [37]. Another important parameter, called wall-plug efficiency (WPE), can be calculated according to the L-I-V curves. The WPE of a laser diode is the total electrical-to-optical power efficiency (${}^{P_{out}}\!/_{I\,\times\,V}$)*100%, and varies with the injection current as shown in Figure 2.33. In real applications, the WPE of a laser system also includes the loss from the power supply and the power consumed from the cooling system.

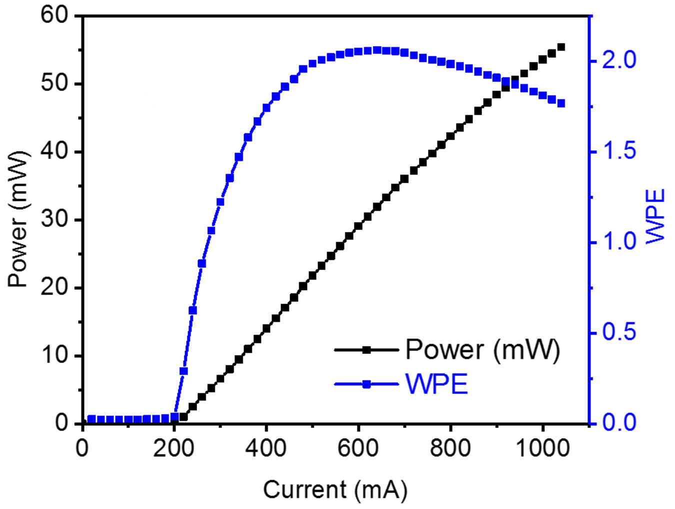

Figure 2.33 L-I curve and WPE plot for an uncoated laser from a single facet.

- **Spectrum and peak wavelength of emission**

The emission spectrum is measured to identify the lasing peak wavelength and lasing linewidth. The linewidth is often defined by the full-width half-maximum (FWHM) of the power spectrum. By changing the injection current, the laser behaviours below and above threshold current can be studied. Figure 2.34 gives an example of the emission spectra of a laser diode with different injection currents. When the injection current was 50 mA, as shown in Figure 2.34 (a), a broad spontaneous emission spectrum appeared with an FWHM of 50 nm at 1318 nm peak wavelength. As the injection current increased, the spectrum became narrower with higher output power at the peak wavelength of 1318 nm. When the injection current exceeded its threshold current to 188 mA (Figure 2.34 (b)), the peak intensity dramatically increased with a narrower FWHM of ~5 nm, which represents typical lasing characteristics in the GS. A high-resolution spectrum is also employed in order to determine the number of spectral lines and the mode separation. Figure 2.35 shows a lasing spectrum of a multi-mode laser device with a high resolution of 0.02 nm.

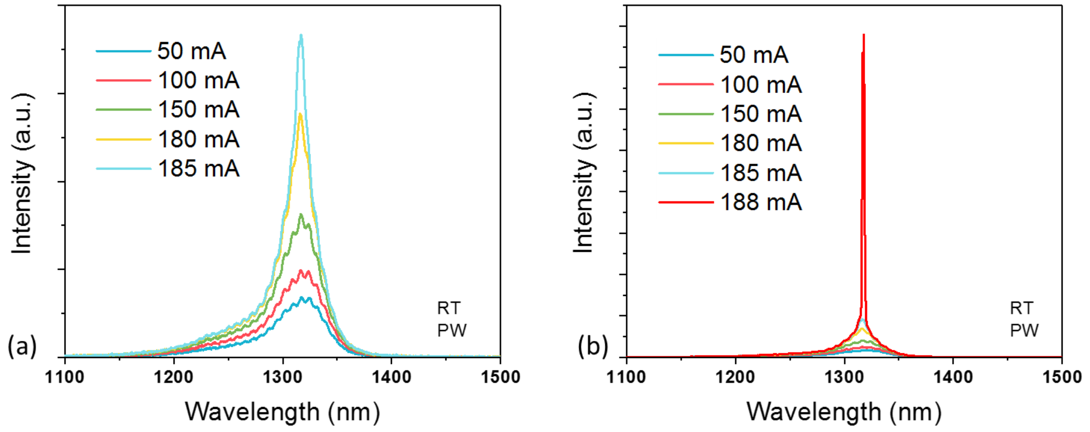

Figure 2.34 Spectra of a laser diode at (a) low injection currents before lasing; (b) various currents after lasing at RT under pulsed-wave operation.

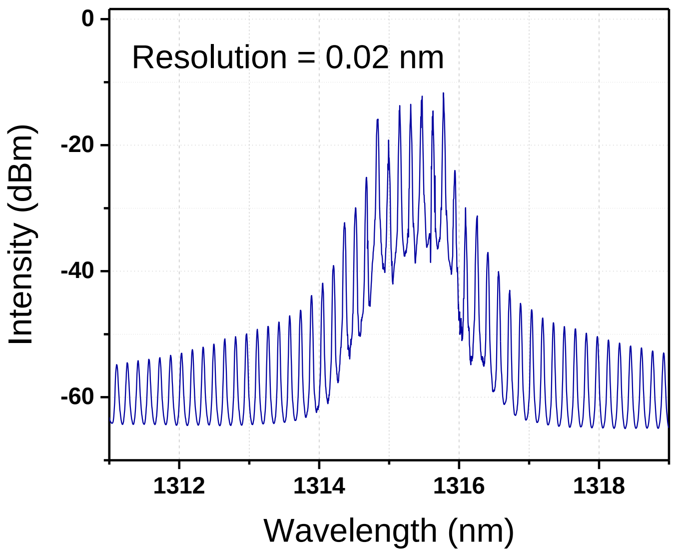

Figure 2.35 Emission spectrum of the laser diode at high injection current with a high resolution.

- **Temperature characteristics**

As per the discussion in Chapter 1, the theoretical QD structure shows a better temperature-independent property than the bulk or QW structure [43]. The characteristic temperature, which is normally referred to by the symbol T_0, of the laser diode, is used to indicate the temperature sensitivity of the device. A high T_0 means the threshold current density and external quantum efficiency increase less rapidly with the increasing temperature, or in other words, it has greater thermal stability. In order to calculate T_0, the threshold currents of a laser device at different temperatures are measured.

In the testing system, the laser device is placed on a heatsink, which is monitored by a temperature control system. Figure 2.36 illustrates the L-I curve as a function of different temperatures for a laser device of 3 mm length and 25 μm width, and the threshold current density (J_{th}) at each temperature can be calculated by equation 2.6. The plotting of J_{th} against the temperature on a logarithmic scale is shown in Figure 2.37, and the equation of T_0 is [37]:

$$T_0 = \frac{\Delta T}{\Delta \ln (J_{th})} \qquad \text{Equation 2.6}$$

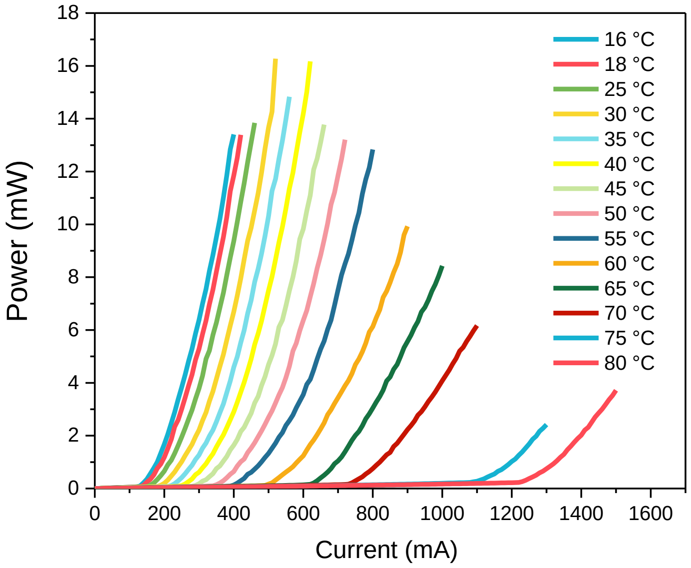

Figure 2.36 L-I curves of the laser diode under pulsed-wave operation at different temperatures.

By measuring the slope of the best linear fitting lines in Figure 2.37, the characteristic temperature of this laser diode is 34.2 K between 16 and 50 ℃ and 21 K between 60 and 80 ℃. The reason for the smaller value of T_0 at higher temperatures is that the carriers can more easily escape from the GS by absorbing thermal energy.

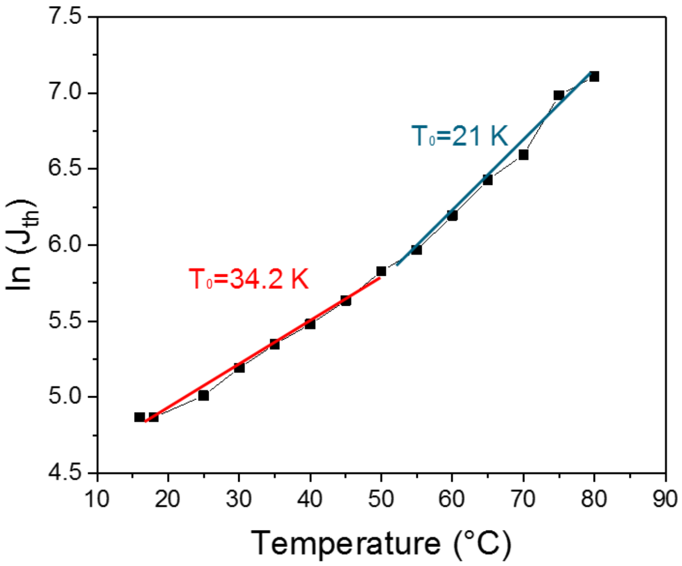

Figure 2.37 Plotting of threshold current density (J_{th}) against various temperatures in logarithmic scale. T_0 equals 34.2 K when the temperature is between 16 ℃ and 50 ℃, 21 K between 60 ℃ and 80 ℃.

2.3.2 Relative intensity noise

In an optical transceiver (transmitter + receiver), the major optical noise sources are coming from the laser diode, RF amplifier in the transmitter, photodiode and RF amplifier in the receiver [44]. For the laser diode, the output power exhibits fluctuations in its intensity, phase and frequency even where the injection current is ideally constant. The reason for the fluctuations is because of the random recombination of the carrier and photons. It causes a time variation in carrier and photon density by spontaneous emissions. This variation of photon density results in the fluctuation of output power, which provides a noise floor, also called relative intensity noise (RIN) [44]. In a high-speed optical system, the RIN can lead to a limited signal-to-noise ratio (SNR), and therefore an increased bit-error-rate (BER) restricts the system under certain conditions [44]. Since the low magnitude of RIN enables reducing the total optical noise in communication systems, it is essential for laser development.

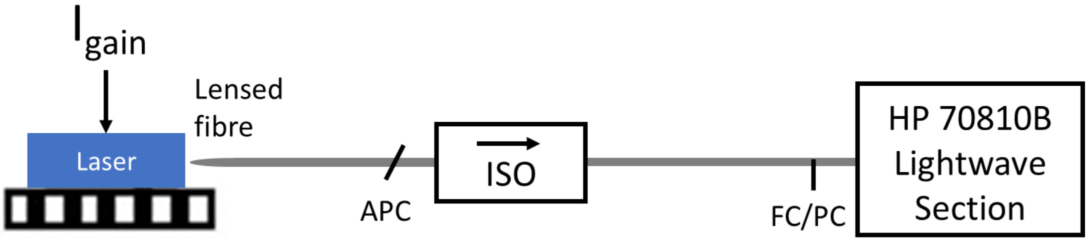

Figure 2.38 Experimental setup of RIN measurement. ISO: optical isolator.

The RIN of a laser is defined as the ratio of the intensity noise within a defined bandwidth to the overall average output intensity:

$$RIN = \frac{<\Delta P^2>}{P_0^2} \quad [{}^{dB}/_{Hz}] \qquad \text{Equation 2.7}$$

where $< \Delta P^2 >$ is the mean squared intensity fluctuation and P_0^2 is the squared average output power [44]. The RIN is always normalised to a 1 Hz bandwidth so that it can compare the intensity noise of the lasers with different bandwidths used [44]. Figure 2.38 displays the setup for the RIN measurement. The QD laser was biased by using two electrical probes. The laser output was collected by a 16° spherical-lensed SMF with 1.7 μm spot size. The fibre was fixed on a three-axis fibre alignment stage by tapes. By adjusting the alignment stage, a maximum coupling efficiency can be achieved. The fibre was then connected with an optical isolator (ISO) by an APC connector to prevent feedback into the laser cavity. The output light was then detected and analysed by a commercial instrument, HP 70810B Lightwave Section by FC/PC connectors. In this instrument, a built-in InGaAs photodiode, covering the wavelength range between 1200 nm and 1600 nm, is used for light collection. After the photodiode, the Lightwave module can be split into a DC component for the average output power (P_0) measurement, and an AC component to detect the amplified noise spectrum by the electrical spectrum analyser. The preamplifier from the AC component provides a 32-dB gain with an 8-dB noise figure, resulting in excellent sensitivity over 100 kHz to 22 GHz range. The equivalent electrical and optical noise-floor sensitivities are -165 dBm/Hz and -73 dBm/Hz, respectively [45].

The measured noise (i_p) from the HP 70810B is higher than the actual RIN because it is equal to:

$$i_p = i_{RIN} + i_{th} + i_{shot} \qquad \text{Equation 2.8}$$

where i_{th} denotes the thermal noise and i_{shot} is the shot noise. Both of the shot and thermal noise cause current fluctuations in the photodetectors, even the incident optical power is constant. The thermal noise is due to the Brownian movement of electrons by the thermal energy. It is measured by turning off all the light into the photodetector, and it is around -174 dBm/Hz at RT and usually constant [44]. The shot noise comes from the quantum nature of light that is incident on the photodetector; it is current-dependent and can be calculated by:

$$<i_{shot}^2(t)> \; = 2qi_pB \qquad \text{Equation 2.9}$$

where q is the electronic charge, i_p is the photocurrent, and B is the electronic bandwidth of the measurement system, typically normalised to 1 Hz. After subtracting the thermal noise and shot noise, the actual RIN value can be obtained.

2.4 Contribution statement

In this chapter, the device processing and characteristics for QD lasers have been developed with an aim to provide a coherent overview of all techniques utilised in this thesis. I would like to acknowledge the various technical support, including the assistance with the operation of EBL and FIB by Dr Suguo Huo, the setup of the RIN measurement with the help from Dr Lalitha Ponnampalam, and the cleanroom facilities at London Centre of Nanotechnology (LCN) and Southern University of Science and Technology (SUST).

2.5 References

[1] M. Fox, “Photoluminescence,” in *Optical properties of solids*, Second Edition, Oxford University Press, 2010, pp. 118–126.

[2] S. Perkowitz, *Optical characterization of semiconductors: infrared, raman, and photoluminescence spectroscopy*. Academic Press, 1993.

[3] G. Binnig, C. Quate, and C. Gerber, “Atomic Force Microscope,” *Phys. Rev. Lett.*, vol. 56, no. 9, pp. 930–933, 1986.

[4] L. Gross, F. Mohn, N. Moll, P. Liljeroth, and G. Meyer, “The chemical structure of a molecule resolved by atomic force microscopy,” *Science.*, vol. 325, no. 5944, pp. 1110–1114, Aug. 2009.

[5] H. Seiler, “Secondary electron emission in the scanning electron microscope,” *J. Appl. Phys.*, vol. 54, no. 11, pp. R1–R18, Nov. 1983.

[6] R. Rüdenberg, “The Early History of the Electron Microscope,” *J. Appl. Phys.*, vol. 14, no. 8, pp. 434–436, Aug. 1943.

[7] C. Scheu and W. D. Kaplan, “Introduction to Scanning Electron Microscopy,” in *In-Situ Electron Microscopy: Applications in Physics, Chemistry and Materials Science*, G. Dehm, J. M. Howe, and J. Zweck, Eds. Weinheim, Germany: Wiley-VCH Verlag GmbH & Co. KGaA, 2012, pp. 1–37.

[8] C. A. Mack and J. E. Connors, “Fundamental differences between positive- and negative-tone imaging,”, *Proc. SPIE 1674, Optical/Laser Microlithography V*, 1992.

[9] P. S. Gwozdz, “Positive Versus Negative: A Photoresist Analysis,” *Proc. SPIE 0275, Semiconductor Microlithography VI*, 1981.

[10] J. D. Plummer, M. Deal, and P. D. Griffin, *Silicon VLSI Technology: Fundamentals, Practice, and Modeling*. Pearson, 2001.

[11] T. A. Brunner and C. A. Fonseca, “Optimum tone for various feature types: positive versus negative,”, *Advances in Resist Technology and Processing XVIII*,

Proc. SPIE 4345, 2001.

[12] A. G. Baca and C. I. H. Ashby, *Fabrication of GaAs devices*. Institution of Engineering and Technology, 2005.

[13] MicroTech, “MA/BA6.” [Online]. Available: https://www.suss.com/brochures-datasheets/mask-aligner-ma-ba-6.pdf. [Accessed: 06-Jul-2019].

[14] F. C. M. J. M. Van Delft, “Delay-time and aging effects on contrast and sensitivity of hydrogen silsesquioxane,” *J. Vac. Sci. Technol. B Microelectron. Nanom. Struct.*, vol. 20, no. 6, pp. 2932–2936, Dec. 2002.

[15] N. Clark, A. Vanderslice, R. Grove, and R. R. Krchnavek, “Time-dependent exposure dose of hydrogen silsesquioxane when used as a negative electron-beam resist,” *J. Vac. Sci. Technol. B Microelectron. Nanom. Struct.*, vol. 24, no. 6, pp. 3073–3076, Nov. 2006.

[16] “E-beam writer with high resolution: RAITH150 Two,” *Raith*. [Online]. Available: https://www.raith.com/products/raith150-two.html. [Accessed: 20-Feb-2020].

[17] K. Nojiri, *Dry etching technology for semiconductors*. Cham: Springer International Publishing, 2015.

[18] J. L. Merz and R. A. Logan, “GaAs double heterostructure lasers fabricated by wet chemical etching,” *J. Appl. Phys.*, vol. 47, no. 8, pp. 3503–3509, Aug. 1976.

[19] Y. Tarui, Y. Komiya, and Y. Harada, “Preferential etching and etched profile of GaAs,” *J. Electrochem. Soc.*, vol. 118, no. 1, 1971.

[20] G. A. Hebner, C. B. Fleddermann, and P. A. Miller, “Metastable chlorine ion kinetics in inductively coupled plasmas,” *J. Vac. Sci. Technol. A Vacuum, Surfaces, Film.*, vol. 15, no. 5, pp. 2698–2708, Sep. 1997.

[21] M. Volatier, D. Duchesne, R. Morandotti, R. Arès, and V. Aimez, “Extremely high aspect ratio GaAs and GaAs/AlGaAs nanowaveguides fabricated using chlorine ICP etching with N_2-promoted passivation,” *Nanotechnology*, vol. 21, no. 13, p. 134014, Apr. 2010.

[22] J. W. Lee *et al.*, “Advanced selective dry etching of GaAs/AlGaAs in high density inductively coupled plasmas,” *J. Vac. Sci. Technol. A Vacuum, Surfaces, Film.*, vol. 18, no. 4, pp. 1220–1224, Jul. 2000.

[23] M. Huff and M. Pedersen, “Electrical field-induced faceting of etched features using plasma etching of fused silica,” *J. Appl. Phys.*, vol. 122, no. 2, p. 023302, Jul. 2017.

[24] DOW, “Processing Procedures for CYCLOTENE 3000 Series Resins,” *CYCLOTENE Advanced Electronic Resins*. [Online]. Available: https://www.nanotech.ucsb.edu/wiki/images/7/72/BCB-cyclotene-3000-revA.pdf. [Accessed: 16-Jul-2019].

[25] V. Malina, E. Hájková, J. Zelinka, M. Dapor, and V. Micheli, “Non-alloyed Ti/Au and Ti/Pt/Au ohmic contacts to p-type InGaAsP,” *Thin Solid Films*, vol. 223, no. 1, pp. 146–153, Jan. 1993.

[26] T. J. Kim and P. H. Holloway, “Ohmic contacts to GaAs epitaxial layers,” *Crit. Rev. Solid State Mater. Sci.*, vol. 22, no. 3, pp. 239–273, Sep. 1997.

[27] Y. C. Shih, M. Murakami, E. L. Wilkie, and A. C. Callegari, “Effects of interfacial microstructure on uniformity and thermal stability of AuNiGe ohmic contact to n-type GaAs,” *J. Appl. Phys.*, vol. 62, no. 2, pp. 582–590, Jul. 1987.

[28] A. G. Baca, F. Ren, J. C. Zolper, R. D. Briggs, and S. J. Pearton, “A survey of ohmic contacts to III-V compound semiconductors,” *Thin Solid Films*, vol. 309, pp. 599–606, Oct. 1997.

[29] MicroTech, “LOR and PMGI Resists.” [Online]. Available: http://microchem.com/pdf/PMGI-Resists-data-sheetV-rhcedit-102206.pdf. [Accessed: 24-May-2017].

[30] J. Schrauwen, D. Van Thourhout, and R. Baets, “Iodine enhanced focused-ion-beam etching of silicon for photonic applications,” *J. Appl. Phys.*, vol. 102, no. 10, p. 103104, Nov. 2007.

[31] F. A. Stevie, L. A. Giannuzzi, and B. I. Prenitzer, “The Focused Ion Beam

Instrument,” in *Introduction to Focused Ion Beams*, L. A. Giannuzzi and F. A. Stevie, Eds. Boston, MA: Springer US, 2005, pp. 1–12.

[32] F. I. Allen *et al.*, “Gallium, neon and helium focused ion beam milling of thin films demonstrated for polymeric materials: study of implantation artifacts,” *Nanoscale,* vol. 11, no. 3, pp. 1403–1409, 2019.

[33] G. Hlawacek, V. Veligura, R. van Gastel, and B. Poelsema, “Helium ion microscopy,” *J. Vac. Sci. Technol. B, Nanotechnol. Microelectron. Mater. Process. Meas. Phenom.*, vol. 32, no. 2, p. 020801, Mar. 2014.

[34] H. Luo, R. Jing, Y. Cui, H. Wang, and R. Wang, “Improvement of fabrication precision of focused ion beam by introducing simultaneous electron beam,” *Prog. Nat. Sci. Mater. Int.*, vol. 20, pp. 111–115, Nov. 2010.

[35] L. A. Giannuzzi, B. I. Prenitzer, and B. W. Kempshall, “Ion - Solid Interactions,” in *Introduction to Focused Ion Beams,* L. A. Giannuzzi and F. A. Stevie, Eds. Boston, MA: Springer, 2005, pp. 13–52.

[36] M. Nastasi, J. Mayer, and J. K. Hirvonen, *Ion-Solid Interactions: Fundamentals and Applications*. Cambridge University Press, 1996.

[37] K. Mobarhan, “Test and characterization of laser diodes: determination of principal parameters,” *Newport Corp.*, 1995.

[38] M. Kanskar *et al.*, “High power conversion efficiency 970 nm aluminum-free diode lasers,” in *The 17th Annual Meeting of the IEEELasers and Electro-Optics Society*, 2004, vol. 2, pp. 475–476.

[39] P. J. A. Thijs and T. van Dongen, “High quantum efficiency, high power, modulation doped GaInAs strained-layer quantum well laser diodes emitting at 1.5 μm,” *Electron. Lett.*, vol. 25, no. 25, p. 1735, 1989.

[40] “1240-1300 nm quantum dot laser,” *QD Laser*. [Online]. Available: https://www.qdlaser.com/en/products/list.html. [Accessed: 23-Nov-2019].

[41] M. Sugawara, K. Mukai, and H. Shoji, “Effect of phonon bottleneck on quantum-dot laser performance,” *Appl. Phys. Lett.*, vol. 71, no. 19, pp. 2791–2793, Nov.

1997.

[42] M. Rudan, *Physics of Semiconductor Devices*. Hoboken, NJ, USA: John Wiley & Sons, Inc., 2015.

[43] Y. Arakawa and H. Sakaki, “Multidimensional quantum well laser and temperature dependence of its threshold current,” *Appl. Phys. Lett.*, vol. 40, no. 11, pp. 939–941, Jun. 1982.

[44] G. P. Agrawal, *Fiber-optic communication systems*, 4th edition. John Wiley & Sons, 2010.

[45] Keysight, “70810B Lightwave Section, 100 kHz to 22 GHz [Obsolete].” [Online]. Available: https://www.keysight.com/en/pd-29780-pn-70810B/lightwave-section-100-khz-to-22-ghz?pm=PL&nid=-536900334.536883013&cc=GB&lc=eng. [Accessed: 19-Aug-2019].

Chapter 3

RIN measurement and data transmission of Si-based QD laser

3.1 Introduction

In a resonant cavity light emitter, the fraction of spontaneous emission which is coupled into the longitudinal modes by this cavity is a significant figure of merit of the dynamic characteristics of the laser. It is called the spontaneous emission factor β. High-β lasers have been shown to have a reduced spectrum linewidth and low RIN [1][2], since the dominant intensity noise comes from the power fluctuation resulting from the random spontaneous emission [3]. As described in Chapter 1, the nonlinear gain compression of the QD structure is higher than that of the QW structure, which results in a highly damped limited bandwidth modulation response of QD lasers [4]. Therefore, unique low noise characteristics, in term of RIN, are expected from the QD lasers. There have been several investigations into the RIN characteristics of InAs/GaAs QD lasers on native GaAs substrates [5]–[7], and RIN levels as low as −160 dB/Hz have been demonstrated.

Compared with III–V QD lasers on native GaAs, III–V QD lasers epitaxially grown on Si/Ge show a higher level of RIN, which may be related to the high defect density introduced (2–3 orders of magnitude greater than on native substrates) during the direct growth of III–V/Si [8][9]. Several previously studied QD lasers grown on Si/Ge substrates have shown a diminished performance in RIN levels; for example, Liu *et al.* reported a RIN range between –140 and –150 dB/Hz in a QD laser grown on Si with a defect density of 10^8 cm^{-2} [10]. RIN at the level of –120 dB/Hz in a Ge-based QD laser has also been reported [11]. It is known that the defects can be treated as electron traps associated with defect states which capture or absorb carriers and photons in the laser cavity, therefore degenerating the laser performance [12]. Although the effect of the high-density defects on the RIN of the lasers has not been intensively investigated, it is known that a high quality of III–V epi-layers grown on Si contributes to a high-performance laser with a low RIN level.

In this chapter, a single transverse mode FP QD laser grown on Si substrate with an ultra-low RIN of less than –150 dB/Hz, is reported [13]. The Si-based QD laser has also demonstrated high performance in static characteristics, in terms of the low threshold current of 12.5 mA at RT and maximum operating temperature up to 90 °C. The good laser performance and the low RIN value is partly the result of the high quality of GaAs/Si epi-layers, utilisation of the QD structure as the active region and an optimised device fabrication process. As a result, 25.6 Gb/s error-free data transmission by external modulation over 13.5 km standard single-mode fibre (SMF-28) has been achieved. The effect of chromatic dispersion by multi-longitudinal modes in the FP laser has also been discussed [13]. This work is proving the data transmission performance of QD on Si laser for intra-data centre interconnections.

3.2 Material growth and device fabrication

In this work, an InAs/GaAs QD laser structure was grown on an n-doped Si substrate with a 4° offcut by MBE. The Si substrate was firstly deoxidised at 900 °C for 30 minutes.

A thin AlAs NL of 6 nm was deposited by using migration enhanced epitaxy [8]. The three-step growth method for 1 μm GaAs buffer layer was employed to improve the morphology of grown material [14]. After that, a four-period of 10 nm $In_{0.18}Ga_{0.82}As$ and 10 nm GaAs of SLSs as DFLs [15], separated by 300 nm GaAs spacing layers for each period, was deposited after the GaAs buffer layer. Moreover, *in situ* thermal cycle annealing [16] was used during the DFLs growth in order to further reduce TDs within the III–V epi-layers on Si substrate. After these approaches, the density of dislocation is reduced from 10^9 cm^{-2} to the order of 10^5 cm^{-2}. More details of the epitaxial growth of III-V buffer on Si can be found in section 1.2 and in ref [8]. After obtaining well-developed epi-layers, an n-type 1.4 μm $Al_{0.4}Ga_{0.6}As$ cladding layer was deposited as follows. Before the p-type cladding growth, a five-layer undoped InAs/GaAs dot-in-well (DWELL) structure was grown as the active region. For each DWELL layer, 3 ML InAs QD layer was sandwiched by 2 nm $In_{0.15}Ga_{0.85}As$ and 6 nm $In_{0.15}Ga_{0.85}As$ QW, and 45 nm GaAs spacer layer was separated in each DWELL.

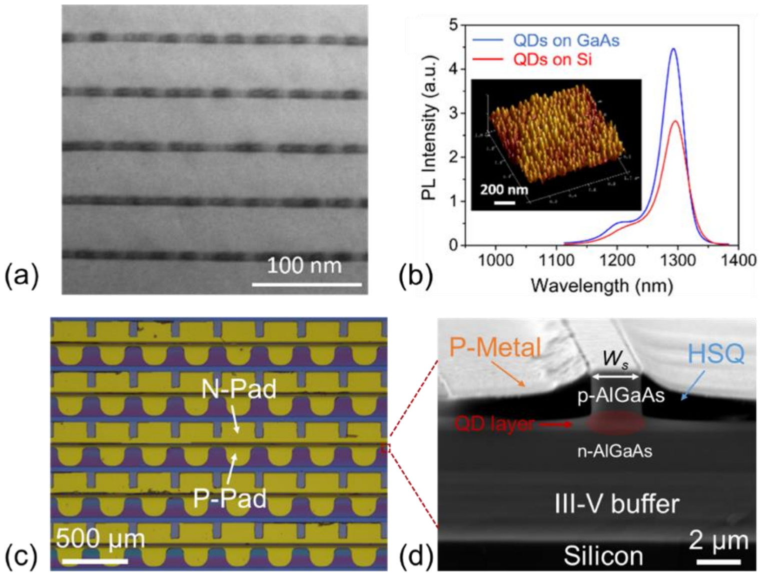

Figure 3.1 (a) TEM image of the InAs/GaAs QD layers. (b) Comparison of PL spectra of QD grown on GaAs and Si substrates. Inset: AFM image of uncapped QDs. (c) Microscope image of rows of fabricated narrow-ridge lasers. (d) A cross-section SEM image of a narrow-ridge laser with as-cleaved facet.

Figure 3.1 (a) shows a cross-section TEM image of the five-layer DWELL, in which a near-defect-free active region is achieved, thanks to the high quality of III–V epitaxial layers. A comparison of the PL spectra of QDs grown on Si and native GaAs substrate is shown in Figure 3.1 (b). The comparable PL emission at ~1290 nm with a strong intensity of QDs on Si is further proof of the good quality of the epi-layers. The inset of Figure 3.1 (b) shows a 3-D AFM image of the uncapped QDs with a QD density of ~3×10^{10} cm^{-2}.

After the material growth and observation of characteristics, the sample was fabricated into a narrow-ridge laser with a fixed ridge width of 2.2 µm, where EBL was used for lithography and ICP was used for the optimal dry etching process. After that, the smooth mesa with anisotropic profile was covered by SiO_2 as the passivation layer to prevent the oxidation of the Al-containing layers with air. Planarisation was carried out by using HSQ thermally cured at 180 ℃ for one hour. Ti/Pt/Au and Ni/AuGe/Ni/Au metallisation were used for the formation of ohmic contacts to the p+ GaAs contacting layer and the exposed n+ GaAs layer, respectively. The details of fabrication recipes and process have been discussed in section 2.2. After lapping the substrate to 120 µm for better heat dissipation, the laser bars were cleaved into the desired cavity length. One of the laser facets was coated with several pairs of SiO_2 and AlN by ion beam sputtering for 95% high-reflection coating. The number of layers and thickness for each deposited layer was simulated for 95 % reflectivity at 1315 nm before the deposition. By using a demo wafer along with the laser device during the sputtering, the actual reflectivity can be measured from the demo sample. The fabricated laser bars were then mounted epi-side up on a copper heatsink using indium-silver paste and direct probes for testing. Figure 3.1 (c) shows an optical microscope image of the top view of the laser arrays with labelled N-pads and P-pads. A cross-section SEM image of the as-cleaved laser facet is presented in Figure 3.1 (d). In this work, unless stated otherwise, laser characteristics s were tested under CW operation.

3.3 Characterisation and discussion

3.3.1 Static characteristics

Figure 3.2 (a) shows RT CW L-I curves of a 2.2 µm × 2.5 mm narrow-ridge QD laser for the total power and the SMF-28 coupled power at an enlarged scale. The measured threshold current and slope efficiency are 12.5 mA and 0.162 W/A, respectively. The L-I-V measurement is presented in Figure 3.2 (b), where the turn-on voltage is 1.5 V, and the total output power is 25 mW at 200 mA. Figure 3.2 (c) and (d) compare the L-I curves of two different cavity lengths, 2.5 mm and 4 mm, of the QD lasers at different sink temperatures. When the cavity length is 2.5 mm, the working temperature can reach at least 65 ℃, while a higher temperature of 90 ℃ can be achieved by the 4 mm Si-based

QD laser. This can be explained by the fact that the reduced threshold gain from the longer cavity is easier to reach before GS saturation as the temperature increases [17].

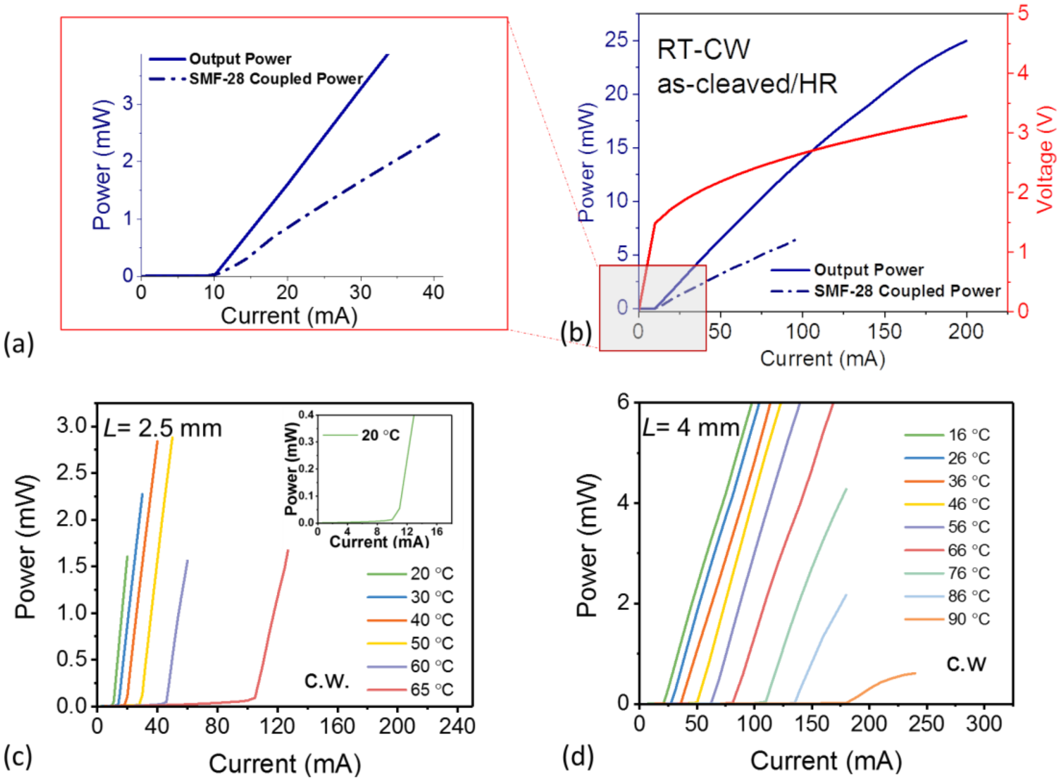

Figure 3.2 (a) L-I curves of Si-based QD laser for total power (solid line) and single-mode coupled power (dashed line) at RT at an enlarged scale. (b) L-I-V curves of the QD laser on Si with bias current from 0 to 200 mA. (c) CW L-I curves of Si-based laser with 2.5 mm cavity length at different temperatures. Inset: Enlarged L-I plot at 20 °C. (d) CW L-I curve of Si-based laser with 4 mm cavity length at different temperatures.

Figure 3.3 (a) demonstrates the lasing spectra of the Si-based QD laser with 4 mm cavity length under different injection currents. At low injection (5–20 mA), the broad spontaneous emission is observed at a peak wavelength of 1315 nm. As the current density increases to 25 mA (above the threshold current), the peak at 1315 nm increases sharply in intensity and narrows to ~4.6 nm, which is clear evidence of lasing. A high-resolution RT lasing spectrum of the QD laser with 2.5 mm length measured at 40 mA (which corresponds to 3.2 times the threshold current) is displayed in Figure 3.3 (b), showing a few FP longitudinal modes centred at ~1315 nm with the measured full-width of the lasing spectrum of ~2.4 nm. In Figure 3.4, the near-field measurement is illustrated. The lasing intensity profiles are plotted under different injection currents, and the inset shows an infrared camera picture of a lasing spot at 20 mA. The spot intensity is greatest at the centre and tails off at the edges, following a Gaussian profile. This profile reduces in width as the threshold current is reached and maintains a single-mode profile with increasing current, which proves the single transverse mode TME_{00} achieved by our narrow-ridge laser.

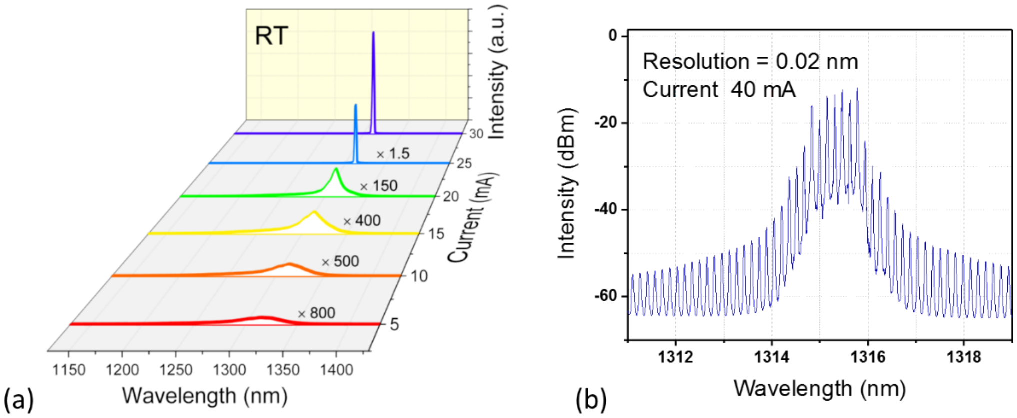

Figure 3.3 (a) Lasing spectra of narrow-ridge laser with 4 mm length under different CW injection currents. (b) High-resolution lasing spectrum of the QD laser with 2.5 mm length at an injection current of 40 mA.

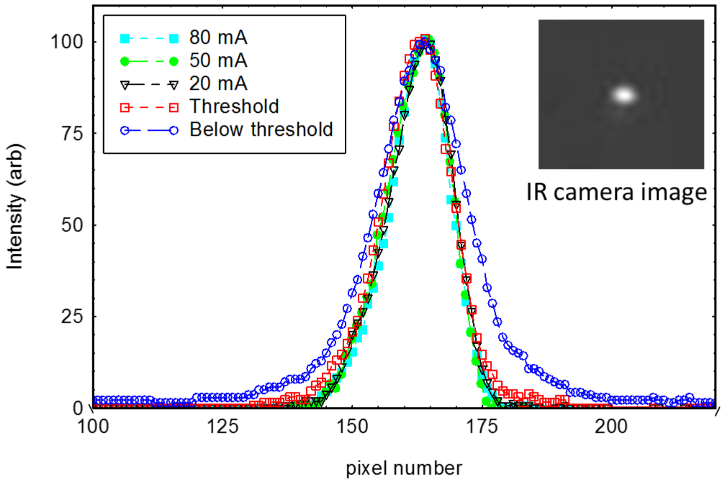

Figure 3.4 Lateral near-field intensity profiles with different injection currents. Inset: infrared IR camera image of lasing near-field at injection current of 20 mA.

3.3.2 RIN measurement

The setup for the RIN measurement is described in Chapter 2. Figure 3.5 shows the RIN measurement results of a 2.2 μm × 2.5 mm narrow-ridge QD laser with 12.5 mA threshold current. Figure 3.5 (a) demonstrates the RIN spectrum up to 16 GHz for the bias currents of 40, 60 and 80 mA with an optical isolator. The measured RIN is less than −150 dB/Hz when biased at gain currents greater than 60 mA ($I/I_{th} > 4.8$). This RIN value is normally lower than the case in the conventional QW lasers [18]. For the QW lasers with multi-mode lasing, the RIN is increased significantly by the random redistribution between each longitudinal mode of the laser, which refers to the mode partition noise [19][20]. In contrast, due to the high gain compression factor as well as the heavy damped photon-carrier interaction, the QD laser shows a dramatically reduced RIN of individual FP modes [7]. To confirm this, theoretical modelling exhibiting the RIN levels between −140 and −155 dB/Hz for the FP QD lasers has been reported [4]. Similarly, experimental measurements were also reported recently for the FP lasers with QD structure [5]–[7], which are in agreement with our measured results. Although the level of RIN depends on the various factors, such as differential gain and cavity length, our primary argument remains that the QD structure shows a superior capability of ultra-low RIN even for the multi-mode FP lasers.

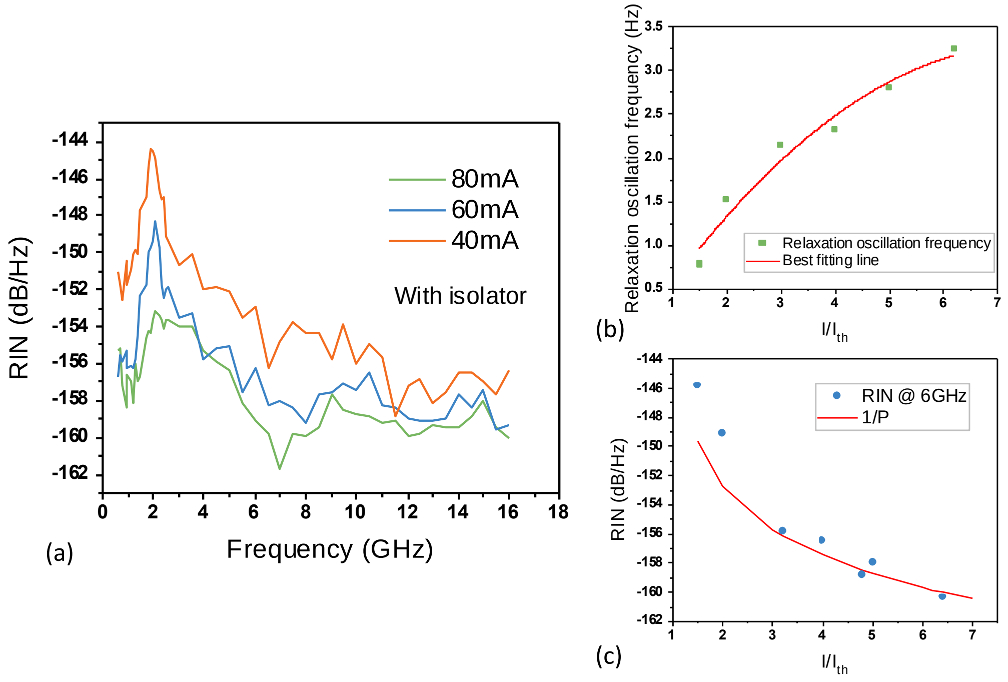

Figure 3.5 (a) RIN spectrum of the QD laser at gain currents of 40, 60 and 80 mA with isolator. (b) Relaxation oscillation frequency and with different biases. (c) Measured RIN in 6–10 GHz region with different biases.

The peak of the RIN spectrum indicating the relaxation oscillation frequency f_r, is shifting from 1 to 3 GHz when the gain current is increased from 20 to 80 mA, as shown in Figure 3.5 (b). This relatively low bandwidth of the laser is a result of a longer photon lifetime due to its longer cavity length (2.5 mm). After the f_r, the RIN value decreases rapidly as frequency increased, since the laser is not able to respond to fluctuations at such high frequencies [3].

Figure 3.5 (c) shows the measured RIN with the bias currents (power); the RIN decreases with an increase in power with a P^{-3} dependence firstly at lower powers (two deviated points at lower bias) and then decreases with an increase in power with a P^{-1} dependence at higher power (fitted points when I/I_{th} is bigger than 3). This trace can be explained by the small-signal analysis of the rate equation [21], the RIN spectrum at low frequency can be expressed as [22]:

$$RIN = \frac{1}{\pi^3}\delta f_{ST}(\frac{\gamma_0}{f_r^2} + K)^2 \qquad \text{Equation 3.1}$$

where δf_{ST} is the Schawlow–Townes formula [23] and inversely proportional to the laser output power P. According to equation 1.22 in Chapter 1, the relaxation oscillation frequency ${f_r}^2$ is proportional to the output power P, thus the RIN has a power dependency of P^{-3} in the low-power region. At higher power, the measured RIN is dominated by K^2 and has a dependency of P^{-1} [2][3]. The theoretical model of the rate equation is consistent with our measured RIN.

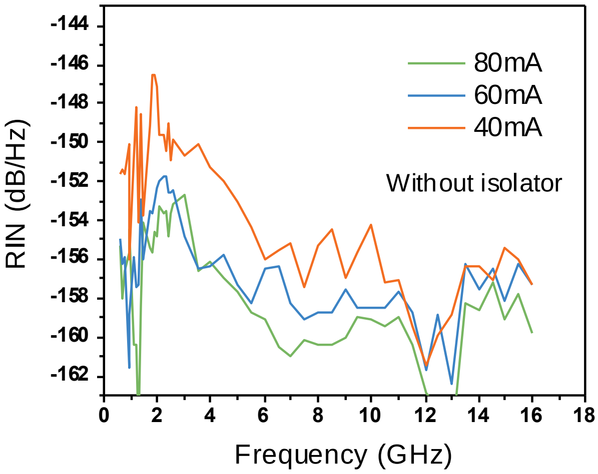

Figure 3.6 RIN spectrum of the QD laser without an isolator.

The state-of-art commercial QW transmitter chip is always accompanied by the optical isolator for the purpose of reducing the optical feedback and introduced noise [3]. However, the integration of isolator aggravates the package cost, process complexity and the total loss introduced in the system. Thus, it is highly desirable to operate laser without an isolator. Compared with QW laser, the QD laser has been shown a better optical feedback tolerance [24][25]. Notably, researchers from John Bowers's group at UCSB have reported that the feedback induced noise also can be highly supressed in QD lasers epitaxially grown on Si substrates [10]. In their work, by measuring the RIN under different feedback levels (between –60 dB to –10 dB), the RIN of lasers still maintained at low levels over the entire feedback range. A nearly 20 dB reduced sensitivity to the feedback was achieved by the Si-based QD lasers, compared with the conventional QW laser. Their results demonstrate the potential of isolator-free operation of the Si-based QD laser for future Si photonics system.

Here, in our work, we have carried out the initial study of direct comparison of RIN levels with and without isolator, while the identical laser was used in both of RIN measurements in a controlled experiment. As shown in Figure 3.6, the RIN spectrum without isolator shows a similar trend to the RIN with isolator, and the overall RIN still keeps at a low-level. It is in agreement with the previous reports and can be explained theoretically by the higher K-factor and smaller α factor of the QD structure relatively with the QW structure according to the Equation 1.25 [26]. Since the feedback level in our system was not measured at that time, a systematic study based on the feedback tolerance of our device is needed in the future.

3.3.3 Data transmission

The FP laser with ultra-low RIN is significantly desirable for optical signal generation, especially for the direct modulation, which can be used for the short-reach transmissions with low-cost. Unfortunately, the direct modulated transmission has not been executed due to the setup limitation. More experiments based on direct modulation are expected in the future. Nevertheless, the small-signal measurement of our QD laser device has been performed by our collaborative institution, which shows a limited modulation bandwidth of 1.6 GHz of the laser by the long device cavity [27]. The details will be discussed later in section 3.3.4. Alternatively, in this work, a data transmission experiment employing the external modulation for on-off keying is performed to prove the suitability of this Si-based QD laser for high-speed transmissions.

Given that the RIN spectra measured with and without isolator show similar trends and noise levels, to evaluate the feasibility of isolator-free QD FP laser for future low-cost short-reach data centre applications, here, QD FP laser without an optical isolator was employed in the data transmission experiment. The setup of the data transmission is presented in Figure 3.7. The 2.5 mm long monolithic QD laser was mounted on a copper heatsink and had its temperature stabilised at 25 ℃ via a thermoelectric cooling controller. The laser was biased at a fixed current of 40 mA ($I/I_{th} = 3.2$), which emitted 6.9 dBm (4.9 mW) output power from the L-I curve (Figure 3.2 (b)). The emitted lasing was coupled by a 1.7 µm lensed fibre with 3.7 dBm power which was coupled into the SMF-28, evidencing the primary transverse mode of the laser is the fundamental mode. After the polarisation controller, the CW lasing light was subsequently modulated by an X-cut Mach-Zehnder modulator (MZM) biased at quadrature with a π-voltage of 7V. The MZM was driven by a pseudorandom pattern generator (PPG) that generated a pseudorandom bit sequence of a non-return-to-zero on-off-keying modulated signal with a length of 2^{15}-1. The generated PPG signals had 0.5 V (-2 dBm) peak-to-peak voltage and were amplified by a RF amplifier with 17-dB gain, 6 dB noise figure, 45 GHz for high frequency 3 dB point and 35 kHz for low frequency 3 dB point [28]. Thus, the corresponding driving power of MZM equals to 15 dBm. The static value of 23 dB extinction ratio was measured with on down biased MZM. The modulated signal had –2.3 dBm power and was launched into a spool of 13.5 km SMF-28 with a dispersion of ~1.2 ps/(nm·km) and a total loss of –4.2 dB. It should be noted that this 13.5 km SMF was used to comply with the IEEE 802.3 standard for long optical reach [29].

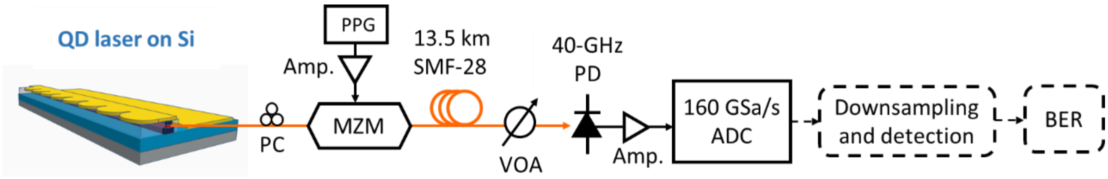

Figure 3.7 Setup of data transmission experiment. PC: polarisation controller; Amp: RF amplifier; PPG: pseudorandom pattern generator; SMF-28: standard single-mode fibre; PD: photodetector; ADC: analogue-to-digital converter; BER: bit-error rate.

After transmission, a variable optical attenuator was used to change the optical power into the receiver. The receiver consists of a 40 GHz photodetector with 0.6 A/W responsivity and 50 Ω load resistance, followed by the RF amplifier with same parameters as described above [28]. The electrical signal was captured by a 63 GHz, 160 GS/s analogue-to-digital converter (ADC) [30]. The actual resolution of the ADC is determined by the effective number of bits of ~ 4.7 bits under 25.6 GHz and 50 mV/div conditions, and resulting in an SNR of 30 dB. Two detection schemes were implemented to emulate the analogue signal detection in a data centre transceiver. In the first scheme, we downsampled the captured signal to one sample per symbol and conducted threshold detection after clock recovery and pattern synchronisation. This emulates the simplest data receiver that is widely deployed in data centre interconnection. In the second scheme, the captured samples were downsampled to two samples per symbol before being equalised by a seven-tap two-sample-per-symbol-spaced feed forward equaliser and a one-sample-per-symbol decision feedback equaliser with one feedback tap. This emulates a receiver with simple equaliser to compensate for the frequency roll-off and dispersion in a site-to-site data centre interconnection scenario [29]. Due to the limitation of the offline process, the maximum BER can only be calculated from 327670 bits.

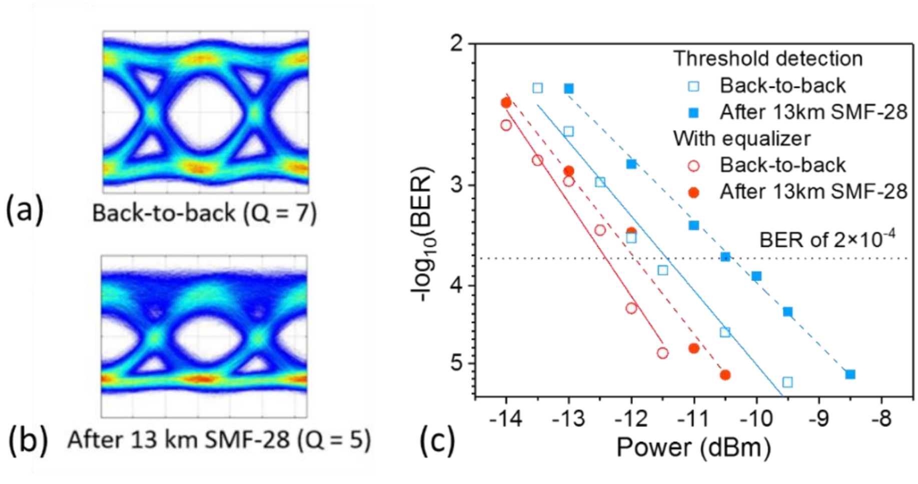

Figure 3.8 25.6 Gb/s eye diagram at (a) back-to-back (received power of –7 dBm) and (b) after transmission over 13 km SMF-28; (c) BER at different received power at back-to-back (open shapes) and after transmission (solid shapes) using threshold detection (blue colour) and equalisation (red colour).

Figure 3.8 (a) and (b) show the eye diagrams of the received signal back-to-back, and after transmission, both measured at a received power of –7 dBm. An opened eye diagram with a Q factor of 7 was obtained in the back-to-back scenario. After transmission, the eye diagram has a noisier bit 1 level and a longer rise and fall time due to the dispersion caused by inter-symbol interference (ISI), reducing the Q factor to 5.

Figure 3.8 (c) shows the measured BER as a function of the received optical power at back-to-back (open markers) and after transmission (closed markers). The blue markers show the BER results using the threshold detection scheme, and the red markers represent the BER results using the equaliser. Using the threshold detection scheme, we achieved a sub-forward error correction (FEC)-threshold BER for both back-to-back and through fibre transmission, when the received powers were higher than –9 dBm and –8 dBm, respectively. In the FEC scheme, errors are detected and corrected at the receiver without any retransmission. This error control is realized by adding extra bits at the end of the transmitted signal in a judicial manner [3]. The transmission power penalty at the FEC threshold of 2×10^{-4} was 1.1 dB, which was primarily due to the impact of chromatic dispersion. This leaves loss budgets of 10 dB and 8.75 dB for the 25.6 Gb/s data communications at back-to-back and after 13.5 km fibre transmission, respectively. According to the dispersion-limited distance equation [3], the calculated maximum distance of transmitted fibre is ~14 km by using parameters of 1.2 ps/(nm·km) dispersion of fibre and 2.4 nm linewidth of our laser at 25.6 Gb/s. This calculated result is in agreement with the experiment result. For a longer distance transmission, the single frequency DFB laser with narrow linewidth is necessary as discussed in perspective in section 1.4.

Compared to the threshold detection, the equaliser-assisted detection scheme improved the receiver sensitivity by 1 and 1.6 dB, for a back-to-back and after transmission, respectively, at the FEC threshold of 2×10^{-4}. The feed-forward equaliser is used to equalize and recover the data by reducing the pulse spreading from the SMF dispersion. For the decision feedback equaliser, the ISI can be eliminated by using the previously detected symbols on the currently detecting symbols [31]. Indeed, the equaliser offers 1.6 dB higher power budget at the cost of extra power consumption. In practical data centre interconnections, the equaliser can be switched. In both detection schemes, the received optical power shows a linear relationship to the −log10 (BER) scale.

The equation of SNR of a receiver can be written as [3]:

$$SNR = \frac{signal\ power}{thermal\ noise + shot\ noise} = \frac{signal\ power}{{4kTB}/{R} + 2BIq}$$

where k is Boltzmann constant, T is the absolute temperature, B is effective noise bandwidth, R is load resistance, I is photocurrent and q is the electric charge. When the received optical power/photocurrent is small, the impact of the shot noise can be neglected. Only the thermal noise dominates the system performance, and SNR is proportional to the signal power [3]. Since −log10 (BER) is also proportional to the SNR, it can be concluded that the linear relationship between the received optical power and −log10 (BER) reveals the thermal limited system performance by the optical receiver [3]. Thus, it proves the Si-based QD laser is suitable for data centre interconnection without involving extra noise.

3.3.4 Other dynamic characteristics

In addition to RIN and data transmission measurement, our QD lasers on Si were also examined for other dynamic characteristics including gain switching [32] and small-signal modulation [27] by our collaborative institution, the University of Cambridge. The 50 µm × 3.1 mm broad-area laser was used to generate gain-switched optical pulses by short- and high-amplitude electrical pulses. The shortest observed pulses had widths between 175 ps and 200 ps and 66 W peak power. Based on these results, some important laser parameters can be revealed by a three-level rate equation model. The simulation indicates that the limited gain of 14 cm^{-1} and high gain compression factor of 9×10^{16} cm^{3} are the main factors which contributed to the increased pulse width [32].

The 2.2 µm × 2.5 mm narrow-ridge Si-based QD laser demonstrates 3 dB modulation bandwidths of 1.6 GHz, modulation current efficiencies of 0.4 GHz/mA$^{1/2}$, and K-factors of 2.4 ns and 3.7 ns [27]. The limited modulation bandwidth is due to the long cavity length and long photon lifetime. The simulated maximum 3 dB modulation bandwidth of 5 GHz to 7 GHz can be achieved by the short cavity of 0.77 mm with the internal loss of 3 cm^{-1} [27]. Lasing with a shorter cavity could be achieved by increasing either the QD density or the dot layers for higher modal gain in the future [33][34]. Moreover, modelling the dislocation impact of dynamic properties shows that the enhanced non-radiative recombination centres by the dislocations leave the modulation bandwidth of the Si-based

QD laser almost unaffected, as sufficient modal gain is provided by the QD [27]. Both the gain switching and small-signal modulation measurements indicate that improving the gain of QDs is an essential factor in achieving better dynamic characteristics.

3.4 Conclusion

In this work, a high-performance narrow-ridge QD laser grown on Si substrates with a low RT CW threshold current of 12.5 mA and operation temperature up to 90 °C has been demonstrated by applying several strategies for high-quality III–V buffer growth and the optimal fabrication process. Ultra-low RIN characteristics have been measured at the level of < –150 dB/Hz at frequencies up to 16 GHz. Due to this low RIN value and the fundamental TEM_{00} mode of the QD laser, error-free 25.6 Gb/s data transmission was achieved after transmitting over 13.5 km SMF-28 without an isolator. This result shows that the Si-based QD laser has strong feasibility as a light-emitting source for low-cost and highly integrated optical interconnections at terabit speeds for Si photonics.

3.5 Contribution Statement

In this chapter, I would like to acknowledge the various technical support, including the supply of the QD sample by Dr Mingchu Tang and Prof. Huiyun Liu, the help for high reflection coating by Institute of Semiconductors, Chinese Academy of Sciences, the assistance of near field measurement by Dr Samuel Shutts at Cardiff University and the contribution of data transmission measurement by Dr Zixin Liu, Dr Siming Chen and Mr Zichuan Zhou. The measurement data of gain switching [32] and small-signal modulation [27] were supplied by Ms Constanze Hantschmann, and Mr Peter P Vasil'ev at the University of Cambridge.

3.6 References

[1] M. Yamada, “Variation of intensity noise and frequency noise with the spontaneous emission factor in semiconductor lasers,” *IEEE J. Quantum Electron.*, vol. 30, no. 7, pp. 1511–1519, Jul. 1994.

[2] F. Koyama, K. Morito, and K. Iga, “Intensity Noise and Polarization Stability of GaAlAs-GaAs Surface Emitting Lasers,” *IEEE J. Quantum Electron.*, vol. 27, no. 6, pp. 1410–1416, Jun. 1991.

[3] G. P. Agrawal, *Fiber-optic communication systems*. John Wiley & Sons, 2010.

[4] M. Sanaee and A. Zarifkar, “Theoretical modeling of relative intensity noise in p-doped 1.3-µm InAs/GaAs quantum dot lasers,” *J. Light. Technol.*, vol. 33, no. 1, pp. 234–243, Jan. 2015.

[5] A. Capua *et al.*, “Direct correlation between a highly damped modulation response and ultra low relative intensity noise in an InAs/GaAs quantum dot laser,” *Opt. Express*, vol. 15, no. 9, p. 5388, Apr. 2007.

[6] M. Krakowski, P. Resneau, M. Calligaro, H. Liu, and M. Hopkinson, “High power, very low noise, c.w. operation of 1.32 µm quantum-dot Fabry-Perot laser diodes,” in *IEEE 20th International Semiconductor Laser Conference*, 2006, pp. 39–40.

[7] A. Gubenko *et al.*, “Error-free 10 Gbit/s transmission using individual Fabry-Perot modes of low-noise quantum-dot laser,” *Electron. Lett.*, vol. 43, no. 25, p. 1430, 2007.

[8] S. Chen *et al.*, “Electrically pumped continuous-wave III–V quantum dot lasers on silicon,” *Nat. Photonics*, vol. 10, no. 5, pp. 307–311, May 2016.

[9] M. A. Tischler, T. Katsuyama, N. A. El-Masry, and S. M. Bedair, “Defect reduction in GaAs epitaxial layers using a GaAsP-InGaAs strained-layer superlattice,” *Appl. Phys. Lett.*, vol. 46, no. 3, pp. 294–296, Feb. 1985.

[10] A. Y. Liu, T. Komljenovic, M. L. Davenport, A. C. Gossard, and J. E. Bowers, “Reflection sensitivity of 1.3 µm quantum dot lasers epitaxially grown on silicon,” *Opt. Express*, vol. 25, no. 9, p. 9535, May 2017.

[11] Y. G. Zhou, C. Zhou, C. F. Cao, J. B. Du, Q. Gong, and C. Wang, “Relative intensity noise of InAs quantum dot lasers epitaxially grown on Ge,” *Opt. Express*, vol. 25, no. 23, p. 28817, Nov. 2017.

[12] A. Liu, R. Herrick, O. Ueda, P. Petroff, A. Gossard, and J. Bowers, “Reliability of InAs/GaAs quantum dot lasers epitaxially grown on silicon,” *IEEE J. Sel. Top. Quantum Electron.*, vol. 21, no. 6, 2015.

[13] M. Liao *et al.*, “Low-noise 1.3 μm InAs/GaAs quantum dot laser monolithically grown on silicon,” *Photonics Res.*, vol. 6, no. 11, p. 1062, Nov. 2018.

[14] M. Akiyama, Y. Kawarada, and K. Kaminishi, “Growth of single domain gaas layer on (100)-oriented Si substrate by MOCVD,” *Jpn. J. Appl. Phys.*, vol. 23, no. 11, pp. 843–845, Nov. 1984.

[15] M. Tang *et al.*, “Optimizations of defect filter layers for 1.3-μm InAs/GaAs quantum-dot lasers monolithically grown on Si substrates,” *IEEE J. Sel. Top. Quantum Electron.*, vol. 22, no. 6, pp. 50–56, Nov. 2016.

[16] J. R. Orchard *et al.*, “In situ annealing enhancement of the optical properties and laser device performance of InAs quantum dots grown on Si substrates,” *Opt. Express*, vol. 24, no. 6, p. 6196, Mar. 2016.

[17] G. Park, O. B. Shchekin, and D. G. Deppe, “Temperature dependence of gain saturation in multilevel quantum dot lasers,” *IEEE J. Quantum Electron.*, vol. 36, no. 9, pp. 1065–1071, Sep. 2000.

[18] M. Tatham, I. Lealman, C. Seltzer, L. Westbrook, and D. Cooper, “Resonance frequency, damping, and differential gain in 1.5 μm multiple quantum-well lasers,” *IEEE J. Quantum Electron.*, vol. 28, no. 2, pp. 408–414, 1992.

[19] K. Ogawa, “Chapter 8 Semiconductor Laser Noise: Mode Partition Noise,” in *Semiconductors and Semimetals*, vol. 22, no. Part C, Elsevier, 1985, pp. 299–330.

[20] K. Y. Lau, C. M. Gee, T. R. Chen, N. Bar-Chaim, and I. Ury, “Signal-induced noise in fiber-optic links using directly modulated Fabry-Perot and distributed-feedback laser diodes,” *J. Light. Technol.*, vol. 11, no. 7, pp. 1216–1225, Jul. 1993.

[21] R. S. Tucker, “High-speed modulation of semiconductor lasers,” *IEEE Trans. Electron Devices*, vol. 32, no. 12, pp. 2572–2584, Dec. 1985.

[22] T. Fukushima, R. Nagarajan, J. E. Bowers, R. A. Logan, and T. Tanbun-Ek, “Relative intensity noise reduction in InGaAs/InP multiple quantum well lasers with low nonlinear damping,” *IEEE Photonics Technol. Lett.*, vol. 3, no. 8, pp. 688–693, Aug. 1991.

[23] A. L. Schawlow and C. H. Townes, “Infrared and Optical Masers,” *Phys. Rev.*, vol. 112, no. 6, pp. 1940–1949, Dec. 1958.

[24] G. Huyet *et al.*, “Quantum dot semiconductor lasers with optical feedback,” *Phys. Status Solidi Appl. Res.*, vol. 201, no. 2, pp. 345–352, Jan. 2004.

[25] D. O’Brien *et al.*, “Feedback sensitivity of 1.3 μm InAs⁄GaAs quantum dot lasers,” *Electron. Lett.*, vol. 39, no. 25, p. 1819, 2003.

[26] J. Helms and K. Petermann, “A simple analytic expression for the stable operation range of laser diodes with optical feedback,” *IEEE J. Quantum Electron.*, vol. 26, no. 5, pp. 833–836, May 1990.

[27] C. Hantschmann *et al.*, “Understanding the bandwidth limitations in monolithic 1.3 μm InAs/GaAs quantum dot lasers on silicon,” *J. Light. Technol.*, vol. 37, no. 3, pp. 949–955, Feb. 2019.

[28] “Datasheet SHF 803 P Broadband Amplifier,” *SHF Communication Technologies AG*, 2004. [Online]. Available: https://www.shf-communication.com/wp-content/uploads/datasheets/datasheet_shf_803p.pdf. [Accessed: 20-Feb-2020].

[29] “IEEE P802.3ba 40Gb/s and 100Gb/s Ethernet Task Force.” [Online]. Available: http://www.ieee802.org/3/ba/. [Accessed: 23-Oct-2019].

[30] “Infiniium Z-Series Oscilloscopes - Data Sheet -Keysight,” *Keysight*. [Online]. Available: https://www.keysight.com/cn/zh/assets/7018-04251/data-sheets/5991-3868.pdf. [Accessed: 20-Feb-2020].

[31] A. Grami, *Introduction to Digital Communications*. Elsevier, 2016.

[32] C. Hantschmann *et al.*, “Gain switching of monolithic 1.3 μm InAs/GaAs quantum dot lasers on silicon,” *J. Light. Technol.*, vol. 36, no. 18, pp. 3837–3842, Sep. 2018.

[33] A. R. Kovsh *et al.*, “InAs/InGaAs/GaAs quantum dot lasers of 1.3 μm range with enhanced optical gain,” *J. Cryst. Growth*, vol. 251, no. 1–4, pp. 729–736, Apr. 2003.

[34] L. F. Lester *et al.*, “Optical characteristics of 1.24-μm InAs quantum-dot laser diodes,” *IEEE Photonics Technol. Lett.*, vol. 11, no. 8, pp. 931–933, Aug. 1999.

Chapter 4

Post-fabrication of Si-based QD lasers for different applications by FIB

4.1 Introduction

In the previous chapter, we examined the modulation properties of our Si-based QD laser and found that a single fundamental mode and ultra-low RIN was achieved. The results indicate that this laser is capable of data transmission in the optical link as a reliable light source emitter. In this chapter, efforts were made to identify the possibility of integrating the Si-based QD laser with other optical components on the same Si platform. In general, the hetero-epitaxial integration of different functional photonic devices requires selective area growth of III–V compounds on the pattered substrate [1] or selectively etching to delineate the III–V region after the whole wafer growth [2]. However, the coupling issue is still an open question for edge-emitting lasers in integration studies. Several pioneering works have proposed or demonstrated integrated semiconductor lasers with EA modulators [3] or SOAs [4] on the native platform. Both building blocks have the same epitaxy layers and can be grown at the same time; also, the light can be easily coupled between the components at the same height via the butt-jointed coupling. This low-cost "platform technology" is capable of providing a variety of applications for Si photonics without involving regrowth or changing the basic fabrication process [4]. Although the realisation of such an integrated transmitter chip on Si is still a daunting challenge, we are able to prove that the concept is feasible by the post-fabrication of our Si-based QD laser using the FIB as the prototyping test.

In the individual FP laser fabrication, the reflective mirrors are normally made by crystal cleaving, which however is impractical for multi-device integration on one platform. For the commercial photonic integration circuits, the formation of optical feedback is generally achieved by a dry etching technique. It can be used to form etched facet for simple FP cavity [5], DFB [6][7] or distributed Bragg reflector [8] for single-mode lasers. In this chapter, we first discuss FP laser facet creation by FIB etching. Angled facet etching was then performed to investigate the feasibility of converting the QD laser into other components with just a slight cavity change [9]. The broadband light source, i.e. the superluminescent light-emitting diode (SLD), which has wide application both in the communication [10]–[12] and biological area [13], and the SOA, which both rely on the ASE, can be realised by the tilted facet angle. In addition, we also discuss a groove etching study for potential multi-section devices, such as a coupled-cavity laser [14], mode-locked laser [15], and EA modulators [16] for photonic integrated circuits.

4.2 Experimental method

4.2.1 Angled facet etching

In this work, a standard Si-based InAs/GaAs QD laser was used for the post-fabrication. As shown in Figure 4.1, the well-developed 2.4 μm III–V epi-layers, which consisted of a 5 nm AlAs NL, 1 µm GaAs buffer and four layers of DFLs, were deposited on a 4° offcut Si substrate to reduce the material defects [9]. After that, a 1.4 µm n-doped AlGaAs cladding layer with 2×10^{18} cm^{-3} by Si and a 30 nm lower undoped AlGaAs guiding layer were grown on the optimised III–V epi-layers. An undoped seven-layer InAs/InGaAs/GaAs DWELL active region was deposited as follows: a 30 nm undoped upper AlGaAs guiding layer and a 1.4 µm p-doped AlGaAs cladding layer with 6×10^{17} cm^{-3} by Be were grown above the active region. Finally, a 300 nm highly p-doped GaAs contact layer with 1×10^{19} cm^{-3} was grown to finish the laser structure.

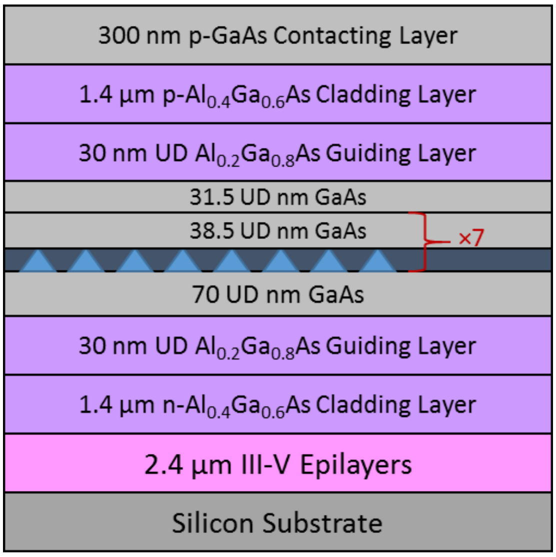

Figure 4.1 (a) Schematic diagram of the InAs QD laser structure grown on Si substrates [9].

The laser structure was then fabricated into a broad-area laser 25 µm in width and 3 mm in length following the fabrication process described in Chapter 2. The as-cleaved laser device was first characterised as normal and implemented for the post-fabrication of front facet angle cutting studies by Ga$^+$ FIB. The cutting angles (θ) were set as 0°, 5°, 8°, 10°, 13° and 16°, respectively, as illustrated by Figure 4.2. FIB milling was performed using a Zeiss XB 1540 “cross-beam” FIB microscope with a probe current of 500 pA for coarse milling and 100 pA for surface polishing. The laser device with each FIB-etched facet angle was measured and characterised under CW operation at RT.

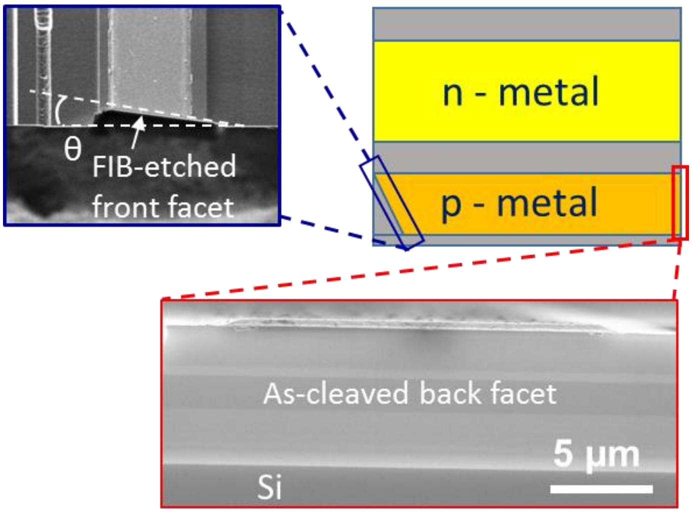

Figure 4.2 Top-left SEM image shows typical FIB-made angled front facet of Si-based InAs QD laser. Bottom-right cross-sectional SEM image shows a typical as-cleaved back facet of the Si-based InAs QD laser.

4.2.2 Groove etching for multi-section device

The as-cleaved laser device with 25 μm width and 3.5 mm length was used for the groove etching study. After obtaining the laser device characteristics (L-I curves), the narrow groove was then etched on the laser ridge by the FIB. In fact, the parameters for groove etching, such as the width, depth, position and ratio of the long to the short section, strongly affect the device performance and need to be optimised for different applications. However, in this study, only simple shallow and deep groove etching were compared to determine the possibility of using the QD laser on Si as a multi-section device. The stimulation for the optimal parameters will be implemented, such as by 2D scattering matrix method [17], in the future work.

First, a groove with 1.3 μm width and 1 μm depth is etched at a position 0.5 μm from a single facet of the laser device, as shown in Figure 4.3 (a). The groove with 1 μm depth isolates the p-type metal contact and the highly-doped contact layer of the laser device, as well as part of the p-cladding layer. As described in Chapter 2.2.6, the depth of FIB milling depends on the value of the dose and the number of ions absorbed by the target materials. 1 μm depth can be achieved at a dose value of 0.8 nC/μm^2. An acceleration voltage of 30 keV and probe current of 100 pA were used for the fine sidewalls. After that, the L-I curve of the device with a groove was measured from the short section side by electrically pumping the 3 mm long section under pulsed operation (1% duty cycle and 1 µs pulse width) while the 0.5 mm short section was unbiased.

A deeper groove was then etched on this device in the same position. This time, the width of the groove was kept the same, but the depth was increased to 3.8 µm, as demonstrated in Figure 4.3 (b). This depth is intended to pass the active region, to obtain electrical and optical isolation. The FIB parameters for this milling were 30 keV acceleration voltage, 100 pA probe current and 3 nC/µm^2 dose value for the additional 2.8 µm depth. The L-I curve of the device with the deeper groove was also measured after the milling. Figure 4.4 shows the position of the groove on the laser device, which is parallel to the laser facet.

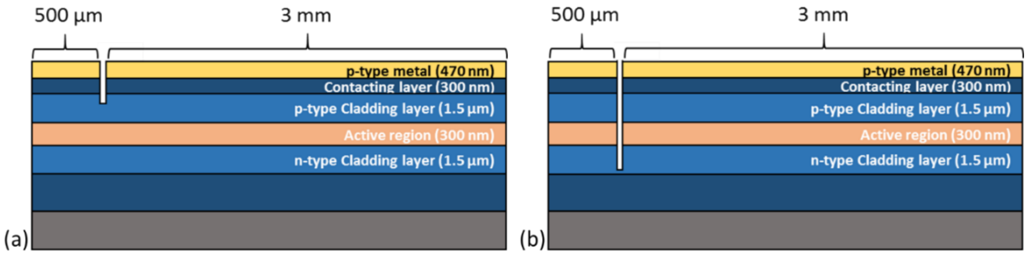

Figure 4.3 Schematic diagrams (not to scale) of two-section Si-based laser device isolated by a 1.3 µm width groove into short section of 500 µm and long section of 3 mm, with different groove depths of (a) 1 µm and (b) 3.8 µm.

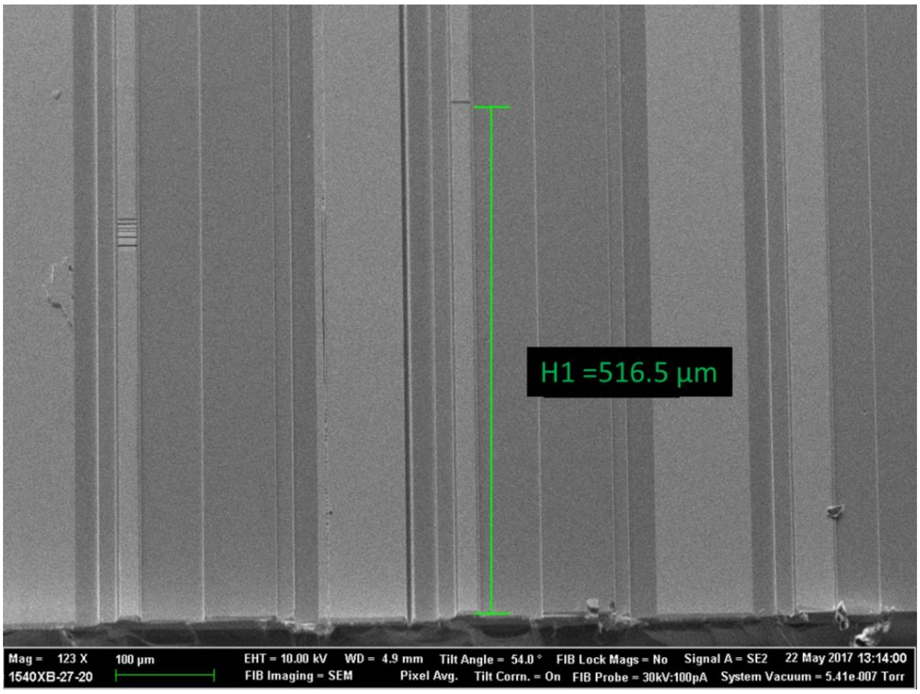

Figure 4.4 SEM image of the groove on a p-type region 517 µm away from the facet of the laser.

4.3 Results and discussion

4.3.1 Angled facet etching

We first compare the as-cleaved and FIB-made (0° cutting angle) facets, whose SEM images are shown in Figure 4.5 (a) and (b). In order to shorten the FIB operation time and reduce the re-deposition by the sputtered materials, the depth of the milling area is intended to pass the active region layer. Although there is slight re-deposition below the active region of the FIB-etched III/V region, a clean, smooth and vertical sidewall are still obtained. Figure 4.6 shows the comparison of the L-I-V curves of the QD lasers on Si with the as-cleaved and FIB-milled front facet (0°) under CW operation at RT. The measured series resistances of these two lasers are very similar, at 3.62 ± 0.01 Ω and 3.65 ± 0.02Ω, respectively. The laser threshold current of the QD laser with the as-cleaved facet is 200 mA, and the slope efficiency is 0.125 W/A. The Si-based QD laser performance has slight degeneration after facet milling by the FIB, with 222 mA threshold current and 0.095 W/A slope efficiency. This slight degeneration of the laser in terms of the threshold current and slope efficiency is associated with the increased mirror loss, which is caused by the ion implantation, re-deposition and bombardment of the energetic

Ga$^+$ ions during FIB milling. Another thing to note is that the Ga$^+$ ion beam is not a suitable FIB beam source for GaAs/AlGaAs material milling, as the extra Ga$^+$ ions may be induced and change the composition of the original materials. Although there are other beam sources (He$^+$ and Ne$^+$) available for material milling, they are only competent for nanostructures due to their ultra-low milling speed by the low atomic mass and small probe currents [18]. For the large volume milling works, such as our laser device in μm scalar, the Ga ion beam is a more favourable choice with much faster etching speed. A more appropriate method is to use gas-assisted FIB milling [19] to reduce the deposition effect.

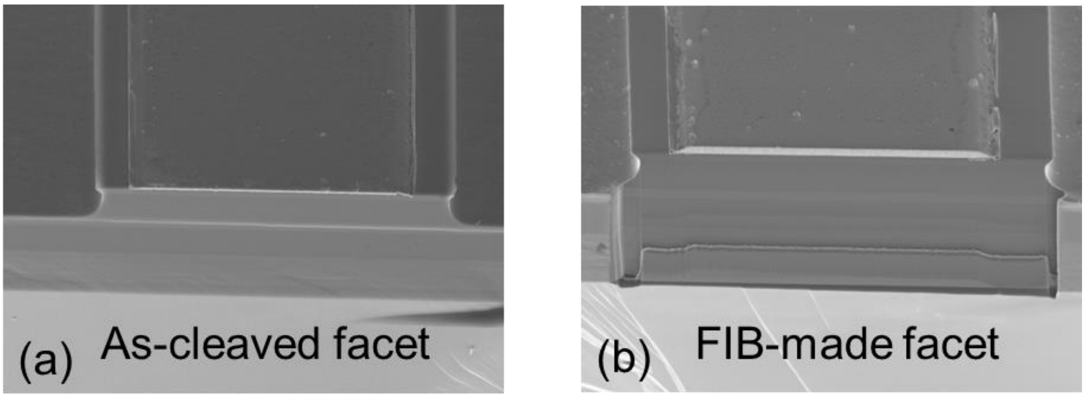

Figure 4.5 Typical SEM images of (a) as-cleaved facet and (b) FIB-made front facet of Si-based InAs QD laser.

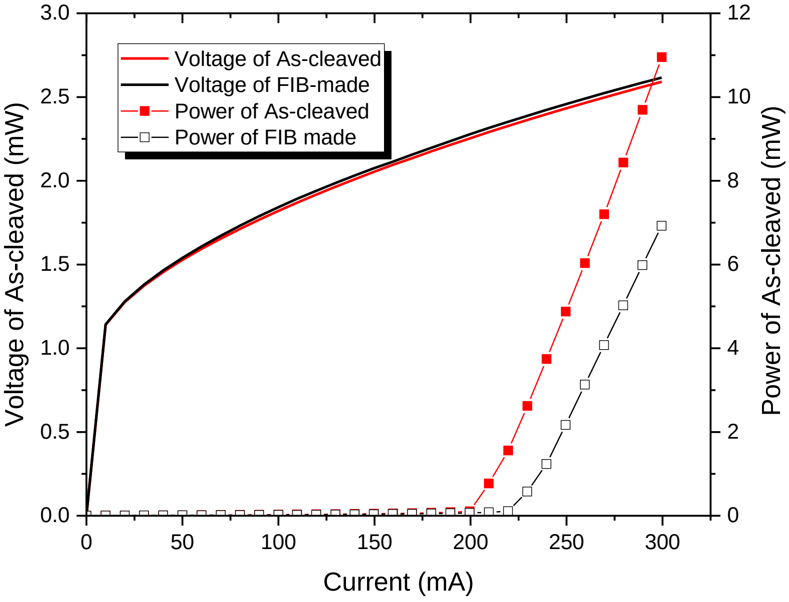

Figure 4.6 L-I-V characteristics of Si-based InAs/GaAs QD laser with as-cleaved and FIB-made facets measured under CW operation at RT.

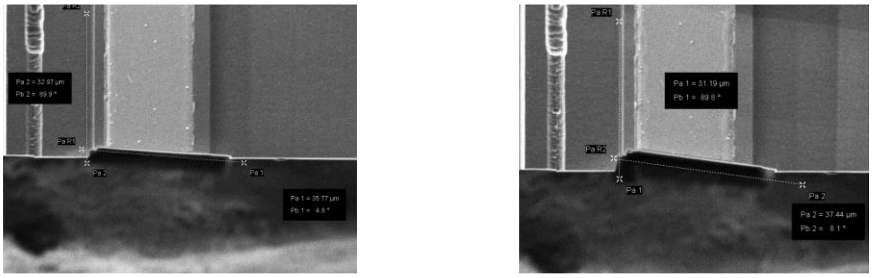

5 degree facet 8 degree facet

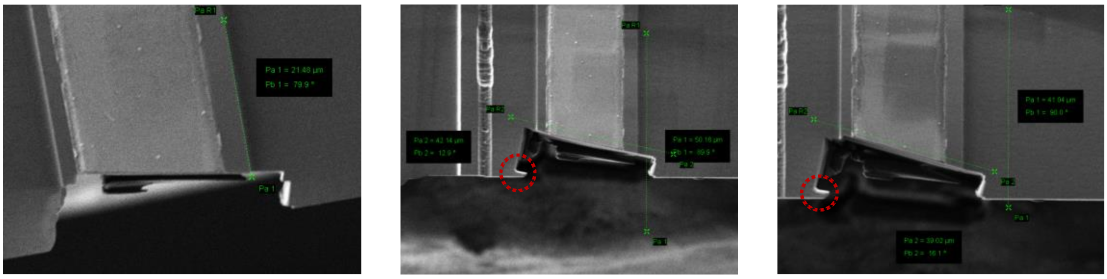

10 degree facet 13 degree facet 16 degree facet

Figure 4.7 Top view of SEM images of FIB-made facets with 5°, 8°, 10°, 13° and 16° angle.

Top-view SEM images of 5°, 8°, 10°, 13° and 16° angled facets by FIB are shown in Figure 4.7. The mean error of the etched facet angle is around 0.1°. There is a small triangular edge on the left sidewall in front of the laser facet for both the 13° and 16° angle, which blocks the light beam from the angled facets during the laser measurements and should be removed completely. This uncompleted FIB operation will be avoided in future work. Figure 4.8 (a) demonstrates the L-I plotting of the InAs/GaAs QD laser directly grown on Si substrate with the as-cleaved facet and 0°, 5°, 8°, 10°, 13° and 16° angled facets, respectively. The laser device shows typical laser characteristics when the etched angle is smaller than 8°. The threshold current is increased from 222 mA to 280 mA when the facet angle is raised from 0° to 5°. This phenomenon can be explained by the effectively reduced reflectivity of the angled facet, which means less reflection light was coupled back to the laser cavity compared with the 0° facet. The slope efficiency is also degraded by the increased mirror loss. Figure 4.8 (b) displays the L-I characteristics of the Si-based QD devices at an enlarged scale when the etched angle is bigger than 8°. The QD device with 8° facet shows typical superluminescent behaviour, which was evidenced by the superlinear increased output power with the current injection. This superlinear relationship of power–current is due to the ASE. The maximum RT output power is 0.56 mW at 600 mA injection current, and the power was then saturated by the junction heating at the higher driving current. As mentioned above, the re-deposition phenomenon was found during facet etching by FIB, as shown in Figure 4.9; these re-deposited residuals induced additional mirror loss and degenerated the device performance. As the etched angle was increased further to 13°, an LED-like L-I curve was observed.

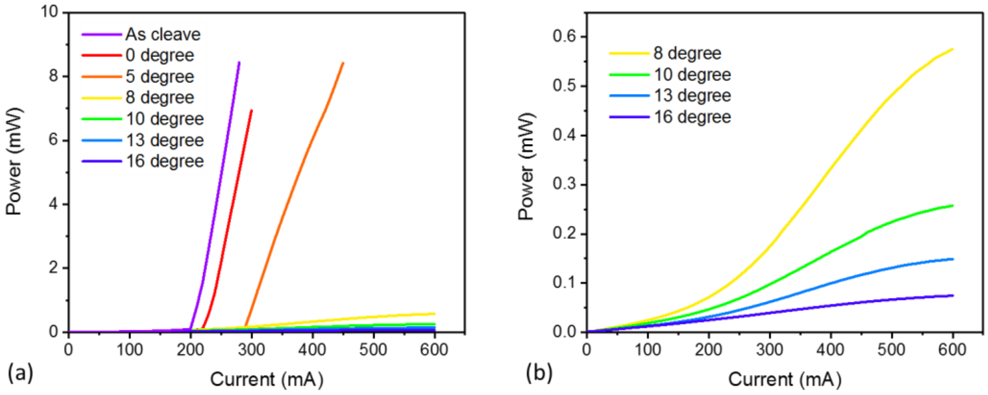

Figure 4.8 L-I characteristics of a 25 μm × 3000 μm Si-based InAs/GaAs QD device with different front facet angles of 0^{o}, 5^{o}, 8^{o}, 10^{o}, 13^{o} and 16^{o} under CW operation at RT.

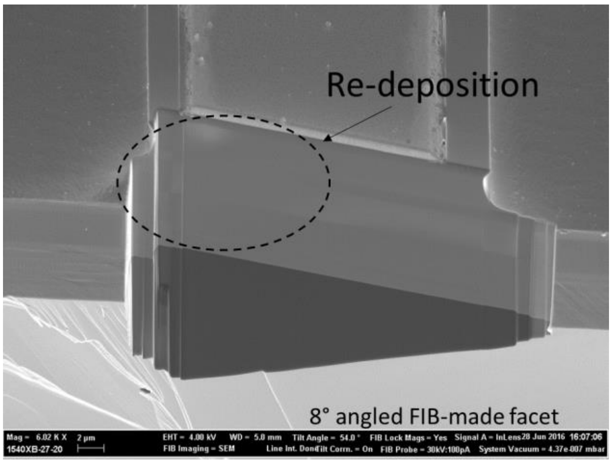

Figure 4.9 SEM image of 8° angled FIB-made facet with Ga^{+} re-deposition.

Figure 4.10 compares the RT electroluminescence (EL) spectra of QD devices directly grown on Si with 5°, 8°, 10° and 13° facet angles at different injection currents. These EL spectra provide strong evidence of the different device characteristic behaviours among devices with different facet angles. The evolutions of the measured FWHM of 5° and 8° devices against the various currents are summarised in Figure 4.10. For the QD device with 5° angled facet, the FWHM is reduced gradually from 52.5 nm to 30 nm when the injection current is smaller than the threshold current. When the current increases to 300 mA (above the threshold current), the FWHM dramatically drops to only 2.4 nm and the output power is suddenly increased. This typical laser behaviour shows that the lasing oscillation has occurred even with an effectively reduced mirror reflection coming from the 5° front laser facet. Compared with the 5° device, the 8° device shows completely different behaviour. The FWHM is slightly narrowed from 54 nm to 45.5 nm as the injection current raises from 100 mA to 600 mA, which evidences the fully inhibited lasing characteristics in this 8° device cavity. The working mechanisms of the narrowing spectrum can be explained as follows. When the QD device works as an SLD or SOA, the modal gain is larger than the internal loss within a limited wavelength range in the middle of the gain spectrum. The middle of the spectrum, therefore, is dominated by the ASE. Towards the edge of the spectrum, the wavelength-dependent modal gain decreases and thus the light is dominated by the spontaneous emission. The spectrum narrowing is an indirect indication of the existence of ASE. A similar phenomenon occurred in the device with 10° facet.

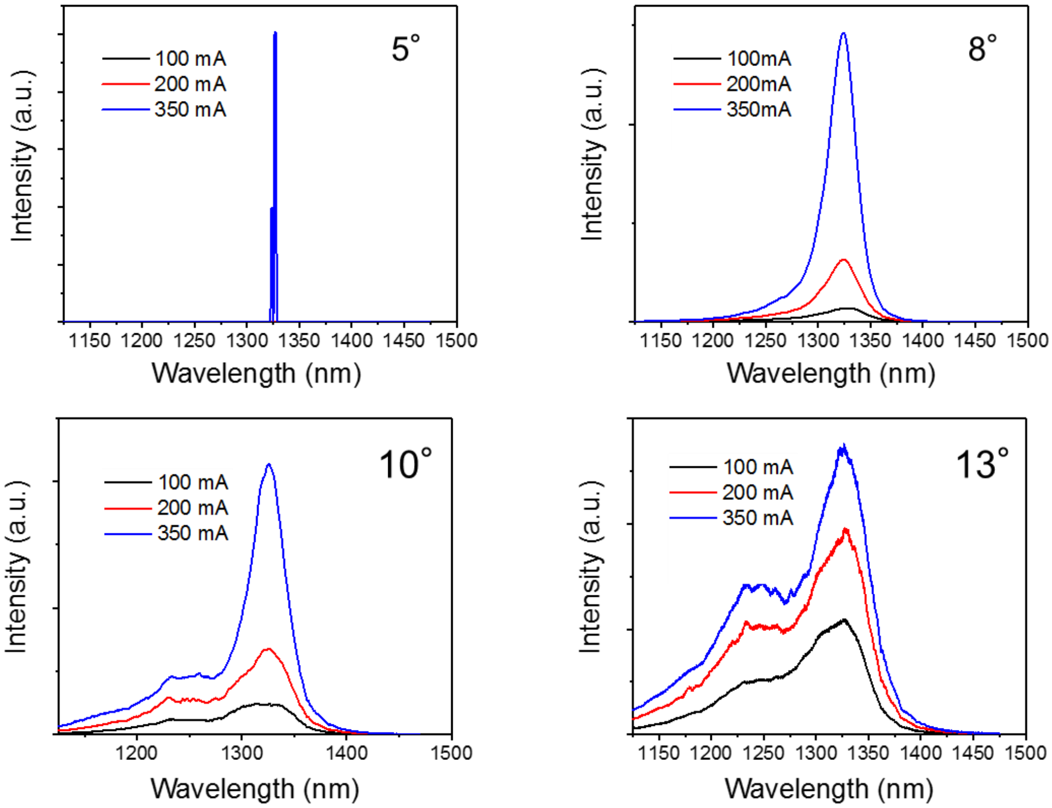

Figure 4.10 RT EL spectra for Si-based QD devices with different front facet angles of 5°, 8°, 10° and 13° at various CW injection currents.

From Figure 4.10 (c) and (d), the secondary peak on short-wavelength side can be found as the injection current increased. It is corresponding to the first excited state transition of the QD structure. This is typical behaviour of QD broadband device when the GS lasing is suppressed [20]. It should be mentioned that the FWHM of the InAs/GaAs QD device on Si reported here is much smaller than the QD SLD/SOA on native substrates. The reason for this is that the design of the InAs/GaAs QD is for a laser device with optimised small dot inhomogeneity. The improved bandwidth could be expected by using the techniques of chirped QDs [21], QD intermixing [22] or hybrid QW/QD structures [20]. The EL spectrum of the device with 13° facet is displayed in Figure 4.10 (d), where the linear increased spectrum peak intensity with the increased injection current indicates nominal LED-like behaviour, which was a result of the fully suppressed optical feedback by the tilted device facet.

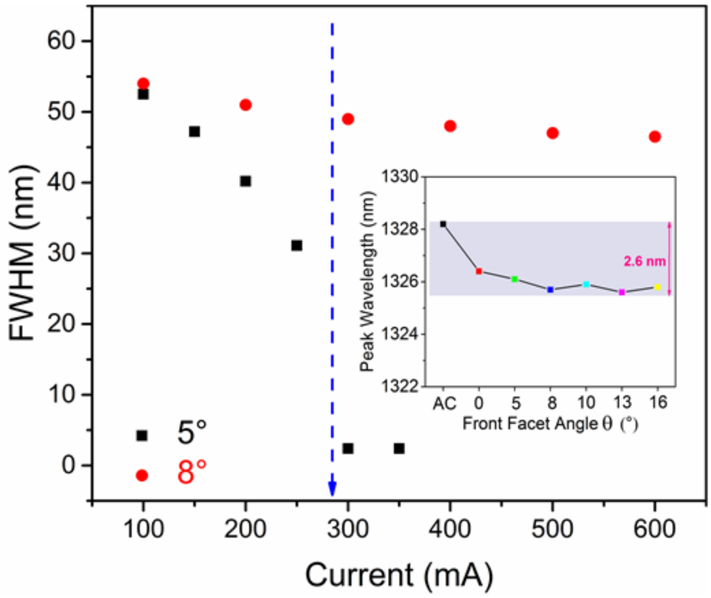

Figure 4.11 Measured FWHM for devices with 5° and 8° facet angles as a function of injection current. Inset shows the evolution of the peak wavelength (measured at 300 mA) for Si-based QD devices versus the etched facet angle [9].

The plotting curve of the peak wavelength (measured at 300 mA) against the front facet angle θ is demonstrated in Figure 4.11. It can be clearly seen that the peak wavelength of the Si-based QD device remains almost unchanged at ~1326 nm with different etched angles; in some cases, the device behaviour is even changed significantly. This result indicates that the FIB technique is a powerful tool for the semiconductor post-fabrication and prototype test; it allows direct and flexible modification of existing photonic devices without severely damaging the device performance and maintaining desired communication wavelengths.

A rate equation model of the facet angle cutting studies has been developed by researchers from Sheffield University [9]. According to Fresnel equations [23], the angle of the reflected light by the tilted laser facet can be calculated, as shown in Figure 4.12 (a):

$$n_1 sin\theta_i = n_1 sin\theta_r = n_2 sin\theta_t \qquad \text{Equation 4.1}$$

And the reflectivity for the parallel polarization (R_p) and perpendicular polarization (R_s) are:

$$R_p = \frac{tan^2(\theta_i - \theta_t)}{tan^2(\theta_i + \theta_t)} \qquad \text{Equation 4.2}$$

$$R_s = \frac{sin^2(\theta_i - \theta_t)}{sin^2(\theta_i + \theta_t)} \qquad \text{Equation 4.3}$$

where n_1 and n_2 is the refractive index of two different media of the interface; θ_i, θ_r and θ_t are angles of the incident light, reflection light and transmission light.

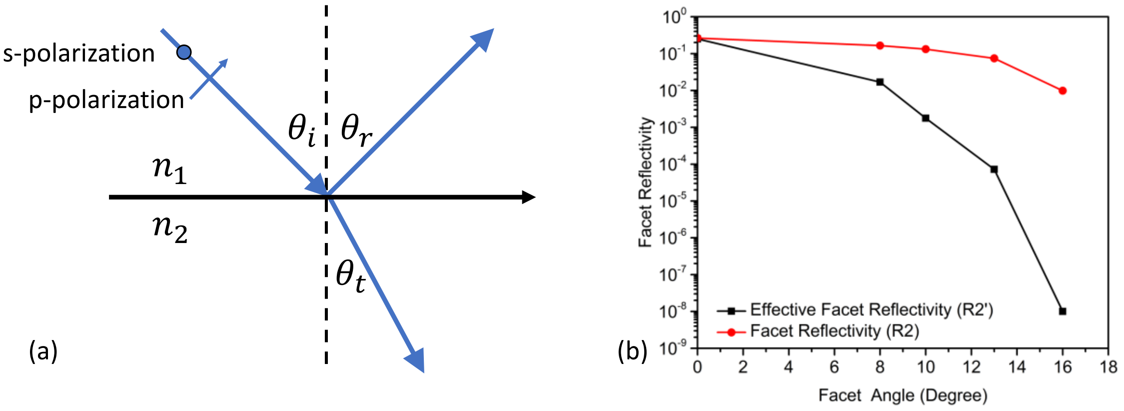

Figure 4.12 (a) Reflection and transmission of an incidence light at an interface. (b) The calculated facet reflectivity and effective facet reflectivity as a function of facet angle [9].

For the FP cavity, most of reflected light into the cavity is by parallel polarization; thus the angled facet reflectivity can be calculated by Equation 4.1 and 4.2. Figure 4.12 (b) shows the calculated facet reflectivity R2 as a function of facet angle.

Moreover, in order to calculate the reflected light intensity that is coupled back into the waveguide, we need to calculate a coupling factor, taking the waveguide mode profiles into account. This can be done theoretically using the overlap integral method [30]. Figure 4.13 demonstrates a model for reflectivity calculation.

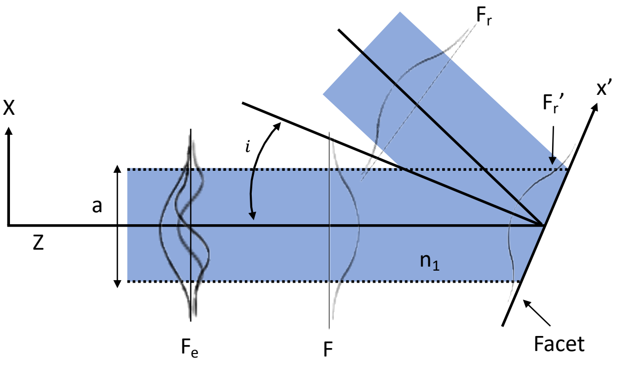

Figure 4.13 Model for reflectivity calculation.

A incident wave field F is expressed by sinusoidal function in the waveguide region, the fundamental reflected mode F_r and excited fields F_e are expressed by equations [30]:

$$F_r = F_r'(x')e^{-j\beta_z x' sin\ \theta_i} \qquad \text{Equation 4.4}$$

$$F_e = F_e'(x')e^{-j\beta_z x'\, sin\,\theta_i} \qquad \text{Equation 4.5}$$

where x' is coordinate of facet, β_z is the propagation constant in the z direction. $F_r'(x')$ is the mode function of the reflected mask at the facet, which only includes cos function for fundamental mode. $F_e'(x')$ has sin for odd modes and cos for even modes. The term $e^{-j\beta_z x' \sin\ \theta_i}$ is the phase distribution across the tilted facet. Therefore, the coupling factor (effective facet reflectivity) can be calculated from the overlap integral [30]:

$$R2' = \left|\int_{-\infty}^{\infty} F_r^* F_e dx'\right|^2 / (\int_{-\infty}^{\infty} |F_r|^2 dx' \int_{-\infty}^{\infty} |F_e|^2 dx') \qquad \text{Equation 4.6}$$

In practice, a further reduction of coupling will occur as a result of the facet roughness caused by material re-deposition. In our work, we have optimized the value of the effective facet reflectivity (R2') to obtain the best fitting results during the modelling [9]. As shown in Figure 4.12 (b), the increased difference between R2 and R2' suggests the coupling coefficient to guided modes is significant reduced with increasing facet angles, which contributes to the suppression of lasing. According to the R2', we have adopted the effective mirror loss as:

$$\alpha_m' = \frac{1}{2L} ln\,(\frac{1}{R1R2'}) \qquad \text{Equation 4.7}$$

Using this parameter, the carrier and photon dynamics for this tilted facet device is described by the following equations:

$$\frac{dN}{dt} = \eta_i \frac{I}{qV} - (AN + BN^2 + CN^3) - v_g \Gamma g N_p \qquad \text{Equation 4.8}$$

$$\frac{dN_p}{dt} = v_g \Gamma g N_p + \beta B N^2 - v_g(\alpha_i + \alpha'_m)N_p \qquad \text{Equation 4.9}$$

where N and N_p are the carrier and photon densities respectively, A is the defect recombination coefficient, B is the spontaneous emission coefficient, C is the Auger recombination coefficient, Γ is the optical confinement factor, v_g is group velocity of light, V is the volume of the active region, η_i is the internal efficiency, α_i is the internal optical loss, and β is the spontaneous emission factor.

Figure 4.14 shows the simulated results of L-I curves by the rate equation compared with the measured results. A good agreement is found between the simulation and actual measurement for all facet angles at low injection current. The obvious mismatched data after 300 mA injection current is due to the thermal effects in the ASE device. When the device is biased at high injection, the abundant non-radiative recombination produces heat within the device [24]. This self-heating tends to increase the thermal escapes of carriers and reduce the maximum modal gain of materials [25]. Moreover, dynamic thermal resistance is also an important effect causing the severer thermal roll-off at high injection current [26].

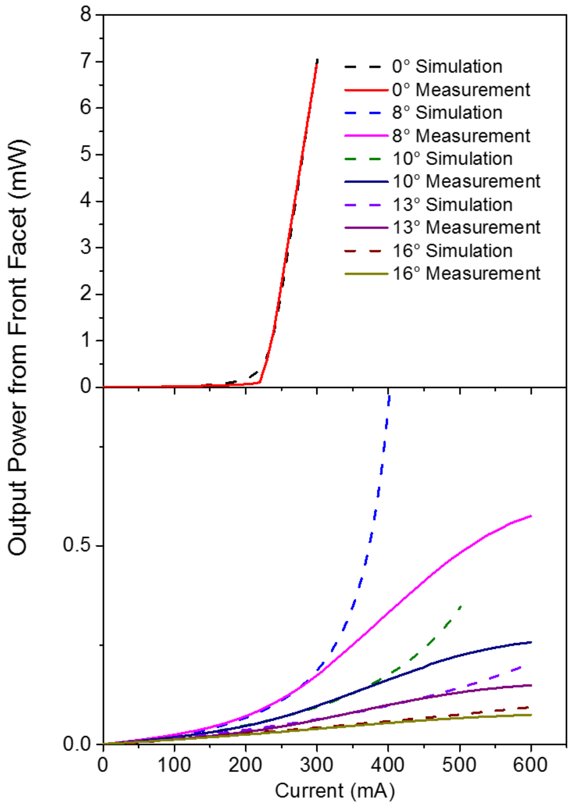

Figure 4.14 Comparison of simulated and measured L-I curves of QD laser device with different facet angles.

4.3.2 Groove etching for multi-section device

Figure 4.15 (a) shows the SEM image of the first shallow groove with 1 µm depth and 1.3 µm width. Although several residuals were left on the sidewall and bottom of the trench, a quite uniform and smooth sidewall was obtained by FIB milling. The purpose of this shallow etch is to create electrical isolation; 2.5 MΩ resistance between the adjacent contacts was obtained by this shallow trench, as shown in Figure 4.15 (b).

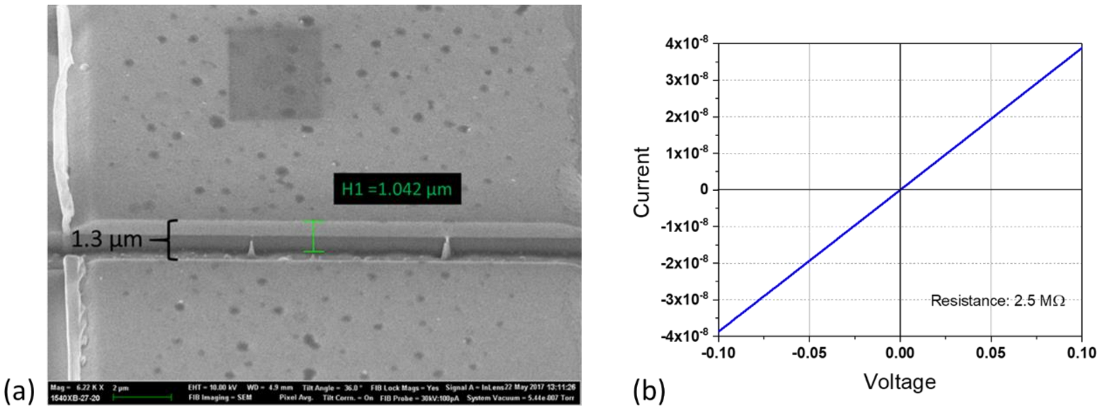

Figure 4.15 (a) SEM image of the groove with 1.04 µm depth and 1.3 µm width on QD laser on Si substrate. (b) I-V curve of the adjacent p-type contact by the etched groove with a resistance of 2.5 MΩ.

An SEM image of the deep trench etching is shown in Figure 4.16. It should be noted that the width of the groove narrows from 1.3 µm to 1.26 µm during the deep etching (Figure 4.17 (a)). This phenomenon can be explained by the re-deposition while creating the features of high aspect ratio (deep narrow trenches) [27]. During the deep etching, the sputtering materials are re-deposited on the sidewall (Figure 4.17 (b)) of the groove rather than being removed by the vacuum system. This re-deposition degrades the facet quality, but the issue can be solved by etching the trenches with low aspect ratio [27] or gas-enhanced etching [28] to help the sputtering contribution. The adjacent contact resistance for the deep etching groove was kept almost the same as the shallow etch.

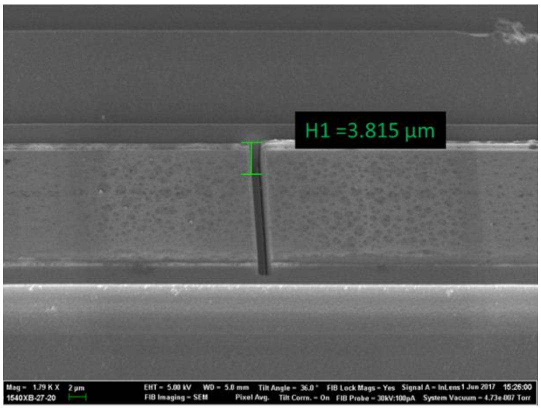

Figure 4.16 SEM image of the groove with 3.8 µm depth on QD laser on Si substrate with 36° tilted angle.

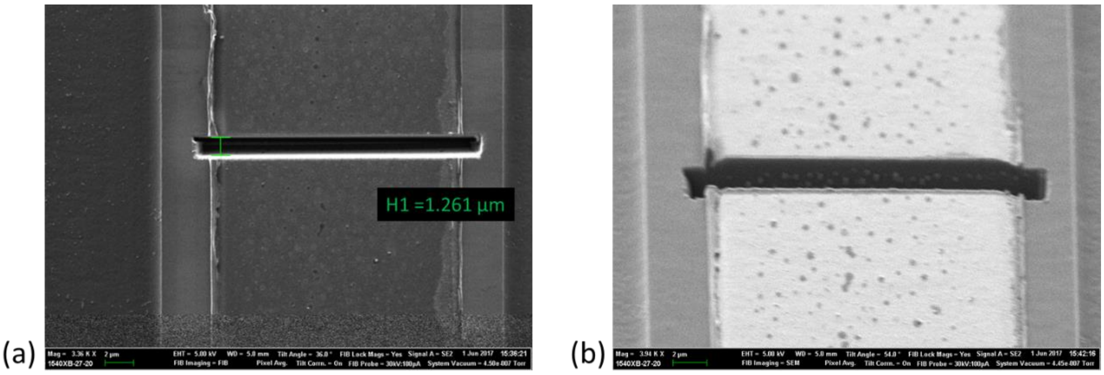

Figure 4.17 (a) SEM image of the deeper groove narrowing from 1.3 µm to 1.26 µm due to the re-deposition. (b) SEM showing re-deposition on the sidewall.

Figure 4.18 (a) compares the L-I curves of the laser device before and after the FIB milling with different depth grooves. For the devices with grooves, the injection current was pumped to the long section by the pulsed-wave operation. The photodetector was measured from the short section. The measured threshold current density and output power were 400 A/cm^2 and 10.8 mW before the FIB milling. The two-section device with 1 µm depth groove was also measured with a threshold current of 560 A/cm^2 and 4.6 mW output power. For the shallow groove, the interface between the long section and short section offers weak reflection and strong transmission [29]. In this case, most of the photons which were generated in the long cavity section were coupled into the short section with a small reflection rate. The unbiased 0.5 mm section can be treated as an absorber, as it absorbs part of the light in the cavity and increases the internal loss α_i due to the overlapped gain and absorption spectra between the short and long section. According to the threshold gain g_{th} equation,

$$g_{th} = \frac{1}{2L} ln\left(\frac{1}{R_1 R_2}\right) + \alpha_i \qquad \text{Equation 4.10}$$

The increased α_i causes higher threshold gain and threshold current density, as well as reduced output power.

Figure 4.18 (b) shows the L-I curve of the two-section device with a deeper trench; the output power is dramatically decreased to ~0.25 mW, and the threshold current density is increased to ~653 A/cm^2. The reason for this device degeneration can be explained as follows. The resonant cavity of the laser device was reduced from 3.5 mm to 3 mm, and also one of the laser mirrors was becoming to the etched sidewall of the trench. Thus, the mirror loss was increased due to the re-deposition of the sputtering material on the sidewall. When the device was biased in the long section, the light was generated and oscillated between the etched facet and the end facet in the long section cavity. Due to the low coupling efficiency of the etched trench and light absorption by the unbiased short section, only a small amount of lasing (~0.25 mW) could be measured from the facet of the short section.

In order to study the integration of the laser device with the EA modulator on the same substrate, high coupling efficiency and low transmission loss are required when the modulator is biased at 0 V. For this situation, and a shallow etched groove is a better choice. However, the shallow groove still shows a significant power loss due to the same bandgap energy of the two sections. Thus, the technique for reducing the cavity loss in multiple-bandgap material will be discussed in Chapter 5.

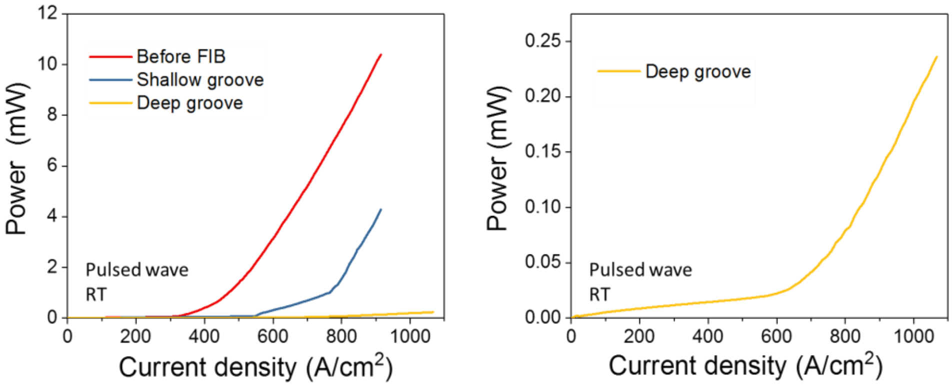

Figure 4.18 (a) Comparison of L-I curves for the laser device before FIB and with different depth grooves under pulsed-wave operation at RT. (b) L-I curve for the device with 3.8 µm depth groove at a larger scale.

4.4 Conclusion

In this chapter, the post-fabrication study of Si-based III–V QD lasers for other applications using Ga^+ ion beam FIB for Si photonics is reported. The high performance of an RT CW InAs/GaAs QD laser device on Si was achieved by a FIB milled facet. By gradually increasing the etched front facet angle of the laser device using the FIB technique, a Si-based QD SLD with CW operation at RT has been realised for the first time. This achievement demonstrates that reliable electrical pumped light-emitting sources, such as laser devices and SLDs as well as SOAs, directly grown on Si could be achieved by the etched facet. Secondly, a comparison study of a groove to separate a laser device into two independent sections by FIB is introduced. By changing the depth of the groove, the threshold current density and output power of the device could be compared. A shallow etched groove with a higher coupling coefficient is desirable for the integration of lasers with EA modulators in future work. Once the angle of facet for SOA and dimension of the groove for multi-section device have been optimized, the standard photolithography and wet/dry etching will be implemented for large volume manufacture.

4.5 Contribution Statement

I would like to acknowledge the research help including, the supply of the QD sample by Dr Mingchu Tang and Prof. Huiyun Liu, the assistance of FIB etching by Dr Suguo Huo, and the contribution of the simulation of laser performance by Mr Si Chen, and Dr Chaoyuan Jin at the University of Sheffield.

4.6 Reference

[1] S. Lourdudoss, “Heteroepitaxy and selective area heteroepitaxy for silicon photonics,” *Curr. Opin. Solid State Mater. Sci.*, vol. 16, no. 2, pp. 91–99, Apr. 2012.

[2] J. Yang and P. Bhattacharya, “Integration of epitaxially-grown InGaAs/GaAs quantum dot lasers with hydrogenated amorphous silicon waveguides on silicon,” *Opt. Express*, vol. 16, no. 7, p. 5136, Mar. 2008.

[3] S. A. Sobhani *et al.*, “Proposal for common active 1.3-µm quantum dot electroabsorption modulated DFB laser,” *IEEE Photonics Technol. Lett.*, vol. 31, no. 6, pp. 419–422, Mar. 2019.

[4] L. A. Coldren, G. A. Fish, Y. Akulova, J. S. Barton, L. Johansson, and C. W. Coldren, “Tunable Semiconductor Lasers: A Tutorial,” *J. Light. Technol.*, vol. 22, no. 1, pp. 193–202, Jan. 2004.

[5] L. Coldren, K. Furuya, B. Miller, and J. Rentschler, “Etched mirror and groove-coupled GaInAsP/InP laser devices for integrated optics,” *IEEE J. Quantum Electron.*, vol. 18, no. 10, pp. 1679–1688, Oct. 1982.

[6] G. Meneghini *et al.*, “CH4/H2 RIE of InGaAsP/InP materials: An application to DFB laser fabrication,” *Microelectron. Eng.*, vol. 21, no. 1–4, pp. 321–324, Apr. 1993.

[7] Y. Wang *et al.*, “Monolithic quantum-dot distributed feedback laser array on silicon,” *Optica*, vol. 5, no. 5, p. 528, May 2018.

[8] S. Thomas and S. W. Pang, “Dry etching of horizontal distributed Bragg reflector mirrors for waveguide lasers,” *J. Vac. Sci. Technol. B Microelectron. Nanom. Struct.*, vol. 14, no. 6, p. 4119, Nov. 1996.

[9] M. Liao *et al.*, “Monolithically integrated electrically pumped continuous-wave III-V quantum dot light sources on silicon,” *IEEE J. Sel. Top. Quantum Electron.*,

vol. 23, no. 6, art no. 1900910, Nov. 2017.

[10] H. D. Kim, S.-G. Kang, and C.-H. Le, “A low-cost WDM source with an ASE injected Fabry-Perot semiconductor laser,” *IEEE Photonics Technol. Lett.*, vol. 12, no. 8, pp. 1067–1069, Aug. 2000.

[11] J. S. Lee, Y. C. Chung, and D. J. DiGiovanni, “Spectrum-sliced fiber amplifier light source for multichannel WDM applications,” *IEEE Photonics Technol. Lett.*, vol. 5, no. 12, pp. 1458–1461, Dec. 1993.

[12] Q. Hu, C. Yu, and H. Kim, “5-Gb/s upstream transmission using an RSOA seeded by ultra-narrow spectrum-sliced incoherent light,” *Opt. Fiber Technol.*, vol. 21, pp. 137–140, Jan. 2015.

[13] D. Huang *et al.*, “Optical coherence tomography,” *Science*, vol. 254, no. 5035, pp. 1178–1181, Nov. 1991.

[14] W. T. Tsang, N. A. Olsson, and R. A. Logan, “High-speed direct single-frequency modulation with large tuning rate and frequency excursion in cleaved-coupled-cavity semiconductor lasers,” *Appl. Phys. Lett.*, vol. 42, no. 8, pp. 650–652, Apr. 1983.

[15] E. U. Rafailov, M. A. Cataluna, and W. Sibbett, “Mode-locked quantum-dot lasers,” *Nat. Photonics*, vol. 1, no. 7, pp. 395–401, Jul. 2007.

[16] Z. Mi, J. Yang, P. Bhattacharya, G. Qin, and Z. Ma, “High-performance quantum dot lasers and integrated optoelectronics on Si,” *Proc. IEEE*, vol. 97, no. 7, pp. 1239–1249, Jul. 2009.

[17] Q. Y. Lu *et al.*, “Analysis of slot characteristics in slotted single-mode semiconductor lasers using the 2-D scattering matrix method,” *IEEE Photonics Technol. Lett.*, vol. 18, no. 24, pp. 2605–2607, Dec. 2006.

[18] F. I. Allen *et al.*, “Gallium, neon and helium focused ion beam milling of thin films demonstrated for polymeric materials: study of implantation artifacts,” *Nanoscale*, vol. 11, no. 3, pp. 1403–1409, 2019.

[19] J. Schrauwen, D. Van Thourhout, and R. Baets, “Iodine enhanced focused-ion-beam etching of silicon for photonic applications,” *J. Appl. Phys.*, vol. 102, no. 10, p. 103104, Nov. 2007.

[20] S. Chen *et al.*, “Hybrid quantum well/quantum dot structure for broad spectral bandwidth emitters,” *IEEE J. Sel. Top. Quantum Electron.*, vol. 19, no. 4, pp. 1900209–1900209, Jul. 2013.

[21] L. H. Li, M. Rossetti, A. Fiore, L. Occhi, and C. Velez, “Wide emission spectrum from superluminescent diodes with chirped quantum dot multilayers,” *Electron. Lett.*, vol. 41, no. 1, pp. 41-43, 2005.

[22] K. J. Zhou *et al.*, “Quantum dot selective area intermixing for broadband light sources,” *Opt. Express*, vol. 20, no. 24, p. 26950, Nov. 2012.

[23] A. Lvovsky, “Fresnel Equations,” in *Encyclopedia of Optical Engineering*, New York: Taylor and Francis, 2013, pp. 1–6.

[24] J. Piprek, J. K. White, and A. J. SpringThorpe, “What limits the maximum output power of long-wavelength AlGaInAs/InP laser diodes?,” *IEEE J. Quantum Electron.*, vol. 38, no. 9, pp. 1253–1259, Sep. 2002.

[25] T. Yukutake *et al.*, “Temperature dependence of gain characteristics in p-doped 1.3-µm quantum dot lasers,” in *IEEE 19th International Conference on Indium Phosphide & Related Materials*, 2007, pp. 563–566.

[26] Z. Zang, K. Mukai, P. Navaretti, M. Duelk, C. Velez, and K. Hamamoto, “Thermal resistance reduction in high power superluminescent diodes by using active multi-mode interferometer,” *Appl. Phys. Lett.*, vol. 100, no. 3, p. 031108, Jan. 2012.

[27] L. A. Giannuzzi, B. I. Prenitzer, and B. W. Kempshall, “Ion - Solid Interactions,” in *Introduction to Focused Ion Beams*, L. A. Giannuzzi and F. A. Stevie, Eds. Boston, MA: Springer, 2005, pp. 13–52.

[28] N. Takado *et al.*, “Chemically enhanced focused ion beam etching of deep grooves and laser-mirror facets in GaAs under Cl_2 gas irradiation using a fine nozzle,” *Appl.*

Phys. Lett., vol. 50, no. 26, pp. 1891–1893, Jun. 1987.

[29] L. A. Coldren, B. I. Miller, K. Iga, and J. A. Rentschler, “Monolithic two-section GaInAsP/InP active-optical-resonator devices formed by reactive ion etching,” *Appl. Phys. Lett.*, vol. 38, no. 5, pp. 315–317, Mar. 1981.

[30] G. A. Alphonse and M. Toda, “Mode coupling in angled facet semiconductor optical amplifiers and superluminescent diodes,” J. Light. Technol., vol. 10, no. 2, pp. 215–219, 1992.

Chapter 5

Selective area intermixing of QD laser on Si

5.1 Introduction

In the last chapter, we described the post-fabrication of Si-based QD lasers using the FIB technique for rapid prototype tests. By angled facet etching for ASE devices and trench etching for multi-section device, the feasibility of integrating laser devices with other components (such as EA modulator) has been demonstrated. However, as described in section 1.4, to realise a monolithically integrated photonic circuit, the ability to engineer the bandgap across the wafer spatially is one of the critical points to reduce optical loss during the transmission [1]. Different components have different bandgap shifting requirements. For example, to achieve a low-loss III-V waveguide integrated with lasers or detectors, the bandgaps of the waveguide needs to be above the photon energy as far as possible to minimise the band edge absorption [2]. In contrast, when it comes to the specific application, EA modulated laser, the residual band edge absorption is the key factor. In other words, the EA modulator requires a variable absorption coefficient by a reverse voltage bias to achieve the acceptable extinction ratio for the on-off signals [3]. The bandgap of the modulator region needs to be larger than the laser region; thus, the photons emitted from the laser can be propagated with less absorption for the “on” signals. When the reverse bias is applied to modulator section, the bandgap of material will have a redshift (reduced bandgap energy) due to the QCSE [3][4], as shown in Figure 5.1. This redshift compensates the bandgap difference between the laser and modulator section; thus, an increased absorption coefficient causes the “off” signals. Therefore, the required bandgap difference for the EA-modulated laser depends on the bandgap tuning by the QCSE. According to the QCSE studies of the QD structure, the Stark peak shift can be up to 35 meV (45 nm) by the reverse bias [5]–[7]. For this propose, the method of achieving the multiple bandgap QD materials is studied in this chapter.

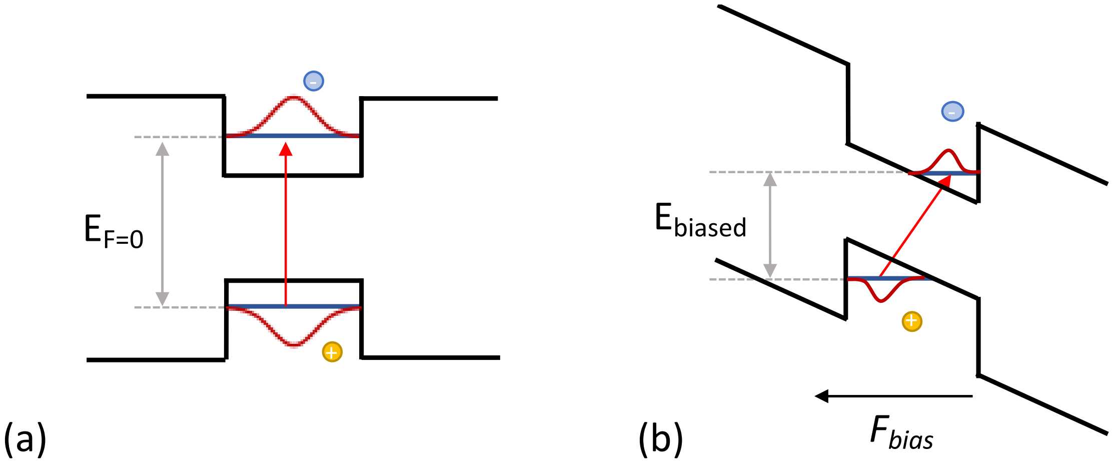

Figure 5.1 (a) Bandgap diagram with no electrical field (b) red shift of bandgap energy via the Quantum confined Stark effect.

In general, multiple bandgaps can be approached by two methods: selective area epitaxial regrowth or intermixing techniques [8]. The intermixing approach by rapid thermal annealing (RTA) is a relatively simple approach compared with the regrowth method and is widely used in modifying the wavelength of materials, either for QWs [8]–[10] or QDs [11]–[13]. Among the various intermixing methods, impurity-free vacancy disordering assisted by dielectric layers is particularly attractive for optical integrated circuit fabrication, because it does not involve the introduction of extra impurities or damage [1]. The dielectric layers, which are deposited on top of the III–V epitaxy layers, play an important role in controlling the intermixing levels by their different thermal expansion coefficients. As shown in Figure 5.2 (a), a thin layer of SiO_2 with a thermal expansion coefficient of 0.52×10^{-6} $°C^{-1}$ has been shown to produce a significant enhancement of the intermixing when it was capped on an InAs/GaAs QD structure [13]. The SiO_2 layer is deposited by PECVD at high temperatures, such as 350 °C. Due to the thermal expansion coefficient mismatch between GaAs ($\sim6.5\times10^{-6}$ $°C^{-1}$) and SiO_2, the GaAs is shrinking more than SiO_2, when the wafer is cooled down to the room temperature. Thus, a compressive strain is produced at the interface of GaAs/SiO_2. This compressive strain tends to create atom vacancies at the interface, and Ga atoms are migrated into the SiO_2 cap during the thermal process. In the InAs/GaAs QD structure, the Ga migration is diffused through the III–V epi-structures and cause the intermixing process of InAs QD with the surrounding capping layer (InGaAs or GaAs) at the active region. The reduced In the composition of QD thus causes a significant blue shift. In comparison with SiO_2, the TiO_2 layer has a much larger thermal expansion coefficient of $\sim8.2\times10^{-6}$ $°C^{-1}$ than GaAs, and a tensile strain at the interface will restrict Ga migration produced during RTA, thus suppressing the inter-diffusion rate [14] (Figure 5.2 (b)). Therefore, the multiple bandgaps of III–V QD materials could be achieved by laterally patterning SiO_2 and TiO_2 on top before the RTA process to provide a selective area intermixing technique. Using this technique, we can intentionally engineer the bandgap for individual photonic devices, such as QD lasers, EA modulators and low-loss waveguides, all monolithically integrated on the same platform. Although there are significant pioneering works on selective area intermixing for QD materials on native substrates [13][14], the intermixing effect of III–V QDs monolithically grown on Si substrate, which may become more complicated due to the high-density of defects involved, has not been reported previously. In additional to the higher density of defects, another concern is the larger thermal mismatch between GaAs and Si, as mentioned in section 1.2.2. The ultrahigh temperature RTA for the intermixing, which is much higher than the epitaxy growth temperature, may aggravate the thermal crack issue according to Equation 1.2. However, this issue is not discussed in this project and will be investigated to find the solution in the future.

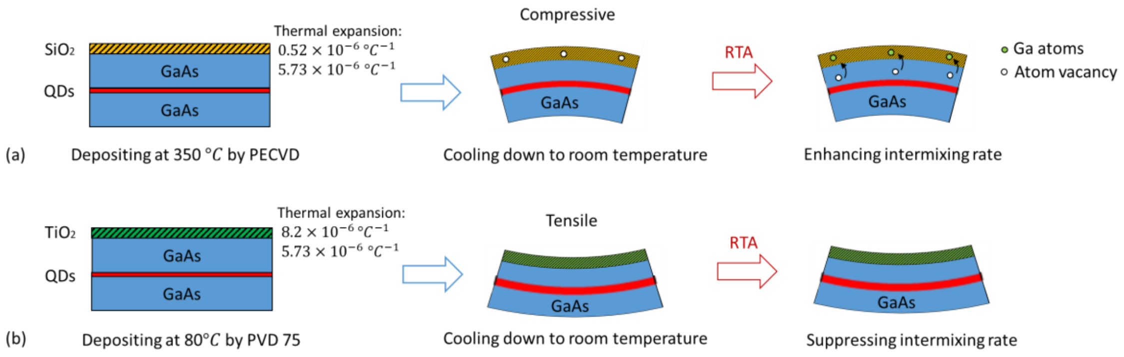

Figure 5.2 Schematic diagrams of InAs/GaAs QD intermixing by dielectric layers of (a) SiO_2 and (b) TiO_2.

In this chapter, we first report on a comparative study of the intermixing effect in InAs/GaAs QDs directly grown on Si capped by separated SiO_2 and TiO_2 layers, to determine the optimal thermal annealing conditions. A detailed analysis of annealed QDs with different temperatures of the two capping layers, in terms of physical shape, sizes and size distributions, has been performed using high-resolution aberration (C_s)-corrected scanning transmission electron microscopy (STEM). Based on the optimised annealing conditions from each individual study, different bandgaps of III–V QD structure material can be realised using the selective area intermixing technique. Thus, electrically pumped InAs/GaAs QD lasers directly grown on Si with two different emission wavelengths of 1275 nm and 1313 nm have been fabricated from this thermally processed wafer, showing that this selective area intermixing technology can be used in optical integrated circuits for Si photonics without severe degeneration of the QD material quality.

5.2 Experimental methods

5.2.1 Optimisation of RTA conditions for SiO_2- and TiO_2-capped samples

In this work, as shown in Figure 5.3 (a), the III–V QD structure was grown by the MBE system on n-doped Si (001) substrate with an oriented offcut of 4° towards the [110] direction. After a 1000 nm GaAs buffer layer and three layers of five periods of InGaAs/GaAs SLSs as DFLs, the TD density was reduced from the order of 10^9 cm^{-2} to the order of 10^7 cm^{-2}. To gain a better understanding of the emission properties of the QDs from PL measurement, very thin AlGaAs upper and lower cladding layers of 100 nm were used for this test sample. In the active region, five layers of unintentionally-doped DWELL structure were grown, separated by 50 nm GaAs spacer layers. Each DWELL layer consisted of a 2 nm InGaAs wetting layer, 3 ML InAs QDs and a 6 nm InGaAs capping layer (Figure 5.3 (b)). On top of the sample, uncapped 3 ML InAs QDs were grown for QD density measurement using AFM. Figure 5.3 (b) shows the AFM image of QD density, which is around 3×10^{8} cm^{-2}. The doping levels for each layer have been labelled in Figure 5.3. It should be noted that the wafer sample in this study is unoptimised, and shows a relatively high defect density and low QD density.

Before the thermal annealing process, the sample was cleaved into two and capped with a 200 nm SiO_2 film by the PECVD at 350 ℃ and 200 nm TiO_2 film by a thin film deposition system (Kurt J. Lesker PVD75 [15]) at 80 ℃, respectively. The two samples were then cleaved into many pieces for further comparative studies. For the SiO_2-capped samples, an RTA duration study was implemented for 0, 5, 30 and 60 s at 700 ℃. Based on the optimal annealing duration for a significant blue shift and undegraded optical emission, different annealing temperatures of 700, 725, 750, 775 and 800 ℃ were then trialled. The annealing temperature study for TiO_2-capped samples was then executed at 700, 725, 750 and 775 ℃. PL measurements of each as-grown and annealed sample were conducted under excitation using a solid-state laser of wavelength 532 nm at RT.

In this work, high angle annular dark-field (HAADF) STEM images were obtained using a C-FEG JEOL R005 double aberration-corrected TEM/STEM operating at 300 kV accelerating voltage. Comparing with other TEM imaging techniques, the HAADF provides more information of atomic species and number within the specimen [16], for a better understanding of the effect of intermixing on the InAs QDs with the surrounding matrix.

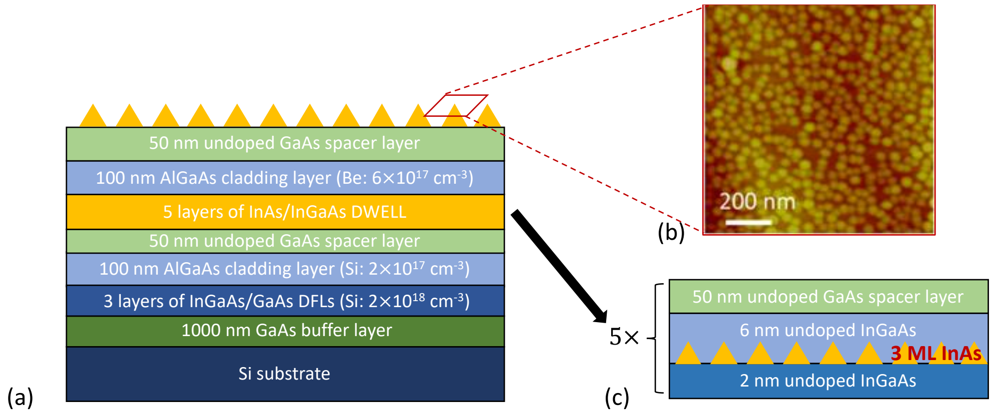

Figure 5.3 (a) Schematic diagram of InAs/GaAs DWELL grown on Si with thin cladding layers. (b) AFM image of the top uncapped QDs with a dot density of 3×10^{8} cm^{-2}. (c) Epitaxial structure of a DWELL layer.

5.2.2 Selective area intermixing and laser device fabrication

For selective area intermixing, the real laser structure of InAs/GaAs QDs on Si substrate was grown, as shown in Figure 5.4 (a). The epitaxy layers and growth method were identical to the previous test sample (Figure 5.3 (a)), except for the two thick cladding layers of 1.5 µm and a highly doped (Be: 1×10^{19} cm^{-3}) 300 nm GaAs contact layer on the top. A quarter of the 2-inch wafer was then covered by 200 nm thickness SiO_2 and TiO_2 thin film in equal parts, as shown in Figure 5.4 (b). A trade-off RTA condition of duration and temperature was applied from the previous optimisation studies for both SiO_2 and TiO_2 caps. After thermal annealing, PL mapping was executed to check the bandgap changes of the QD materials. The dielectric layers were then removed using hydrofluoric acid (HF) before further device fabrication. 25 µm width broad-area lasers were fabricated by standard photolithography, wet chemical etching and metallisation. Ti/Pt/Au and Ni/GeAu/Ni/Au were deposited for p-type and n-type ohmic contacts, respectively. The laser devices were then cleaved into 3 mm length cavities, without any facet coatings, and mounted on the copper heatsinks.

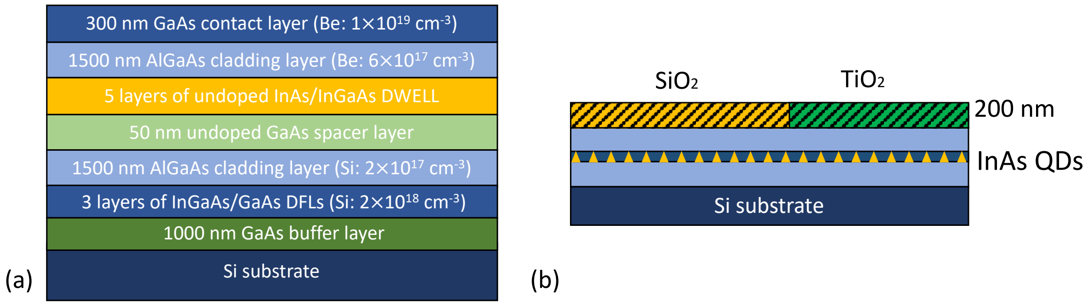

Figure 5.4 (a) Schematic diagram of the InAs/GaAs DWELL laser structure. (b) Schematic diagram of a cross-section of SiO_2 and TiO_2 dielectric layer on III–V/Si DWELL for selective area intermixing.

5.3 Results and discussion

5.3.1 SiO_2 capping

- **PL spectra analysis**

Figure 5.5 (a) shows the RT PL spectra of the intermixing duration study of the DWELL structure capped by SiO_2 for as-grown, 5 s, 30 s and 60 s RTA. The inset of Figure 5.5 (a) shows the PL peak intensity as a function of the annealing duration, showing an increase with longer annealing time and reaching the maximum point when the duration is 30 s. The increased PL intensity is mainly contributed to by the reduced TD density after the high RTA. The high-temperature annealing enhances the mobility of dislocations and increases the probability of interaction and self-annihilation of the TDs [17]. Moreover, the RTA also tends to increase the strain in the material, thus, resulting in varied carrier confinement of the QDs [18]. As a result, the combined effect of the reduced dislocations and the residual strain in and around QDs [19] leads to more distinct improvements in the different RTA conditions. As shown in Figure 5.5 (b), the peak wavelength of PL was decreased with increased annealing time. This small blue-shift is due to the inter-diffusion of In and Ga atoms between the interface of InAs QDs and GaAs barrier layers. The change of FWHM of PL for the duration study is also shown in Figure 5.5 (b); the FWHM is raised at first when the annealing time is 10 s, and then decreases with longer annealing times. The decreased FWHM indicates an improved QD size homogeneity when the annealing time is longer than 30 s. By considering the peak intensity, wavelength and

FWHM, an annealing time of 30 s was chosen for the subsequent annealing temperature study, as it shows a relatively larger blue-shift and peak PL intensity.

Figure 5.5 (c) shows the PL spectra of the annealing temperature study from 700 ℃ to 800 ℃ with 25 ℃ intervals for a 30 s annealing duration. At first, the PL intensity is increased and reaches the maximum point when the annealing temperature is 700 ℃; then it decreases gradually as the annealing temperature is increased further (inset of Figure 5.5 (c)). Although the RTA can help to reduce the TD density, higher annealing temperatures can degenerate the material quality, thus causing a dramatic PL intensity decline [20]. The high temperature also causes a bigger blue-shift of PL emission. A comparison of peak wavelengths at different temperatures is shown in Figure 5.5 (d). It should be noted that the PL spectra become broader when the annealing temperature is raised from 725 ℃ to 775 ℃. However, the linewidth narrows at a very high temperature of 800 ℃, as shown in Figure 5.5 (d). The broader linewidth accompanied by the large blue-shift is the contribution from an inhomogeneous diffusion of Ga atoms at relatively low annealing temperature [21]. Therefore, we presume that the RTA leads to a distinct change of emission peak and an increased linewidth at relatively low temperatures with a SiO_2 cap. At 800 ℃, the influence of annealing on the size distribution is more dominant. As a result, the FWHM reduces again, and the blue-shift of the PL spectrum becomes larger than that at other temperatures. This conclusion is further confirmed by our STEM observations.

The purpose of these studies is to find the most suitable RTA conditions, in terms of the annealing time and temperature, of the SiO_2-capped DWELL structure for a relatively large wavelength shift and an appropriate QD optical emission without serious material degradation. By considering results from both annealing time and temperature studies, RTA with 30 s duration at 725 ℃ causing a ~34 nm blue-shift in PL peak position and a ~15.9% increase in PL intensity is the most useful choice. This is the reference for further RTA studies of TiO_2-capped DWELL and selective area intermixing.

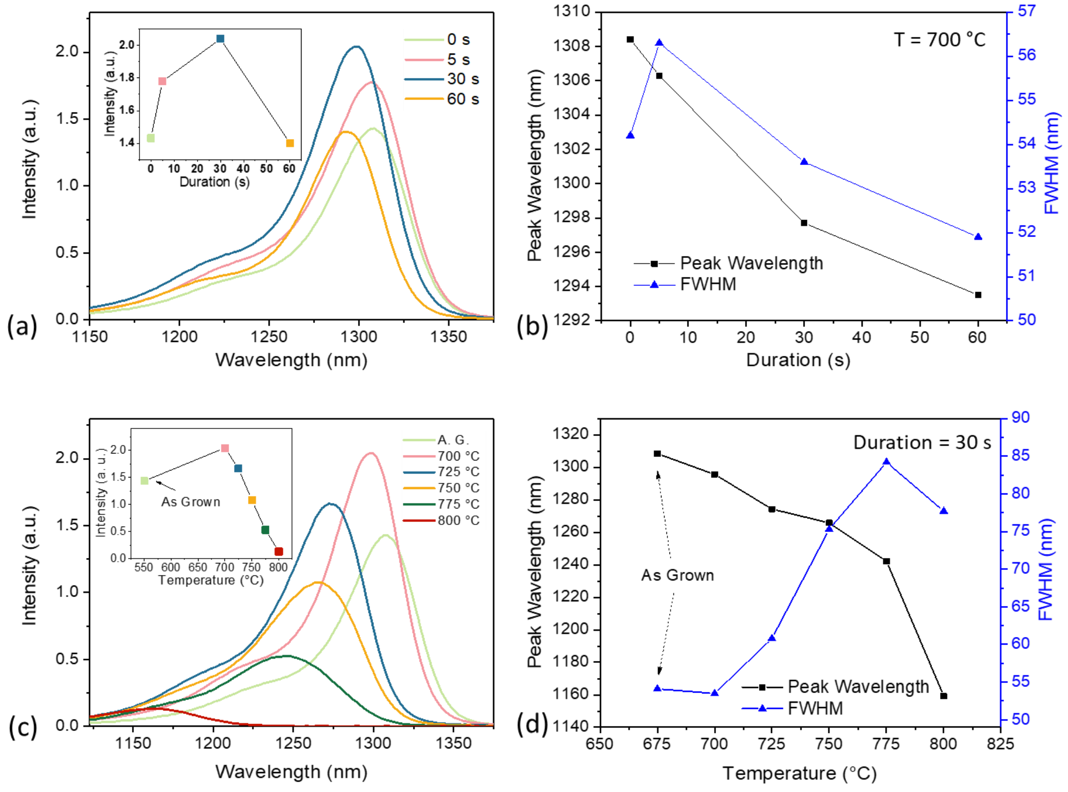

Figure 5.5 (a) PL spectra of SiO_2-capped InAs/GaAs DWELL structure grown on Si substrate with different duration times at 700 ℃. Inset: PL intensity against the annealing durations. (b) Plots of PL peak wavelength and FWHM against the annealing durations at 700 ℃. (c) PL spectra of SiO_2-capped InAs/GaAs DWELL structure grown on Si substrate with 30 s duration at different temperatures. Inset: the PL intensity against the annealing temperature. (d) Plots of PL peak wavelength and FWHM against the annealing temperatures with 30 s duration.

- **QD morphologic and size distribution analysis**

HAADF STEM images of as-grown and annealed specimens were obtained at relatively low magnification (at ~600 kX, for size distribution analysis) while detailed STEM images of individual QDs have been taken at high magnification (at ~4 MX) for comparison. By assuming only Rutherford scattered [22] electrons have been collected, the image contrast in the HAADF image is approximately proportional to the square of the effective atomic number (Z). In Z-contrast images, the contrast intensity appears brighter with higher Z value and darker with lower Z [16]. Therefore, it offers an insight into the relative local chemistry of the features.

Figure 5.6 (a) shows the HAADF STEM images for SiO$_2$-capped DWELL of the as-grown, 700 ℃ and 800 ℃ annealed samples and a corresponding schematic diagram of the morphological evolution. As the images show, QDs in the as-grown sample exhibit a sharp interface and inhomogeneous dot size. After 700 ℃ annealing, the interface between the QDs and the surrounding matrix became less distinct, possibly due to the thermal intermixing process. However, after 800 ℃ annealing, the QD uniformity significantly improved, with an increase in the average dot size.

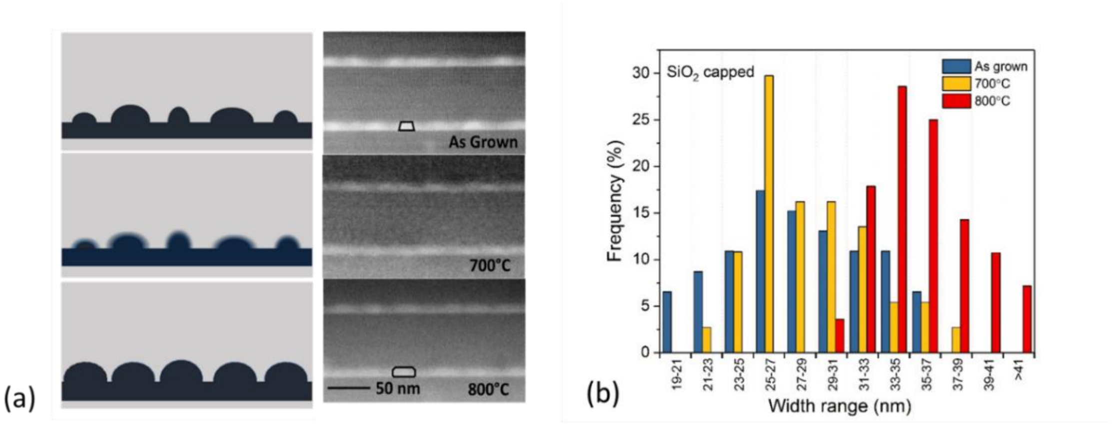

Figure 5.6 (a) C$_s$-corrected HAADF STEM images of SiO$_2$-capped DWELL as a function of annealed temperature and related schematic diagram. (b) Histogram of SiO$_2$-capped QD widths in as-grown, 700 ℃ annealed and 800 ℃ annealed samples.

Approximately 100 QDs were measured for each of the as-grown, 700 ℃ annealed and 800 ℃ annealed samples using HAADF imaging at ~600 k magnification to determine the width and height of the QDs. The widths and heights of the QDs were measured by drawing intensity line profiles across the HAADF images. Table 5.1 displays the widths, heights and height/width ratios of QDs in the as-grown, 700 ℃ and 800 ℃ annealed samples. The widths of QDs in the 700 ℃ and 800 ℃ annealed samples increase by 2.1% and 27.7%, respectively. On the other hand, the heights do not appear to change significantly, when measurement error is taken into consideration. This phenomenon would suggest that inter-diffusion predominates within the (100) plane rather than the [100] growth direction. Considering the theoretical QD geometries proposed in references [23][24], this means the ratio between the height *h* and the base length *b* is smaller after the post-growth annealing.

Table 5.1 Summary of the widths, heights and height/width ratios of SiO_2-capped QDs in as-grown, 700 ℃ and 800 ℃ annealed samples.

Sample	Width (nm)	Height (nm)	Height/width ratio
As-grown	28.2±4.4	8.8±1.0	0.31
700 ℃	28.8±3.7	9.0±0.8	0.31
800 ℃	36.0±3.3	9.5±0.9	0.26

A more detailed width distribution of QDs capped by SiO_2 is given by the histogram presented in Figure 5.6 (b). The standard derivation of the 100 QDs' size from the as-grown sample is around 4.4 nm. After the high-temperature thermal annealing, the standard derivation is decreased to 3.7 nm, and 3.3 nm from the 700 ℃ and 800 ℃ annealed samples, respectively. These results are evidence to support our previous assumption from the PL measurement. The decrease of the FWHM at 700 ℃ and 800 ℃ is due to the improved uniformity of the QD size distribution after the RTA.

Figure 5.7 shows a series of lattice-resolved HAADF STEM Z-contrast images (presented in false colour) of typical single QDs as a function of annealing temperature. The increased contrast brightness in the region of the QD reflects the higher mean atomic number due to the presence of indium. While the Z-contrast images are not specifically indium concentration maps, they highlight the changes in the QD morphology, which is likely to be associated with localised indium diffusion. The typical as-grown dot is ~25 nm in diameter. After 700 ℃ annealing, the image contrast became more uniform across the dot region, and the quantum dot size increased laterally. After 800 ℃ annealing, the lateral dot size further increased. It is important to note that although the overall aspect ratio appears to change as a function of annealing temperature, the basic shape morphology of QDs remains essentially the same.

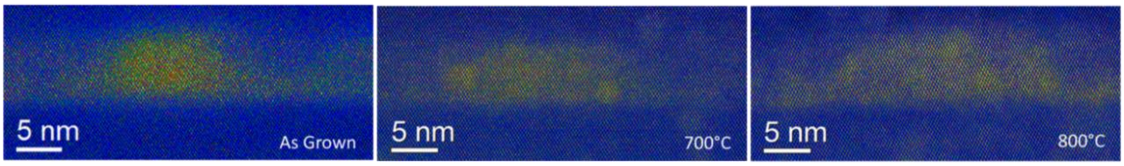

Figure 5.7 C_s-corrected high-resolution HAADF STEM images (shown in false colour) of a single QD of SiO_2-capped DWELL as a function of annealing temperature with 30 s duration.

5.3.2 TiO_2 capping

- **PL spectra analysis**

Due to the larger thermal expansion coefficient of TiO_2, the inter-diffusion rate inside of the TiO_2-capped DWELL structure is restricted during the RTA. Figure 5.8 (a) shows the comparison of the PL spectra between the as-grown and TiO_2-capped DWELL structures with 30 s annealing duration at different temperatures from 700 ℃ to 775 ℃. Since the annealing temperature of 800 ℃ is too high to maintain the material quality for the SiO_2 cap, this temperature is not employed in the following studies. The inset of Figure 5.8 (a) is the plot of the peak intensity of PL as a function of the annealing temperature. The peak intensity is first raised and reaches its maximum point at 700 ℃, then reduces as the temperature increases. The intensity trace of the TiO_2 cap is similar to the SiO_2 annealing temperature study, where an appropriate annealing temperature could enhance the self-annihilation of the dislocations, thus improving the PL intensity. As the temperature increases further, the material quality and QDs are degenerated or destroyed, gradually causing the PL intensity to drop. Compared with SiO_2-capped DWELL, TiO_2-capped DWELL shows a much smaller blue-shift under the same annealing conditions. As demonstrated in Figure 5.8 (b), the blue-shift of the TiO_2-capped DWELL structure is only ~6.4 nm by RTA for 30 s at 725 ℃ compared with 34 nm shift of SiO_2-capped sample. It should be noticed that, due to the existence of doped cladding layers around the DWELL region, the diffusion routes/atom vacancies are already present in the samples by the dopants [25]. The intermixing phenomenon will still appear by the RTA, even the samples are not covered by any dielectric materials. Therefore, the TiO_2 which provides the tensile strain is necessary to suppress this intermixing effect. Also, the FWHM has a slight decrease at temperatures up to 725 ℃ owing to the narrower size distribution of QDs.

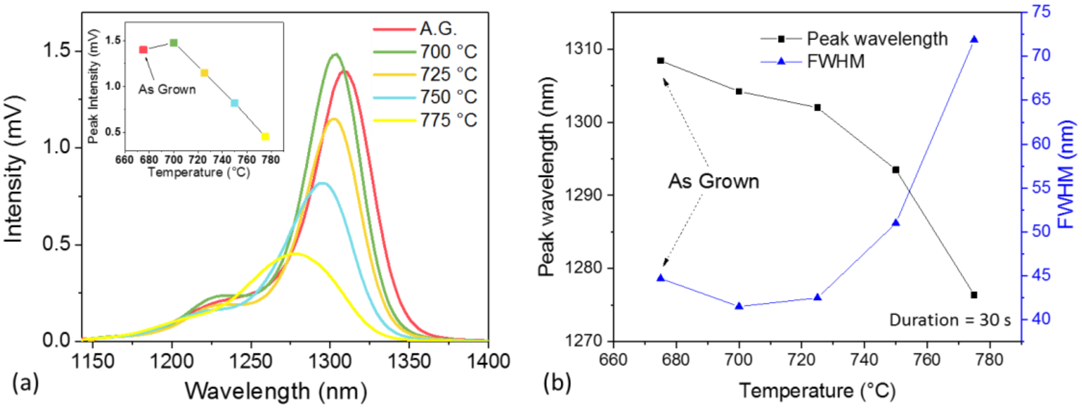

Figure 5.8 PL spectra of TiO_2-capped InAs/GaAs DWELL structure grown on Si substrate with 30 s duration RTA at different temperatures. Inset: PL intensity against the annealing temperatures. (b) Plots of PL peak wavelength and FWHM against the annealing temperatures with 30 s duration.

- **QD morphologic and size distribution analysis**

Figure 5.9 (a) shows the HAADF STEM images of the DWELL of the as-grown, 700 ℃ annealed and 775 ℃ annealed samples capped by TiO_2, with a corresponding schematic diagram of morphological evolution shown on the left-hand side. Compared with the SiO_2-capped DWELL, the QDs capped by TiO_2 still retained a sharp interface and inhomogeneous dot size even after 700 ℃ annealing. When the annealing temperature increased to 775 ℃, the surrounding matrix of dots became less distinct, and the average dot size was slightly increased due to the intermixing process at a very high temperature. This intermixing phenomenon happened at 700 ℃ for SiO_2-capped QDs, which proves that the TiO_2 with a larger thermal expansion coefficient could effectively restrict the intermixing process.

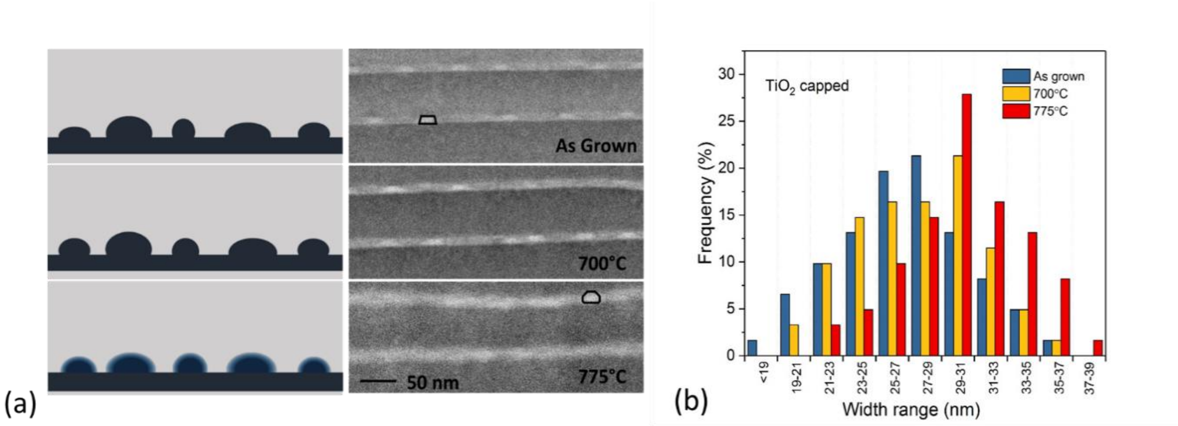

Figure 5.9 (a) HAADF STEM images of TiO_2-capped DWELL as a function of annealed temperature and related schematic diagram. (b) Histogram of TiO_2-capped QD widths in as-grown, 700 ℃ annealed and 775 ℃ annealed samples.

Table 5.2 shows the average size of QDs in width and height for as-grown, 700℃ and 775 ℃ annealed samples. The widths of TiO_2-capped QDs for 700 ℃ and 775 ℃ annealed samples are increased by 1.9% and 11.5%, respectively, compared with the as-grown sample. The error bars were calculated from the standard deviation, where the insignificant changes for different annealing temperature samples mean the size distribution of TiO_2-capped QDs for each sample remained almost the same. A detailed histogram of TiO_2-capped QDs widths in as-grown, 700 ℃ annealed and 775 ℃ annealed samples is shown in Figure 5.9 (b).

Table 5.2 Summary of the widths, heights and height/width ratios of TiO_2-capped QDs in as-grown, 700 ℃ and 800 ℃ annealed samples.

Sample	Width (nm)	Height (nm)	Height/width ratio
As-grown	26.9±3.9	8.7±0.8	0.32
700 ℃	27.4±3.8	8.8±0.8	0.32
775 ℃	30.0±3.4	9.0±0.9	0.3

The HAADF STEM Z-contrast images of typical QDs as a function of the annealing temperature are shown in Figure 5.10. The indium distribution of a single dot is highlighted with contrast brightness. For TiO_2-capped QDs, the image contrasts of the single QDs of the as-grown sample and the 700 ℃ annealed sample are almost unchanged. Only a slight indium diffusion happens at the edge of QDs at 700 ℃ annealing due to the intermixing process. After 775 °C annealing, the indium diffusion became more pronounced. Although it still retains a basic shape morphology, the dot lateral dimension increases further as with the SiO_2-capped QD annealed at temperatures above 700 °C. The TEM results are consistent with the observations from the PL measurements in Figure 5.8.

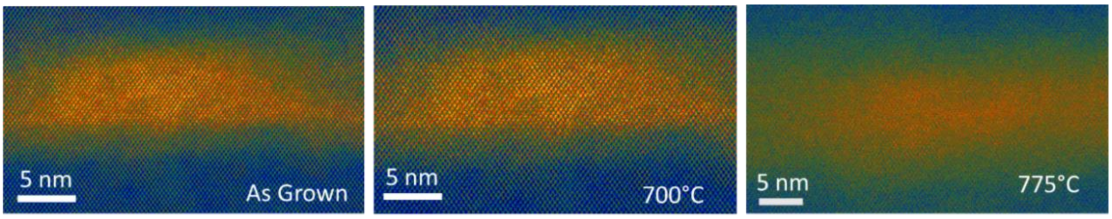

Figure 5.10 C_s-corrected high-resolution HAADF STEM images (shown in false colour) of a single QD of TiO_2-capped DWELL as a function of annealed temperature with 30 s duration.

5.3.3 Selective area intermixing and laser results

Based on the previous studies of the annealing conditions of SiO_2 and TiO_2 caps, the RTA process with 30 s duration at 725 °C was chosen for selective area intermixing. Figure 5.11 (a) and (b) compare the PL mapping of the peak wavelength for a QD wafer sample for as-grown and after the RTA with the SiO_2- and TiO_2-capped regions labelled. The small non-uniformity of the QDs in terms of the emission wavelength with a standard deviation of 1.49% is shown for the as-grown epitaxial sample, which is caused by the slight temperature variance (~10 °C) of the heating stage between the centre and outside during the MBE growth. The higher temperature in the stage centre increases the mobility of the In, causing smaller quantum dots and shorter wavelength. For the sample after the RTA, a clear square pattern could be found on the right side of the sample, which was covered by TiO_2. As expected from previous studies, the SiO_2-capped region shows a bigger wavelength shift in PL measurement compared with the TiO_2-capped region. In addition, an even larger wavelength shift and a reduced intensity were obtained on the edge of the SiO_2-capped region. It is likely that the RTA caused serious degradation of the material quality at the wafer edge. Figure 5.11 (c) and (d) show the comparisons of the PL spectra at the centres of SiO_2- and TiO_2-capped regions before and after RTA, respectively.

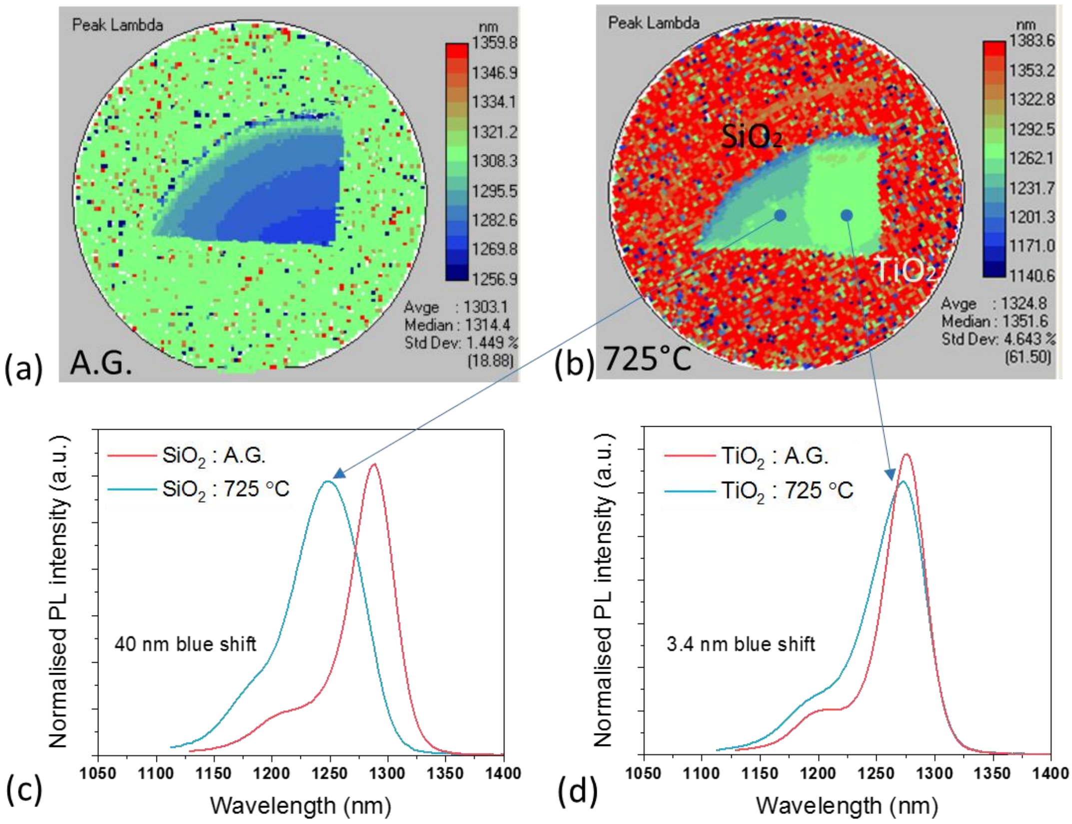

Figure 5.11 PL mappings of InAs/GaAs DWELL laser sample on Si for (a) as-grown and (b) selective area intermixing at 725 °C for 30 s. Comparison of PL spectra of InAs/GaAs DWELL laser sample before and after the RTA process in (c) SiO_2-capped region and (d) TiO_2-capped region.

Table 5.3 summarises the wavelength-dependent results of the PL spectra. There is a ~40 nm blue-shift of the wavelength in the SiO_2-capped region after RTA and only a ~3.4 nm peak wavelength shift in the TiO_2-capped region. This RTA introduces a broader linewidth of the PL spectra for both the SiO_2- and TiO_2-capped regions. The SiO_2 region has a bigger change in FWHM and a larger blue-shift compared with TiO_2. It should be noted that, compared with the test samples (Figure 5.3) in the previous studies, the real laser samples (Figure 5.4) have much thicker cladding layers and a highly doped contact layer of 1×10^{19} cm^{-3}. Although this high concentration of dopants does not play a role in enhancing the inter-diffusion rate, they provide diffusion routes as the point defects [12]. As the results, the intermixing effect of the real sample is even stronger than the test samples and also causing slight material degeneration from both the SiO_2- and TiO_2-capped wafers. More interestingly, the blueshift of our TiO_2-capped region is compatible with the pioneering works of InAs/GaAs QD selective area intermixing on the native substrate [13][14]. However, the blueshift (40 nm) of SiO_2 region of our DWELL on Si is generally smaller than reports in ref [13] and [14], which had demonstrated up to 100 nm wavelength shift. The possible reason for the reduced intermixing rate of the QD material grown Si, may relate to the thermal strain between the Si substrate and the grown III-V epi-layers. The thermal expansion coefficient of Si of 2.6×10^{-6} °C^{-1} is smaller than GaAs; therefore, this thermal mismatch may cause the reduced intermixing effect in SiO_2 region.

Table 5.3 Comparison of PL parameters, in terms of peak wavelength, intensity, FWHM and blue-shift, for SiO_2 and TiO_2-capped DWELL structure before and after RTA with 30 s duration at 725 ℃.

Sample	Peak wavelength (nm)	FWHM (nm)	Blue shift (nm)
SiO2: As-grown	1289.2	44.7	/
SiO2: 725 ℃	1249.3	72.5	40
TiO2: As-grown	1276.1	41.5	/
TiO2: 725 ℃	1272.7	57.4	3.4

Figure 5.12 shows the comparison of the lasing spectra of the Si-based QD laser devices fabricated by this thermally processed wafer. Two different lasing wavelengths indicating the SiO_2- and TiO_2-capped regions are shown, which gives ~ 37 nm lasing wavelength difference. The inset of Figure 5.12 is the light–current plots of the two different wavelength lasers under pulsed operation at RT with 1% duty cycle and 1 μs pulsed width. The measured threshold currents are 150 mA and 175 mA for the TiO_2-capped and SiO_2-capped region, respectively. The single output power and slope efficiencies are 10 mW (at 400 mA) and 0.0563 W/A for the TiO_2 region, and 7.23 mW (400 mA) and 0.0499 W/A for the SiO_2 region. The degraded device performance from the SiO_2-capped region is related to the material degeneration from the intermixing. The TiO_2 region material has less of an effect on the RTA compared with SiO_2 due to the suppressed inter-diffusion rate from the large thermal expansion coefficient of TiO_2.

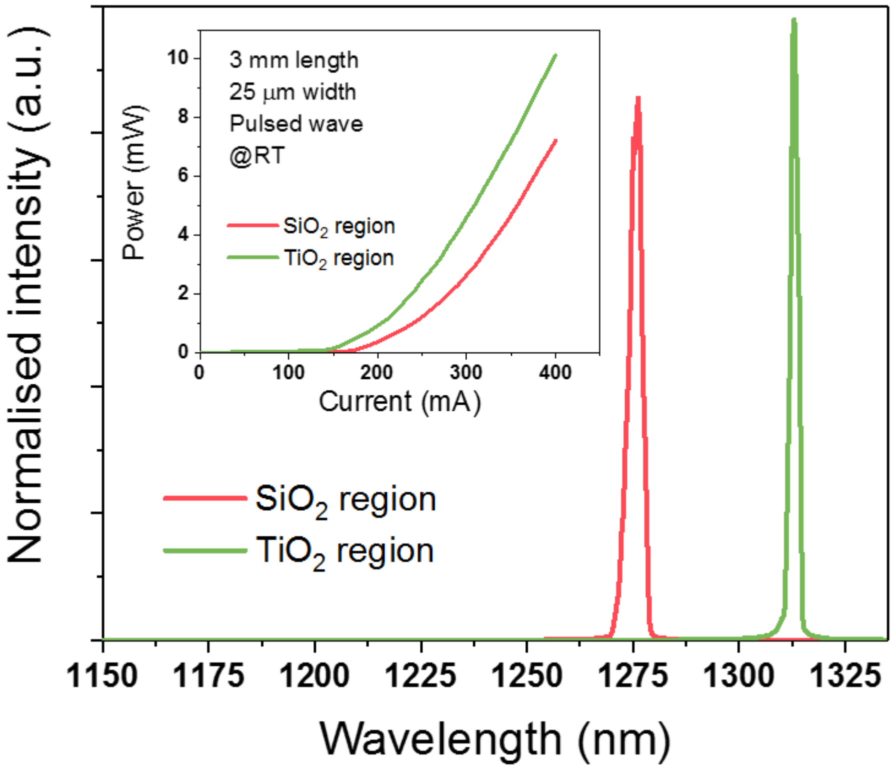

Figure 5.12 Normalised emission spectra of QD lasers on Si after the RTA process in SiO_2*- and* TiO_2*-capped region under pulsed operation. Inset: L-I curves of QD lasers on Si after the RTA process in* SiO_2*- and* TiO_2*-capped region under the pulsed-wave operation with 1% duty cycle and 1 μs pulsed width.*

5.4 Conclusion

In this chapter, we have performed a comparative study of the intermixing effects on InAs/GaAs QDs directly grown on Si capped by separated SiO_2 and TiO_2 layers. The optimisation of annealing conditions in terms of the temperature and duration and STEM analysis were implemented for both capping materials. Electrically pumped InAs/GaAs QD lasers directly grown on Si with two different emission wavelengths of 1275 nm and 1313 nm (38 nm difference) were achieved from one single wafer by the selective area intermixing method. These results are fulfilling the requirement of the bandgap difference of QD laser and EA modulator for realising Si-based optical integrated circuits [21].

5.5 Contribution Statement

I would like to acknowledge the technical support of the QD sample supply by Dr Mingchu Tang and Prof. Huiyun Liu and the help of TEM operation by Dr Wei Li at the Beijing University of Technology.

5.6 References

[1] B. S. Ooi *et al.*, “Selective quantum-well intermixing in GaAs-AlGaAs structures using impurity-free vacancy diffusion,” *IEEE J. Quantum Electron.*, vol. 33, no. 10, pp. 1784–1792, 1997.

[2] R. J. Deri and E. Kapon, “Low-loss III-V semiconductor optical waveguides,” *IEEE J. Quantum Electron.*, vol. 27, no. 3, pp. 626–640, Mar. 1991.

[3] G. P. Agrawal, *Fiber-optic communication systems*. John Wiley & Sons, 2010.

[4] S. J. Chua and B. J. Li, “Introduction to optical switches,” in *Optical Switches*, Elsevier, 2010, pp. 1–4.

[5] Y. Chu, M. G. Thompson, R. V Penty, I. H. White, and A. R. Kovsh, “1.3 µm Quantum-Dot Electro-Absorption Modulator,” in *Conference on Lasers and Electro-Optics/Quantum Electronics and Laser Science Conference and Photonic Applications Systems Technologies*, 2007, p. CMP4.

[6] P. Jin *et al.*, “Quantum-confined Stark effect and built-in dipole moment in self-assembled InAs⁄GaAs quantum dots,” *Appl. Phys. Lett.*, vol. 85, no. 14, pp. 2791–2793, Oct. 2004.

[7] I. B. Akca *et al.*, “Electro-optic and electro-absorption characterization of InAs quantum dot waveguides,” *Opt. Express*, vol. 16, no. 5, p. 3439, 2008.

[8] J. H. Marsh, “Quantum well intermixing,” *Semicond. Sci. Technol.*, vol. 8, no. 6, pp. 1136–1155, Jun. 1993.

[9] G. Zhang and M. Pessa, “Thermal processing of strained-layer InGaAs/GaAs quantum well interface,” *Appl. Surf. Sci.*, vol. 75, no. 1–4, pp. 274–278, Jan. 1994.

[10] B. Elman, E. S. Koteles, P. Melman, and C. A. Armiento, “GaAs/AlGaAs quantum-well intermixing using shallow ion implantation and rapid thermal annealing,” *J. Appl. Phys.*, vol. 66, no. 5, pp. 2104–2107, Sep. 1989.

[11] D. Bhattacharyya, A. S. Helmy, A. C. Bryce, E. A. Avrutin, and J. H. Marsh,

"Selective control of self-organized $In_{0.5}Ga_{0.5}As$/GaAs quantum dot properties: Quantum dot intermixing," *J. Appl. Phys.*, vol. 88, no. 8, p. 4619, 2000.

[12] Y. Ji, W. Lu, G. Chen, X. Chen, and Q. Wang, "InAs/GaAs quantum dot intermixing induced by proton implantation," *J. Appl. Phys.*, vol. 93, no. 2, pp. 1208–1211, Jan. 2003.

[13] K. J. Zhou *et al.*, "Quantum dot selective area intermixing for broadband light sources," *Opt. Express*, vol. 20, no. 24, p. 26950, Nov. 2012.

[14] H. S. Lee *et al.*, "Selective area wavelength tuning of InAs/GaAs quantum dots obtained by TiO_2 and SiO_2 layer patterning," *Appl. Phys. Lett.*, vol. 94, no. 16, p. 161906, Apr. 2009.

[15] "PRO Line PVD 75 – Versatile Sputtering, Electron Beam, & Thermal Evaporation Deposition Platform," *Kurt J. Lesker Company*. [Online]. Available: https://www.lesker.com/newweb/vacuum_systems/deposition_systems_pvd_prolinepvd75.cfm. [Accessed: 20-Feb-2020].

[16] E. Carlino and V. Grillo, "Atomic-resolution quantitative composition analysis using scanning transmission electron microscopy Z-contrast experiments," *Phys. Rev. B*, vol. 71, no. 23, p. 235303, Jun. 2005.

[17] W. Li *et al.*, "Effect of rapid thermal annealing on threading dislocation density in III-V epilayers monolithically grown on silicon," *J. Appl. Phys.*, vol. 123, no. 21, p. 215303, Jun. 2018.

[18] M. Srujan, K. Ghosh, S. Sengupta, and S. Chakrabarti, "Presentation and experimental validation of a model for the effect of thermal annealing on the photoluminescence of self-assembled InAs/GaAs quantum dots," *J. Appl. Phys.*, vol. 107, no. 12, p. 123107, Jun. 2010.

[19] Y. Zhang, Z. Wang, B. Xu, F. Liu, Y. Chen, and P. Dowd, "Influence of strain on annealing effects of In(Ga)As quantum dots," *J. Cryst. Growth*, vol. 244, no. 2, pp. 136–141, Oct. 2002.

[20] S. J. Xu *et al.*, “Effects of rapid thermal annealing on structure and luminescence of self-assembled InAs/GaAs quantum dots,” *Appl. Phys. Lett.*, vol. 72, no. 25, pp. 3335–3337, Jun. 1998.

[21] T. M. Hsu, Y. S. Lan, W.-H. Chang, N. T. Yeh, and J.-I. Chyi, “Tuning the energy levels of self-assembled InAs quantum dots by rapid thermal annealing,” *Appl. Phys. Lett.*, vol. 76, no. 6, pp. 691–693, Feb. 2000.

[22] R. L. Meek, “A Rutherford scattering study of catalyst systems for electroless Cu plating,” *J. Electrochem. Soc.*, vol. 122, no. 11, p. 1478, 1975.

[23] M. A. Cusack, P. R. Briddon, and M. Jaros, “Electronic structure of InAs/GaAs self-assembled quantum dots,” *Phys. Rev. B,* vol. 54, no. 4, pp. R2300–R2303, Jul. 1996.

[24] J. Kim, L. W. Wang, and A. Zunger, “Comparison of the electronic structure of pyramidal quantum dots with different facet orientations,” *Phys. Rev. B - Condens. Matter Mater. Phys.*, vol. 57, no. 16, pp. R9408–R9411, Apr. 1998.

[25] J. Pakarinen *et al.*, “Annealing of self-assembled InAs/GaAs quantum dots: A stabilizing effect of beryllium doping,” *Appl. Phys. Lett.*, vol. 94, no. 7, p. 072105, Feb. 2009.

Chapter 6

Conclusion and future work

6.1 Conclusion

This thesis is aimed to make a contribution to the monolithically integrated optical transmitter on the Si platform. The whole works are based on the well-studied III–V QD lasers directly grown on Si substrates as the on-chip light source for Si transmitter.

In Chapter 1, the motivation for developing monolithically integrated QD lasers on Si for Si photonics was first presented. Next, the challenges and respective strategies for III–V integration on Si were reviewed. The superiorities in both the static and dynamic properties of QD lasers coming from their unique delta-like DOS were then discussed. The big picture of a low-cost optical transmitter, including a DFB QD laser, a QD EA modulator and low-loss SOI waveguide, integrated on a Si platform had been proposed.

Chapter 2 detailed the experimental methods used to obtain the material characteristics by AFM, PL and SEM. We also discussed device fabrication optimisation for broad-area and narrow-ridge lasers, as well as the laser device characteristics.

In Chapter 3, the noise (RIN) and reliability in the real transmission of the Si-based QD laser have been examined. The RIN of the InAs/GaAs QD laser growth on Si is measured at an ultra-low level of –150 dB/Hz. Using this low-noise Si-based laser, we then demonstrated 25.6 Gb/s data transmission over 13.5 km SMF-28 by external modulation. These low-cost FP laser devices are promising candidates to provide cost-effective solutions for use in uncooled Si photonics transmitters.

The feasibility of integrated the grown QD laser with other components on Si has been investigated in Chapter 4. By using the rapid prototype technique, FIB, the post-fabrication of Si-based QD lasers with etched facet was examined at first. Facet angles and groove etching were also investigated to convert the laser device to the ASE devices and two-section devices for future integration studies.

Chapter 5 demonstrated the selective area intermixing technique, which could tailor the bandgap of III–V compound semiconductors spatially across the wafer up to 28 meV (38 nm), by two different dielectric materials. This result fulfils the requirement of integration of grown QD laser and EA modulator and provides a potential shortcut for optical integrated circuits for Si photonics.

6.2 Future work

Figure 6.1 reviews the concept of the monolithically integrated optical transmitter on Si proposed in section 1.4. Although the research in the thesis made several contributions to the realisation of this perspective, there are still a lot of roadblocks that need to be solved. In this section, future works, in terms of increasing modal gain for single transverse mode QD DFB laser and travelling wave electrodes design for high-speed EA modulator, are proposed.

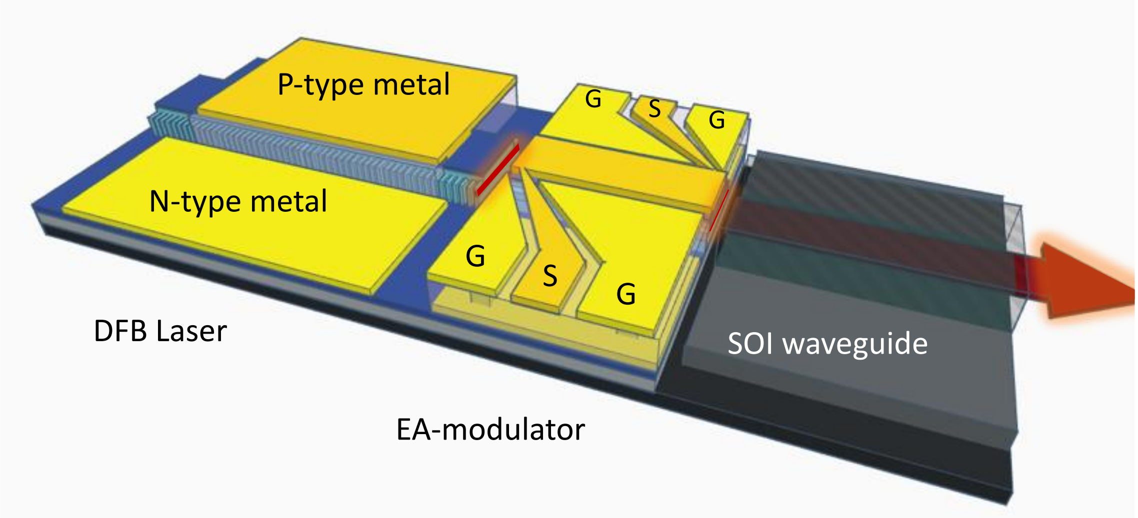

Figure 6.1 Schematic diagram of monolithic integration of a QD DFB laser, QD EA modulator and SOI waveguide on Si platform.

6.2.1 Improving modal gain of QDs

As described in Chapter 1, the reported first QD DFB laser grown on Si has shown second-order mode transverse lasing [1], which is undesired for data transmission. Due to a large refractive index difference by the special lateral surface grating technique for the DFB laser [2], the device requires a narrower laser ridge to achieve the single transverse mode lasing [3] compared with the simple FP laser. However, the reduced ridge width as well as the grating etching process involve additional optical loss, thereby leading to an increased threshold gain and even excited states lasing [4]. It can be explained in Figure 6.2, which shows the plotting of modal gain against the current density of an edge-emitting QD laser. If the necessary threshold gain (dash line of $G_{th}(1)$ in Figure 6.2) is smaller than the maximum modal gain of GS, low-threshold GS lasing takes place. However, the reduced device size increases the threshold gain (dash line of $G_{th}(2)$ in Figure 6.2) above the GS modal gain, the first excited state lasing occurs instead of GS lasing [3]. A high GS modal gain, thus, offers more optical loss budget and smaller cavity of devices lasing at GS.

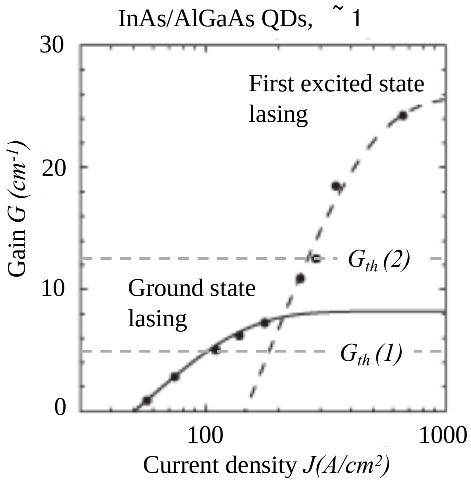

Figure 6.2 Modal gain against the current density of a QD laser with a fitting line of GS lasing and first excited state lasing. [3]

The reported Si-based DFB laser used seven layers of DWELL with a dot-density of ~3×10^{10} cm^{-2} for each QD layers [1]. The estimated modal gain of GS is around 14.7 cm^{-1} [5], which is inferior to the pioneering works grown on a native substrate (> 30 cm^{-1}) [6][7]. Therefore, the fundamental issue for the Si-based QD DFB laser is the insufficient modal gain of the QD material. Comparing with the InAs/GaAs QD grown on a native substrate, it is more challenging to grow QD on the Si substrate. In addition to the DFB laser, the QD EA modulator also requires a high QD density in order to achieve high absorption and thus keep the extinction ratio with shorter device length, thereby significantly increasing the modulation bandwidth [8].

The maximum modal gain (g_{max}) of QD is related to several parameters [9]:

$$g_{max} \propto \frac{1}{\tau_{spon}} \cdot \frac{1}{\Delta\varepsilon_{inhom}} \cdot \frac{\Gamma}{a} \cdot N_{QD} Z_L \qquad \text{Equation 6.1}$$

where τ_{spon} is the spontaneous radiative lifetime, $\Delta\varepsilon_{inhom}$ is the inhomogeneous line broadening, Γ is the optical confinement factor, *a* is the mean size of QDs, N_{QD} is the QD density and Z_L is the number of DWELL layers. The modal gain of GS of QDs (g_{GS}) equals [3],

$$g_{GS} = g_{max}(2p-1), p = {}^{N_{GS}}\!\Big/_{2N_{QD}} \qquad \text{Equation 6. 2}$$

where p is the occupancy ratio and N_{GS} is the carrier density in the GS. According to these two equations, the modal gain can be raised by increasing QD uniformity, QD density and QD layers during the MBE growth. The significant research efforts on improving the quality of InAs/GaAs QDs on GaAs have been made from different groups for many years, which can be the guidance for InAs QDs growth on Si.

A number of researches show that the QD uniformity can be increased by using an InGaAs strain reduced layer (SRL) over the InAs QDs, which can effectively suppress the compositional mixing or segregation of QDs during covering. By this approach, the PL linewidth can be reduced from a typical value of 38 meV to 21 meV [10]. A similar method of using a gradient composition SRL for InAs QD covering has been reported with an ultra-high QD density of 1×10^{11} cm^{-2} [11]. In this technique, the various In contents provides a smaller lattice mismatch of InAs QD with surrounding matrix and a larger strain relaxation effect within the critical thickness of the spacer layer. Moreover, the optimized growth conditions and sequence for suppressing In out-diffusion during QD coverage also brings a high-optical-gain of QD [12]. Figure 6.3 (a) and (b) compares two QD samples with the dot density of 5.9×10^{10} cm^{-2} and QD of 3×10^{10} cm^{-2}. As shown in Figure 6.3 (c), the doubled QD density results in a significant enhancement of modal gain to 35 cm^{-1} [13].

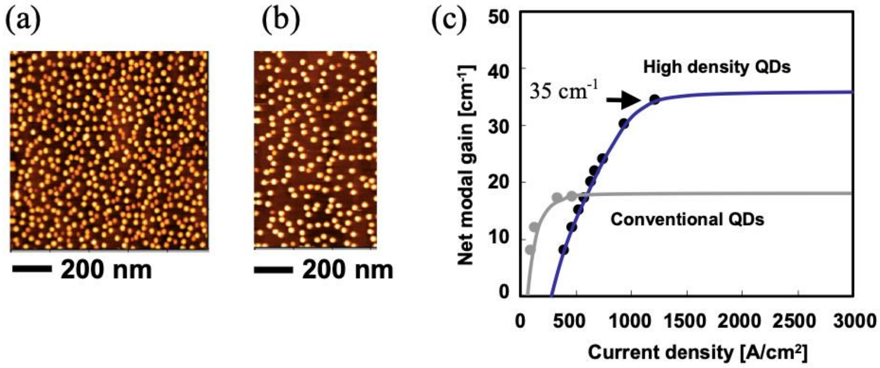

Figure 6.3 AFM images of (a)high density and (b) conventional QDs. (c)net modal gain against current density [13].

Another method of improving GS modal gain is to stack more DWELL layers. However, the accumulated overall strain in the material by the stacked layers will cause defects and nonuniform QDs, since the formation of QDs is extremely sensitive to the strain field inside the structure [14]. The main point is the ability to keep the strain conditions the same for each layer. By optimizing the growth conditions and thickness of the spacer layer between each DWELL layer, five layers of DWELL with high material quality can be achieved [15]. The QD laser with ten-stack of DWELL has also been reported with a low transparency current density [16]. There are also some works focusing on using a strain compensation layer of $In_xGa_{1-x}P$ [17] or GaN_xAs_{1-x} [18] for ten-stack and even 30-stack DWELL layers, respectively.

6.2.2 High-speed EA modulator with travelling-wave electrodes

As mentioned in Chapter 5, the EA modulator uses the Franz-Keldysh effect [19]/QCSE [20] to reduce the bandgap of material by the applied electric field. The transparent active layer begins to absorb light; thus, an extinction ratio of more than 15 dB signals can be realised via the reverse voltage biased of a few volts beyond 40 Gb/s [21][22]. High-performance bulk and QW EA modulators have been investigated and reported for many years [23][24]. There are several papers shown the QD structure has an ultra-fast carrier escape rate [25][26], and strong exciton effect due to Coulombic interaction from the increased carrier confinement [22]. These parameters suggest a highly efficient EA modulation property by using the QD structure. However, a practical III-V QD EA modulator with high modulation rate (>25 Gb/s) has not been demonstrated yet [27][28]. One of the possible reasons is the lower carrier density/modal gain of QD compared with the QW structure. The longer length of QD EA modulator device degenerates the 3-dB modulation bandwidth, as described above. Another important effect is the parasitic capacitance from the device and RF matching at high-frequency operation.

Figure 6.4 shows a circuit representation of parasitic capacitance of a normal GaAs ridge waveguide p-i-n device, which can be used as an EA modulator but strongly limited by the RC-time constant. The total capacitance is comprised by the junction capacitance C_j and stray capacitance C_d in parallel [29]. The C_j is due to the carriers lifetime in the active region and incorporated into the rate equations [30][31]. The stray capacitance C_d is contributed by the different dielectric constants between the highly conducted layers, which can be further divided into two capacitance of C_f and C_b in series. The C_f is due to the separation between metal and surface of p-type layer by the dielectric material (BCB); the C_b is due to the separation of the p-type layer to the top of n-type layer [29].

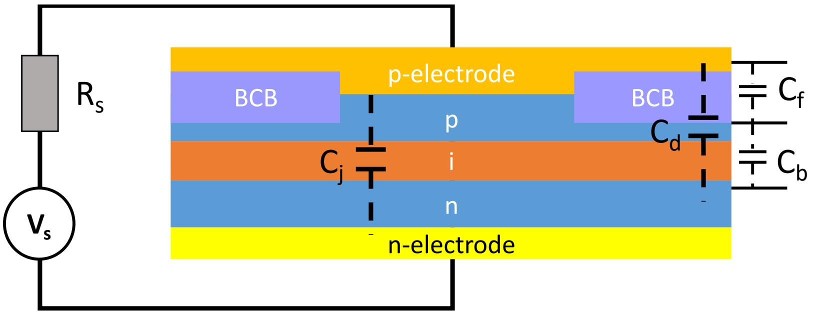

Figure 6.4 The schematic diagram of the parasitic capacitance presented in a simplified GaAs p-i-n device [29].

The junction capacitance is equal to

$$C_j = \varepsilon_{r(GaAs)}\varepsilon_o \frac{A_j}{w_d} \qquad \text{Equation 6.3}$$

where $\varepsilon_r(GaAs)$ is the relative permittivity of GaAs, ε_o is the vacuum permittivity, A_j is the junction area, and w_d is the depletion region width. And the stray capacitance of C_d equals,

$$C_d = (\frac{1}{C_f} + \frac{1}{C_b})^{-1} \ , C_f = \varepsilon_{r(BCB)}\varepsilon_o \frac{A_i}{w_f}, \quad C_b = \varepsilon_{r(GaAs)}\varepsilon_o \frac{A_i}{w_b} \qquad \text{Equation 6. 4}$$

where $\varepsilon_r(BCB)$ is the relative permittivity of BCB, A_i is the area covered by p-type metal, w_f is the thickness of BCB and w_f is the total thickness of the semiconductor device apart from the n-layer, since it connects to the ground. Therefore, the limited-frequency by the electric driving scheme can be calculated by [29]:

$$f_0 = \frac{1}{\pi R_s C_{total}}, \quad C_{total} = C_j + C_d \qquad \text{Equation 6.5}$$

where R_s is the internal impedance coming from the device and the RF source. According to the above equations, the cut-off frequency can be simply increased by reducing the capacitance via a reduced ridge width/p-electrode area [32] and increased thickness of the intrinsic layer/dielectric material [33]. However, the enhanced frequency has an upper limit by these approaches, which may sacrifice the device performance, such as a reduced modulation depth by a thick intrinsic layer and larger optical loss by the narrower ridge width [34]. It is calling for a special design, a travelling wave (TW) electrode structure can overcome the RC limitation, and has been widely utilised in the high-speed EA modulator [34]–[36].

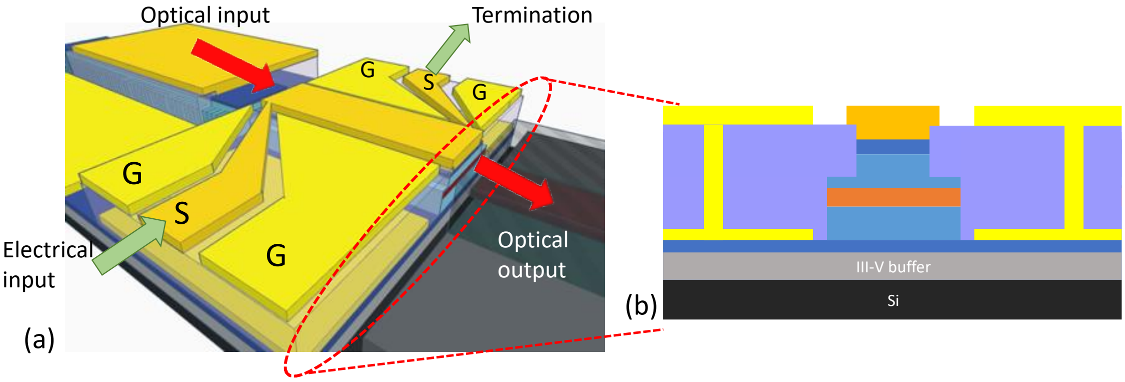

Figure 6.5 (a) Schematic diagram and (b) cross-section of the EA modulator with a travelling wave electrode design for Si-based transmitter.

In the concept of the Si-based transmitter, coplanar waveguide (CPW) electrodes are used as microwave input feed line and output load (termination) line of high-speed electrical transmission, as shown in Figure 6.5 (a). The thick BCB of >3.5 μm thickness with an ultra-low dielectric constant of 2.65, is deposited underneath the electrodes (Figure 6.5 (b)). Moreover, the metal area of the p-electrode is reduced as narrow as the waveguide ridge to a minimum the stray capacitance.

Besides reducing waveguide capacitance, the operation speed of the EA modulator with the TW electrode is also driven by other important factors [34]. One of the factors is impedance matching. In a transmission line, there is a large reflection from the unterminated port, which severely affects the frequency response of the device [37]. A proper choice of termination can significantly increase the frequency response. The termination choice depends on the impedance value of the modulator device itself. A low impedance value is desirable to extend the electrical bandwidth, and it is decided by the geometry of the CPW [34]. Thus, the dimensions of G-S-G pads in Figure 6.5 (a) are needed to be optimized by the simulation to achieve maximum frequency response. Figure 6.6 compares the measured frequency response of a TW-EA modulator without and with different loads (50 Ω and 32 Ω), where the 32 Ω shows the highest response frequency. Although the impedance value of the load can be estimated from a circuit model for a unit length of TW-EA modulator transmission line [38], the accurate value should be measured from a small signal S-parameter measurements [39][40].

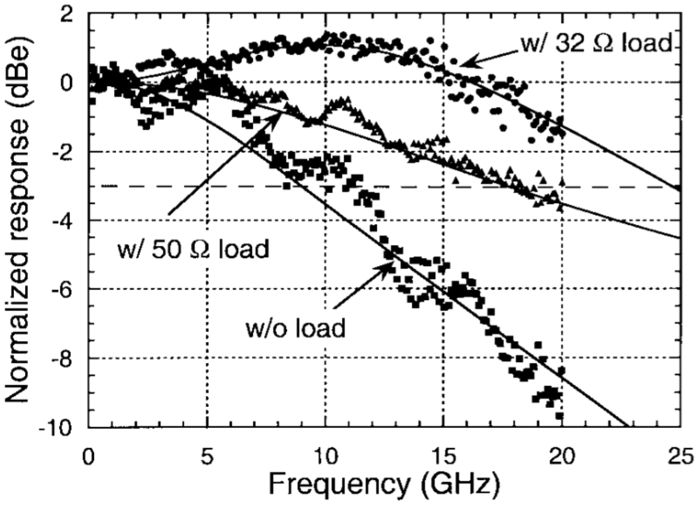

Figure 6.6 Frequency responses of EA modulator with the travelling wave electrodes with no termination (w/o), 50-Ω termination, and 32-Ω termination [35].

Other impact factors of modulator performance are including the velocity matching and the microwave attenuation, which are also affected by the area of the electrodes [38]. All of these parameters need to be carefully simulated and further investigated in future works.

6.3 References

[1] Y. Wang *et al.*, "Monolithic quantum-dot distributed feedback laser array on silicon," *Optica*, vol. 5, no. 5, p. 528, May 2018.

[2] A. I. Laakso, J. Karinen, and M. Dumitrescu, "Modeling and design particularities for distributed feedback lasers with laterally coupled ridge-waveguide surface gratings," *Proc. SPIE 7399, Physics and Simulation of Optoelectronic Devices XIX*, p. 79332K, 2011.

[3] V. M. Ustinov, A. E. Zhukov, A. Y. Egorov, and N. A. Maleev, *Quantum Dot Lasers*. Oxford University Press, 2003.

[4] P. G. Eliseev, H. Li, T. Liu, T. C. Newell, L. F. Lester, and K. J. Malloy, "Ground-state emission and gain in ultralow-threshold InAs-InGaAs quantum-dot lasers," *IEEE J. Sel. Top. Quantum Electron.*, vol. 7, no. 2, pp. 135–142, 2001.

[5] C. Hantschmann *et al.*, "Understanding the bandwidth limitations in monolithic 1.3 μm InAs/GaAs quantum dot lasers on silicon," *J. Light. Technol.*, vol. 37, no. 3, pp. 949–955, Feb. 2019.

[6] M. T. Todaro *et al.*, "High-performance directly modulated 1.3-μm undoped InAs–InGaAs quantum-dot lasers," *IEEE Photonics Technol. Lett.*, vol. 19, no. 4, pp. 191–193, Feb. 2007.

[7] A. Salhi *et al.*, "Enhanced performances of quantum dot lasers operating at 1.3 μm," *IEEE J. Sel. Top. Quantum Electron.*, vol. 14, no. 4, pp. 1188–1196, Jul. 2008.

[8] H. Yu and W. Bogaerts, "An equivalent circuit model of the traveling wave electrode for carrier-depletion-based silicon optical modulators," *J. Light. Technol.*, vol. 30, no. 11, pp. 1602–1609, Jun. 2012.

[9] L. V. Asryan, M. Grundmann, N. N. Ledentsov, O. Stier, R. A. Suris, and D. Bimberg, "Maximum modal gain of a self-assembled InAs/GaAs quantum-dot laser," *J. Appl. Phys.*, vol. 90, no. 3, pp. 1666–1668, Aug. 2001.

[10] K. Nishi, H. Saito, S. Sugou, and J. Lee, "A narrow photoluminescence linewidth

of 21 meV at 1.35 μm from strain-reduced InAs quantum dots covered by $In_{0.2}Ga_{0.8}As$ grown on GaAs substrates," *Appl. Phys. Lett.*, vol. 74, no. 8, pp. 1111–1113, Feb. 1999.

[11] T. Amano, T. Sugaya, and K. Komori, "Highest density 1.3 μm InAs quantum dots covered with gradient composition InGaAs strain reduced layer grown with an As2 source using molecular beam epitaxy," *Jpn. J. Appl. Phys.*, vol. 44, no. No. 14, pp. L432–L434, Mar. 2005.

[12] K. Nishi *et al.*, "Molecular beam epitaxial growths of high-optical-gain InAs quantum dots on GaAs for long-wavelength emission," *J. Cryst. Growth*, vol. 378, pp. 459–462, Sep. 2013.

[13] Y. Tanaka *et al.*, "1.3 μm InAs/GaAs high-density quantum dot lasers," in *2009 IEEE LEOS Annual Meeting Conference Proceedings*, 2009, pp. 668–669.

[14] E. C. Le Ru, A. J. Bennett, C. Roberts, and R. Murray, "Strain and electronic interactions in InAs/GaAs quantum dot multilayers for 1300 nm emission," *J. Appl. Phys.*, vol. 91, no. 3, pp. 1365–1370, Feb. 2002.

[15] H. Y. Liu *et al.*, "Improved performance of 1.3μm multilayer InAs quantum-dot lasers using a high-growth-temperature GaAs spacer layer," *Appl. Phys. Lett.*, vol. 85, no. 5, pp. 704–706, Aug. 2004.

[16] C. Y. Liu, S. F. Yoon, Q. Cao, C. Z. Tong, and H. F. Li, "Low transparency current density and high temperature operation from ten-layer p-doped 1.3μm InAs⁄InGaAs⁄GaAs quantum dot lasers," *Appl. Phys. Lett.*, vol. 90, no. 4, p. 041103, Jan. 2007.

[17] N. Nuntawong, S. Birudavolu, C. P. Hains, S. Huang, H. Xu, and D. L. Huffaker, "Effect of strain-compensation in stacked 1.3μm InAs⁄GaAs quantum dot active regions grown by metalorganic chemical vapor deposition," *Appl. Phys. Lett.*, vol. 85, no. 15, pp. 3050–3052, Oct. 2004.

[18] R. Oshima, T. Hashimoto, H. Shigekawa, and Y. Okada, "Multiple stacking of self-assembled InAs quantum dots embedded by GaNAs strain compensating

layers," *J. Appl. Phys.*, vol. 100, no. 8, p. 083110, Oct. 2006.

[19] J. Liu *et al.*, "Waveguide-integrated, ultralow-energy GeSi electro-absorption modulators," *Nat. Photonics*, vol. 2, no. 7, pp. 433–437, Jul. 2008.

[20] I. B. Akca *et al.*, "Electro-optic and electro-absorption characterization of InAs quantum dot waveguides," *Opt. Express*, vol. 16, no. 5, p. 3439, Mar. 2008.

[21] G. P. Agrawal, *Fiber-optic communication systems*, 4th editio. John Wiley & Sons, 2010.

[22] D. A. B. Miller, D. S. Chemla, and S. Schmitt-Rink, "Electroabsorption of highly confined systems: Theory of the quantum-confined Franz–Keldysh effect in semiconductor quantum wires and dots," *Appl. Phys. Lett.*, vol. 52, no. 25, pp. 2154–2156, Jun. 1988.

[23] A. Abbasi *et al.*, "56 Gb/s electro-absorption modulation of a heterogeneously integrated InP-on-Si DFB laser diode," in *Optical Fiber Communication Conference*, 2017, p. Th4G.2.

[24] T.-H. Wu, Y.-J. Chiu, and F.-Z. Lin, "High-speed (60 GHz) and low-voltage-driving electroabsorption modulator using two-consecutive-steps selective-undercut-wet-etching waveguide," *IEEE Photonics Technol. Lett.*, vol. 20, no. 14, pp. 1261–1263, Jul. 2008.

[25] D. B. Malins, A. Gomez-Iglesias, S. J. White, W. Sibbett, A. Miller, and E. U. Rafailov, "Ultrafast electroabsorption dynamics in an InAs quantum dot saturable absorber at 1.3μm," *Appl. Phys. Lett.*, vol. 89, no. 17, p. 171111, Oct. 2006.

[26] D. B. Malins, A. Gomez-Iglesias, P. Spencer, E. Clarke, R. Murray, and A. Miller, "Quantum-confined Stark effect and ultrafast absorption dynamics in bilayer InAs quantum dot waveguide," *Electron. Lett.*, vol. 43, no. 12, p. 686, 2007.

[27] S.-Y. Lee, S.-F. Yoon, A.-C. Ngo, and T. Guo, "Effects of annealing on performances of 1.3-μm InAs-InGaAs-GaAs quantum dot electroabsorption modulators," *Nanoscale Res. Lett.*, vol. 8, no. 1, p. 59, Dec. 2013.

[28] Y. Chu, M. G. Thompson, R. V Penty, I. H. White, and A. R. Kovsh, “1.3 μm Quantum-Dot Electro-Absorption Modulator,” in *Conference on Lasers and Electro-Optics/Quantum Electronics and Laser Science Conference and Photonic Applications Systems Technologies*, 2007, p. CMP4.

[29] X. Huang, “Monolithically integrated quantum confined Stark effect tuned semiconductor lasers,” Ph.D dissertation, Department of Electronic and Electrical Eng., University College London, 1998.

[30] J. Strologas and K. Hess, “Diffusion capacitance and laser diodes,” *IEEE Trans. Electron Devices*, vol. 51, no. 3, pp. 506–509, Mar. 2004.

[31] S. A. Gurevich, *High Speed Diode Lasers*. Singapore: World Scientific Publishing, 1998.

[32] Y. Matsui, H. Murai, S. Arahira, S. Kutsuzawa, and Y. Ogawa, “30-GHz bandwidth 1.55-μm strain-compensated InGaAlAs-InGaAsP MQW laser,” *IEEE Photonics Technol. Lett.*, vol. 9, no. 1, pp. 25–27, Jan. 1997.

[33] J. E. Bowers, B. R. Hemenway, A. H. Gnauck, and D. P. Wilt, “High-Speed InGaAsP Constricted-Mesa Lasers,” *IEEE J. Quantum Electron.*, vol. 22, no. 6, pp. 833–844, Jun. 1986.

[34] G. L. Li, C. K. Sun, S. A. Pappert, W. X. Chen, and P. K. L. Yu, “Ultrahigh-speed traveling-wave electroabsorption modulator-design and analysis,” *IEEE Trans. Microw. Theory Tech.*, vol. 47, no. 7, pp. 1177–1183, Jul. 1999.

[35] C. Z. Zhang, Yi-Jen Chiu, P. Abraham, and J. E. Bowers, “25 GHz polarization-insensitive electroabsorption modulators with traveling-wave electrodes,” *IEEE Photonics Technol. Lett.*, vol. 11, no. 2, pp. 191–193, Feb. 1999.

[36] H. Yu and W. Bogaerts, “An equivalent circuit model of the traveling wave electrode for carrier-depletion-based silicon optical modulators,” *J. Light. Technol.*, vol. 30, no. 11, pp. 1602–1609, Jun. 2012.

[37] W. A. Davis and K. K. Agarwal, *Radio Frequency Circuit Design*. New York,

USA: John Wiley & Sons, Inc., 2001.

[38] S. Irmscher, R. Lewen, and U. Eriksson, “Influence of electrode width on high-speed performance of traveling-wave electroabsorption modulators,” in *13th International Conference on Indium Phosphide and Related Materials.*, 2001, pp. 436–439.

[39] H. Liao, X. Mei, K. Loi, C. Tu, P. Asbeck, and W. Chang, “Microwave structures for traveling-wave MQW electroabsorption modulators for wideband 1.3-μm photonic links,” *Proc. SPIE 3006, Optoelectronic Integrated Circuits*, 1997.

[40] M. Wang, J. Zhou, X. Zhou, X. Li, and X. Jiang, “Microwave properties of GaAlAs/GaAs MQW traveling-wave interferometer optical modulator,” in *Proceedings of the Sixth Chinese Optoelectronics Symposium*, 2003, pp. 74–77.